Mercury Clusters

from van der Waals molecules to the metallic solid

A thesis submitted in partial fulfillment of the requirements of the degree
of
Doctor of Philosophy
in
Theoretical Chemistry
at
Massey University, Albany
New Zealand.

Nicola Gaston
August 3, 2005

Abstract

The nature of mercury clusters is studied in an attempt to reconcile the behaviour of the solid with that of the smallest molecules. Related systems such as Zn, Cd, and Ba are investigated for comparison. A range of *ab initio* methods are employed, and their accuracy assessed. Density functional theory (DFT) based methods are shown to be unreliable. Different functionals vary widely in their description of a particular system, such as the dimer, while individual functionals vary in accuracy when applied across a range of system sizes. This is related to the neglect of van der Waals forces by DFT for the smaller systems, but raises interesting questions about the solid.

Wavefunction-based methods are seen to be much more reliable than DFT, although a high-level description of correlation is required. Hartree-Fock (HF) calculations are shown to be consistent in their description of systems of all sizes, and therefore although inadequate on its own the addition of a correlation potential derived from the many-body perturbational (MP2) calculation for the dimer corrects HF to produce exactly the correct bond lengths (when compared to the best known data) for all sizes up to the bulk lattice. The use of higher order many-body potentials is investigated and compared to the situation observed for the noble gases, since for small sizes these are the closest analogues of the neutral mercury clusters.

The question of how to simulate transitions in large clusters is addressed. Transitions of interest in clusters are the liquid to solid phase transition, the metal to non-metal transition, or a structural transition from one isomeric motif to another. Therefore the ability to calculate the properties of these clusters accurately is as important as the question of structure. Four-component DFT calculations for the mercury dimer polarisability agree well with the anisotropy derived from Raman spectroscopy.

Various isomers proposed in the literature are compared for the smaller mercury clusters. The structures of cationic clusters are also optimised, and their electronic excitation spectra are investigated through CIS(D) and TD-DFT calculations and

compared to experimental results. The structures of anionic zinc clusters are obtained and the density of states compared with experiment. The structures and spectra of these clusters are related to those seen for the magnesium analogues, and the effect of the *d*-electrons in perturbing the jellium model description of these clusters is considered.

Acknowledgements

I wish to acknowledge the support of the Tertiary Education Commission in the form of a Top Achiever Doctoral scholarship. Thanks to the physics department at the Albert-Ludwigs-Universität, Freiburg, especially Dr Michael Moseler, Dr Bernd von Issendorf, and Professor Dr Hellmut Haberland. Thanks are also due to the Deutsche Akademische Austauschdienst.

I wish to thank Trond Saue for his hospitality in Strasbourg, and help with the frequency dependent polarisability calculations. I appreciate also the assistance of Beate Paulus with the work on solid mercury, for helpful discussions and material.

I am grateful to many coworkers who have helped at various stages of progress. In semi-chronological order, thanks go to Ralf Wesendrup, Gloria Moyano, Ivan Lim, Ralf Tonner, Johannes Gierlich, Tilo Söhnel, Radovan Bast, Bernd Huber, Robert Krawczyk, Behnam Assadollahzadeh, and Mattias Lein. Thanks to Inez Lees for ruthless editing advice.

By far the most important person to thank is my supervisor Peter Schwerdtfeger. Thank you for the privilege of working with you, and for the many useful discussions which I hope will be ongoing for some time yet.

Contents

List of Figures

List of Tables

Chapter 1

Mercury, and clusters

The study of mercury clusters is motivated firstly by the many efforts that have gone into the area of cluster physics in the last couple of decades, which has created a wealth of experimental data. The strong size-dependence of the properties of these small nano-particles, comprised of tens or hundreds or thousands of atoms, has given rise to great hope of a new class of materials. The ability to tailor physical and electronic properties by manipulation of the number of atoms has great implications for modern technology. In the case of mercury, which even in elemental form has unique properties that are not yet fully understood, the motivation to learn what happens in the fundamental interactions between atoms is even greater.

An early paper found deviations from van der Waals behaviour at a size of 12 atoms, and noted behaviour at $n = 13$ that defied the trend, marking it as a uniquely symmetric icosahedral structure [Bréchignac et al., 1988]. This is consistent with what one would expect from arranging close-packed spheres on the surface of a sphere, which is a mathematical problem that goes back to Newton. Rademann, Hensel and co-workers published in 1992 a study of the photoelectron spectra of the neutral clusters sized up to 200 atoms [Rademann et al., 1992]. They observed a non-structured absorption between 4.3 and 6.3 eV up to a cluster size of 13 atoms, but found that for clusters of 20 or more atoms the observed spectra fit closely the Drude model of metallic mercury, and they extracted approximate bond-lengths of 3.1 Å, known to be much closer to the bulk value than that of the dimer. This was accompanied by a similar work [Kaiser and Rademann, 1992], also by Rademann, which found that cluster sizes of about 60 atoms were sufficient for there to be a high density of p-states near the Fermi level. Moreover available theoretical (tight-binding) calculations available at the time found an increase of p-character in clusters between

13 and 19 atoms, indicating an increase in covalency. The p-character of a cluster of 79 atoms was also found to agree very closely with the bulk value. A study of caesium-mercury clusters (Hg_nCs^+) also agreed with the assumption of a transition from van der Waals to covalent (and therefore metallic) bonding at a relatively small size of 30 atoms [Ito et al., 1993].

Later experiments would disagree strongly with these first findings. The definition of metallicity is less stringent for a particle of finite size than for the bulk material, and thus different experiments have come to somewhat different conclusions. A study of the s-p gaps of negatively charged mercury clusters in 1998 by Cheshnovsky and co-workers predicted a very much higher value for the onset of metallicity, at an approximate value which they extrapolated to 400 atoms. Their data covered the range $3 \leq n \leq 250$ [Busani et al., 1998]. At this stage it became clear that the simple concept of a metal to non-metal transition at small sizes, which has been very useful in much of cluster physics, must become in the case of mercury a very complicated evolution from van der Waals behaviour at small sizes, gradually to covalently bound clusters and then eventually to the metallic state. However this is no simple monotonic behaviour, as it is constantly interrupted by the changing structure of the clusters themselves. For small clusters the addition of a single atom may change many properties though the underlying structural motif is constant, such as is observed with the completion of the icosahedron on going from 12 atoms to 13. In large clusters the impact of adding a single atom may be less at first glance, except that it has been shown that competing geometries may be favoured differently at neighbouring sizes due to the extra stability involved in completing a symmetrical structure such as an icosahedron. Thus no simple model of the metal to non-metal transition can be expected to work well for mercury, and a true understanding of the processes involved requires careful examination over a range of sizes, of different isomers, their stabilities, electronic structures and associated properties.

1.1 Mercury

The quantum mechanical description of mercury - the atom, clusters, and the bulk - is a challenge for many reasons. Mercury is one of the heaviest elements in the periodic table, 80th out of 94 naturally occuring species. It is one of the largest atoms to assume such an importance in so many disciplines of chemistry, and precisely due to its size is a challenge for theoretical chemistry. With 80 electrons around a heavy (80-proton) nucleus, it is a highly complicated system, especially with the inclusion

of relativistic effects which are very important. It demands the most accurate quantum mechanical methods available to obtain results comparable with experiment. Moreover, experimental data is scarce and often unable to be compared directly with calculated quantities such as energies, or the structure of clusters.

The element itself has a long history, and in some respects it has been thoroughly studied due to its unique physical properties. The chemical symbol, Hg, is derived from the latin *hydrargyrum*, meaning liquid silver. The german *Quecksilber* comes from 'quick silver', which is echoed in english by the meaning of the adjective 'mercurial'. It has the unique property amongst metals of being liquid at temperatures down to $-40°C$, a much lower temperature than any other metal[1]. A simple conclusion that one may draw from this unusual behaviour is that the interatomic forces are weaker than in other systems; this can even be neatly explained by the relativistic stabilisation of the valence shell $6s$-shell, which renders it much more inert than could otherwise be expected.

Since it not only melts at a low temperature but also has a low boiling point, gaseous mercury has been studied extensively. In the vapour phase fluid mercury is quite different from normal insulating fluids such as the inert gases in that its electronic structure and interparticle interaction are strongly density dependent. The most striking manifestation of this density dependence is the nonmetal to metal transition which occurs when mercury vapour is compressed beyond the region of its liquid-vapour critical point [Hensel and Warren, 1999].

There is evidence that the transition to the near metallic state occurs at large cluster size, although this may be anywhere in the range from 70 to 400 atoms [Bréchignac et al., 1988, Haberland et al., 1990, Busani et al., 1998]. There are, however, still a number of fundamental questions remaining for the simple dimer Hg_2. Recent calculations [Wilson and Peterson, 2003, Schwerdtfeger et al., 2001] have made some progress towards characterising the nature of this small molecule, but the picture is still far from complete due to the many difficulties in accurately describing such a weakly interacting heavy element system.

1.1.1 Relativistic effects

Albert Einstein's theory of special relativity has had profound impact on fundamental physics, but would seem to have little place in chemistry. Certainly most chemically interesting objects; molecules, atoms, nuclei, are moving at classical speeds well below

[1] Francium melts at 27°C, the nearest transition metal after mercury is cadmium which melts at 321°C.

the speed of light. However on closer examination it only takes one relativistic electron to make a relativistic atom. In an atom the size of mercury, with a nucleus of charge $Z = 80$, the 80 electrons surrounding it range from being very tightly bound to the nucleus in the case of the $1s$ or $2s$ electrons, to quite loosely bound in the case of the valence electrons due to shielding by the inner electrons. The core electrons are so tightly bound that their kinetic energy corresponds to relativistic speeds, comparable to the speed of light. This may be interpreted as resulting in an increase of effective mass. The Bohr radius is

$$a_0 = \frac{4\pi\epsilon_0\hbar^2}{me^2} \tag{1.1}$$

and the relativistic mass increase is

$$m = \frac{m_0}{\sqrt{1 - v^2/c^2}} \tag{1.2}$$

so that the radius of a $1s$-electron will decrease by a factor of $\sqrt{1 - v^2/c^2}$. The average speed of a $1s$-electron is Z a.u., which means that for Hg a rough calculation gives a radius of only $\sqrt{1 - 80^2/137^2} \simeq 0.81$ times what it would be non-relativistically.[2] This is a very simple argument, but nevertheless gives a feeling for the origin of relativistic effects in atoms.

However, so much of chemistry relies only on the "slow" valence electrons in the atom that one might argue that relativity cannot play any important part in chemistry. Indeed this was the position taken by Paul Dirac himself in 1929 when he stated that relativistic effects were 'of no importance in the consideration of atomic and molecular structure and ordinary chemical reactions'. Despite the small velocities of the valence electrons, in heavy atoms relativity plays an important role. Due to orthogonality constraints, the valence s-electrons must be affected by the changed core orbitals. In fact, because the probability density of s-orbitals extends in towards the nucleus even for valence states, the valence s-orbitals also contract markedly; the $p_{1/2}$-orbitals do likewise but to a lesser extent. The shielding of the nucleus is improved by the relativistically contracted s- and p-shells, so the $p_{3/2}$-, d- and f-shells actually expand; this is commonly called an *indirect* relativistic effect. In the case of mercury, therefore, the valence $6s$-orbitals are lower in energy while the $6p$-orbitals are slightly higher; the gap between the $6s$-valence and unoccupied $6p$-orbitals[3] is therefore greater than it would be in the nonrelativistic case. Gold

[2] The speed of light is $c = 137.036$ in atomic units.

[3] This $6s$-$6p$ gap becomes the all-important band gap due to hybridisation in clusters and bulk mercury.

exhibits the largest change in behaviour (in the third row of the transition series) due to relativistic effects. It is closely followed by mercury, due to the relativistically increased $6s$-$6p$ and decreased $5d$-$6s$ gaps. The qualitative effects of relativity are often demonstrated by the statements that a) non-relativistic gold would be colourless, like silver, and not yellow; b) mercury is a liquid at room temperature due to relativistic effects. Unfortunately only the first of these claims has been verified by band structure calculations (although it may still be due to surface plasmons).

A variety of properties of the atom (and simple molecules) have been well studied using relativistic methods. The importance of relativistic effects can be quickly understood by comparing the non-relativistic and relativistic valence orbital energies. Even though relativistic effects are greatest near the nucleus, the indirect effects of screening on the outer electrons results in large effects for the valence orbitals. The valence $6s$-orbital contraction with respect to the non-relativistic orbital affects all behaviour of the element. Thus for example polarisabilities and ionisation potentials show entirely different trends depending on whether they are calculated non-relativistically (NR) or relativistically (R) [Seth et al., 1997], as shown in Figures 1.1 and 1.2.

In fact almost all the characteristics of mercury that are of interest to chemistry or physics will be strongly affected by relativistic effects. These may include not only the low temperature melting behaviour, but also the shortened bond lengths and 2-coordinate complexes, as was suggested and explained by Pekka Pyykkö in an important early paper of relativistic quantum chemistry [Pyykkö, 1988]. Of more direct relevance to the study of clusters are the results of Singh, which suggest that non-relativistic clusters would become metallic at a much smaller size, around 13 atoms [Singh, 1994].

1.1.2 Weak interactions and van der Waals bonds

The term 'van der Waals molecule' arises from the assumptions required to derive the van der Waals (vdW) equation

$$\left(P + \frac{a}{\overline{V}^2}\right)(\overline{V} - b) = RT \tag{1.3}$$

which is a modification of the ideal gas law to allow molecules to be hard spheres which attract at long range. The parameters a and b describe the interaction strength and finite extension of the molecules respectively. $P, \overline{V}, R$, and T are likewise the pressure, molar volume, gas constant and temperature.

The distinctive behaviour of vdW bonded species requires special attention. A

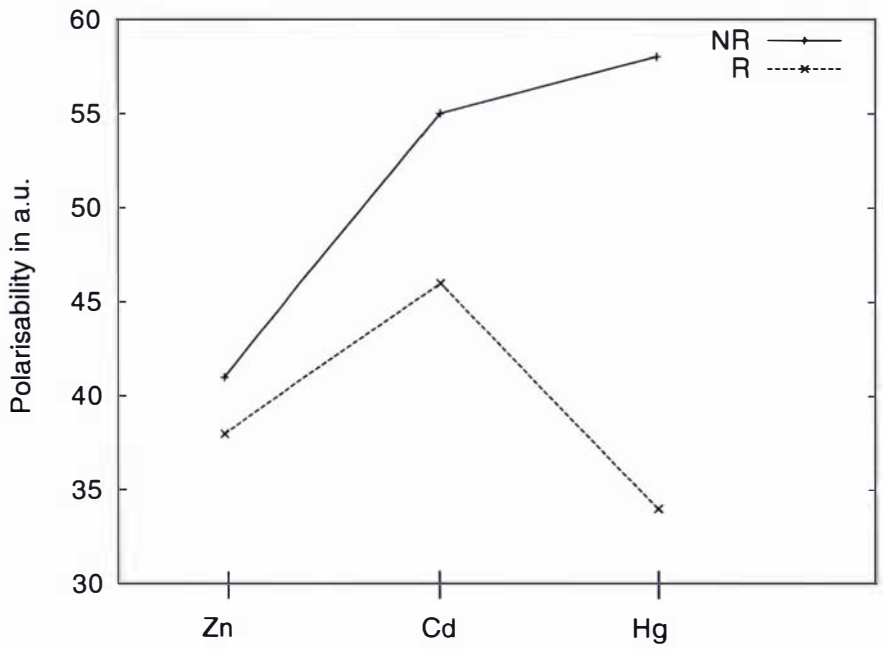

Figure 1.1: Non-relativistic and relativistic coupled cluster (CCSD(T)) calculations of the atomic polarisability, as in ref. [Seth et al., 1997]

weak interaction may be characterised loosely as one with a small dissociation energy and long bond-length, compared to a covalently bonded species which might be structurally the same.

A simple example of this is the hydrogen molecule. The singlet state, $^1H_2$, is formed from two hydrogen atoms with antiparallel spins;

$$H(\uparrow) + H(\downarrow) = {}^1H_2 \tag{1.4}$$

whereas if the atoms approach with parallel electron spins

$$H(\uparrow) + H(\uparrow) = {}^3H_2 \tag{1.5}$$

then a triplet state is formed, which is a weakly bound vdW molecule. The binding energies for these two species are 432 kJmol^{-1} and 0.05 kJmol^{-1} for the covalent and vdW species respectively [Hobza and Zahradnik, 1980]. For the vdW species, this energy is so small that this state is normally termed the repulsion state. However this small non-covalent binding energy is responsible for a great number of physical

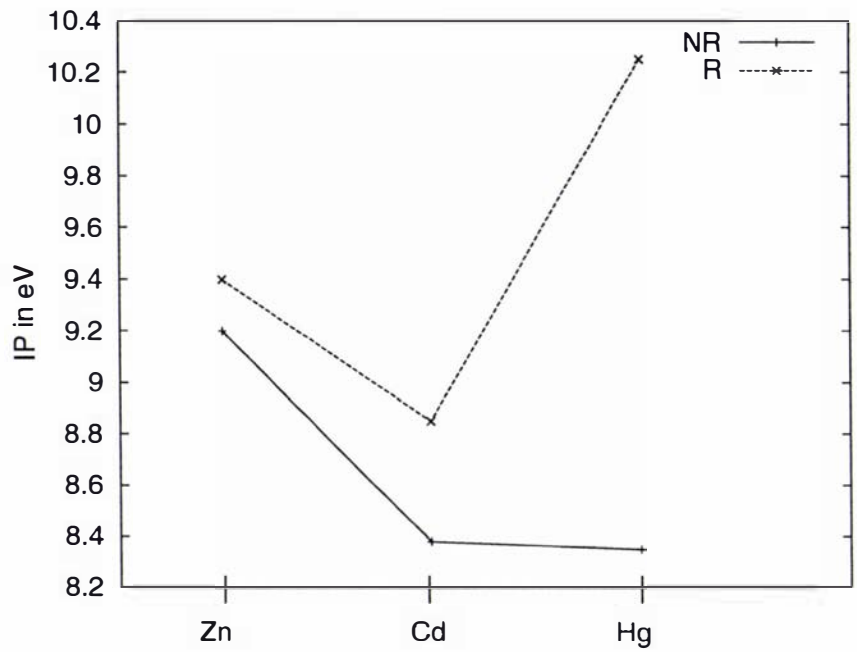

Figure 1.2: Non-relativistic and relativistic coupled cluster (CCSD(T)) calculations of the atomic ionisation potential, after ref. [Seth et al., 1997]

phenomena: e.g. intermolecular interactions such as the H_2O dimer or the hydrogen bonding responsible for determining the configuration of proteins. Noble gas dimers are similarly bound only by a closed-shell interaction which is non-covalent.

All these systems share the same basic physics underlying the form of the dimer potential. There is a short-range atom-atom (or molecule-molecule) repulsion which increases rapidly once two nuclei become close. Over a middle range the electron-electron interaction is attractive, but decays away as the bond length is increased.

The Lennard-Jones potential [Jones, 1924] is commonly used to model this behaviour. The repulsive potential is then represented by a term of the form;

$$V_R(r) = \frac{c_R}{r^{12}} \tag{1.6}$$

and the attractive part is

$$V_A(r) = -\frac{c_A}{r^6} \tag{1.7}$$

where the r^{-12} dependence is somewhat arbitrary but is computationally advantageous due to the r^{-6} attraction. The r^{-6} term is derived from the interaction energy

of two dipoles,

$$E = -\frac{\mu_1 \mu_2}{4\pi\varepsilon_0 r^3} \tag{1.8}$$

where μ_i is the dipole moment of atom (or molecule) i, and the dipoles are arranged linear and parallel, separated by a distance r:

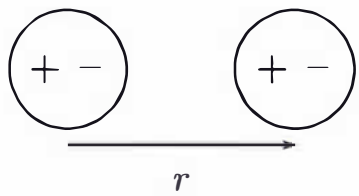

Then as the dipoles are rotated with respect to each other this is more generally

$$E = -\frac{\mu_1 \mu_2}{4\pi\varepsilon_0 r^3}\left[(\sin\Theta_1 \sin\Theta_2 \cos(\Theta_1 - \Theta_2) - 2\cos\Theta_1 \cos\Theta_2)\right] \tag{1.9}$$

where the angles Θ_i are those describing the rotation of each molecule with respect to the other either as considered in plane i (say the plane of the paper is 1 and the perpendicular plane is 2) such that if the dipoles are mutually orthogonal the interaction is zero.

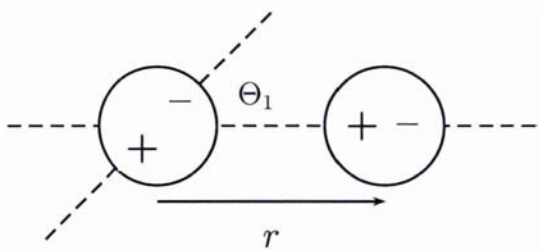

Therefore by averaging over all possible orientations the expression

$$E = -\frac{2\mu_1^2 \mu_2^2}{3kT(4\pi\varepsilon_0)^2 r^6} \tag{1.10}$$

is obtained [Hobza and Zahradnik, 1980]. This is the origin of the r^{-6} term used in the Lennard-Jones potential; although dipole-quadrupole and quadrupole-quadrupole interactions (r^{-8} and r^{-10} respectively) may modify the interaction energy a little, they are very much weaker within this model.

In the case of a closed shell atom such as mercury or the noble gases, there is no permanent dipole. The vdW interaction therefore arises as the result of induced

dipole interactions. This is called the induction energy when a permanent dipole induces a dipole moment, and the dispersion energy when time-dependent fluctuations in the polarisation of each atom result in an 'induced-dipole-induced-dipole' (DD) interaction. In the latter case the charge fluctuations within one atom will create a (time-dependent) electric field **E**. This will then induce a dipole moment $\boldsymbol{\mu}_{ind}$ in a neighbouring closed-shell atom proportional to the polarisability α of that atom:

$$\boldsymbol{\mu}_{ind} = \alpha \mathbf{E}. \tag{1.11}$$

The vdW interaction energy here is described by an expression analogous to that of equation (1.10);

$$E = -\frac{3\alpha^2 E_1}{4(4\pi\varepsilon_0)^2 r^6} = \frac{C_6}{r^6} \tag{1.12}$$

where α is the polarisability of the atom or molecule and E_1 is the first ionisation energy. The coefficient C_6 in equation (1.12) is given approximately according to the Drude model (see for example reference [Rigby et al., 1986]). The origin of this term is the 'induced-dipole-induced-dipole' interaction, but with the inclusion of analogous dipole-quadrupole (DQ) and quadrupole-quadrupole (QQ) interactions one obtains the leading terms of the series

$$E_{dispersion} = \frac{C_6}{r^6} + \frac{C_8}{r^8} + \frac{C_{10}}{r^{10}} + \ldots \tag{1.13}$$

where the higher order terms are commonly negligible at long distances but become important at distances around r_{min}.

The Lennard-Jones potential is commonly written in the form

$$V_{LJ}(r) = \varepsilon \left\{ -2\frac{r_{min}^6}{r^6} + \frac{r_{min}^{12}}{r^{12}} \right\} \tag{1.14}$$

where ε is a constant with the unit of energy which defines the binding energy of the potential at the minimum; r_{min} is the equilibrium bond length.

1.1.3 Simulations

The challenge of reproducing the unique melting behaviour of mercury from *ab initio* simulation of the system is still a long way from being feasible. The first step necessary in a simple algorithm might be to reproduce correctly the diatomic potential curve, for which some experimental data is available. For mercury the non-additive many-

body corrections, which must eventually converge towards the bulk limit of millions of atoms interacting, should also be examined.

In the most general case the potential energy of a system of N atoms is given by

$$V = \sum_i v_i(r_i) + \sum_i \sum_{j>i} v_2(r_i, r_j) + \sum_i \sum_{j>i} \sum_{k>j>i} v_3(r_i, r_j, r_k) + \ldots \tag{1.15}$$

where the indices on the sums prevent double counting of pairs, triplets etc. The first term allows for the effect of some field on the energy of a particle at some position r_i, the second is the pair potential, the third is the triplet or three-body potential. One of the most common pair potentials used is the Lennard-Jones potential described in the preceeding section; the three-body and higher order terms are most often neglected. Although 3-body effects are undoubtedly important in many cases, they are computationally much more expensive than the two-body interaction and so most commonly an effective pair potential is used:

$$V_{\text{eff}} \simeq \sum_i v_i(r_i) + \sum_i \sum_{j>i} v_2^{\text{eff}}(r_i, r_j) \tag{1.16}$$

where $v_2^{\text{eff}}(r_i, r_j)$ will be based on the binding potential of a many-body system, and partially includes higher order effects. However as a consequence the effective potential may turn out to depend on the density or more generally the size of the system, which is unsatisfying.

In simulating the bulk, periodic boundary conditions are applied in order to remove surface and finite size effects. Therefore the calculation will be of the total pair potential over a certain number of atoms situated in a box. The boundary conditions will then allow for the movement of an atom out of this box and into a neighbouring one. A matching atom is then constrained to move into the simulation box from the opposite direction. Thus a constant number of atoms is kept in the box at all times, without restricting the movement of atoms into and out of this simulation space [Allen and Tildesley, 1986].

In studying the transition from liquid to solid behaviour, there are a number of characteristics of each phase that can be observed, and which may be used to determine the appropriate phase as a function of the simulation parameters. First, the order of the solid lattice is manifested in a radial structure function $g(r)$ which is a measure of the density of atoms as one moves along any direction from a point centered on an atom. Thus when r equals the nearest neighbour distance of the lattice, the first peak is observed; at the second nearest neighbour distance a smaller

peak appears[4]. As temperature is increased these peaks become much broader until they essentially overlap. At this point, when there is a finite density of atoms between the lattice sites, the solid may be said to have melted. This is shown in Figure 1.3 where the temperature and bond length are given in reduced units, such that the nearest neighbour distance (given on the x-axis) is one, and the temperature is given in terms of the potential minimum energy as $T_{\text{reduced}} = kT/E_{min}$.

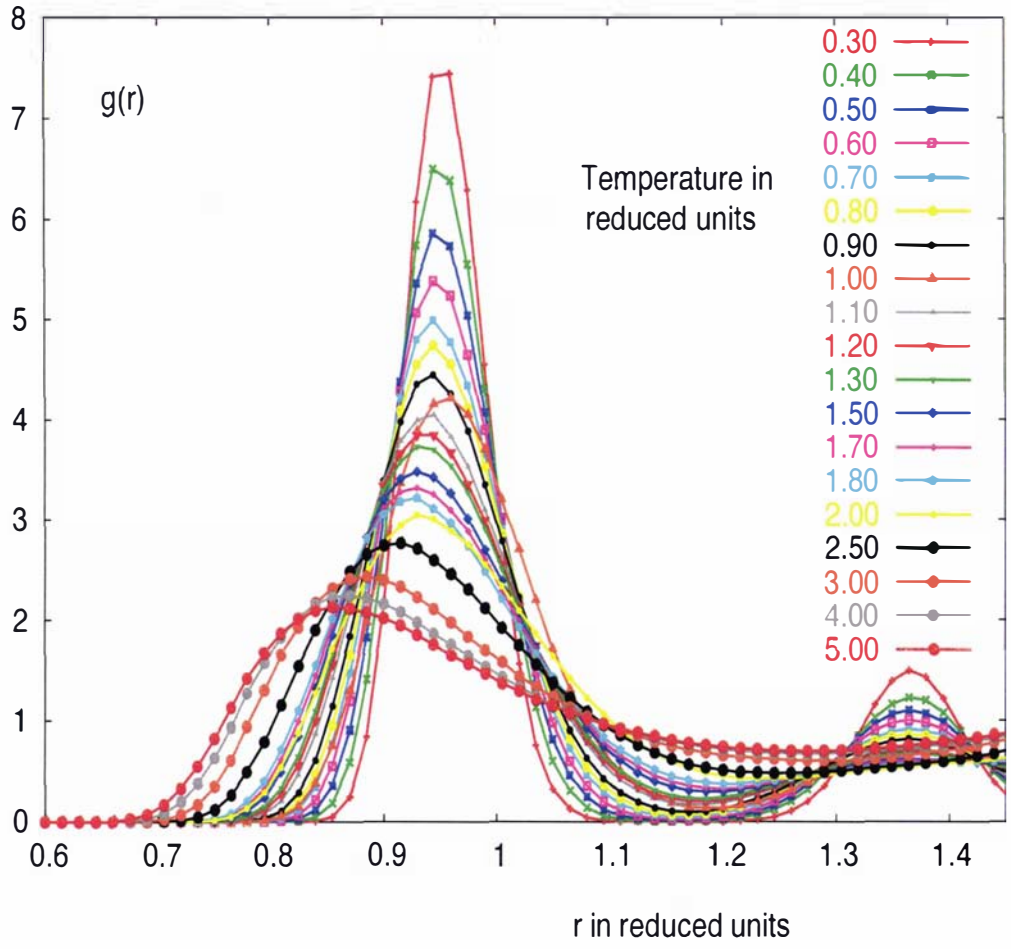

Figure 1.3: The radial distribution function $g(r)$. The distance r is expressed in factors of the nearest neighbour distance in the bulk. The temperature is expressed in reduced units relative to the depth of the potential well, which here is the Lennard-Jones potential.

[4]Since the spherical volume defined by this second nearest neighbour radius is larger, the associated density must be less.

These temperature effects are simulated commonly with the use of statistical mechanics and Monte Carlo or related statistical methods. A good treatment of the necessary background is given in reference [Allen and Tildesley, 1986], for example.

1.2 Clusters

A cluster is a molecule (M_N) assembled from a number N of identical units M, which may be atoms or molecules themselves. In discussing clusters it is implicit that one is interested in the size-dependent properties of the molecule. This may mean looking at the changing behaviour as the number of particles increases towards the bulk, for example structural transitions or pseudo-phase transitions such as the onset of metallic behaviour. In the case of simple alkali or noble metals the number of electrons in the cluster explains much of the observed behaviour. The dependence of the minimum energy structure of the cluster on the number of atoms can have important consequences for measureable quantities.

In the case of mercury clusters the metal to non metal (MNM) transition has attracted the most attention, although this is now known to be a more complex transition from van der Waals to covalent to metallic bonding, which has a complicated size dependence. [Haberland et al., 1990] The choice of observables with which to follow the transition – whether the singlet-triplet gap, ionisation potentials or a more indirectly related quantity – has a manifest effect on the characterisation of the transition as either sudden or slow, and the quantitative size-dependence.

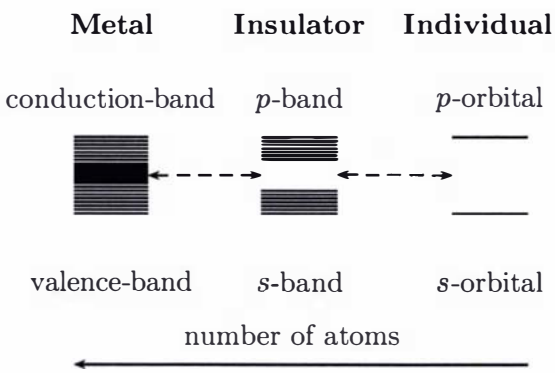

Figure 1.4: Schematic of the development of the band gap from individual orbitals. The number of atoms increases from right to left.

In the case of finite-sized clusters the use of the term metallic can be problematic, but it is generally understood that this describes a pseudo-metallic state where the *s*-*p*-gap, or band-gap, has closed (or becomes smaller than kT).

It is reasonable to divide a general discussion of clusters into two parts; first the electronic effects seen in metallic clusters and described by the jellium model, and secondly a discussion of geometric effects on clusters where parameters such as surface area are important, in contrast to the bulk.[Martin, 1996]

1.2.1 The jellium model

Modern cluster physics started in 1983, when the simple assumption of a spherical potential well containing electrons was observed by Knight and others to predict extremely well the abundance spectra of alkali metal clusters. [Knight et al., 1984a, Knight et al., 1984b] At the same time, Ekardt developed the jellium model (JM) for clusters in which the cluster is a sphere of positive charge in which the electrons behave as a uniform electron gas. The electronic shell structure predicted by this model is analogous to the shell structure in nuclei; and for electronically closed shell clusters is a good approximation for many purposes. In the case of open-shell systems, one must allow for geometrical distortions according to the Jahn-Teller effect; as a consequence the spheroidal shell model (with two equal axes; $R_x = R_y \neq R_z$) and the elipsoidal shell model ($R_x \neq R_y \neq R_z$) were developed as extensions. For non-simple metals, such as mercury, with more than one valence electron per atom, the JM is less satisfactory, although it is still very useful as a first approximation. However in simple metals, the geometrical structure of the cluster can be assumed to have very little effect on its stability which is primarily determined by its electronic shell structure. [de Heer, 1993, Brack, 1993]

The JM may be derived from the standard Coulomb Hamiltonian with the assumption of a background positive charge to replace the nuclei and core (localised) electrons. This equates to the use of the Born-Oppenheimer approximation to neglect motion of the nuclei as is standard in quantum chemistry, and the replacement of the nucleus-electron potential

$$V_{Ne} = \frac{Z}{r_{Ne}} \tag{1.17}$$

with a constant background charge $\rho_I(r)$, the density of which depends on the metal; the electrons then move in the mean-field so described, with shell effects arising as a result of their quantisation. In the spherical jellium model, the background charge

has the density

$$\rho_I(r) = \rho_{IO}\Theta(r - R_I), R_I = r_s N^{\frac{1}{3}} \tag{1.18}$$

of a uniformly charged sphere of radius R_I given by the number of ions, N. The constant density

$$\rho_{IO} = \left[\frac{4\pi}{3} r_s^3\right]^{-1} \tag{1.19}$$

is given by the Wigner-Seitz radius, r_s, which characterises the metal, and is commonly taken from the bulk lattice. The function Θ ensures that the background charge disappears at the edges of the sphere, and may be defined as

$$\begin{aligned} \Theta(x) &= 1; \quad x < 0 \\ &= 0; \quad x \geq 0. \end{aligned} \tag{1.20}$$

To demonstrate the way that shell effects appear in this model, the simple case of a three-dimensional isotropic oscillator is useful. For electrons of mass m this has the following Hamiltonian;

$$\hat{H} = \frac{p^2}{2m} + \frac{m\omega_0^2 q^2}{2} - U\hbar\omega_0 \left[l^2 - n(n+3)/6\right], \tag{1.21}$$

where p and q are one-electron operators for the mometum and position respectively, l is the angular momentum, and n is the shell number. The third term is an anharmonic correction which modifies the shape of the well, keeping the average shell energy constant. Thus $U = 0$ corresponds to a harmonic well, and small positive values of U reduce the curvature of the bottom of the well, such that a value of $0.02 < U < 0.08$ corresponds to a square well (the appropriate value of U depends on the value of n. This gives energy eigenvalues

$$E_n = \hbar\omega_0 \left\{ \left(n + \frac{3}{2}\right) - U\left[l^2 - n(n+3)/6\right] \right\}. \tag{1.22}$$

In the harmonic case, with $U = 0$, for shell number $n = 1, 2, 3, 4, 5, 6 \ldots$, the resulting occupation is $N = n(n+1) = 2, 6, 12, 20, 30, 42, 56$ electrons. This corresponds to the filling of the $1s, 1p, 2s, 2p, 3s, 3p$ shells (and so on).[5] Taking progressively the sum of these it is clear that the spherically stable 'magic' clusters will be those with 2, 8, 20, 40, 70, 112, and 168 valence electrons. In the particularly relevant case of simple metals (i.e Na, K) with one valence electron per atom, this

[5]Note that this corresponds to the notation of nuclear physics and not to atomic notation.

becomes the magic number of atoms for a particularly stable cluster.

The ellipsoidal shell model corresponds to allowing shell numbers $n_x \neq n_y \neq n_z$, with the resulting energy eigenvalues;

$$E_{(n_x,n_y,n_z)} = \hbar\omega_0 \left[(n_x + \frac{1}{2})\frac{R_0}{R_x} + (n_y + \frac{1}{2})\frac{R_0}{R_y} + (n_z + \frac{1}{2})\frac{R_0}{R_z} \right] \tag{1.23}$$

with R_x, R_y, R_z being the axes of the ellipsoid, the volume is constrained by $R_x R_y R_z = R_0^3$, and the anharmonic term has been dropped for the sake of simplicity. This model allows us to determine the minimum energy states of open-shell clusters, as either oblate or prolate spheroids.

1.2.2 The geometry of clusters

Although electronic effects play a large part in determining the geometries of many clusters, in the case of mercury and other closed shell systems a simple packing model is the best place to start. If atoms are assumed to be simple spheres, and the number of possible bonds is maximised, then it is clear that symmetric, close to spherical geometries will be favoured - as opposed to, for example, two-dimensional sheets or one dimensional strings. Starting with 2, 3, or 4, atoms, the line, triangle and tetrahedron respectively are clearly the favoured structures on the basis of symmetry, maximising the 2-body interaction between pairs of atoms. However as the number of atoms is increased the problem quickly becomes more difficult. Atoms may be placed on the surface of the tetrahedron, so as to bond to the three atoms on the surface, and it is possible to continue in this fashion for some time. However, eventually the surface triangles of such a structure become too small to accept a new sphere, and therefore tetrahedral packing will no longer fill space.

The densest possible packing of space is face-centered-cubic (fcc) packing, where in two dimensions there is a hexagonal arrangement of spheres, which fit exactly into the gaps in the next layer of atoms. Hexagonal close packing (hcp) is closely related and is similarly dense, as it can also be constructed from the two-dimensional close-packed planes. Any form of packing that may be assembled from infinite planes, is of course space filling. However while tetrahedra, octahedra, and cuboctahedra may be cut out of a fcc packed lattice, this does not make them automatic candidates for cluster structures.

An important consideration is the minimisation of surface area with respect to the volume of the cluster. Surface atoms are necessarily participants in fewer bonds than internal atoms, and therefore the higher the surface area, the less stable the

cluster can be. This consideration explains the special stability of the icosahedron. Each of the faces of an icosahedron may be constructed of close-packed spheres, and the structure has the highest symmetry of all discrete point groups. However the improved bonding over the surface comes at a cost; the distance between shells, or an inner layer of atoms and the next is increased in order to obtain the close packed surface. Therefore in clusters that are sufficiently large enough that there are many more inner atoms than surface atoms, the advantage of the icosahedron is lost, and other forms of packing will become more stable.

The size at which this transition occurs is a difficult question, and much debated. It is certainly gradual, involving switches between geometries when a cluster size is reached that produces a 'complete' cluster of a certain geometry. For example at 55 atoms a perfect icosahedron is formed, 147 atoms is a perfect cuboctahedron, and 309 atoms form a truncated decahedrom with square faces. However a simple argument shows that for a cluster of 1000 atoms, the surface area is approximately

$$S.A. = 4\pi \left(\sqrt[3]{1000 \frac{3}{4\pi}} \right)^2 = 483 \tag{1.24}$$

i.e., about 50% of the atoms in the cluster are (by this primitive definition) surface atoms [Martin, 1996]. Of a million atoms, only about 5% are surface atoms. This gives an idea of the range of sizes over which the concept of a cluster applies; even a million atoms does not correspond to the bulk material exactly. In the case of any simple two-body potential such as the Lennard-Jones potential, clusters of icosahedral symmetry are observed up to quite large sizes [Wales et al., 2004]. Although the first two complete icosahedra contain 13 and then 55 atoms, a special stability is also associated with the decahedra of five-fold symmetry that make up partial icosahedra. These include the 7-atom pentagonal bi-pyramid, the 19 atom capped icosahedron which can also be viewed as two fused 13 atom icosahedra, the 23 atom cluster (3 fused) and so on. Therefore, analogous to the magic numbers of the jellium model based on electronic shells, geometric (in this case icosahedral) magic numbers may be based on shells of atoms.

1.2.3 Structural optimisation of clusters

The most thoroughly investigated systems in terms of the search for global minima and structural optimisation are the Lennard-Jones clusters, along with others of the same type (described by a simple two-body potential). The Lennard-Jones potential

has been given previously, in equation (1.14). The Morse potential

$$V_{\text{Morse}} = \epsilon \left(1 - e^{-\beta(r-r_0)}\right)^2 \tag{1.25}$$

has also been widely used, in the case of $\beta r_0 = 6$ it has the same curvature at the bottom of the well as the LJ potential. Many other potentials have been used, fitted to the interaction between two atoms or molecules. They have been applied systematically up to cluster-sizes of hundreds of atoms, and based on certain numbers of interest such as the specially stable magic numbers of different structural regimes, up to tens of thousands of atoms [Northby, 1987, Wales et al., 2004, Doye et al., 1995, van der Waal, 1996, van der Waal et al., 2000] It has been acknowledged that a simple two-body potential will not capture the physics of interactions between many particles. The Axilrod-Teller potential was a first attempt at parametrising the long range three-body interaction in van der Waals molecules based on a perturbational approach to the second order. [Axilrod and Teller, 1943] It has only recently become feasible to include such three-body potentials in algorithms for structural optimisation. Higher-order contributions are consistently neglected, an approximation that is suitable for some systems but may lead to intolerable errors in others.

One of the most important conceptual differences between the macro-scale bulk material and the nano-scale cluster, is that the concept of phase (implying a system in thermodynamic equilibrium) is ill-defined, as the concept of temperature is in fact not applicable to these particles of finite size. Nonetheless, a number of attempts have been made at simulating both the effect of temperature on structure [Moore and Al-Quraishi, 2000] [Bukowski and Szalewicz, 2001] but also on properties such as metallicity [Johnston, 1998] which also require an adapted definition to fit the finite-size regime.

The next step after an analysis of the archetypical Lennard-Jones cluster, is to fit such a potential to a system of physical interest, and then optimise the structures of these specific systems based either on experimental data or an *ab initio* potential [Aziz and Chen, 1968, Aziz, 1993, Christiansen et al., 1981]. For example the Cambridge Cluster database is a compiled list of optimum structures for various noble gas clusters as well as the LJ cluster [Wales et al., 2004].

1.2.4 Experimental synthesis

The production of clusters experimentally is done in a number of ways. The most important sources are

Seeded supersonic nozzle sources which produce metal vapour in a hot oven, which when mixed with an inert carrier gas and then injected into vacuum, results in a supersonic molecular beam. The mixture is cooled by expanding adiabatically into the vacuum, whereupon the metal vapour becomes saturated and condenses into clusters. This continues until the vapour density is too low, which may result in clusters of thousands of atoms. The carrier gas is very important both for reasons of production (collision cross sections) and stabilisation (cooling due to expansion of the gas).

Gas-aggregation sources use the supersaturation of metal vapour introduced into a flow of cold inert gas to induce aggregation. At low temperature, this occurs with the addition of one atom at a time, ignoring the relative stabilities of the clusters, resulting in cluster abundances which are a smooth function of the cluster size. Clusters produced in this manner can contain more than 10000 atoms.

Laser vapourisation sources are useful for metals which cannot be vapourised in an oven. A pulsed laser is focused on a rod of the metal, which is rotated to expose a new section of the rod to the laser. A cold carrier gas is used to cool the vapourised metal, and causes cluster formation. Adiabatic cooling occurs as in the seeded supersonic nozzle source, but much lower temperatures can be achieved.

Pulsed-arc cluster-ion sources are very similar to the laser vapourisation sources, however an intense electrical discharge is used instead of a laser.

Ion sputtering sources produce clusters by impacting a metal surface with high energy inert-gas ions. The clusters are initially very hot, and cool by evaporating atoms; the resulting abundance spectrum therefore reflects the relative stabilities of the cluster sizes.

The type of source chosen for a given experiment will therefore depend on the size range, temperature, production intensity, and the nature of the metal under investigation. Once produced, the nature of the clusters will undergo a series of analyses.

1.2.5 Spectra

The first step in an analysis of the synthesised clusters is a separation according to mass. This relies on an ionisation of the clusters to allow acceleration through an

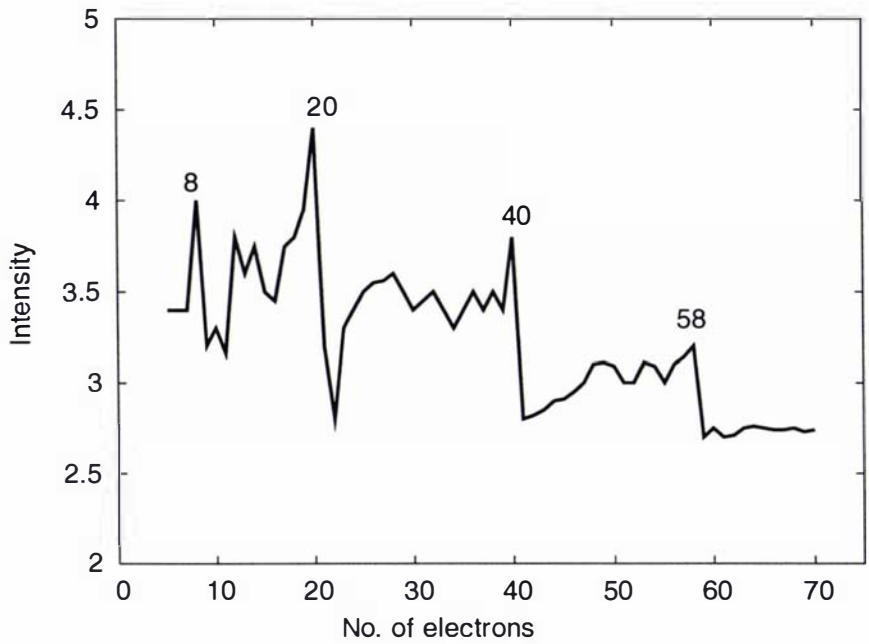

Figure 1.5: Typical experimental mass spectrum showing jellium model magic numbers.

electric field and a subsequent determination of the charge to mass ratio based on the time of flight of the ion. A mass abundance spectrum will reflect the relative stabilities of the cluster sizes, if the production mechanism allowed for cooling by evaporation for example. A typical mass spectrum such as would be observed according to the jellium model is shown in Figure 1.2.5 [de Heer, 1993]. The intensity of the spectrum depends both on the production intensity, and on the efficiencies of the ionisation and detection processes. The spectrum in Figure 1.2.5 shows magic numbers corresponding to the Jellium model.

In order to go beyond an analysis of stability to obtain more information about the nature of the cluster, more sophisticated spectra are required.

In *photoionisation spectra*, the electronic binding energies of a cluster are investigated. Mass-selected clusters are excited by a laser, the emitted electrons are detected and their flight time distribution is then converted into a binding energy distribution. The vertical ionisation potential (VIP) or in the case of anionic clusters, vertical detachment energy (VDE) is then directly available. This corresponds to the difference between the binding energy of the cluster and that of the ionised cluster, where the

geometries of the ionised and un-ionised clusters are the same. On the time-scale of the electron emission, there is no possibility for the structure of the cluster to relax. This is not the same as the adiabatic ionisation potential (AIP), which is the difference in energy between the ground states of the clusters. When such spectra are measured, the discrete ionisation energies are broadened by a number of mechanisms. Thermal effects (i.e. vibrational energy) and detector accuracy limitations result in peaks with the general form of a Gaussian distribution. Therefore in theoretical attempts to reproduce the density-of-states (DOS) shown in the PES, it is common to use Gaussian broadening of the discrete lines obtained.

1.2.6 Charged clusters

Due to limitations on each method of producing clusters, they may often be obtained more easily in an ionised form; therefore there is a lot of experimental data available for both positively and negatively charged clusters. Moreover electronic properties of charged clusters can yield useful information about the bulk, if extrapolated. Cationic clusters are in general more closely related to the neutral species than are the corresponding anions.

The jellium model is often still valid for charged clusters. However sometimes charged clusters may behave differently. For example, it has been shown that in the case of negative cluster synthesis, where the electron is attached after the formation of the cluster, the isomers observed are more likely to be those with the greatest electron affinity (EA) of the corresponding neutral cluster, rather than the global minimum of the negatively charged species as is most often assumed. [Kronik et al., 2002]

In the case of mercury, the noble gas-like behaviour of the neutral clusters must be lost on the introduction of a charge (and therefore charge-induced dipole interactions) into the system. It can be expected that cationic mercury clusters may behave similarly to gold clusters for example, where size and relativistic effects may be most closely comparable.

1.2.7 Metal cluster polarisabilities

In the field of atomic polarisabilities, there is a long history of theoretical work that outstrips the experimental data available. This trend was first commented upon by Miller and Bederson, the latter of whom wrote in the early eighties that based upon a review of the field that *"(a) theorists were ahead of experimentalists, and (b) the open shell atoms (other than the alkali atoms) represented the outstanding gap in out*

knowledge. The present experiments on indium were planned as a response. Still, theorists have remained in the front".

It has however been pointed out that in recent years experimental work in the field of metal clusters has overturned this trend and theoretical work has been rather more restricted [Maroulis, 2005]. Such work includes the polarisability of sodium clusters Na_7 to Na_{93} [Tikhonov et al., 2001], nickel clusters Ni_{12} to Ni_{58} [Knickelbein, 2001], niobium Nb_2 to Nb_{27} [Knickelbein, 2003], copper Cu_9 to Cu_{61} [Knickelbein, 2004], and further work on niobium Nb_2 to Nb_{150} [Moro et al., 2003].

A common feature of such studies is that often there are large variations observed in the per atom polarisability of the cluster on going from one size to the next. This has been correlated with a variation on the clusters' geometric structures. Therefore it is possible that a comparison of experimental polarisabilities with theoretical values predicted for different isomers may give clear information about the structure of the observed cluster. Thus, although no experimental values have been published to date for the polarisability of the neutral mercury clusters, these calculations have been done in this thesis in the hope that in the near future such a comparison may be possible.

Chapter 2

Method review and the dimer potential

Different computational methods are required over the range of sizes from the mercury dimer to the solid state. Firstly, because the properties of the system change (e.g. the bulk solid is periodic). Additionally, the computational cost increases with the size of the system, but more quickly with some methods than with others. In this chapter the most general methods are briefly reviewed, and results for the simplest mercury cluster, Hg_2, are examined.

The potential energy curve of Hg_2 was calculated using a large, uncontracted basis set, with the use of various density functionals as well as Hartree-Fock, Møller-Plesset perturbation, and coupled cluster methods. This gives an overview of the performance of different methods for this system. These results are compared with those of Zn_2, Cd_2, and also the group 2 dimer Ba_2 having the same $6s^2$ configuration as Hg.

Zn and Cd are of interest because they are in the same group as Hg, and can be expected to behave similarly. Differences in behaviour can largely be explained by the influence of relativistic effects. Ba is also of interest for comparison as it does not have the $5d$-electrons and so may exhibit marked differences attributable to their presence.

2.1 Quantum mechanics and molecules

The underlying problem in all of quantum chemistry is that of charged (charge q) and massive (mass m) particles interacting according to the Schrödinger equation:

$$\hat{H}\Psi = E\Psi \tag{2.1}$$

where the Hamiltonian operator $\hat{H}$ is

$$\hat{H} = -\frac{1}{2}\sum_i \frac{\nabla_i^2}{m_i} + \sum_{i<j} \frac{q_i q_j}{|\mathbf{r}_i - \mathbf{r}_j|}. \tag{2.2}$$

Atomic units are used such that the electron mass (m_e) and charge (q_e) are 1. Solving the Schrödinger equation for this Coulomb Hamiltonian becomes an increasingly difficult problem as the number of electrons increases, and consequently a series of approximations is necessary. The obvious place to start is by removing the nuclear degrees of freedom, and the fundamental step in electronic structure theory is to separate the electronic from the nuclear motion. Effectively this amounts to asssuming that in any motion of the nuclei, the electrons follow instantaneously; this is well justified by the difference between electronic and nuclear mass, a factor of 10^3 to 10^5, and is known as the Born-Oppenheimer approximation. Thus the total Hamiltonian can be written with nuclear coordinates μ, ν and electronic coordinates i, j as the sum of electronic (kinetic energy), electron-nuclear, electron-electron, and pure nuclear (Coulomb) terms:

$$\hat{H} = -\frac{1}{2}\sum_i \nabla_i^2 - \sum_{\mu,i} \frac{Z_\mu}{|\mathbf{r}_\mu - \mathbf{r}_i|} + \sum_{i<j} \frac{1}{|\mathbf{r}_i - \mathbf{r}_j|} + \sum_{\mu<\nu} \frac{Z_\mu Z_\nu}{|\mathbf{r}_\mu - \mathbf{r}_\nu|}. \tag{2.3}$$

By applying this to the electronic wavefunction ψ_{el}

$$\hat{H}(\mathbf{r},\mathbf{R})\psi_{el}(\mathbf{r},\mathbf{R}) = E_{el}(\mathbf{R})\psi_{el}(\mathbf{r},\mathbf{R}) \tag{2.4}$$

the electronic energy and wavefunction still depend on the nuclear coordinates $\mathbf{R}$, as well as the electronic coordinates $\mathbf{r}$. For any given nuclear coordinates $\mathbf{R}$, the Hamiltonian can then be written purely in terms of $\mathbf{r}$ by neglecting the nuclear-electron and pure nuclear terms. In practice the errors in the Born-Oppenheimer approximation are negligible for any chemical problem where the notion of molecular structure is valid, and it is this E_{el} which is generally referred to as the exact quantum

chemical solution for the electronic Schrödinger equation.

2.2 Basis sets

Electronic orbitals result from the independent particle model and thus dictate the cost of all quantum chemical calculations. A lot of effort can be saved by constructing an appropriate set of basis functions that describe these electronic orbitals, in a mathematically simple way while preserving their original properties, such as antisymmetry through the use of the Slater determinant. From the hydrogenic Schrödinger equation it can be seen that each orbital or single electron wavefunction is always of the form

$$\psi(r) = NR(r)Y_{lm}(\theta, \phi) \tag{2.5}$$

where N is a normalisation constant and the radial function $R(r)$ can only be found exactly in the case of a one-electron atom. The $Y_{lm}(\theta, \phi)$ are the spherical harmonic functions that describe the angular dependence of the orbital. A practical approximation which simplifies the evaluation of two-electron integrals is the Gaussian basis function;

$$\chi^{GTO}(r) = NP(r)e^{-\alpha r^2}Y_{lm}(\theta, \phi) \tag{2.6}$$

where $P(r)$ may be a simple polynomial function. In practice the computational requirements can be further reduced by forming contracted Gaussian type orbitals (CGTOs) as a linear combination of GTOs,

$$\chi_p^{CGTO} = \sum_a C_{ap}\chi_a^{GTO}. \tag{2.7}$$

Then the number of contracted functions will affect the cost of a calculation. An idea of this is given by the commonly used zeta notation, in which single (SZ), double (DZ), and triple (TZ) basis sets contain one, two, and three times the number of atomic orbitals occupied in the neutral atom. While SZ basis sets are almost always too small to be useful, DZ and TZ basis sets are often used, especially with the addition of higher angular momentum (polarisation) functions.

The way that such basis sets are constructed can vary. For example, dual family basis sets may be used in which one set of exponents is used for each even angular momentum number ($s, d, g, \ldots$) basis functions ($l = 0, 2, 4, \ldots$) and another set for all odd ($l = 1, 3, 5, \ldots$). This is the case for the large (all-electron) DZ and TZ basis sets used for the dimer polarisability calculations in Chapter 3.

2.3 Hartree-Fock

The electronic Hamiltonian for a many-electron system is

$$\hat{H} = \sum_i \hat{h}_i + \sum_{i<j} \hat{g}_{ij} + \hat{h}_0 \tag{2.8}$$

where the sum over i is of the one-electron terms, and the $i < j$ summation is of two-electron interaction terms. The $\hat{h}_0$ zero-electron term is the inter-nuclear repulsion, a constant for fixed nuclear positions, and can be omitted by the use of the Born-Oppenheimer approximation. Then

$$\hat{h}_i = -\frac{1}{2}\nabla_i^2 - \sum_\mu \frac{Z_\mu}{r_{i\mu}} \tag{2.9}$$

is the one-electron kinetic energy and interaction with the nuclei labelled by μ, and

$$\hat{g}_{ij} = \frac{1}{r_{ij}} \tag{2.10}$$

is the two-electron operator, the Coulomb interaction between two particles of unit charge. The energy of this system as described by this Hamiltonian is evaluated as the expectation value of the Hamiltonian in terms of the one-electron orbitals φ_i [1]

$$E[\psi] = \left\langle \psi \left| \hat{H} \right| \psi \right\rangle = \sum_i \left\langle \varphi_i \left| \hat{h} \right| \varphi_i \right\rangle + \sum_{i<j} \langle \psi \, | \hat{g} | \, \psi \rangle \tag{2.11}$$

where the indices have been dropped from the one and two-electron operators as these are implicit by definition. Then

$$\sum_{i<j} \langle \psi \, | \hat{g} | \, \psi \rangle = \sum_{i<j} \{ \langle \varphi_i \varphi_j \, | \hat{g} | \, \varphi_i \varphi_j \rangle - \langle \varphi_i \varphi_j \, | \hat{g} | \, \varphi_j \varphi_i \rangle \} \tag{2.12}$$

because only contributions from the identity permutation, and the transposition of i with j are considered. These constraints introduce the so called 'exchange' interaction into what is otherwise a Hamiltonian based purely on Coulomb forces. This is then

[1] It is common to denote a wavefunction Ψ by the use of the bra-ket notation, where $|\Psi\rangle$ is a ket vector and the adjoint of the wavefunction $\Psi^\dagger = \langle \Psi |$ is a bra, such that the expectation value of the Hamiltonian may be written $\langle \Psi | \hat{H} | \Psi \rangle$ in brackets. This is equivalent to writing $\int \Psi^* \hat{H} \Psi d\mathbf{r}$.

written as

$$\sum_{i<j}\{\langle\varphi_i\varphi_j\,|\hat{g}|\,\varphi_i\varphi_j\rangle - \langle\varphi_i\varphi_j\,|\hat{g}|\,\varphi_j\varphi_i\rangle\}$$
$$= \frac{1}{2}\sum_i \left\langle\varphi_i\left|\hat{J}-\hat{K}\right|\varphi_i\right\rangle \tag{2.13}$$

where the Coulomb and exchange operators $\hat{J}_j$ and $\hat{K}_j$ respectively describe the Coulomb repulsion and the effect of exchange (fermion permutation) symmetry. The total Coulomb and exchange operators are defined as

$$\hat{J} = \sum_i \hat{J}_i \tag{2.14}$$

$$\hat{K} = \sum_i \hat{K}_i \tag{2.15}$$

The initial wavefunction is only approximate, constructed as a linear combination of atomic orbitals approximated using Gaussian functions, and thus Hartree-Fock calculations rely on the variational principle.

The Fock operator is defined as $\hat{F} = \hat{h} + \hat{J} - \hat{K}$, and the Hartree-Fock equation

$$\hat{F}\tilde{\varphi}_j = \epsilon_j\tilde{\varphi}_j \tag{2.16}$$

Although the one-electron energies are expectation values of the Fock operator:

$$\epsilon_i = \left\langle\varphi_i\left|\hat{F}\right|\varphi_i\right\rangle \tag{2.17}$$

the total energy is not the sum of the orbital energies. Rather;

$$E = \sum_i \epsilon_i - \frac{1}{2}\sum_i \left\langle\varphi_i\left|\hat{J}-\hat{K}\right|\varphi_i\right\rangle. \tag{2.18}$$

2.4 Density functional theory

Density functional theory (DFT) is an approach to the same problem as that outlined so far, but from a different perspective. From a macroscopic point of view, in particular that of solid state physics, the electronic energy depends on the electron density, without any need for individual electrons to be accounted for explicitly. In fact the Schrödinger Hamiltonian is determined exactly once the positions of the nu-

clei and their charges are known. The exact electron density, $\rho(\mathbf{r})$, will have cusps at the nuclear positions, and the gradient of the density will give the nuclear charges. These simple results were formalised by Kohn, Hohenberg and Sham in the sixties and seventies. [Fiolhais et al., 2003]

2.4.1 The Hohenberg-Kohn theorems

The first requirement is that the electron density, alone, may determine the energy. Thus: *The electron density $\rho(\mathbf{r})$ determines the external potential.* The potential $v_1(\mathbf{r})$ is an external potential due to $\rho(\mathbf{r})$. Then

$$E_1^0 = \left\langle \Psi_1 \left| \hat{H}_1 \right| \Psi_1 \right\rangle \tag{2.19}$$

and due to the variational principle, the introduction of another potential $v_2(\mathbf{r})$, for which the ground state energy is

$$E_2^0 = \left\langle \Psi_2 \left| \hat{H}_2 \right| \Psi_2 \right\rangle \tag{2.20}$$

gives

$$E_1^0 = \left\langle \Psi_1 \left| \hat{H}_1 \right| \Psi_1 \right\rangle < \left\langle \Psi_2 \left| \hat{H}_1 \right| \Psi_2 \right\rangle \tag{2.21}$$

$$\left\langle \Psi_2 \left| \hat{H}_1 \right| \Psi_2 \right\rangle = \left\langle \Psi_2 \left| \hat{H}_2 \right| \Psi_2 \right\rangle + \left\langle \Psi_2 \left| \hat{H}_1 - \hat{H}_2 \right| \Psi_2 \right\rangle \tag{2.22}$$

$$= E_2^0 + \int \rho(\mathbf{r})[v_1(\mathbf{r}) - v_2(\mathbf{r})]dr \tag{2.23}$$

which can only be true for both E_1^0 and E_2^0 if $v_1(\mathbf{r}) = v_2(\mathbf{r})$. Hence the external potential is uniquely determined by $\rho(\mathbf{r})$. As a consequence the energy may be written as a functional of the density;

$$E[\rho] = V_{ne}[\rho] + T'[\rho] + V_{ee}[\rho] \tag{2.24}$$

$$= \int \rho(\mathbf{r})v(\mathbf{r})d\mathbf{r} + T[\rho] + V_{ee}[\rho] \tag{2.25}$$

where $T'[\rho]$ is the kinetic energy, $V_{ne}[\rho]$ is the electron nucleus interaction and $V_{ee}[\rho]$ is the electron electron interaction energy (containing the Coulomb interaction).

Secondly, it is still necessary to use approximate descriptions of the wavefunction and therefore the variational principle is required. Therefore it must be that: *The variational principle is valid for approximate densities.* For an approximate density

$\tilde{\rho}$ which creates the potential $v(\mathbf{r})$ and has wavefunction $\tilde{\Psi}$, equation (2.25) gives,

$$\left\langle \tilde{\Psi} \middle| \hat{H} \middle| \tilde{\Psi} \right\rangle = \int \tilde{\rho}(\mathbf{r}) v(\mathbf{r}) d\mathbf{r} + T[\tilde{\rho}] + V_{ee}[\tilde{\rho}] \tag{2.26}$$

$$= E[\tilde{\rho}] \geq E[\rho] \tag{2.27}$$

which is a consequence of the first theorem. The true energy is a strict lower bound as required by the variational principle for semi-bound operators.

2.4.2 The Kohn-Sham equations

To define the density, ρ, and kinetic energy, T, in a simple fashion, a model system of N noninteracting electrons in N orbitals φ_i is used. Then the kinetic energy of the system and its density can be written

$$T_s[\rho] = \sum_i^N \left\langle \varphi_i \middle| -\frac{1}{2}\nabla^2 \middle| \varphi_i \right\rangle \tag{2.28}$$

$$\rho(\mathbf{r}) = \sum_i^N |\varphi_i|^2 \tag{2.29}$$

$$\tag{2.30}$$

where the potential energy $v(\mathbf{r})$ is included as usual;

$$\left[-\frac{1}{2}\nabla^2 + v_s(\mathbf{r}) \right] \varphi_i = \epsilon_i \varphi_i \tag{2.31}$$

The subscript s specifies this noninteracting system of electrons and the energy is given by

$$E[\rho] = T_s[\rho] + \int v_s(\mathbf{r}) \rho(\mathbf{r}) dr. \tag{2.32}$$

Then including the interaction V_{ee} between electrons, the result of inserting the Coulomb interaction J into equation (2.25) is

$$E[\rho] = \int v(\mathbf{r}) \rho(\mathbf{r}) d\mathbf{r} + T[\rho] + V_{ee}[\rho] \tag{2.33}$$

$$= \int v(\mathbf{r}) \rho(\mathbf{r}) d\mathbf{r} + T_s[\rho] + J[\rho] + (T[\rho] - T_s[\rho]) \tag{2.34}$$

$$+(V_{ee}[\rho] - J[\rho])$$

$$= \int v(\mathbf{r}) \rho(\mathbf{r}) d\mathbf{r} + T_s[\rho] + J[\rho] + E_{xc}[\rho] \tag{2.35}$$

where the Coulomb interaction is

$$J[\rho] = \frac{1}{2}\int\int \frac{1}{\mathbf{r}_{12}}\rho(\mathbf{r}_1)\rho(\mathbf{r}_2)d\mathbf{r}_1 d\mathbf{r}_2. \tag{2.36}$$

The exchange-correlation energy is defined as

$$E_{xc}[\rho] = T[\rho] - T_s[\rho] + V_{ee}[\rho] - J[\rho]. \tag{2.37}$$

This has the exchange-correlation potential as its functional derivative

$$v_{xc}(\mathbf{r}) = \frac{\delta E_{xc}[\rho]}{\delta\rho(\mathbf{r})} \tag{2.38}$$

which with equation (2.31) gives

$$\left[-\frac{1}{2}\boldsymbol{\nabla}^2 + v(\mathbf{r})\int \frac{\rho(\mathbf{r}')}{|\mathbf{r}-\mathbf{r}'|}d\mathbf{r}' + v_{xc}(\mathbf{r})\right]\varphi_i(\mathbf{r}) = \epsilon_i\varphi_i(\mathbf{r}). \tag{2.39}$$

These eigenvalue equations are the Kohn-Sham equations, and would give the exact energy if the exact exchange-correlation functional could be determined. However this remains unknown and so approximate physical models are used.

2.4.3 The local density approximation

The local density approximation, LDA, is motivated by properties of the uniform electron gas, and that this is a good model of the behaviour of simple metals in the bulk. If the ion cores (nucleus + core electrons) in a real metal lattice were replaced by a uniform positive background charge, then the valence electrons (delocalised to give a uniform electron density $\rho(\mathbf{r})$), become a uniform electron gas in the limit of the number of electrons $N \to \infty$ and cubic volume $l^3 = V \to \infty$. The orbitals must fit within this cube and are therefore plane waves,

$$\varphi_{\mathbf{k}}(\mathbf{r}) = \frac{1}{V^{\frac{1}{2}}}e^{i\mathbf{k}\mathbf{r}} \tag{2.40}$$

with wavenumber $k = \frac{2\pi}{l}n$; $n_x, n_y, n_z = 0, \pm1, \pm2, \ldots$. Then the total energy of the system including contributions from both electronic and ionic charges is

$$E[\rho] = T_s[\rho] + J[\rho] + E_{xc}[\rho] + \int v(\mathbf{r})\rho(\mathbf{r})d\mathbf{r} \tag{2.41}$$

and as the system is neutral, the Coulomb terms for positive and negative densities must cancel, as must the integral over ρ, the electron density and $v(\mathbf{r})$, the potential due to the positive density. Therefore

$$E[\rho] = T_s[\rho] + E_{xc}[\rho] \tag{2.42}$$

and the exchange correlation energy E_{xc} may also be written as the sum of an exchange energy E_x and a correlation energy, E_c. In the case of the electron gas, the noninteracting kinetic energy and the Slater exchange energy are given by[2]

$$T_s[\rho] = \frac{3}{10}(3\pi^2)^{2/3}\int \rho(\mathbf{r})^{5/3}d\mathbf{r} \tag{2.43}$$

$$E_x[\rho] = \frac{3}{4}(3\pi^{-1})^{1/3}\int \rho(\mathbf{r})^{4/3}d\mathbf{r} \tag{2.44}$$

but for the correlation energy, numerical simulations of the electron gas using quantum Monte Carlo methods have been used to fit most functionals.

2.4.4 Spin in the local density approximation

The local spin density approximation, or LSDA, is essentially the same as the LDA except that the α and β spin densities are allowed to differ. This is necessary for open shell systems for example, and requires little change other than incorporating the sum of the two densities into the above integrals and an additional prefactor.

2.4.5 The exchange functional

The most important deficiency of LDA is that the asymptotic behaviour of the exchange energy is incorrect, as might be expected when transferring a model from an infinite system to one of finite dimensions. The $e^{-\rho r/3}$ dependence of the exchange energy in LDA was first corrected by Becke [Becke, 1988]. Properly if the exchange energy is written in terms of an exchange density, then

$$E_x[\rho] = \int \rho(\mathbf{r}_1)\epsilon_x(\mathbf{r}_1)d\mathbf{r}_1 \tag{2.45}$$

$$\epsilon_x = \frac{1}{2}\int \frac{\rho_{xc}(\mathbf{r}_1,\mathbf{r}_2)}{\mathbf{r}_{12}}d\mathbf{r}_2 \tag{2.46}$$

[2] Given for the simplest case of identical α and β spin density. [Fiolhais et al., 2003]

which means that

$$\lim_{r_1 \to \infty} \epsilon_x(\mathbf{r}_1) = -\frac{1}{2\mathbf{r}_1}. \tag{2.47}$$

Becke corrected this by adding a new term of the form

$$\epsilon_x^B = -\beta\rho^{1/3}\frac{x^2}{1 + 6\beta x \sinh^{-1} x} \tag{2.48}$$

$$x = \frac{\nabla\rho}{\rho^{4/3}} \tag{2.49}$$

which has one adjustable parameter which was originally chosen by fitting to the exchange energies of 6 noble gas atoms.

2.4.6 Density gradient corrections

The use of the density gradient in Becke's correction of the exchange energy can be easily motivated. The shift from a continuous system of constant density to the finite regime of molecules with their sharply varying density means that simple knowledge of the density is no longer sufficient. Naturally enough, the electronic density in molecules varies due to the inherent shell structure; this may only be reproduced to a degree by DFT by the inclusion of a $|\nabla\rho|$ dependence. Other functionals have since been introduced with the general form

$$E_{xc} = \int F(\rho_\alpha, \rho_\beta, \nabla_{\alpha\alpha}, \nabla_{\beta\beta}, \nabla_{\alpha\beta}) d\mathbf{r} \tag{2.50}$$

which are commonly known as generalised gradient approximation (GGA) functionals. These are the most commonly used functionals in computational chemistry, in particular the hybrid functional[3] B3LYP is widely popular and very successful for certain types of molecules (generally light and organic). This is not so surprising as these functionals are often fitted to experimental data for the systems of interest. LDA and the Becke GGA corrected version (often labeled BP86, after Becke-Perdew and the year of publication) are however not parametrised in such a way.

2.4.7 The Perdew-Wang 91 functional

In a recent paper, Langlet *et al.* [Langlet et al., 2004] describe "an interesting property of the PW91 functional". They have compared terms arising from symmetry-

[3]The term hybrid is used to indicate that Hartree-Fock exchange is included to correct for deficiencies in the underlying model.

adapted perturbation theory (SAPT) for the exchange repulsion and dispersion, which they define as

$$E_{vdW} = \left[E^{(10)}_{exch-rep} + E^{(1)}_{exch}(\mathrm{CCSD})\right] + \left[E^{(20)}_{disp} + E^{(21)}_{disp} + E^{(22)}_{disp} + E^{(20)}_{exch-disp}\right] \quad (2.51)$$

with a term calculated from DFT which they call the Pauli repulsion. This they define as the repulsion due to the antisymmetrisation of the wavefunction, through a density deformation of the monomer orbitals, a change in kinetic energy, and consequent changes in the effective exchange and correlation potentials. This term is designed to exclude the purely electrostatic interaction of the monomers' charge densities, and the orbital interaction that is obtained by solving the Kohn-Sham equations for the antisymmetrised wavefunction.

Both the SAPT and DFT derived terms are considered to approximate the dispersion interaction of a van der Waals molecule.

In calculations on a number of weakly interacting systems, they find the correlation between these two terms to be remarkably better with PW91 than for any other functional. They do not propose any theoretical basis for this coincidence, but do suggest that it may be more than just a "fortuitous cancellation" that makes this functional particularly appropriate for vdW-bonded systems.

An examination of the original papers by Perdew and Wang shows that the parametrisation of this functional was originally aimed at improving the representation of the correlation energy for a uniform electron gas [Perdew and Wang, 1991a, Perdew and Wang, 1991b, Perdew and Wang, 1992]. Although no fundamental explanation is given, the numerical evidence of reference [Langlet et al., 2004] leads us to expect that this functional may describe the vdW bonding in small mercury systems better than others.

2.5 Møller-Plesset perturbation theory

Møller Plesset perturbation theory is the most common application of many-body perturbation theory to the calculation of electron correlation effects. It uses the Hartree-Fock wavefunction as the reference wavefunction and adds correlation as a perturbation to the Fock operator:

$$\hat{H} = \hat{F} + \hat{V}. \quad (2.52)$$

The perturbation operator $\hat{V}$ is defined for correlation as

$$\hat{V} = \sum_{i<j} r_{ij}^{-1} - \hat{V}_{HF} \tag{2.53}$$

$$= \sum_{i<j} r_{ij}^{-1} - \sum_{i} v_{HF}(i) \tag{2.54}$$

i.e. the difference between the exact Coulomb interaction and the Hartree-Fock interaction. Applying this to the reference wavefuction Ψ_{HF} gives

$$\hat{H}\,|\Psi\rangle = (\hat{F} + \hat{V})\,|\Psi\rangle = \epsilon\,|\Psi\rangle\,, \tag{2.55}$$

$$\hat{F}\,|\Psi_{HF}\rangle = E_{HF}\,|\Psi_{HF}\rangle \tag{2.56}$$

$$\epsilon = E_0^{(0)} + E_0^{(1)} + E_0^{(2)} + \ldots \tag{2.57}$$

where E_{HF} is the ground state HF energy, and $\Psi_{HF} = |0>$ is the ground state wavefunction.

The first order correction is

$$E_0^{(1)} = \left\langle 0|\hat{V}|0 \right\rangle \tag{2.58}$$

$$= \left\langle 0 \left| \sum_{i<j} r_{ij}^{-1} \right| 0 \right\rangle - \left\langle 0 \left| \sum_{i} v_{HF}(i) \right| 0 \right\rangle \tag{2.59}$$

$$= \frac{1}{2} \sum_{ij} \langle ij||ij\rangle - \sum_{i} \langle i|v_{HF}|i\rangle \tag{2.60}$$

$$= -\frac{1}{2} \sum_{ij} \langle ij||ij\rangle \tag{2.61}$$

$$\tag{2.62}$$

Comparison with equation (2.18) shows that the HF energy is the sum of the zeroth and first order energies.

$$E_{HF} = E_0^{(0)} + E_0^{(1)} \tag{2.63}$$

$$= \sum_{i} \epsilon_i - \frac{1}{2} \sum_{ij} \langle ij||ij\rangle \tag{2.64}$$

$$\tag{2.65}$$

where the second term comes from the antisymmetry of the wavefunction. Therefore the next useful correction comes at second order.

The second order energy is

$$E_0^{(2)} = \sum_{n>0} \frac{\left|\left\langle 0 \left| \hat{V} \right| n \right\rangle\right|^2}{E_0^{(0)} - E_n^{(0)}}; \tag{2.66}$$

$$|0\rangle = |\Psi_{HF}\rangle\,, \tag{2.67}$$

$$|n\rangle = |\Psi_{ab}^{rs}\rangle \tag{2.68}$$

where n labels the sum over all doubly excited states. Here the doubly excited wavefuntion $|\Psi_{ab}^{rs}\rangle$ uses indices a, b for unoccupied and r, s for occupied orbitals. This then gives us the second order perturbative correlation to the Hartree-Fock energy, and is commonly known as MP2 (for Møller Plesset in second order). If the expansion is carried out to higher orders then MP3, MP4, and so on are obtained. As the expense of the calculation scales as N^{n+3} for an MPn calculation[4] without a great improvement in accuracy, calculations are not usually carried out to higher than fourth order. If higher accuracy is required, a coupled cluster calculation is usually preferred.

2.6 Coupled cluster theory

The best way of including electron correlation in a calculation is to include all possible configurations of the electrons in the wavefunction (consisting of Slater determinants). Therefore the wavefunction is written as a sum over the ground state plus all the possible singly excited and doubly excited determinants and so on to the limiting possibility of a full configuration interaction. This sum would be modulated by coefficients which would control the contribution of each determinant to the wavefunction. However in practice this is only possible for the smallest systems, and some truncation of the series of excited wavefunctions is necessary. The problem with this is that any such truncation results in a wavefunction that is no longer *size-extensive*, that is, that the energy of two non-interacting atoms is no longer the same as the sum of their energies calculated separately, for example. Obviously for molecules this is a considerable challenge, and has led to the development of coupled cluster theory, where the excited states are included in the wavefunction in such a way as to keep the calculations size-extensive. The excitation from the ground state into the various

[4]Here N is the number of basis functions.

excited determinants may be described by an excitation operator, T,[5] where

$$T = T_1 + T_2 + T_3 + \ldots \tag{2.69}$$

T_1 being responsible for all single excitations,

$$T_1 = \sum_A \sum_I t_I^A a_A^\dagger a_I \tag{2.70}$$

where the sums are over unoccupied A and occupied states I, the t_I^A are the coefficients corresponding to each Slater determinant, and the $a_A^\dagger$ and a_I are operators correponding to the creation of an electron in an unoccupied state and the annihilation of an electron in an occupied state, respectively. The combination therefore describes a single excitation. The essential requirement of coupled cluster theory is to write the wavefunction as an *exponential*:

$$\Psi_{CC} = e^T \Psi_0 \tag{2.71}$$

instead of the sum of determinants as described above. The exponential operator is defined as

$$\begin{aligned} e^T &= 1 + T_1 + T_2 + T_3 + \ldots && (2.72)\\ &\quad + \frac{1}{2!}T_1^2 + T_1T_2 + \frac{1}{2!}T_2^2 + \frac{1}{3!}T_1^3 && (2.73)\\ &\quad + \frac{1}{4!}T_1^4 + \frac{1}{2!}T_1^2T_2 + T_1T_3 + \ldots && (2.74) \end{aligned}$$

The following is obtained as a direct result from the Schrödinger equation;

$$e^{-T} H e^T \Psi_0 = E\Psi_0. \tag{2.75}$$

The nice thing here is that the left-hand side can be rewritten as

$$e^A B e^{-A} = B + [A, B] + \frac{1}{2!}[A, [A, B]] + \ldots \tag{2.76}$$

which is known as the Hausdorff commutator expansion.[6] Now although this is in principle an infinite expansion, the commutation properties of these excitation operators make the single excitation operator $a_A^\dagger a_I$ commute with T. However more

[5] Here I will leave the hats off operators $\hat{T} = T$ and $\hat{H} = H$ to prevent clutter.

[6] The commutation of two operators is defined as $[A, B] = AB - BA$.

generally $a_P^\dagger a_Q$ does not (using P, Q, R, S to label all general orbitals), meaning that H, written as

$$H = \sum_{PQ}(P|h|Q)a_P^\dagger a_Q + \frac{1}{2}\sum PQRS(PR|QS)a_P^\dagger a_Q^\dagger a_S a_R, \tag{2.77}$$

does not commute with T. In the general case,

$$\begin{aligned} a_P^\dagger a_Q a_A^\dagger a_I &= \delta_{AQ}a_P^\dagger a_I - a_P^\dagger a_A^\dagger a_Q a_I & (2.78)\\ &= \delta_{AQ}a_P^\dagger a_I - a_A^\dagger a_P^\dagger a_I a_Q & (2.79)\\ &= \delta_{AQ}a_P^\dagger a_I - \delta_{PI}a_A^\dagger a_Q + a_P^\dagger a_I a_P^\dagger a_Q & (2.80)\end{aligned}$$

which means that the commutator between H and an excitation operator is

$$[a_P^\dagger a_Q, a_A^\dagger a_I] = \delta_{AQ}a_P^\dagger a_I - \delta_{PI}a_A^\dagger a_Q. \tag{2.81}$$

This has the effect of removing one of the general P, Q, R, S creation and annihilation operators involved in H. Consequently after four such eliminations only excitation operators $a_A^\dagger a_I$ remain, and as these commute with T the Hausdorff expansion terminates, leaving just 5 terms:

$$\begin{aligned} e^{-T}He^T = H + [H,T] + \frac{1}{2!}[H,[H,T]] + \frac{1}{3!}[H,[H,[H,T]]] \\ + \frac{1}{4!}[H,[H,[H,[H,T]]]]. \end{aligned} \tag{2.82}$$

This means that for any number of excitations, an explicit equation may be written for optimising our wavefunction $\Psi_{IJK\ldots}^{ABC\ldots}$ as

$$\begin{aligned} \langle\Psi_0|\, H + [H,T] + \frac{1}{2!}[H,[H,T]] + \frac{1}{3!}[H,[H,[H,T]]] \\ + \frac{1}{4!}[H,[H,[H,[H,T]]]]\,|\Psi_0\rangle = E \end{aligned} \tag{2.83}$$

and also

$$\begin{aligned} \langle\Psi_{IJK\ldots}^{ABC\ldots}|\, H + [H,T] + \frac{1}{2!}[H,[H,T]] + \frac{1}{3!}[H,[H,[H,T]]] \\ + \frac{1}{4!}[H,[H,[H,[H,T]]]]\,|\Psi_0\rangle = 0. \end{aligned} \tag{2.84}$$

This has the effect of introducing excitations of all higher orders into the equations as each term T_n appears to higher powers, thereby including for example a twice doubly excited configuration; T_2^2. These extra excitations are known as *disconnected clusters.*

2.6.1 CCSD(T)

For practical purposes T must of course be truncated at some point. Single excitations by themselves do not contribute to the dynamical correlation, and Hartree-Fock orbitals do not interact with the reference wavefunction. Double excitations are therefore always included, and if single excitations are also included then most of the correlation energy is obtained. This truncation of T to $T_1 + T_2$ results in the CCSD method. However while CCSD contains higher order excitations in the form of disconnected clusters, what it misses are the connected contributions generated directly by the operators $T_3, T_4, \ldots$. The only way to include these is to truncate T at a higher term. For example, $T = T_1 + T_2 + T_3$ results in a CCSDT method. However solving the CCSDT equations scales approximately according to N^8, where N is the number of basis functions. Due to its computational cost, CCSDT has mostly been used in the calibration of approximate methods of including connected triple excitations. The CC equations are to be solved iteratively, and so an immediate way of including the triple excitations approximately at much less cost is through perturbation theory. This results in the widely used method, denoted CCSD(T), which uses the perturbative correction as in Møller Plesset theory, which scales as N^7 and requires no iteration.

2.7 Pseudopotentials

Pseudopotentials, also known as effective core potentials (ECP), are used to replace the inner core electrons by mimicking their affect on the valence states, and reduce the cost of a calculation. They also provide a straightforward way of including relativistic effects, based on the assumption that because relativity affects the core electrons most strongly, and these themselves have little effect on the chemistry of the atom, an effective potential which will allow their effects to be transferred to the outer electrons should suffice. In fact, as the expense of even a non-relativistic calculation increases rapidly with the number of electrons, it is clear that using such an approximation may be the key step in making a large calculation feasible.

A relativistic *ab initio* pseudopotential is derived from an atomic Dirac-Fock (four-component) calculation, and approximates the core-valence interaction. The first effect that must be included is the screening of the nucleus by the core electrons, which is easily obtained by using a Coulomb term times a constant, plus some Gaussian functions such that the behaviour is Z/r at short distances and $(Z - N_c)/r$ at long distance, N_c being the number of core electrons.

The Pauli repulsion, which by constraining the valence electrons to be orthogonal to the core electrons increases their energy, is more difficult to describe. Other effects include the exchange interaction, which is non-local and can therefore not be described by a one-electron operator.

In the pseudopotential approximation the Hamiltonian can be written as

$$\hat{H}_v = -\frac{1}{2}\sum_i^{n_v} \nabla_i^2 + \sum_{i<j}^{n_v} \frac{1}{\mathbf{r}_{ij}} + \sum_i^{n_v}\sum_a^{n_c} \left[V_{PP}^a(\mathbf{r}_{ai}) - \frac{Q_a}{\mathbf{r}_{ai}}\right] + \sum_{a<b}^{n_c} \frac{Q_a Q_b}{\mathbf{r}_{ai}}. \tag{2.85}$$

Here n_v is used for the number of valence electrons and N_c for the number of cores of charge $Q_a = Z_a - n_c^a$, where V_{PP} includes both the core-valence and core-core interactions. The indices a, b are for the cores, and i, j the electrons.

A pseudopotential that is dependent on the orbital angular momentum of the electrons (i.e. V_{PP}^l; $l = s, p, d, \ldots$) is called a semi-local pseudopotential. An accurate pseudopotential must match the real and pseudo wavefunctions outside the core such that the wavefunctions generate identical charge densities;

$$\rho_{AE}(\mathbf{r}) = \rho_{PP}(\mathbf{r}); \quad \mathbf{r} > r_c \tag{2.86}$$

where the subscripts AE and PP denote the all-electron and pseudopotential densities respectively.

The actual potential may be conveniently written as an expansion in terms of Gaussian functions

$$V_l^a(r_{a,i}) = \sum_k A_{lk}^a r n_{lk}^a e^{-B_{lk}^a r_{ai}^2} \tag{2.87}$$

where a and i index respectively the nuclei and electrons that this potential is applied to, l is the angular momentum, k labels the Gaussian functions that have exponents B_{lk}^a and coefficients A_{lk}^a (both multiplied by powers of the electron core distance r_{ai}).

In order to define the core and valence electrons, the electron densities must be examined to find a separation which minimises the interaction between them; i.e.

where there is least overlap. The core should be inert, that is its polarisability should be small, and it should not include electrons that would overlap with the valence electrons of another atom in a molecule. In general, the larger the core, the more likely the approximation is to fail; a good pseudopotential is therefore constructed by considering as many effects as possible. As they are fitted to atomic energies, it is particularly in the description of molecules that they may run into difficulty.

Another advantage of the pseudopotential approximation is that it lessens the basis set superposition error (BSSE). As an atomic basis set is incomplete, a molecular calculation of the same atoms will allow the electrons to take advantage of the basis functions on the other atoms and this will artificially lower the energy of the molecule relative to that of the atoms. When the core electrons are described by a pseudopotential, their contribution to this error vanishes (or is replaced by the PP approximation error).

2.8 Dimers

2.8.1 The Hg dimer

The basis used to assess the performance of different methods was chosen to be as large as practical, and is correlation consistent (i.e. it was obtained by minimising the MP2 atomic energy of Hg). This large basis set is an uncontracted set of $(11s10p9d4f)$

S	P	D	F
21.8086260	9.6051070	4.7157900	3.6000000
11.6433800	7.3316370	3.1115440	1.8480180
6.3522931	3.5744730	1.3203950	0.6240740
2.5799500	2.0696200	0.5810270	0.2500000
1.6183291	1.2513030	0.2417370	
0.7413510	0.6621420	0.0945010	
0.2638270	0.3066990	0.0400000	
0.1090040	0.1341520	0.0150000	
0.0469540	0.0569136	0.0050000	
0.0200000	0.0150000		
0.0050000			

Table 2.1: Large basis set used for Hg_2

functions and is given in Table 2.1. This means that 114 basis functions (135 primitive Gaussians) are based on each atom, in which only 20 electrons are described; the 60 electron core $(1s^2 2s^2 2p^6 3s^2 3p^6 3d^{10} 4s^2 4p^6 4d^{10} 4f^{14})$ is described by a Stuttgart

pseudoptential. [Andrae et al., 1990]

This pseudopotential, used for all the calculations performed on mercury in this thesis, is given in Table 2.2, where the general form of the potentials formed from these exponents and coefficients is given in equation (2.87).

	Exponent	Coefficient
S		
	12.9815487	274.53216892
	6.4907744	49.18219145
P		
	10.5380958	237.39577010
	5.2690479	28.12158416
D		
	8.1017205	114.25203372
	4.0508603	18.49563795
F		
	3.8857911	30.36499643

Table 2.2: Mercury relativistic pseudopotential from reference [Andrae et al., 1990].

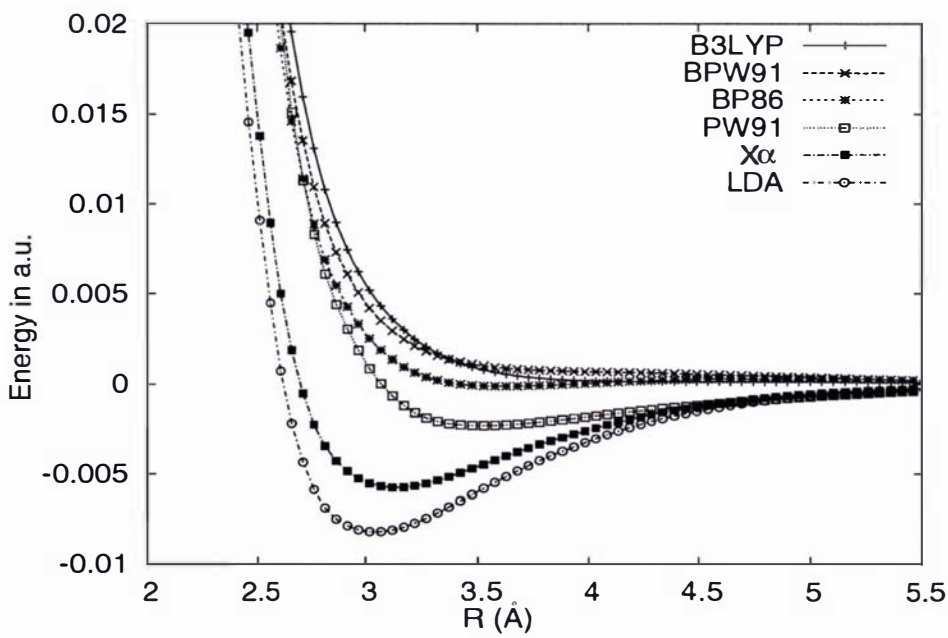

Figure 2.1: Perfomance of various density functionals for the Hg dimer

The diatomic potential curve of mercury was then calculated using a number of different density functionals, in order to compare their behaviour. This is shown in Figure 2.1. It is clear that DFT gives widely varying results for Hg, depending on the functional of choice. One of the most popular functionals for a wide variety of molecules, B3LYP, is entirely repulsive for Hg_2. LDA is typically overbinding, by about a factor of three. It is the PW91 functional (PW91 for both exchange and correlation) that gives by far the most realistic curve.

The highly accurate curve given by Schwerdtfeger *et al.*,[Schwerdtfeger et al., 2001], calculated with the same large basis set, CCSD(T) and with an estimate of the spin-orbit effect included, is compared to the MP2, HF, and PW91 curves in Figure 2.2. The Hartree-Fock case is compared to obtain an idea of the effect of correlation. The CCSD(T) curve is distinct in being only weakly binding and giving the longest

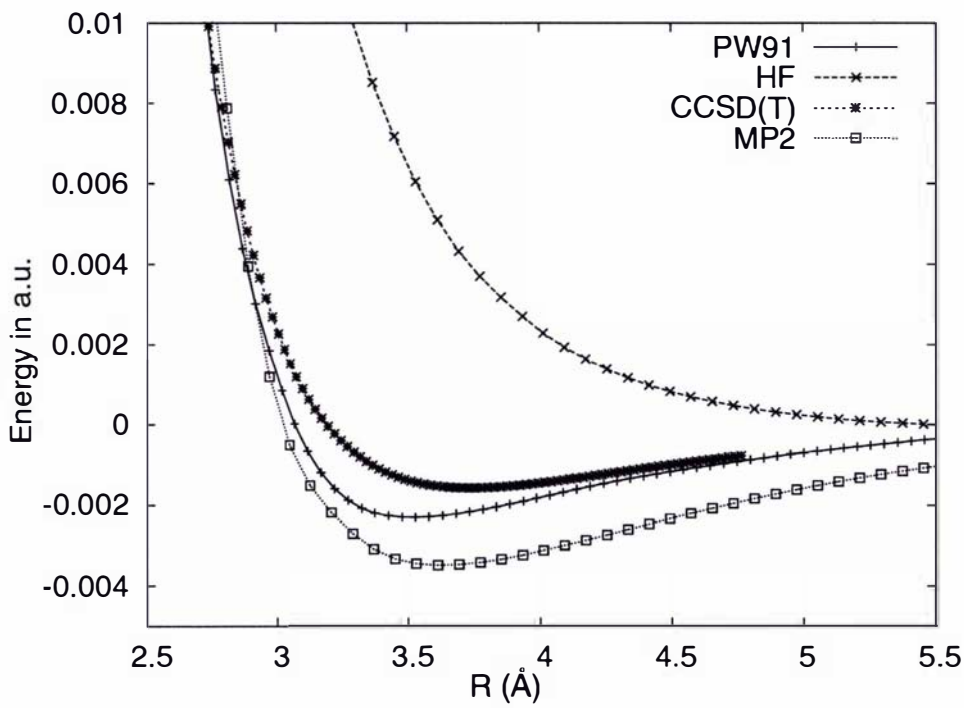

Figure 2.2: Perfomance of various methods for the Hg dimer.

bond length. The simple density functionals LDA and Xα are strongly overbinding, but the GGA-corrected functionals such as B3LYP are generally not better, and can fail to bind the dimer at all. It is not surprising that HF fails to describe van der

Waals bonding, which requires a decent treatment of correlation, but B3LYP and BPW91 fail almost as badly, with BP86 showing just a slight improvement. The best functional is clearly PW91 (used for both exchange and correlation, in contrast to BP91 for example). It produces a curve which has a slightly shorter equilibrium bond length than either MP2 or CCSD(T), but a binding energy intermediate between the two, and at long range (above 4 Å) matches the CCSD(T) curve almost exactly.

A summary of the performance of these methods for Hg_2 is given in Table 2.3, along with the results for Zn, Cd, and Ba.

2.8.2 The Cd dimer

For the cadmium dimer, a similar analysis of the same methods was undertaken. An analogous correlation consistent basis of the same size as that for mercury was used as shown in Table 2.4. The Stuttgart pseudopotential accounted for a core of 28 electrons ($1s^2 2s^2 2p^6 3s^2 3p^6 3d^{10}$). The respective potential curves for Cd_2 are given for a range of density functionals, as well as the CCSD(T) and HF results. The picture

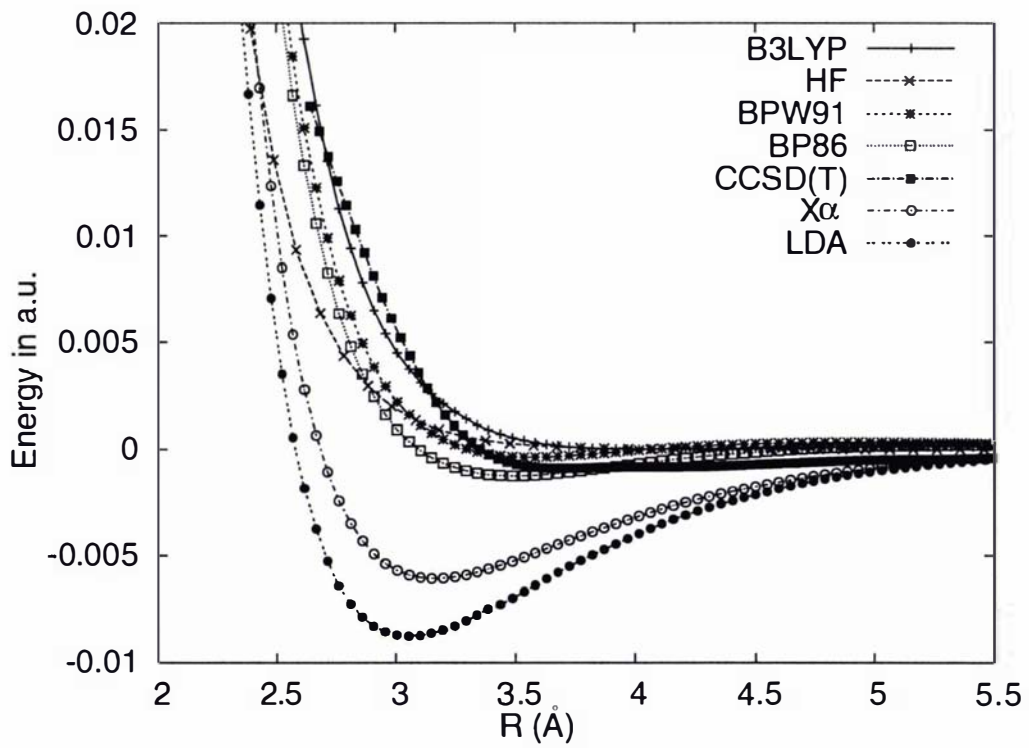

Figure 2.3: Perfomance of DFT and other methods for the Cd dimer

Method	Bond length at potential minimum r_e Hg_2	Cd_2	Zn_2	Ba_2
B3LYP	—	—	—	5.124
BP86	—	3.499	3.213	4.910
BPW91	—	3.567	3.302	4.902
PW91	3.522	3.441	3.173	4.360
Xα	3.128	3.158	2.930	4.925
LDA	3.040	3.055	2.810	4.749
CCSD(T)	3.772	3.738	4.215	5.079
Expt	3.69	4.07	4.19	4.881

Method	Dissociation energy at potential minimum D_e Hg_2	Cd_2	Zn_2	Ba_2
B3LYP	—	—	—	0.003557
BP86	—	0.001132	0.001588	0.007813
BPW91	—	0.000029	0.000904	0.008952
PW91	0.002256	0.003186	0.003047	0.015258
Xα	0.005847	0.006894	0.005354	0.009088
LDA	0.008107	0.009915	0.007776	0.013042
CCSD(T)	0.001628	0.001319	0.001396	0.005027
Expt	0.001731	0.001506	0.001272	0.007423

Method	Harmonic vibrational frequency ω_e Hg_2	Cd_2	Zn_2	Ba_2
B3LYP	—	—	65.731	9.767
BP86	—	33.561	53.099	41.337
BPW91	—	—	40.405	42.866
PW91	25.718	35.499	49.750	23.432
Xα	46.259	54.618	65.731	40.133
LDA	54.951	70.421	88.492	47.465
CCSD(T)	21.537	23.083	27.384	32.762
Expt	19.7	23.0	25.9	35.0

Table 2.3: Calculated spectroscopic parameters for the Hg, Cd, Zn and Ba dimers. Dissociation energies are in atomic units, bond lengths are in Ångstrøm, and frequencies are in cm^{-1}. The experimental data for Cd_2 and Zn_2 are from [Czajkowski and Koperski, 1999], for Hg_2, from [Koperski et al., 1994] and for Ba_2 only theoretical reference data are available, [Allouche et al., 1995]. Dashes indicate that the method was unable to give a result.

S	P	D	F
23.1288900	17.8918050	33.0204760	8.8756640
13.3720370	15.9406890	8.2869860	3.1190300
7.4032940	8.0170153	3.7046220	1.3265000
3.2131447	3.4807459	1.6911011	0.4833040
2.1441356	2.0912912	0.6913572	
1.0133229	1.0500963	0.2425778	
0.4748171	0.5146861	0.1000000	
0.1987521	0.2264356	0.0300000	
0.0667665	0.0923482	0.0100000	
0.0150000	0.0300000		
0.0050000			

Table 2.4: Large basis set used for Cd_2

for Cd is very similar to that for Hg, although the GGA-functionals behave on the whole a little better. Of the functionals tested, only B3LYP is entirely repulsive.

2.8.3 The Zn dimer

For zinc, the third and lightest of the closed shell transition metals, the potential curves were again calculated using a similar correlation consistent basis set, given in Table 2.5. Here the Stuttgart pseudopotential accounted for only 10 electrons ($1s^2 2s^2 2p^6$). Therefore for each of Hg, Cd, and Zn, the basis set described the corresponding set of 20 $ns^2 np^6 nd^{10}(n+1)s^2$ electrons.

S	P	D	F
27.8189900	19.2861750	65.1406540	12.2333720
19.3217370	15.7525290	20.7081300	4.8764620
9.6031930	7.0887213	7.6240140	1.9473111
3.4863537	3.4705979	2.9201221	0.6331333
1.7482956	1.6685402	1.0486878	
0.7883020	0.8548518	0.3274884	
0.2376731	0.5861510	0.1000000	
0.0972165	0.2673118	0.0300000	
0.0429200	0.1037210	0.0100000	
0.0150000	0.0300000		
0.0050000			

Table 2.5: Large basis set used for Zn_2

Again for Zn the overall picture is much the same. It is however noticeable that the difference in bond length between DFT and CCSD(T) is larger than in Cd, close

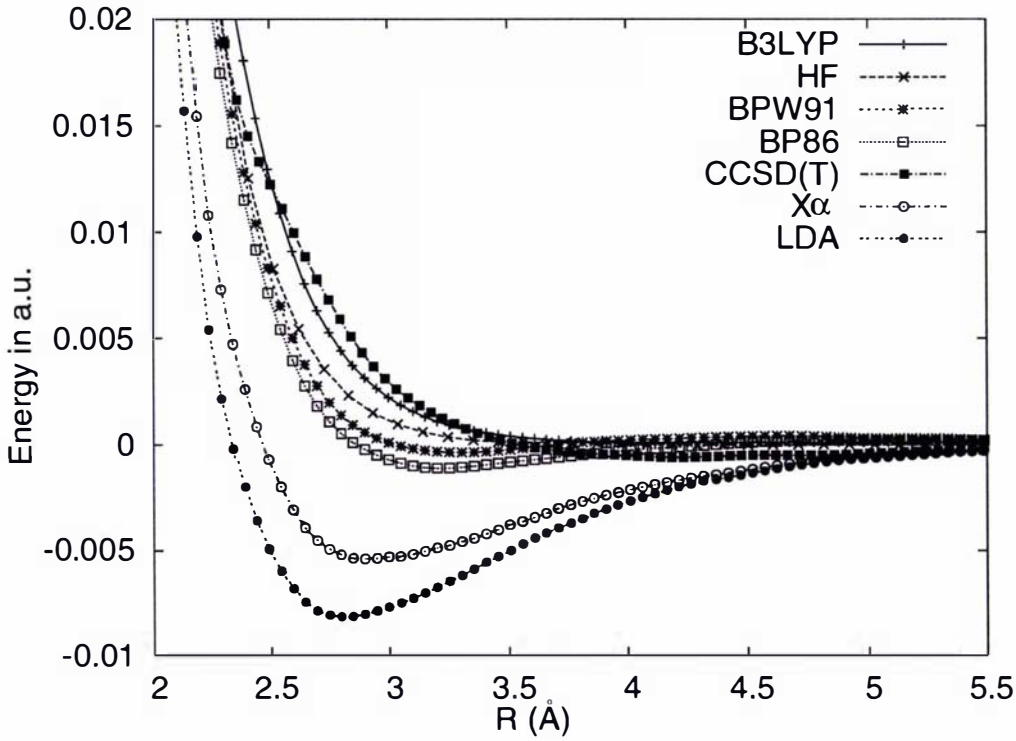

Figure 2.4: Perfomance of DFT and other methods for the Zn dimer

to an Ångstrøm apart. However while DFT would predict the Zn dimer bond length to be shorter than Cd, the experimental values are 4.07 Å for Cd, and 4.19 Å for Zn. This compares reasonably well with the CCSD(T) values given here, 3.738 Å and 4.215 Å respectively.

2.8.4 The Ba dimer

Although barium is not a transition metal, it is nonetheless a metal with a closed s valence shell. As it is close to the same size as mercury and therefore influenced by relativistic effects, it also makes an interesting comparison. For exactly the same reasons, (an inert valence s-shell, relativistically stabilised) the bonding of the dimer is weak, and it might also be described as a pseudo-noble gas. Studies of Ba_n cluster structures have shown similar results to those of mercury and of the noble gases. [Boutou et al., 1998] An MP2-derived correlation consistent basis set of the same size as those for Hg, Cd, and Zn above was used, and is shown in Table 2.6.

The potential curves for Ba_2 are shown in Figure 2.5. The overall behaviour

S	P	D	F
21.8086260	9.6051070	4.7157900	3.6000000
11.6433800	7.3316370	3.1115440	1.8480180
6.3522931	3.5744730	1.3203950	0.6240740
2.5799500	2.0696200	0.5810270	0.2500000
1.6183291	1.2513030	0.2417370	
0.7413510	0.6621420	0.0945010	
0.2638270	0.3066990	0.0400000	
0.1090040	0.1341520	0.0150000	
0.0469540	0.0569136	0.0050000	
0.0200000	0.0150000		
0.0050000			

Table 2.6: Large basis set used for Ba_2

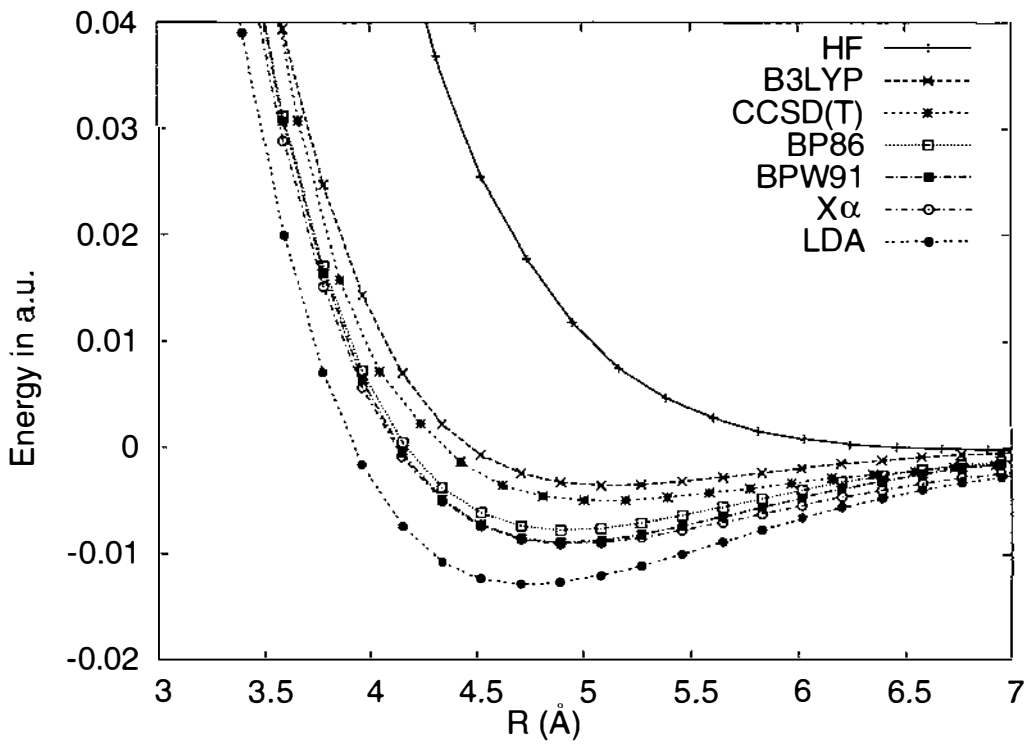

Figure 2.5: Perfomance of DFT and other methods for the Ba dimer

of all methods for Ba is considerably better than for Hg. In particular, the GGA-corrected functionals are all binding, and the agreement between DFT and CCSD(T) is in general much better. This may demonstrate the effect of the relativistically destabilised *d*-electrons in Hg in making the 6*s*-shell particularly inert, to an extent

not seen in Ba.

2.9 Basis set optimisation

The size of the basis set is important in determining the computational cost of a calculation. Hartree-Fock methods formally scale as $\propto N^4$ (N being the number of basis functions) due to the electron-electron interactions involving two coordinates. MP2 calculations scale $\propto N^5$, and CCSD $\propto N^6$, with the perturbative triples scaling $\propto N^7$.

Obviously the smallest possible basis set was required, in order to proceed with CCSD(T) calculations of clusters. The minimum size settled upon is contracted $(6s5p4d1f)$ to $[4s4p3d1f]$. The accuracy of this basis set was assessed using the

	Exponents	Coefficients
S		
	19.4574010	-0.0552906
	11.6982230	0.3960670
	6.2496821	-0.8581300
	0.6095778	1.0000000
	1.3497648	1.0000000
	0.1086466	1.0000000
P		
	14.6845431	0.0241492
	5.6396647	-0.2078700
	1.8643976	1.0000000
	0.7773456	1.0000000
	0.2272886	1.0000000
D		
	5.6700680	-0.0659492
	1.9127247	0.3892000
	0.7668131	1.0000000
	0.2528557	1.0000000
F		
	1.1376527	1.0000000

Table 2.7: Small basis set used for Hg_n

counterpoise procedure of Boys and Bernardi [Boys and Bernardi, 1970], so that a correction due to the basis set superposition error could be estimated. The basis set was obtained by optimising the energy of the atom at the MP2 level, to ensure

consistency with respect to correlation, and to minimise the BSSE at the correlated level. The initial exponents for the contracted functions were taken from a Mulliken population analysis of the large basis set. Following this procedure, the atomic natural orbital (ANO) basis set given in Table 2.7 was obtained.

Figure 2.6 shows the dimer potential curves obtained with this basis set for MP2, MP3, and CCSD(T) correlated methods. The derived spectrscopic parameters are given in Table 2.8, along with the BSSE corrected CCSD(T) and large basis set CCSD(T) results. The BSSE correction is rather larger than desired, but unavoidable with the small size basis set required to enable CCSD(T) calculations of mercury clusters at the sizes required. The MP2 bond-length obtained with the small basis set compares well with the experimental value, but the CCSD(T) value is rather too long.

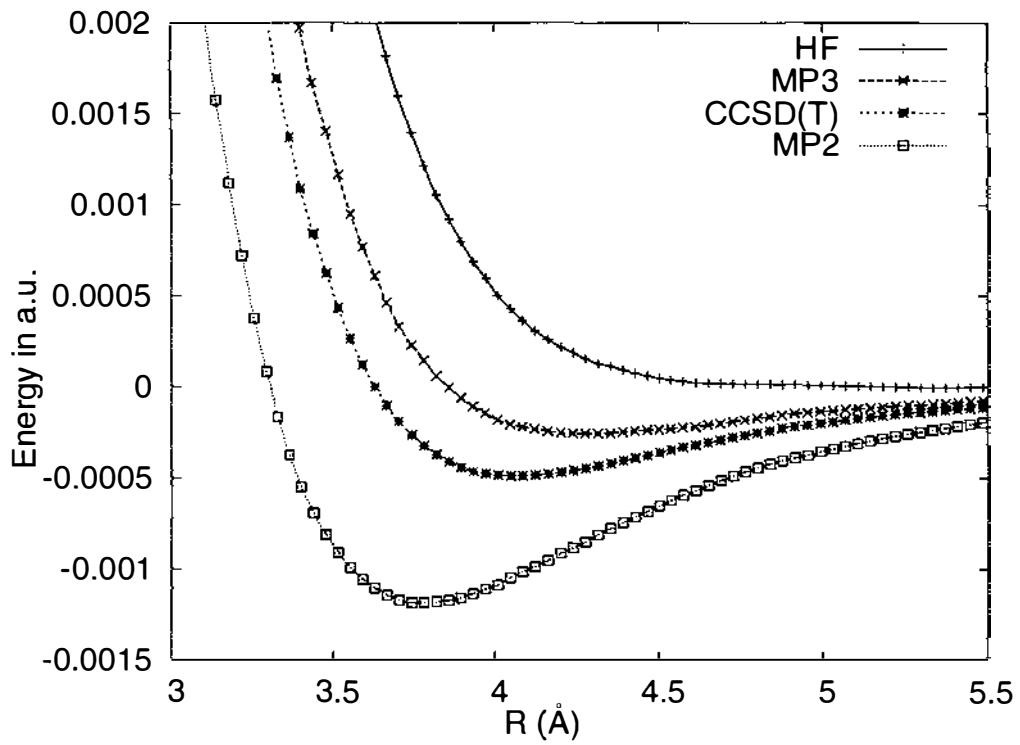

Figure 2.6: The dimer potential for Hg_2 with the small cc-basis.

Basis	Method	r_e	D_e	ω_e
small cc-basis	MP2	3.773	0.001793	19.048
	MP3	4.250	0.000514	9.567
	CCSD(T)	4.064	0.000820	13.666
	CCSD(T)+BSSE	4.341	0.000599	7.844
large cc-basis	CCSD(T)	3.772	0.001628	21.537

Table 2.8: Spectroscopic parameters of the Hg dimer for MP2, MP3, and CCSD(T) as obtained with the small basis set. Energies (D_e) are in atomic units, frequencies (ω_e) are in cm^{-1}, and bond lengths (r_e) are in Ångstrøm.

Chapter 3

Mercury dimer polarisability

In this chapter I will discuss the calculation of the dimer polarisability for Hg_2, and comparison with experimental data. Experimental data are most readily available for the simplest mercury cluster, the dimer. The observable and measurable properties of a system are an important test for theory, that extends past geometries and energies. Electronic and magnetic properties in particular are of great interest and an important field where theory and experiment may now be directly compared.

An interesting example is the diatom polarisability of Hg_2, which was measured by Greif [Greif-Wüstenbecker, 2000] using Raman spectroscopy. The anisotropy of the polarisability[1] can be extracted from the spectrum on the basis of a simple model of the rotational and vibrational energetics. This allows the bond length dependency of the polarisability anisotropy to be calculated, subject to a suitable bonding potential.

Measurement of the collision-induced Raman scattering spectrum in mercury vapour as a function of temperature and pressure provides one of the most direct means of probing the pair interaction potential and the form of the induced pair polarisability anisotropy of the mercury dimer. A relativistic coupled cluster calculation of the distance dependent static polarisability tensor has been recently done, but cannot be compared directly with the experimental results [Schwerdtfeger et al., 2001]. To obtain the frequency dependency of the polarisability, one may apply the Cauchy expansion which is commonly given to three terms:

$$\alpha(\omega) = \sum_{k=0}^{2} S(-2k-2)\omega^{2k} = \alpha(0) + \Delta\alpha(\omega) \tag{3.1}$$

[1] The polarisability anisotropy is the difference between the polarisability of the molecule along its bonding axis, and that perpendicular to it.

where $S(k)$ are the usual Cauchy moments and $\alpha(0) = S(-2)$. This gave too low values of the frequency dependency of the anisotropy component of the dipole polarisability [Moyano et al., 2002] when compared to the experiment [Greif-Wüstenbecker, 2000]. It was not clear at the time whether the theory has to be improved or the experiment reinterpretated. Therefore the dipole polarisability of the mercury dimer has here been calculated at both zero frequency and the frequency used in the experimental measurements (at wavelength λ =488 nm we have $\omega = 20490$ cm^{-1} = 0.09337 a.u.).

3.1 4-component calculations

In previous calculations of the static polarisability of Hg_2 a relativistic pseudopotential together with coupled cluster theory was used [Schwerdtfeger et al., 2001]. In this work a different strategy has been chosen to allow for a more complete treatment of relativistic effects by applying four-component density functional theory (DFT). Two functionals, LDA and B3LYP, have been applied. It is clear from the previous chapter that these two functionals are likely to represent the maximum and minimum bounds of DFT with respect to the binding energy of the dimer. The frequency-dependence of the Hg_2 dipole polarisability is directly obtained with four-component response theory.

The use of pseudopotentials to include relativistic effects in molecular calculations is by far the most widespread method. However it is now possible to directly solve the Dirac equation for moderately sized systems [Saue et al., 2000]. Dirac derived his equation from a consideration of the Schrödinger equation:

$$H\Psi = i\hbar\frac{\partial}{\partial t}\Psi \tag{3.2}$$

where the Hamiltonian contains a second order derivative with respect to space, in contrast to the first order time derivative. The usual expression for the relativistic energy

$$E^2 = p^2c^2 + m^2c^4 \tag{3.3}$$

can be quantised as usual with the identifications;

$$E \rightarrow i\hbar\frac{\partial}{\partial t}, \quad \mathbf{p} \rightarrow -i\hbar\boldsymbol{\nabla} \tag{3.4}$$

to give

$$\left(i\hbar\frac{\partial}{\partial t}\right)^2 \Phi = (i\hbar\boldsymbol{\nabla})^2 c^2\Phi + m^2c^4\Phi. \tag{3.5}$$

This is the Klein-Gordon equation, and can also be written as

$$\left[\left(\frac{1}{c^2}\frac{\partial^2}{\partial t^2} - \boldsymbol{\nabla}^2\right) + \frac{mc}{\hbar}\right]\Phi = 0 \tag{3.6}$$

However this is an equation which is only valid for spin-zero particles, which led Dirac to factorise it such that with the definition of a four-component wavefunction containing spin

$$\Phi = \begin{pmatrix} \Psi_1 \\ \Psi_2 \\ \Psi_3 \\ \Psi_4 \end{pmatrix}, \tag{3.7}$$

it can be rewritten in a factorised form as

$$(p_0 + \alpha_x p_x + \alpha_y p_y + \alpha_z p_z + \beta mc) \times (p_0 - \alpha_x p_x - \alpha_y p_y - \alpha_z p_z - \beta mc)\Phi = 0. \tag{3.8}$$

This factorisation requires the use of 4x4 matrices for the 'α's and β. These may be written:

$$\boldsymbol{\alpha} = \begin{pmatrix} 0 & \boldsymbol{\sigma} \\ \boldsymbol{\sigma} & 0 \end{pmatrix}, \beta = \begin{pmatrix} I_2 & 0 \\ 0 & -I_2 \end{pmatrix} \tag{3.9}$$

where I_2 is the 2x2 identity matrix and $\boldsymbol{\sigma} = (\sigma_x, \sigma_y, \sigma_z)^T$ is the vector of Pauli matrices;

$$\sigma = \left[\begin{pmatrix} 0 & 1 \\ 1 & 0 \end{pmatrix}, \begin{pmatrix} 0 & -i \\ i & 0 \end{pmatrix}, \begin{pmatrix} 1 & 0 \\ 0 & -1 \end{pmatrix}\right]. \tag{3.10}$$

Analogously to non-relativistic calculations, a one-electron operator $\hat{h}$ in the field of N fixed nuclei is defined as

$$\hat{h}_D = \beta' mc^2 + c(\boldsymbol{\alpha} \cdot \mathbf{p}) + \hat{V}_{eN}. \tag{3.11}$$

However in the relativistic regime, energies are shifted by mc^2 which requires the definition of $\beta' = \beta - I_4$.

Due to the 4-component wavefunction, basis sets become more complicated, and are usually split into two parts. The *large component* describes the electronic degrees of freedom, and the *small component* the positronic part of the wavefunction. Commonly the small component (which is not really smaller, but so called because the corresponding part of the wavefunction is less important for electrons) is generated from the large component via the kinetic balance condition, which uses the limit as

$c \rightarrow \infty$;

$$\varphi_S = \frac{1}{2mc}\sigma \mathbf{p}\varphi_L; \quad \Phi = \begin{pmatrix} \varphi_L \\ \varphi_S \end{pmatrix}. \tag{3.12}$$

The great advantage of 4-component calculations, despite the extra cost involved, is that relativistic effects such as spin-orbit coupling are contained within the equations from the beginning on.

3.2 Molecular properties and linear response

As the accuracy of molecular calculations increases, it becomes more important to reduce the discrepancy between experimental and theoretical results by improving the comparison between them. Often the models used to justify the interpretation of experiments may be necessarily less accurate than a high-level calculation. While this is not always the case, the possibility merits cosideration. Response theory is based on describing the response of a molecule to an external perturbation. Thus the polarisability is obtained as the response of a molecule to an electric field, the magnetisability as the analogous response to a magnetic field. The Hamiltonian of equation (3.2) can be written to include the perturbation $V(t)$ as

$$\hat{H} = \hat{H}_0 + \hat{V}(t). \tag{3.13}$$

$\hat{H}_0$ is the time-independent Hamiltonian with solution $|0\rangle$, and energy $E_0^{[0]}$. The time-dependent form of the stationary solution $|0\rangle$ in the presence of the perturbation is then written as

$$e^{-iF(t)} \left|\tilde{0}(t)\right\rangle \tag{3.14}$$

where F(t) is a real function whose time-derivative is denoted the *quasienergy*:

$$\dot{F}(t) = \left\langle \tilde{0}\right| \hat{H} - i\frac{\partial}{\partial t} \left|\tilde{0}\right\rangle \tag{3.15}$$

which in the time-independent limit reduces to the expectation value of $\hat{H}$. The essential points of response theory with respect to a time-averaged quasienergy can be found in reference [Christiansen et al., 1998]. Equation 3.15 can then be rewritten

as

$$\langle\tilde{0}|\,\hat{H}-i\frac{\partial}{\partial t}\,|\tilde{0}\rangle = \langle\tilde{0}|\,\hat{H}_0\,|\tilde{0}\rangle+\sum_i\lambda_i\,\langle\tilde{0}|\,\hat{H}_i\,|\tilde{0}\rangle-\langle\tilde{0}|\,i\frac{\partial}{\partial t}\,|\tilde{0}\rangle \tag{3.16}$$

$$= E_0+\sum_i E_i-S \tag{3.17}$$

$$= Q(t). \tag{3.18}$$

This makes use of the Hellmann-Feynman theorem which for a time-independent wavefunction Ψ, gives for any derivative of the energy[2]

$$\frac{\partial E}{\partial\epsilon} = \left\langle\frac{\partial\Psi}{\partial\epsilon}\middle|\hat{H}\middle|\Psi\right\rangle+\left\langle\Psi\middle|\hat{H}\middle|\frac{\partial\Psi}{\partial\epsilon}\right\rangle+\left\langle\Psi\middle|\frac{\partial\hat{H}}{\partial\epsilon}\middle|\Psi\right\rangle \tag{3.19}$$

$$= E\left[\left\langle\frac{\partial\Psi}{\partial\epsilon}\middle|\Psi\right\rangle+\left\langle\Psi\middle|\frac{\partial\Psi}{\partial\epsilon}\right\rangle\right]+\left\langle\Psi\middle|\frac{\partial\hat{H}}{\partial\epsilon}\middle|\Psi\right\rangle \tag{3.20}$$

$$= E\frac{\partial}{\partial\epsilon}\langle\Psi|\Psi\rangle+\left\langle\Psi\middle|\frac{\partial\hat{H}}{\partial\epsilon}\middle|\Psi\right\rangle \tag{3.21}$$

$$= \left\langle\frac{\partial\hat{H}}{\partial\epsilon}\right\rangle \tag{3.22}$$

so that the energy derivative is simply the expectation value of the derivative of the Hamiltonian. In the time-dependent case, however, the derivative of the quasienergy is

$$\frac{\partial Q}{\partial\epsilon} = \left\langle\frac{\partial\tilde{0}}{\partial\epsilon}\middle|\hat{H}-i\frac{\partial}{\partial t}\middle|\tilde{0}\right\rangle+\left\langle\tilde{0}\middle|\hat{H}-i\frac{\partial}{\partial t}\middle|\frac{\partial\tilde{0}}{\partial\epsilon}\right\rangle+\left\langle\tilde{0}\middle|\frac{\partial\hat{H}}{\partial\epsilon}\middle|\tilde{0}\right\rangle \tag{3.23}$$

$$= Q\left[\left\langle\frac{\partial\tilde{0}}{\partial\epsilon}\middle|\tilde{0}\right\rangle+\left\langle\tilde{0}\middle|\frac{\partial\tilde{0}}{\partial\epsilon}\right\rangle\right]+\left\langle\tilde{0}\middle|\frac{\partial\hat{H}}{\partial\epsilon}\middle|\tilde{0}\right\rangle-i\frac{\partial}{\partial t}\left\langle\tilde{0}\middle|\frac{\partial\tilde{0}}{\partial\epsilon}\right\rangle \tag{3.24}$$

$$= Q\frac{\partial}{\partial\epsilon}\langle\tilde{0}\,|\tilde{0}\rangle+\left\langle\tilde{0}\middle|\frac{\partial\hat{H}}{\partial\epsilon}\middle|\tilde{0}\right\rangle-i\frac{\partial}{\partial t}\left\langle\tilde{0}\middle|\frac{\partial\tilde{0}}{\partial\epsilon}\right\rangle \tag{3.25}$$

$$= \left\langle\frac{\partial\hat{H}}{\partial\epsilon}\right\rangle-i\frac{\partial}{\partial t}\left\langle\tilde{0}\middle|\frac{\partial\tilde{0}}{\partial\epsilon}\right\rangle \tag{3.26}$$

and an extra term remains. However this may be dealt with by assuming that the perturbation $\hat{V}(t)$ is periodic and may be written in terms of its Fourier components

[2]The energy is just the expectation value of the Hamiltonian, $E=\langle\Psi|\,\hat{H}\,|\Psi\rangle$.

as

$$\hat{V}(t) = \sum_{k=-N}^{+N} e^{-i\omega_k t} \sum_X \varepsilon_X(\omega_k)\hat{H}_X, \tag{3.27}$$

where ε is the field strength vector $\varepsilon_X(\omega_k)$ which specifies the strength and polarisation of the external field at frequency ω_k, $\hat{H}_X$ is the property operator, and the first sum takes care of the periodicity. The *time-averaged* quasienergy (written in $\{\}_T$ with period T that we average over) is then

$$\frac{\{\partial Q\}_T}{\partial \epsilon} = \left\{ \left\langle \tilde{0} \left| \frac{\partial \hat{H}}{\partial \epsilon} \right| \tilde{0} \right\rangle \right\}_T - i\frac{1}{T} \int_{-\frac{T}{2}}^{\frac{T}{2}} \frac{\partial}{\partial t} \left\langle \tilde{0} \left| \frac{\partial \tilde{0}}{\partial t} \right\rangle \right. dt \tag{3.28}$$

$$= \left\{ \left\langle \tilde{0} \left| \frac{\partial \hat{H}}{\partial \epsilon} \right| \tilde{0} \right\rangle \right\}_T - i\frac{1}{T} \left[\left\langle \tilde{0} \left| \frac{\partial \tilde{0}}{\partial t} \right\rangle \right. \right]_{-\frac{T}{2}}^{\frac{T}{2}} \tag{3.29}$$

$$= \left\{ \left\langle \tilde{0} \left| \frac{\partial \hat{H}}{\partial \epsilon} \right| \tilde{0} \right\rangle \right\}_T \tag{3.30}$$

$$= E_0(0) + \sum_{k=-N}^{+N} \sum_X \varepsilon_X(\omega_k) E_X(\omega_k) - S \tag{3.31}$$

using equation (3.17) and with the introduction of

$$E_X(\omega_k) = \left\{ \left\langle \tilde{0} \left| \hat{H}_X \right| \tilde{0} \right\rangle e^{-i\omega_k t} \right\}_T \tag{3.32}$$

and

$$S = \left\{ \left\langle \tilde{0} \left| i\frac{\partial}{\partial t} \right| \tilde{0} \right\rangle \right\}_T. \tag{3.33}$$

Properties are defined in terms of derivatives of the quasienergy, such that a first-order property is

$$\left. \frac{d\{Q(t)\}_T}{d\varepsilon_A(\omega_a)} \right|_{\varepsilon=0} = \left[\frac{dQ_0}{d\varepsilon_A(\omega_a)} + E_A(\omega_a) + \left(\sum_{k=-N}^{+N} \sum_X \varepsilon_X(\omega_k) \frac{dE_X(\omega_k)}{d\varepsilon_A(\omega_a)} \right) \right]_{\varepsilon=0}. \tag{3.34}$$

The term in parentheses disappears at zero field strength $\varepsilon = 0$. The time-independent wavefunction may be rewritten as

$$|\tilde{0}\rangle = e^{-\hat{\kappa}(t)} |0\rangle \tag{3.35}$$

with the use of the second quantisation formalism[3] such that the orbital rotation operator is

$$\hat{\kappa}(t) = \sum_{ai} \left[\kappa_{ai}(t) q_{ai}^{\dagger} - \kappa_{ai}^{*}(t) q_{ai} \right], \tag{3.36}$$

with $q_{ai}^{\dagger} = \hat{a}_a^{\dagger}\hat{a}_i$. The zeroth order Hamiltonian can then be written

$$\hat{H}_0 = \sum_{pq} \hat{a}_p^{\dagger}\hat{a}_q + \frac{1}{2}\sum_{pqrs} g_{pq,rs}\hat{a}_p^{\dagger}\hat{a}_r^{\dagger}\hat{a}_s\hat{a}_q. \tag{3.37}$$

The property operators are one electron operators:

$$\hat{H}_X = \sum_{pq} h_{X;pq}\hat{a}_p^{\dagger}\hat{a}_q. \tag{3.38}$$

The polarisation of a system in response to an electric field may be written

$$\mu(\varepsilon) = \mu(0) + \mu'(0)\varepsilon + \mu''(0)\varepsilon^2 + \ldots \tag{3.39}$$

$$= -\left[\left.\frac{\partial E}{\partial \varepsilon_i}\right|_{\varepsilon=0} + \left.\frac{\partial^2 E}{\partial \varepsilon_i \partial \varepsilon_j}\right|_{\varepsilon=0} + \left.\frac{\partial^3 E}{\partial \varepsilon_i \partial \varepsilon_j \partial \varepsilon_k}\right|_{\varepsilon=0} + \ldots \right] \tag{3.40}$$

using standard perturbation theory with $\mu(0)$ being the polarisation in the absense of an electric field, and μ' the dipole polarisability. i.e.

$$\mu'(0) = \left.\frac{\partial^2 E}{\partial \varepsilon_i \partial \varepsilon_j}\right|_{\varepsilon=0} \tag{3.41}$$

$$= -\sum_{n} \frac{e^2 \langle 0|r_i|n\rangle \langle n|r_j|0\rangle + \langle 0|r_j|n\rangle \langle n|r_i|0\rangle}{E_0 - E_n + \omega} \tag{3.42}$$

This means that as $\omega \to E_0 - E_n$ the response property will blow up as the denominator goes to zero. While this places a restriction on the calculation of properties near these poles, it also allows the excitation energies (i.e. $\Delta E_1 = E_0 - E_1$) to be determined from a response calculation.

In the time-dependent theory the same second derivative is used, but this time

[3]The notation is then such that $\hat{a}_p^{\dagger}$ is a creation operator which corresponds to the placement of one electron in one orbital p. The conjugate operator, $\hat{a}_p$ is the annihilation operator which removes the electon from orbital p. Thus this notation is particularly suited to describing excitations - $q_{ai}^{\dagger} = \hat{a}_a^{\dagger}\hat{a}_i$ describes the excitation of an electron from orbital i to orbital a. It is conventional to label occupied orbitals by $i, j, \ldots$, unoccupied (virtual) orbitals by $a, b, \ldots$ and generalised orbitals by $p, q, \ldots$.

with time-averaging, so (see for example reference [Saue and Jensen, 2003])

$$\left.\frac{\partial\{Q\}_T}{\partial\varepsilon_A(\omega_a)\partial\varepsilon_B(\omega_b)}\right|_{\varepsilon=0} = -E_A^{[1]\dagger}\left(E_0^{[2]} - \omega_A S^{[2]}\right)^{-1} E_B^{[1]}\delta\left(\omega_a + \omega_b\right). \tag{3.43}$$

3.3 The calculation of the diatom polarisability

3.3.1 Details

The calculations were performed using the program DIRAC [Saue et al., 2000]. Two basis sets were used, the smaller $[24s20p14d10f]$ a double zeta (DZ) and a larger triple zeta (TZ) $[28s25p25d12f2g]$. These are shown in Tables 3.1 and 3.2. The DZ basis is from Jon Laerdahl and the TZ is from Ken Dyall [Saue, 2003].

The small component basis sets are obtained in DIRAC through the restricted kinetic balance condition.

Not surprisingly, the LDA and B3LYP functionals used in this study give wildly varying descriptions of binding in the dimer in comparison with the more accurate coupled cluster curve [Moyano et al., 2002] as shown in Figure 3.1.

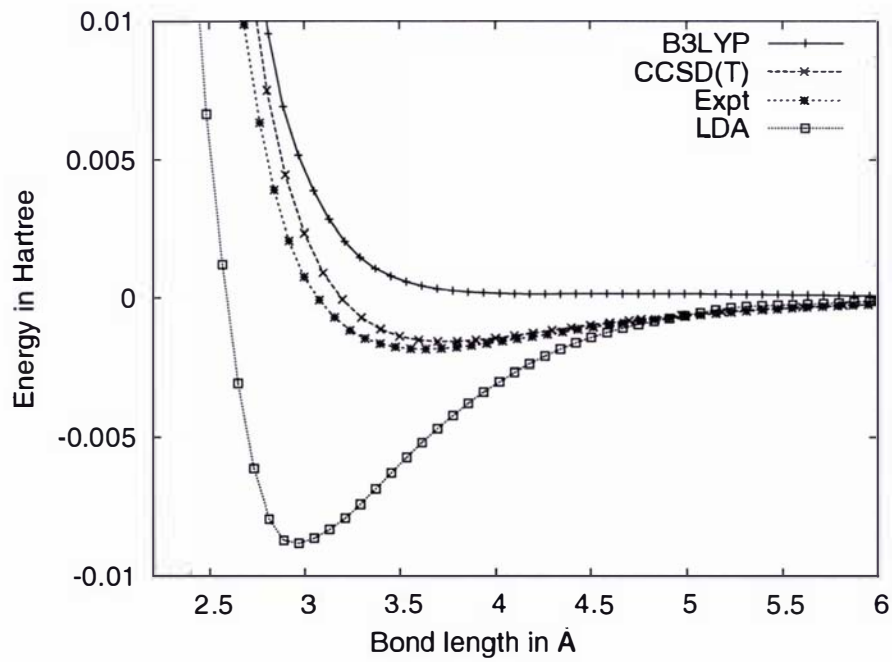

Figure 3.1: A comparison of the dimer potentials.

As expected LDA strongly overbinds, with a binding energy of 0.00874 a.u. at 2.98 Å, (compared to experimental values of 0.0018 at 3.69 Å, [Koperski et al., 1997]) whereas B3LYP produces a uniquely repulsive potential. Moreover, in the outer region where Van der Waals forces are dominant DFT underbinds as one expects. It has been noted that this leads to similar difficulties with a DFT description for the solid state structure even though mercury undergoes a transition to the metallic phase [Moyano et al., 2002]. The first comparison to experiment can be made for the static polarisability of the atom: the DZ and TZ basis sets give in LDA 33.276 a.u. and 32.974 a.u. respectively; the experimental value is 33.92 a.u.[Goebel and Hohm, 1996]. The frequency dependent dipole polarisability of the

Exponent	Exponent	Exponent
S	P	D
42515256.9000000	2614700.0000000	3190.9511000
6366432.9100000	373529.0000000	1381.3224100
1448817.7100000	53361.2373000	616.2636550
410344.8230000	12642.9599000	274.8792560
133820.4890000	4101.8663700	130.2074620
48222.0654000	1564.1560900	63.4061606
18675.4219000	660.3682240	31.5383229
7595.1614100	298.3409460	15.5203160
3190.9511000	141.1517790	7.5148362
1381.3224100	67.5224666	3.5881046
616.2636550	33.5740826	1.5517361
274.8792560	16.5552927	0.6286907
130.2074620	8.0454562	0.2514760
63.4061606	3.8511094	0.1005910
31.5383229	1.6418927	F
15.5203160	0.7063681	298.3409460
7.5148362	0.2743086	141.1517790
3.5881046	0.1097230	67.5224666
1.5517361	0.0438894	33.5740826
0.6286907	0.0175557	16.5552927
0.2514760		8.0454562
0.1005910		3.8511094
0.0402362		1.6418927
0.0160945		0.7063681
		0.2743086

Table 3.1: DZ all-electron uncontracted dual type basis set for mercury.

dimer is plotted in Figure 3.2, and the position of the poles gives the exitation energies of the atom as shown in equation (3.41) above. The experimental values are

Exponent	Exponent	Exponent
S	P	D
61348299.2100000	33483626.7900000	22339.4551000
16350744.6900000	7556509.7280000	10215.3052200
5622750.9540000	2002790.1900000	4728.2685660
2163852.5770000	592553.1162000	2232.0714530
925960.7609000	190993.0206000	1075.8991780
429284.2594000	66189.0219300	527.3706795
211154.0827000	24520.7343800	266.2909859
103195.4160000	9693.4449780	138.1507935
48645.6535000	4079.4096430	73.0861747
22339.4551000	1816.2570060	39.4589592
10215.3052200	848.0925164	21.4362672
4728.2685660	411.5709681	11.4657192
2232.0714530	206.3216386	6.0776230
1075.8991780	105.6061466	3.1552340
527.3706795	54.8921209	1.5690483
266.2909859	29.1635716	0.7385656
138.1507935	15.3632757	0.3248779
73.0861747	7.9334039	0.1302803
39.4589592	4.0431780	0.0503267
21.4362672	2.0008470	F
11.4657192	0.9146807	848.0925164
6.0776230	0.3699421	411.5709681
3.1552340	0.1647966	206.3216386
1.5690483	0.0665427	105.6061466
0.7385656	0.0263329	54.8921209
0.3248779		29.1635716
0.1302803		15.3632757
0.0503267		7.9334039
		4.0431780
		2.0008470
		0.9146807
		0.3699421
		G
		1.5690483
		0.7385656

Table 3.2: TZ all-electron uncontracted dual type basis set for mercury.

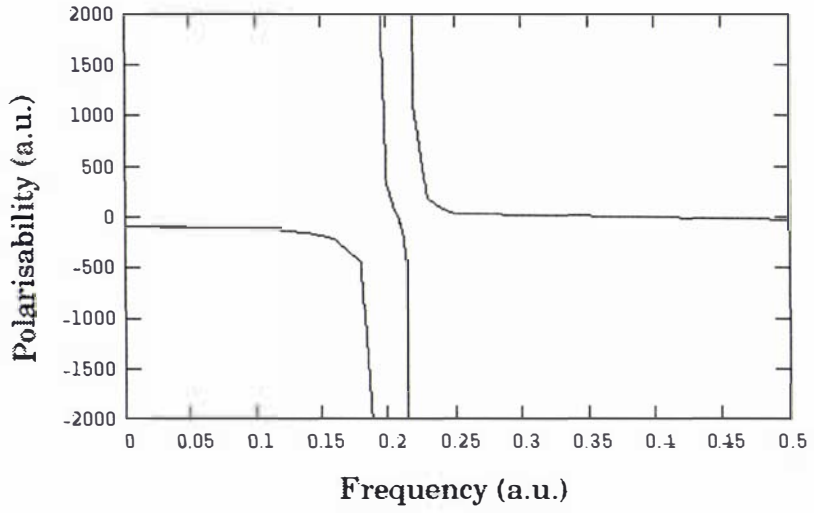

Figure 3.2: The excitation energies of the mercury dimer at the experimental bond length are seen as poles in the calculated frequency-dependent polarisability (LDA)

$^1S_0 \rightarrow {}^3P_1$: 0.180 a.u and $^1S_0 \rightarrow {}^1P_1$: 0.246 a.u. The TZ basis set was used for all the polarisability calculations, and is certainly sufficient as a comparison with the smaller DZ basis shows. Since the atomic polarisability is more sensitive to the choice of functional than the basis set used, the density functional approximation is not accurate enough to justify using a better basis, and the basis set superposition error (BSSE) can be accounted for using the counterpoise method [Fernández et al., 1999]. The polarisability of the atom is calculated in the presence of the basis set belonging to the second ghost atom, at the same geometry; this value is then used as the atomic polarisability in the presence of this basis set ($\alpha_0^{basis}(r)$). The dimer interaction dipole polarisability is then defined as the polarisability of the dimer with twice the atomic value subtracted:

$$\alpha(r) = \alpha_{dimer}(r) - 2\alpha_0^{basis}(r) \tag{3.44}$$

where α_0 is the atomic polarisability, and the superscript indicates that this is calculated in the presence of the basis functions belonging to the second atom in the dimer at the appropriate bond length. With the basis set used (TZ) this correction to the polarisability was consistently very small. It was a maximum of 0.7 a.u. at 2 Å, but less than 0.1 a.u. at 3 Å. This is clearly a general feature and advantage of DFT since BSSEs from wavefunction based correlated methods are known to be

	DZ basis		TZ basis	
	LDA	B3LYP	LDA	B3LYP
Static	33.28	35.42	32.97	35.14
488 nm	37.19	39.24	36.93	38.99

Table 3.3: The atomic polarisability (in a.u., a_0^3) as calculated with different basis sets (DZ and TZ) and density functionals. The experimental value is 33.919(7) a.u. [Goebel and Hohm, 1996]

much larger [Schwerdtfeger et al., 2001].

3.3.2 Polarisabilities

The results for the atomic polarisabilities are given in Table 3.3 for the two chosen functionals LDA and B3LYP. The dependence of the atomic polarisability on the basis set used is clearly less than the effect of the choice of functional. In any case, both functionals give reliable static polarisabilities with respect to the experimental value [Goebel and Hohm, 1996]. For the dynamic part there is a study by Visscher *et al* [Visscher et al., 1997] using a four-component random phase approximation (RPA) for a range of different frequencies. Interpolating their relativistic values and using the Cauchy expansion of equation (3.1), the effect of the frequency $\Delta\alpha(\omega) = 12.6$ a.u. at the RPA level of theory. This is far greater than the current values, i.e. $\Delta\alpha(\omega) = 4.0$ a.u. (LDA) and 3.8 a.u. (B3LYP). However, as has been pointed out, [Visscher et al., 1997] the RPA calculations are missing electron correlation and the first pole belonging to the $^1S_0 \rightarrow {}^3P_1$ transition is too low (0.105 a.u.) compared to the experimental value of 0.180 a.u. [Moore, 1958]. Hence, in their calculations at $\omega = 0.09337$ a.u. they will already be strongly affected by the pole of the first transition. The DFT calculations give poles at 0.204 a.u. (LDA) and 0.214 a.u. (B3LYP) for the first $^1S_0 \rightarrow {}^3P_1$ transition, and 0.242 a.u. (LDA) and 0.255 a.u. (B3LYP) for the second $^1S_0 \rightarrow {}^1P_1$ transition (the experimental value is 0.246 a.u. [Moore, 1958]). For the first transition these are above the experimental value which probably indi-

cates that these $\Delta\alpha(\omega)$ are slightly underestimated. However, if we take the Cauchy moments recently obtained from interferometric measurements of the frequency dependence of the refractive index by Goebel and Hohm [Goebel and Hohm, 1996], i.e. $S(-2) = 33.919(7)$ a.u., $S(-4) = 279.8(2.4)$ a.u. and $S(-6) = 14064(203)$ a.u., the value obtained is $\Delta\alpha(\omega) = 3.50(4)$ a.u. at $\omega = 0.09337$ a.u. in excellent agreement with our values. The less accurate one-term Kramers-Heisenberg dispersion formula to correct for frequency dependence

$$\alpha(\omega) = \alpha(0)\omega_0^2(\omega_0^2 - \omega^2)^{-1} \tag{3.45}$$

gives $\Delta\alpha(\omega) = 12.5$ a.u. with the data from experiment [Goebel and Hohm, 1996] in better agreement with the RPA results [Visscher et al., 1997]. It was however noted by Goebel and Hohm [Goebel and Hohm, 1996] that this formula does not fit their experimental values.

The potential depth is only about 1% of the first excitation energy (266 nm [Zehnacker et al., 1987]) into the $^1P_1(1_u)$ state of Hg_2, which is small compared to errors inherent in DFT response theory, and this should not have much influence on the location of the poles for $\alpha(\omega)$. Indeed, the response theory results are in nice agreement with those of experiment.

For the first $X0_g^+ \rightarrow 1_u$ transition the poles are found at 0.20 (LDA) and 0.21 (B3LYP) a.u. compared to the experimental value of 0.171 a.u. [Zehnacker et al., 1987]. The second transition ($X0_g^+ \rightarrow 0_u^+$) occurs at 0.22 (LDA) and 0.24 (B3LYP) a.u. (exp. 0.179 a.u. [Koperski et al., 1994]). Hence the $\alpha(\omega)$ value for Hg_2 at $\omega = 0.09337$ a.u. is expected to be unaffected by these singularities.

The Cauchy moments for the dimer may be calculated from a fit to the frequency dependent polarisability between zero and 0.12 a.u., i.e. before the first singularity. The fit is done according to the three term Cauchy expansion of equation (3.1), including 9 terms to obtain converged values, which results in Cauchy moments as given in Table 3.4.

The parallel and perpendicular components of the dimer (interaction) polarisability are shown in Figures 3.3 and 3.4. Here both the isotropy and anisotropy go to zero for long bond lengths, as this is the dimer *interaction* polarisability.

3.3.3 Second refractivity virial coefficient

In a dimer the polarisability may be separated into two components, one along the bonding axis $\alpha_{\|}$, which will be greater than that of the two independent atoms (atomic

	$S_{\|\|}(-2)$	$S_{\|\|}(-4)$	$S_{\|\|}(-6)$	$S_{\perp}(-2)$	$S_{\perp}(-4)$	$S_{\perp}(-6)$
LDA	92.300	1647.699	38836.384	60.718	654.278	9881.548
B3LYP	95.422	1468.092	31134.425	64.182	635.005	9838.613

Table 3.4: The first three Cauchy moments at the LDA and B3LYP level of theory for both the parallel and perpendicular components of the polarisability (in a.u.).

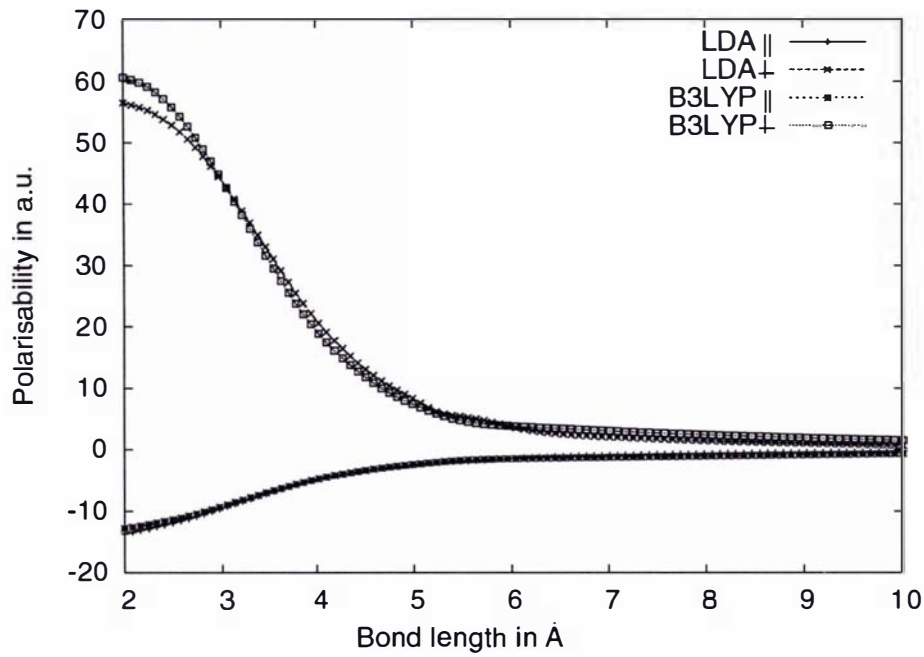

Figure 3.3: The static interaction polarisability in parallel and perpendicular components.

polarisability α_0) due to the orientation of bonding orbitals, whereas the component of the polarisability perpendicular to this axis, $\alpha_{\perp}$ will be reduced accordingly. Therefore when the atomic polarisability is subtracted from that of the dimer, $\alpha_{||}$ and $\alpha_{\perp}$ will have positive and negative signs respectively. An early introduction to much of the background material is given in reference [Buckingham, 1967].

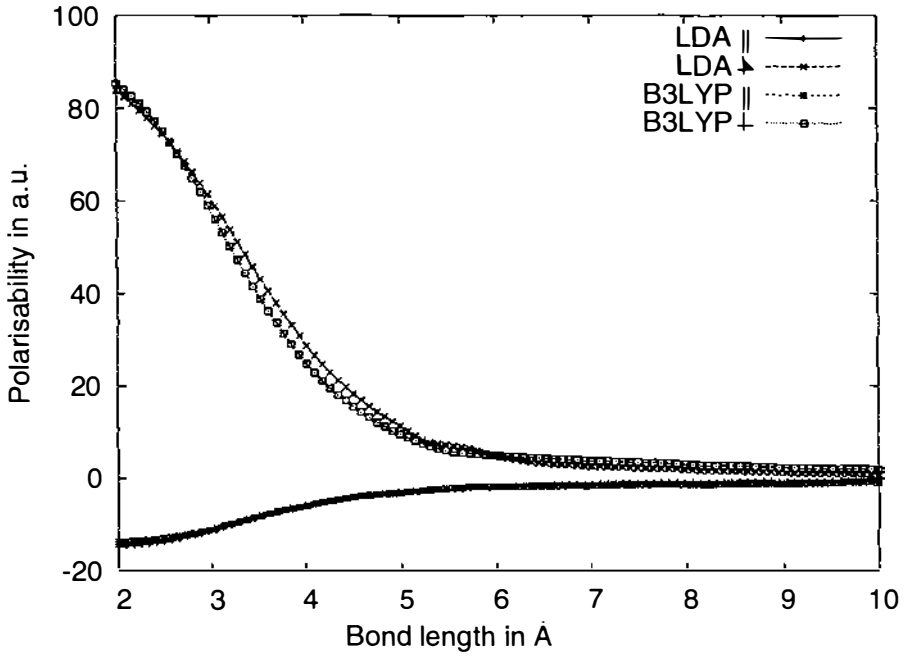

Figure 3.4: The dynamic interaction polarisability in parallel and perpendicular components.

The isotropic part of the dimer polarisability is then defined as a spatial average

$$\alpha = \frac{2\alpha_{\perp} + \alpha_{\parallel}}{3} \tag{3.46}$$

and the anisotropy is

$$\beta = \alpha_{\parallel} - \alpha_{\perp}. \tag{3.47}$$

This interaction induced dimer polarisability isotropy, α (i.e. the total polarisability of the dimer corrected for the atomic values as described in equation (3.44)) is related to the second refractivity virial coefficient $B_R(\omega, T)$. The refractivity virial coefficients are defined in terms of the Clausius-Mossotti function of the refractive index n, expanded in orders of the molar density ρ,

$$\frac{n^2 - 1}{n^2 + 2} = A_R(\omega, T)\rho + B_R(\omega, T)\rho^2 + C_R(\omega, T)\rho^3 + \ldots \tag{3.48}$$

and the first virial coefficient $A_R(\omega, T)$ is related to the atomic polarisability

$$A_R(\omega, T) = \frac{N_A}{3\epsilon_0}\alpha(\omega) \tag{3.49}$$

where N_A is Avogadro's number and ϵ_0 the vacuum permittivity.

The second virial coefficient, $B_R(\omega, T)$, can be calculated from the classical expression

$$B_R(\omega, T) = \frac{N_A^2}{6\epsilon_0} 4\pi \int_0^\infty \alpha(\omega, R) e^{[-V(R)/kT]} R^2 dR \tag{3.50}$$

where V(R) is the dimer potential. [Buckingham and Pople, 1955] These expressions assume units of $a_0^3\epsilon_0$ for α, whereas all values of α given here are in a_0^3. Thus ϵ_0 is only included in the above equations for consistency with other publications, e.g. [Fernández et al., 1999].

The integrand of equation (3.50) is plotted in Figures 3.5 and 3.6 for the LDA and B3LYP values of α respectively, where the dimer potential used is the CCSD(T) potential of Figure 3.1, and $T = 298.15$ K. Strictly speaking such an expression is only valid for energies $< kT$, and thus the potential minimum of 400 cm^{-1} that we have for mercury sets a bound of $T > 575$ K. However we are able to use a range of temperatures, and thus assess the temperature dependence of $B_R(\omega, T)$ in a temperature regime where the classical statistical mechanical expression should hold.

The integration was performed numerically over the 19 distance dependent values of α, for both the static and frequency dependent results. The resulting virial coefficients are given in Table 3.5. The temperature dependence of $B(0, T)$ and

	$B_R(\omega = 0, T = 298.15)$	$B_R(\omega = 0.09337, T = 298.15)$
LDA	2.2443×10^3	3.1269×10^3
B3LYP	1.7008×10^3	2.2807×10^3

Table 3.5: The second refractivity virial coefficients, in a.u. (a_0^6).

$B(\omega = 0.09337, T)$ is plotted in Figure 3.7. The integrand of equation (3.50) is plotted for the temperature dependent static LDA case in Figure 3.8.

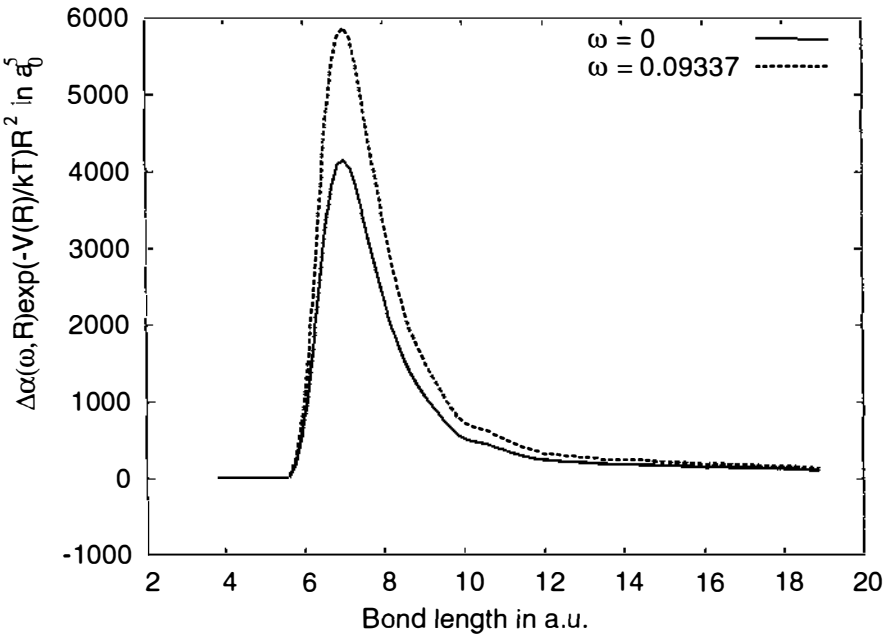

Figure 3.5: The integrand in equation (3.50) with LDA α.

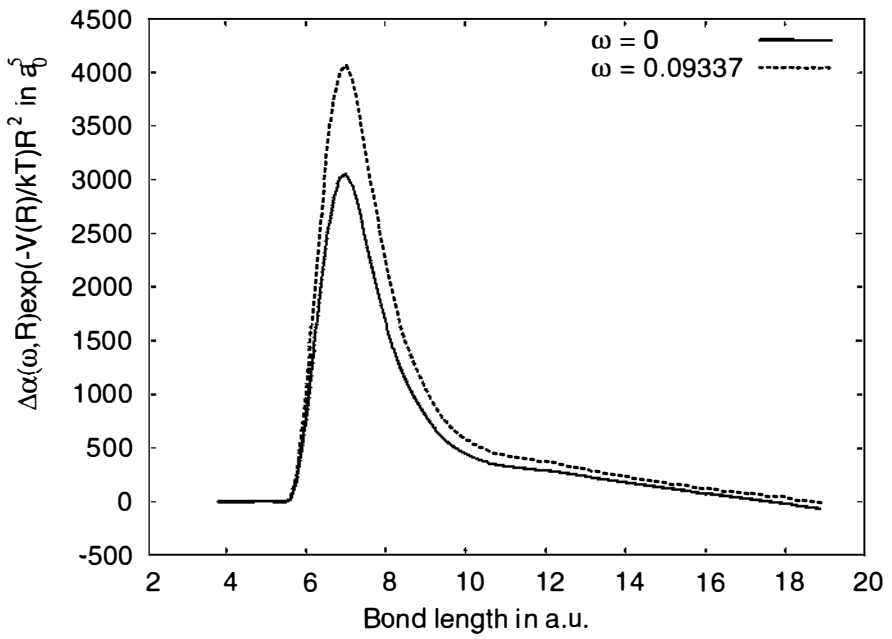

Figure 3.6: The integrand in equation (3.50) with B3LYP α.

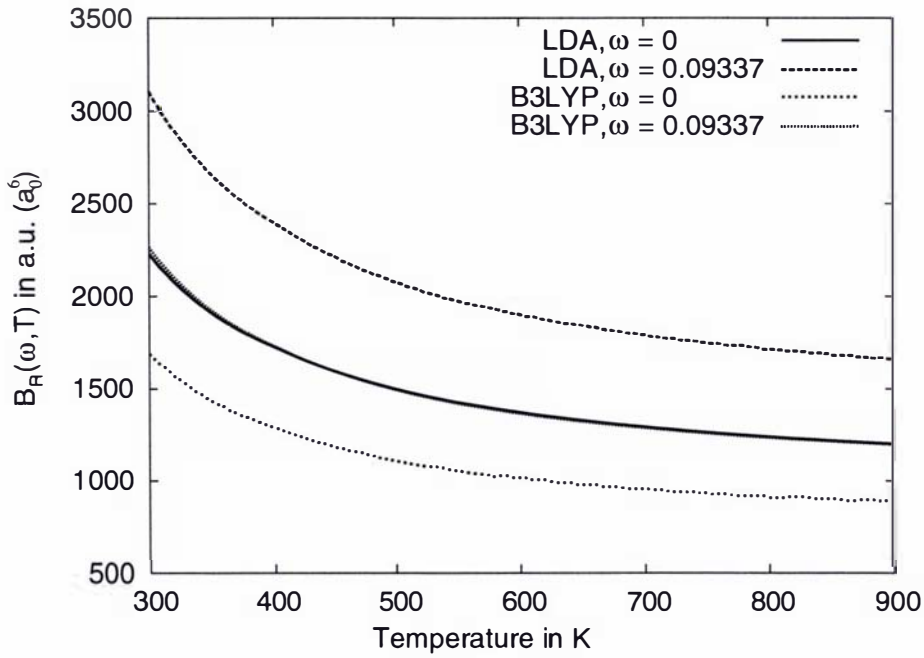

Figure 3.7: Temperature dependence of $B(\omega, T)$ with LDA and B3LYP.

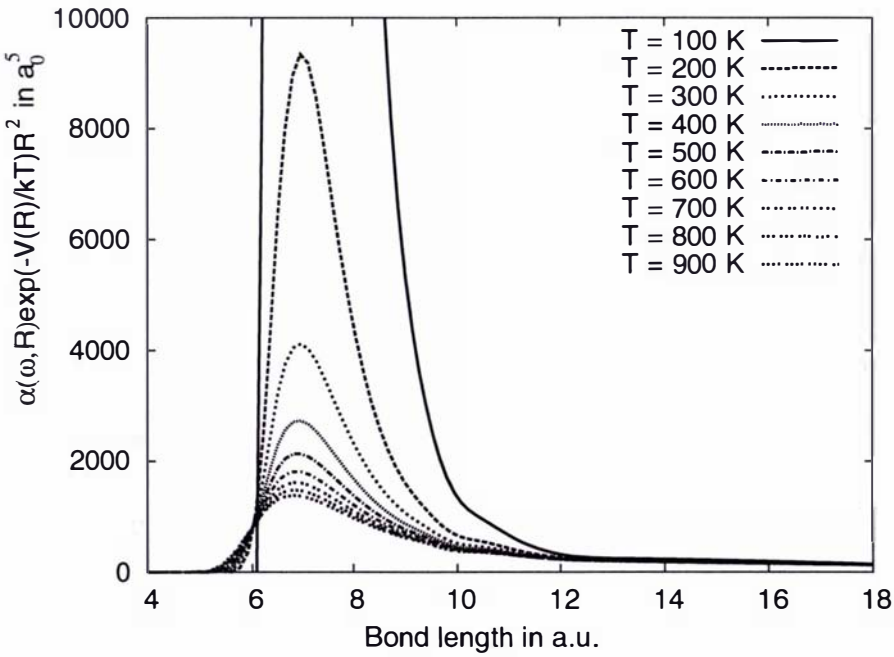

Figure 3.8: Temperature dependence of $\alpha(\omega, T)e^{-V(R)/kT}R^2$, static LDA.

3.3.4 Comparison with experiment

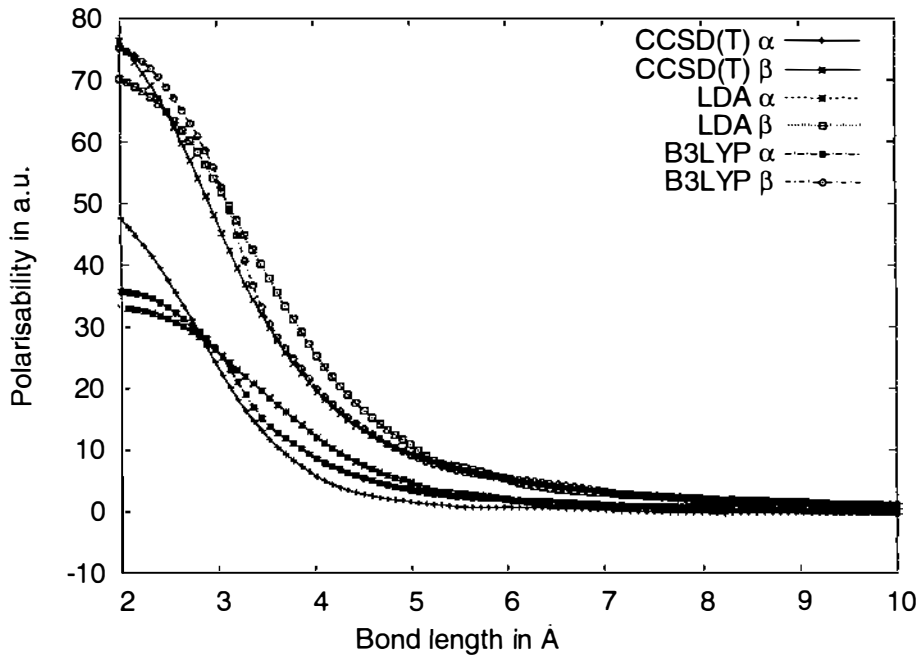

Figure 3.9: The static polarisability in isotropic (α) and anisotropic (β) components.

The static polarisability of Hg dimer has been calculated previously at the scalar relativistic CCSD(T) level [Schwerdtfeger et al., 2001]. However the experiment was - inevitably - conducted at a finite frequency, 488 nm. Therefore both the static ($\omega = 0$) and frequency-dependent ($\omega = 488$ nm) polarisabilities have been calculated in order to be able to compare four-component DFT results with both the experimental and theoretical data available.

The information extracted from the collision induced Raman scattering spectrum is limited to the anisotropic component of the dipole polarisability.

In Figure 3.9 and Figure 3.10 the isotropic average of the molecular polarisability, α, is given as well as a comparison to the CCSD(T) results from reference [Schwerdtfeger et al., 2001]. The anisotropic values are also shown, and may be compared with the experimental curve. The agreement between the anisotropic values and experiment is good, although the curves cross near the potential minimum. Despite the lack of any binding in the B3LYP potential curve, it reproduces the experimental polarisability anisotropy about as closely as LDA.

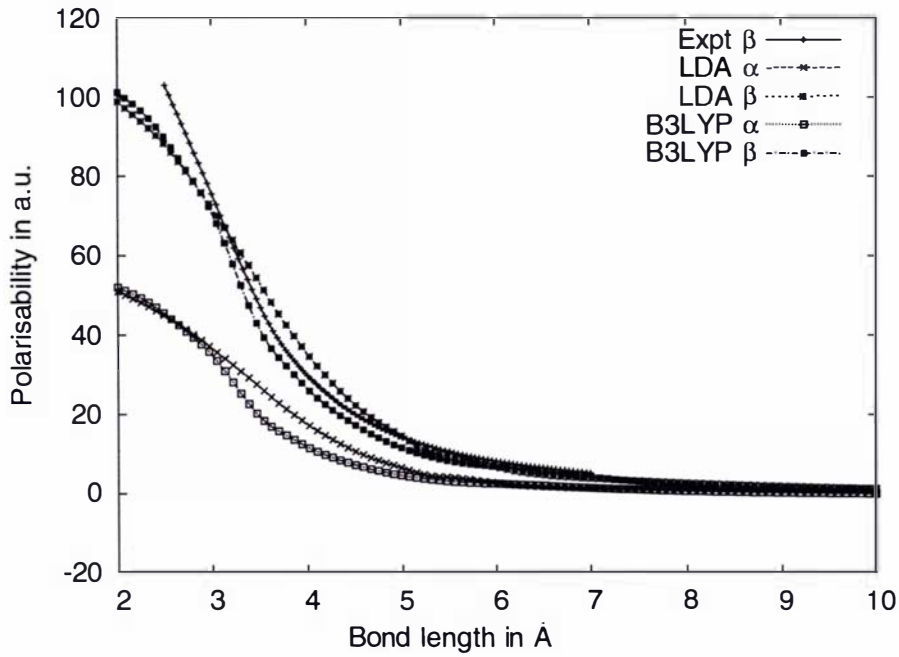

Figure 3.10: The frequency dependent polarisability in isotropic (α) and anisotropic (β) components.

Interestingly the experimental curve behaves similarly to the CCSD(T) static curve, in that it shows greater polarisability below the potential minimum, and very slightly less polarisability anisotropy above the potential minimum.

In [Schwerdtfeger et al., 2001] the CCSD(T) anisotropy was shown to agree very closely with experiment (over intermediate bond lengths) when scaled by a factor of 1.37; this was shown to be approximately equal to

$$\beta(\omega) = \beta\left(1 + \frac{\omega^2}{\omega_0^2}\right) \tag{3.51}$$

which gives a factor of 1.17 if one takes the experimental value of 488 nm as ω, and the most intense transition in Hg_2 at 203 nm for ω_0. The assumption that the anisotropy will increase with frequency is reasonable, as the parallel component will be larger than the perpendicular component of the polarisability due to the transition dipole $\sigma \rightarrow \sigma^*$ (or vice versa) along the bonding axis.

In Figure 3.11 the CCSD(T) static polarisability anisotropy results of Schwerdtfeger *et al* are scaled by 1.37 which is compared to both DFT and experimental

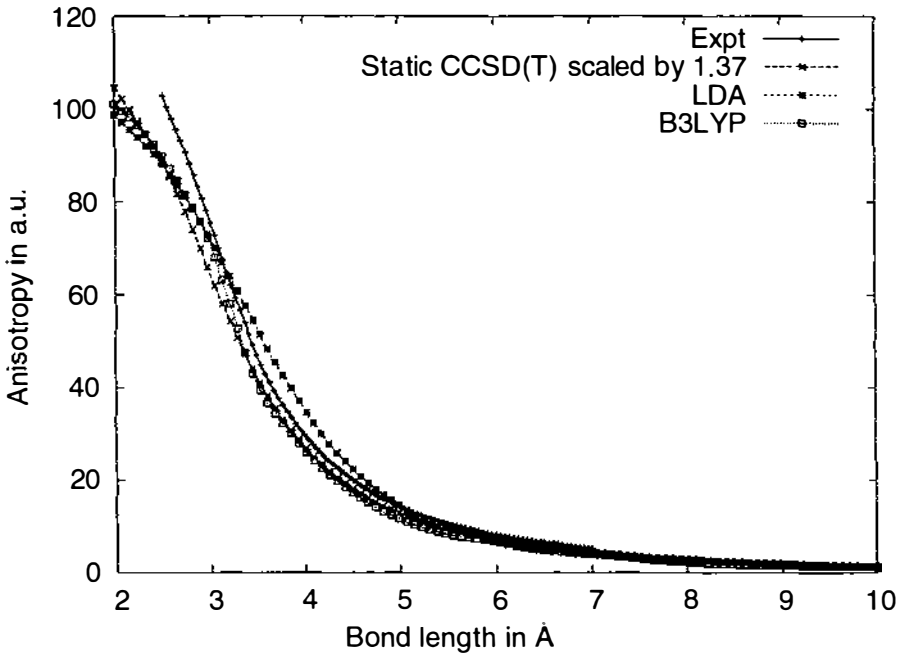

Figure 3.11: Scaling of the static anisotropy compared to the frequency dependent result.

frequency-dependent curves at $\lambda = 488$ nm [Schwerdtfeger et al., 2001].

3.3.5 The simulation of the Raman spectrum

In the extraction of the dipole polarisability anisotropy from the Raman spectrum, the potential curve needs to be given as input. The potential used was fitted to the experimental results of Koperski at short distances, and had a van der Waals tail at long range using *ab initio* dispersion coefficients of Kunz et al. [Hättig et al., 1996]. The potential obtained in this way is plotted in Figure 3.1 with the LDA and B3LYP potentials and also the CCSD(T) potential from reference [Schwerdtfeger et al., 2001] for comparison.

The major disagreement is indeed at short distances, below 3.5 Å the curves diverge and the CCSD(T) potential becomes repulsive at a bond length at least 0.1 Å longer. Figure 3.12 shows a comparison of the experimental and theoretical Raman spectra. Figure 3.13 shows the same spectra presented as the spectrum multiplied by the square of the Raman shift, which enhances the medium part of the spectrum with respect to Figure 3.12. Another consideration is that while the majority of the

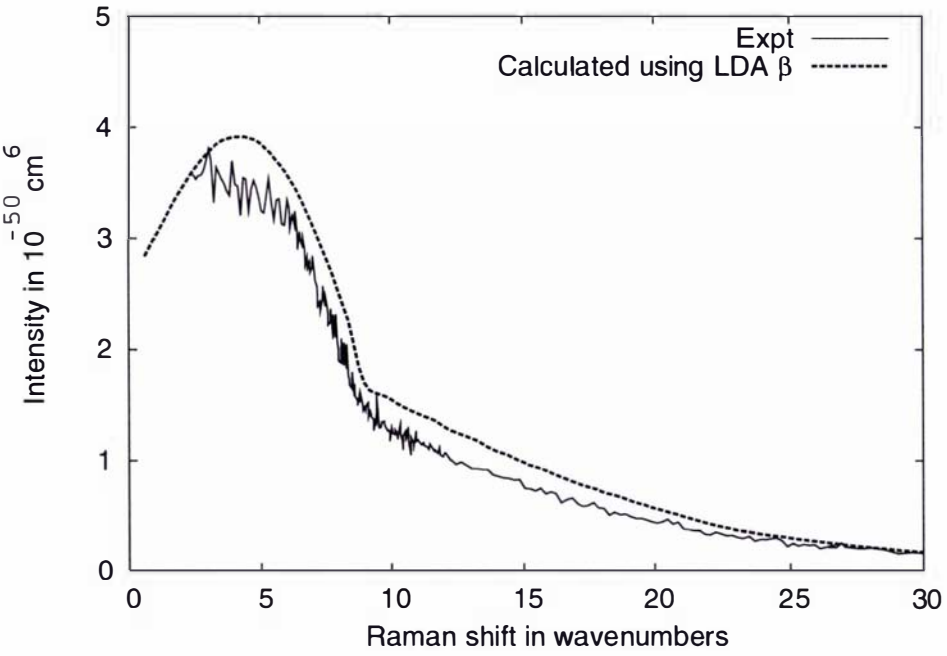

Figure 3.12: Raman spectrum of Hg_2.

experimental spectrum was obtained at a wavelength of $\lambda = 488$ nm, some of the data was in fact measured on higher resolution apparatus at 512 nm. As the better resolved data corresponds most strongly to the shorter bond lengths at which our agreement is worst, it is possible that this is a contibuting factor. However it may also be due to a strong sensitivity to the repulsive region of the potential curve used in the derivation, which is poorly described.

3.4 Conclusions

Despite differing in a few details, the calculated frequency dependent polarisabilities clearly agree with the experimental polarisability anisotropy within the accuracy that one may assume for such secondhand experimental data; that is, data produced through the use of a simplified model making many (necessary) assumptions. Many properties other than the polarisability may now be considered calculable for such a small system to considerable accuracy, within the auspices of DFT and relativistic 4-component theory.

It is also interesting that the description of response properties in DFT in no way

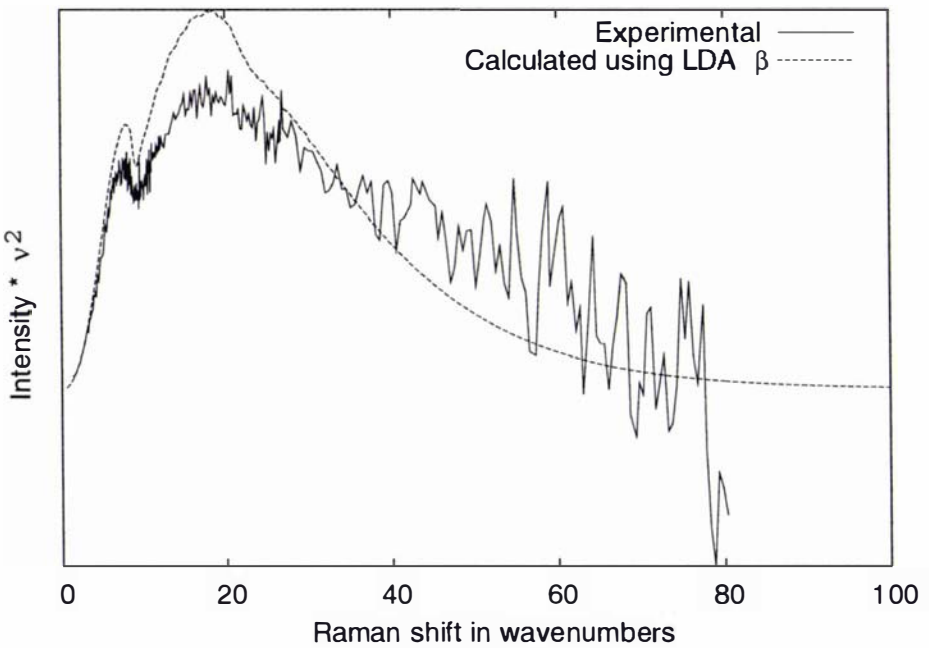

Figure 3.13: The Raman spectrum multiplied by the square of the Raman shift to enhance the medium part of the spectrum. In this range the intermediate range interaction is most pronounced.

relies on a proper description of the binding potential. This slightly surprising result opens up a large number of response properties to investigation by DFT.

Chapter 4

Many-body decomposition

In this chapter an analysis of the many-body potentials in mercury clusters is undertaken. This is motivated by the known behaviour of such potentials for mercury; that is that 2-body potentials are inadequate, and even 3- and 4-body potentials are insufficent and require scaling [Moyano et al., 2002]. A comparison is made with the behaviour of many-body potentials in noble gas clusters, as they are known to be much more accurately modelled by a simple 2-body potential.

The binding of the atoms in a cluster can be decomposed into a sum of many-body potentials;

$$V = V_2 + V_3 + V_4 + V_5 + ... \tag{4.1}$$

where

$$V_2 = \sum_{i<j} V_{ij} \tag{4.2}$$

is the sum of pair-interactions, over each pair of atoms in the cluster under consideration. Thus in a three atom cluster there will be three pair-interactions to consider. In an equilateral triangle these will all be equal, however in a more general triangle there may be three distinct bond-lengths at which to calculate the value of the two-body potential. The three-body energy is defined as the total binding energy of the trimer, less the binding energy due to the pair-interactions. This is best shown with an example. For an octahedral 6-atom cluster, there are 2 different two body interactions, as shown in Figure 4. One is at a distance r_1, which is the shorter bond-length between surface atoms, and appears 12 times. The second is at a distance r_2, which is that between atoms on the diagonal of a central square (or the pair on an axis of four-fold rotational symmetry if you prefer). There are three D_{4h} axes in an octahedral cluster, and thus this pair interaction occurs 3 times. The total number

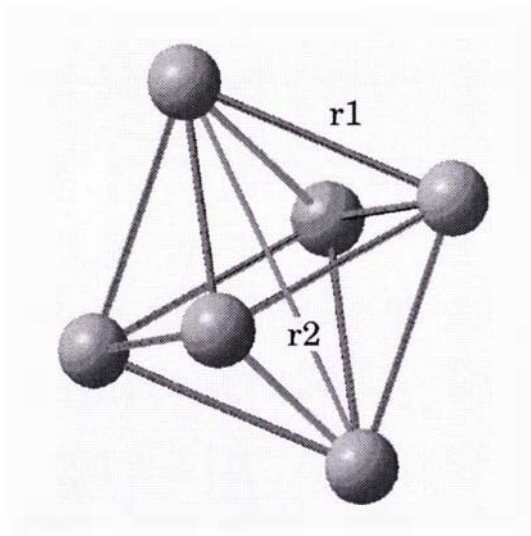

Figure 4.1: A X_6 octahedral cluster, with the two different bond lengths, r_1 and r_2, shown

of pair interactions is given by

$$\frac{n!}{m!(n-m)!} \quad \text{for} \quad n = 6 \text{ and } m = 2 \tag{4.3}$$

which equals $15 = 12 + 3$ two-body ($m = 2$) interactions in a $n = 6$ cluster. The three-body interactions can be counted as triangles within the octahedron. Starting with our two-body interactions we can either form a triangle from three bond-lengths r_1, which are the triangles on the surface of the octahedron, or with two sides r_1 and one side r_2. There are no triangles with more than one side of length r_2 since none of the atoms participate in more than one r_2 pair. Thus we find 8 triangles (r_1, r_1, r_1) and 12 (r_1, r_1, r_2). This is a total of 20 ($n = 6$, $m = 3$ in equation (4.3) three-body interactions in a 6-atom cluster. The four-atom components of the octahedron are either the central squares with sides r_1 and diagonals r_2; or two adjacent surface triangles may form a four-atom cluster. There are 3 squares and 12 of the adjacent triangle type quadruple, the sum of which is 15 ($n = 6$, $m = 4$) four-body interactions in a 6-atom cluster. There is only one sort of five-atom unit in the octahedron, formed by subtracting any one of the 6 atoms, and therefore this unit can be counted six times ($n = 6$, $m = 5$).

Now to find the five-body interaction we must go through the same process, subtracting the number of 4-, 3-, and 2-body interactions succesively. In Table 4.1 is

N	6	5	4 ($r_{1,1,1,1}$)	4 ($r_{1,1,1,2}$)	3 ($r_{1,1,1}$)	3 ($r_{1,1,2}$)	2 r_1	2 r_2
6	1							
5	6	1						
4 (square)	3	1	1					
4 (r_1, r_1, r_1, r_2)	12	4		1				
3 (r_1, r_1, r_1)	8	4		2	1			
3 (r_1, r_1, r_2)	12	4	4	2		1		
2 r_1	12	8	4	5	3	2	1	
2 r_2	3	2	2	1		1		1

Table 4.1: The N-body components of Hg_6 and the number of them that appear in each Hg_6 cluster, as well as the number found in each sub-cluster of the given structure.

given the number of each type of sub-unit in each component of the octahedron.

Therefore there is one square in the 5-atom sub-unit, 4 sets of adjacent triangle-type clusters of four atoms, 4 equilateral and 4 isoceles triangles, 8 r_1 and 2 r_2 pair-interactions. These need to be subtracted from the 5-atom binding-energy in order to find the 5-body interaction energy, which when multiplied by 6 becomes the total 5-body energy in the octahedron.

4.1 Mercury

Mercury is known to behave anomalously in that the three-body potentials are binding in the bonding region, where one would expect an alternation between bonding and repulsive many-body potentials as in the case of the rare gases. Due to the large amount of interest in the properties of bulk mercury, and the infeasibility of direct calculations using wavefunction-based correlation methods such as MP2 or coupled cluster calculations, accurate many-body potentals obtained from the smallest van der Waals systems would be very useful. However it is already known, [Moyano et al., 2002] that the many-body expansion does not converge quickly for mercury, and that 2-,3-, and even 4-body potentials will not be sufficient to describe larger systems.

In view of the transition in the nature of binding from van der Waals to covalent to metallic as the system increases in size, this is not surprising. However conversely it may be possible to extract information from an analysis of the many-body expansion, about the nature of the bonding and transition.

The n-body contributions are shown in Figure 4.2 as a function of the Hg-Hg distance in Hg_6 kept in O_h symmetry. At short bond distances (3.0 Å) the two-body

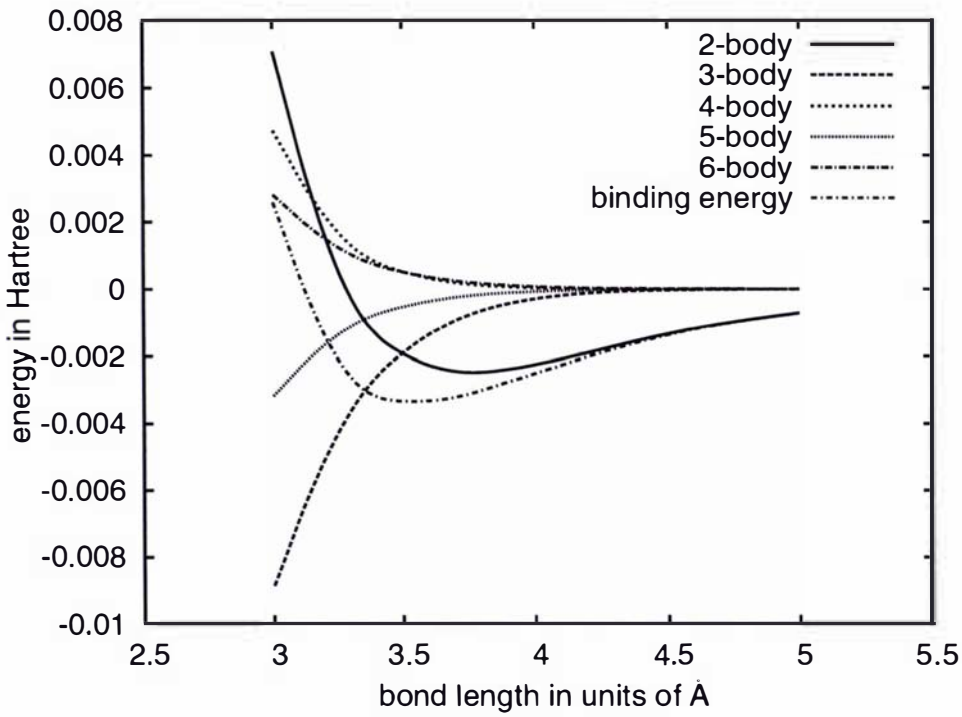

Figure 4.2: The MP2 n-body contributions to Hg_6, as a function of bond length.

part becomes repulsive as expected. However the 3-body part remains attractive, giving -343% of the total energy in contrast to the +274% due to the 2-body interaction. The higher body terms contribute 183%, -123%, and 109% for the 4-, 5-, and 6-body contributions respectively (a negative sign indicates binding here where the total energy is positive in contrast to the case below). At such short distances the HOMO/LUMO gap is still large. Hence, the bad convergence of the many-body expansion is not directly related to the change to the metallic state. Above 3 Å the 2-body part becomes attractive, and the contributions of each many-body term relative to the binding energy of the 6-atom cluster decrease. While at short distances the 3-body term is the contribution of highest magnitude, above 3.5 Å the 2-body term becomes increasingly more important. However even at 4 Å the 3-body term still accounts for +12% of the binding energy, followed by 4-, 5-, and 6-body contributions of -1.4%, 2.9%, and -2.9%. While these contributions are not entirely negligible, it is clear that at longer distances the many-body expansion begins to converge. According to an earlier study we expect mostly vdW behaviour at distances down to 5 Å [Schwerdtfeger et al., 1994]. Therefore the bad convergence of the many-body

expansion is related to the fact that the bond distance shortens dramatically from the more vdW type system of Hg_2 (3.69 Å) to the metallic solid state (3.00 Å).

Figure 4.3 shows the HF, correlation and total n-body contributions for Hg_6 at the optimized MBPT2 equilibrium distance of 3.552 Å. The oscillating behaviour

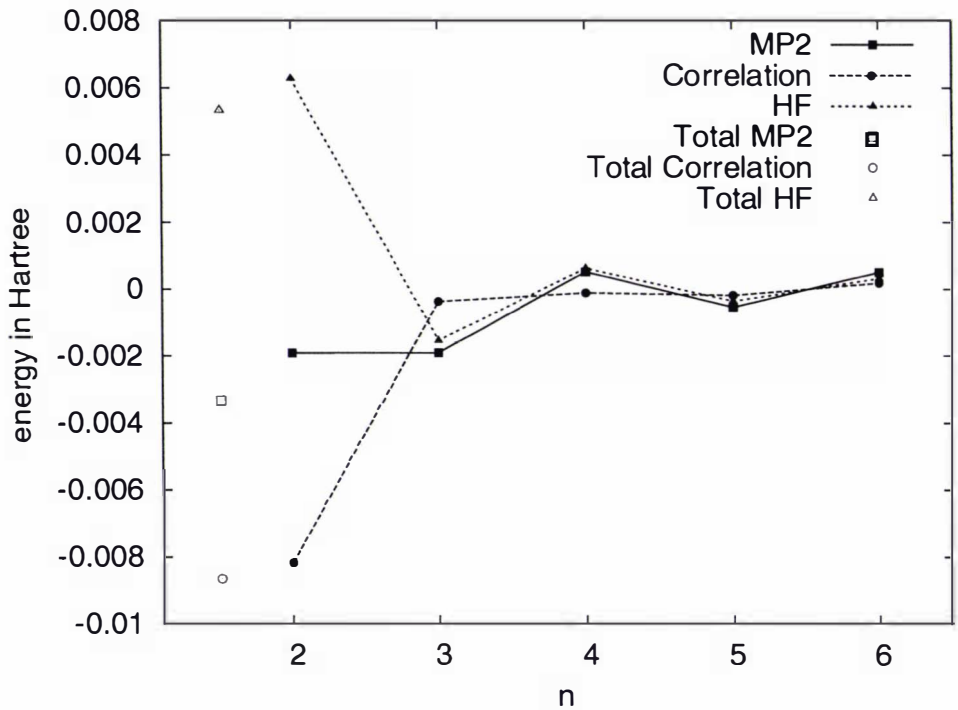

Figure 4.3: The n-body contributions to Hg_6. The total energy, correlation and Hartree-Fock components are shown on the left with open symbols.

of the n-body terms is clearly seen. The 2- and 3-body contributions are almost exactly equal, 58% and 57% of the total binding energy. The 4-, 5-, and 6-body contributions are all important at -16%, +16% and -15% respectively. Figure 4.3 also shows the sum over all n-body contributions (detached symbols shown on the left), which demonstrates that while the n-body expansion is starting to converge, the higher n-body contributions are still not negligible at this size. Hence, the expansion shown in equation (4.1) is of only limited accuracy for free clusters. However, the correlation energy shows a much better convergence behaviour at 3.552 Å, Figure 4.3. Even at 3.0 Å the 2-body correlation energy is 94.3%, the 3-body 2.0%, the 4-body 4.7%, the 5-body 1.2%, and the 6-body -2.3%.

Thus the major correlation contribution comes from the 2-body part. This is an

important finding which will be used later for solid-state calculations.

4.2 Noble gases He, Ne, Ar, and Kr

Many-body decompositions have been widely used in the study of noble gas clusters. It is known that the many-body series converges rapidly, which is why simple two-body potentials such as the Lennard-Jones clusters have had such success. However it is an open question, looking at the distance dependence of the many-body convergence in Hg_6, whether this is a general feature that will also apply to the noble gases. If this is true, it might indicate that the primary reason for the bad convergence observed for bulk mercury is the sharp decrease in bond length from approximately 3.7 Å in the dimer to 3.0 Å in the bulk, due to the transition to metallic bonding. Therefore the same analysis as has been done for Hg_6 has been repeated for the analogous He, Ne, Ar, and Kr clusters. Here we have the opportunity to use coupled cluster methods combined with large correlation consistent basis sets, and we are even able to include the Douglas-Kroll-Hess operator to include scalar relativistic effects. The calculations were all done with Gaussian03 using DK basis sets (cc-pVQZ-DK from www.emsl.pnl.gov) [T. H. Dunning, 1989, Woon and T. H. Dunning, 1993, Wilson et al., 1999]. For neon and argon the hardest d, f and g functions were removed in order to make the CCSD(T) calculations computationally possible. For krypton the basis was left intact and an MP2 calculation was performed instead. The basis sets used are listed in Tables A.1, A.2, A.3, A.4 and A.5 of the appendix.

4.2.1 Helium

For helium the convergence of the many-body series with respect to bond-length is shown in Figure 4.4. The potential minimum is at 3.23 Å, and the repulsive wall crosses the dissociation asymptote at 2.87 Å, the hard sphere radius. The three-body energy becomes noticeably attractive only below 3.1 Å. Near the potential minimum the three-body term becomes very weakly repulsive due to the Axilrod-Teller interaction, this is at most only 0.7% of the binding energy and therefore essentially negligible. The 4-, 5-, and 6-body potentials diverge only below 2.5 Å. Thus over the range of interest, the He_6 binding potential is equal to the 2-body potential.

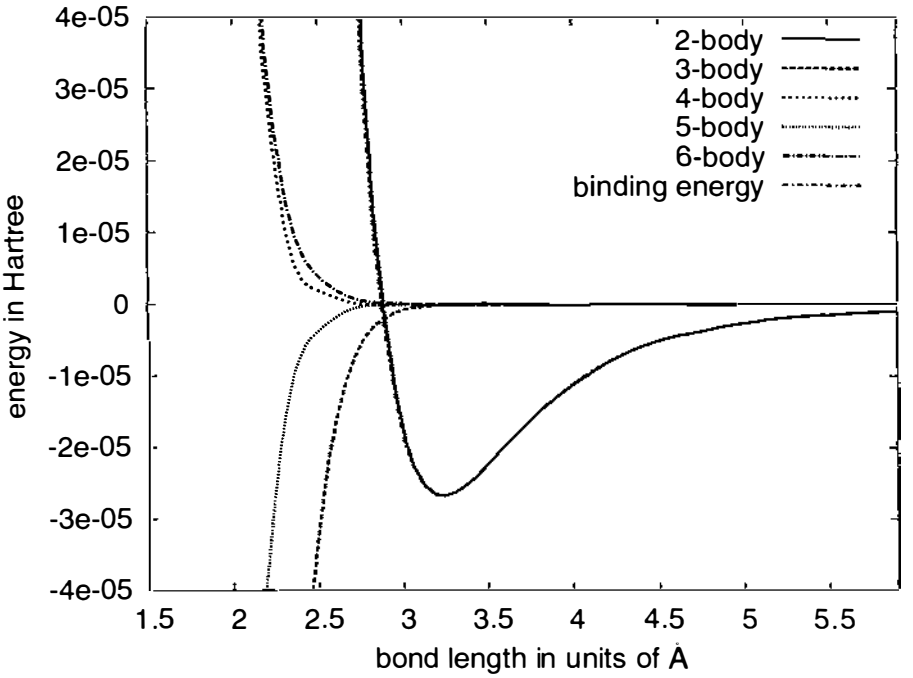

Figure 4.4: Many-body decomposition of the binding energy (per atom) of He_6, using DKH-CCSD(T).

4.2.2 Neon

The convergence of the many-body series for neon with respect to bond-length is shown in Figure 4.5. Similarly to helium, the neon potential minimum is at 3.17 Å, and the repulsive wall crosses the dissociation asymptote at 2.83 Å. However the binding energy of neon is an order of magnitude greater than that of helium.

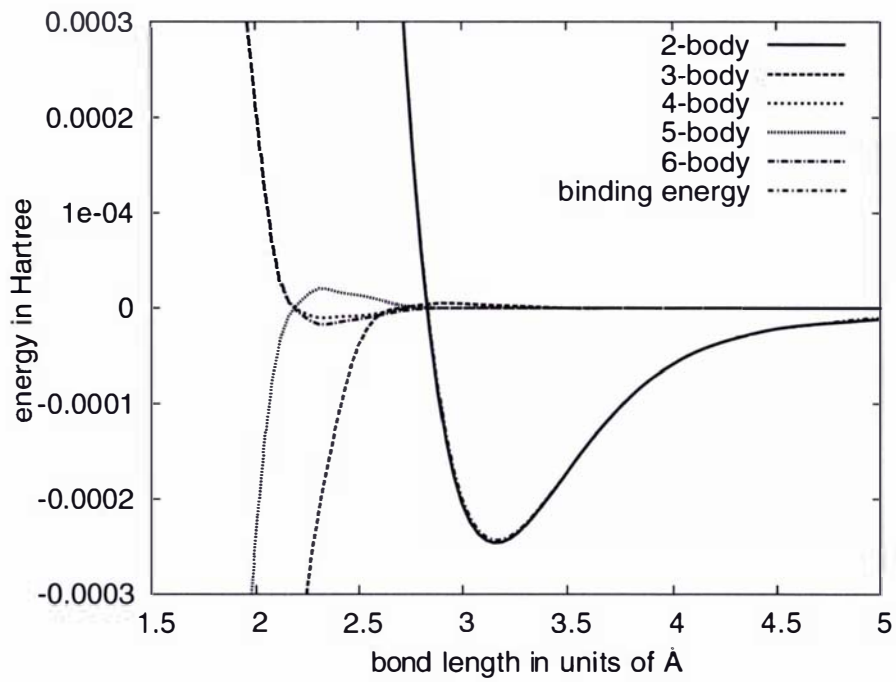

Figure 4.5: Many-body decomposition of the binding energy (per atom) of Ne_6, using DKH-CCSD(T).

The Axilrod-Teller interaction is observed in the three-body potential over the binding part of the Ne_6 potential; the three-body contribution is therefore very slightly repulsive in this region before becoming strongly binding below 2.5 Å. The higher order contributions are all observed to produce a similar hump in the region between 2.0 and 2.5 Å, before diverging strongly below 2.0 Å. These contributions oscillate between attractive potentials for even n and repulsive for odd n, as is consistent with the many body expansion. Figure 4.6 shows the smooth binding curves of each component cluster of the octahedron. These are plotted against the shortest bond length (r_1), and thus the binding energy of the (r_2) component is simply shifted by a factor $\sqrt{2}$. In examining the contribution of each such binding potential to the

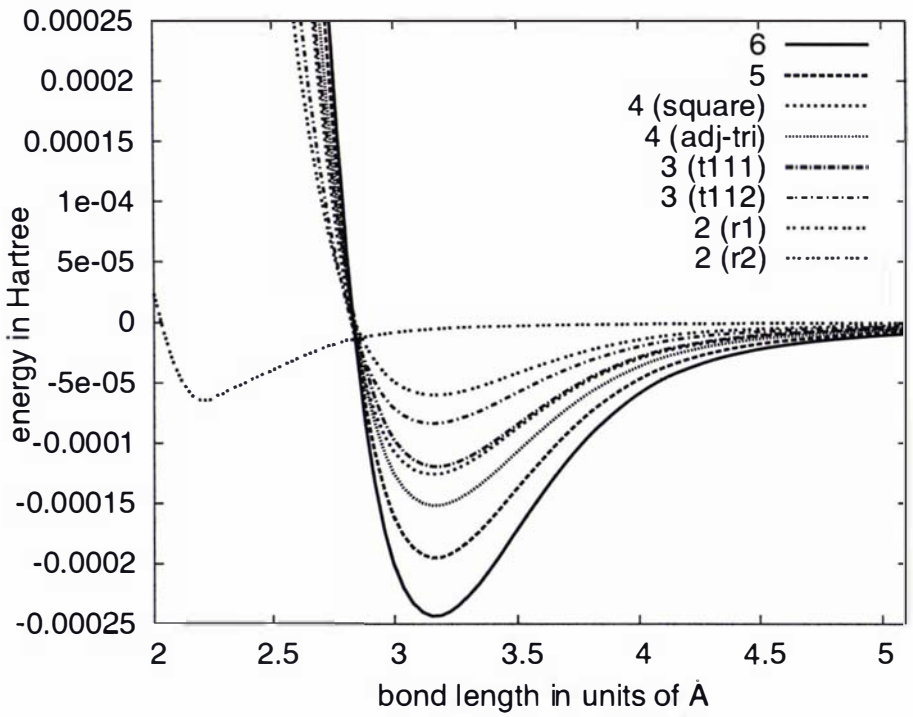

Figure 4.6: Ne_6 DKH-CCSD(T) many-body component binding potentials. Here the binding energy of each component cluster (2-body r_1, or 3-body r_1, r_1, r_2 for example) is shown with respect to the distance r_1 of the octahedron. Thus the potentials for the pairs r_1 and r_2 are identical but shifted by a factor of $\sqrt{2}$; at the r_1 potential minimum the r_2 pair is on the outer (r^{-6}) part of the 2-body potential.

n-body potentials, i.e. where t_{111} is that potential with the 2-body ($3r_1$) subtracted, the Axilrod-Teller interaction first becomes evident (cf. Figure 4.7). This plot shows the behaviour of the 4-, 5-, and 6-body potentials more clearly than the first plot

(Figure 4.5) where these potentials are summed according to the weights given in Table 4.1.

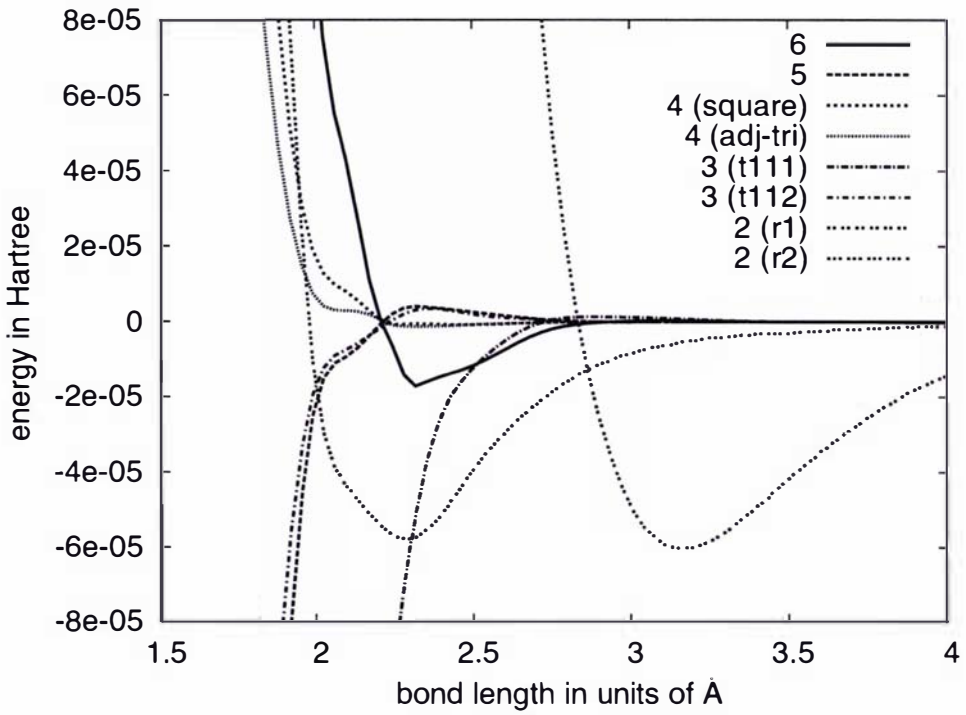

Figure 4.7: Ne_6 DKH-CCSD(T) many-body component contributions to Ne_6. These are the proper n-body potentials where the lower-order potentials have been subtracted from the binding potentials (shown in Figure 4.6), and thus the 6-body potential can be seen to be (at the potential minimum) about a third the magnitude of a single pair potential. The dominance of the lower-order potentials with respect to the total contribution of the cluster is, of course, due to the total of 15 pair-interactions compared with one single 6-atom interaction.

4.2.3 Argon

The convergence of the many-body series for argon with respect to bond-length is shown in Figure 4.8. For argon the potential minimum occurs at a considerably higher bond length, at 3.91 Å, and the hard sphere radius is 3.50 Å. Very similar behaviour as that of helium is otherwise observed, the three-body potential appearing only just below the potential minimum. The higher-body potentials then diverge below 3.0 Å.

The binding energies of the separate n-body components ($r_1, r_2, t_{111}, \ldots$) per atom are plotted in Figure 4.9. These include the lower-order many body potentials (i.e.

they all contain the 2-body interaction) and so all show a minimum at at the same bond length, 3.9 Å. As before the binding potential of r_2 is the same as that of r_1, but plotted with respect to the r_1 distance in the Ar_6 cluster.

The contribution of each component to Ar_6 $(r_1, r_2, (t_{111} - 3r_1), (t_{112} - 2r_1 - r_2) \ldots)$ are shown in Figure 4.10 (again plotted against octahedron bond length r_1). Here again the binding potential of r_2 and r_1 are clearly recognisable. The equilateral 3-body triplet (t_{111}) is responsible for the small binding 3-body interaction close to the potential minimum. This is plotted to show that there is no sign of an Axilrod-Teller interaction such as was clearly evident in Figure 4.7 for Ne.

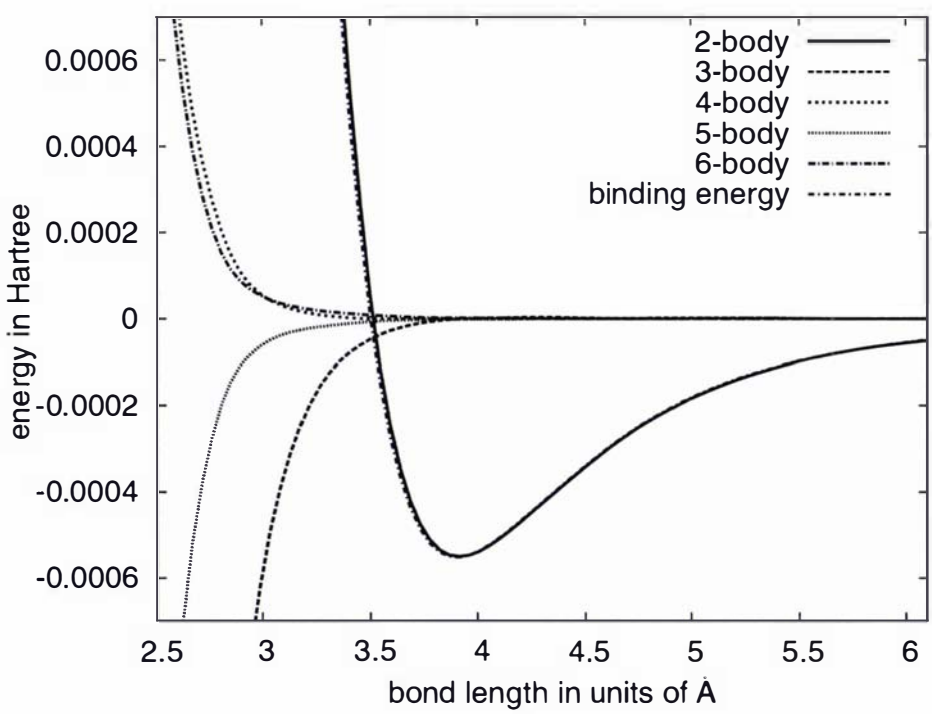

Figure 4.8: Many-body decomposition of the binding energy (per atom) of Ar_6, using DKH-CCSD(T).

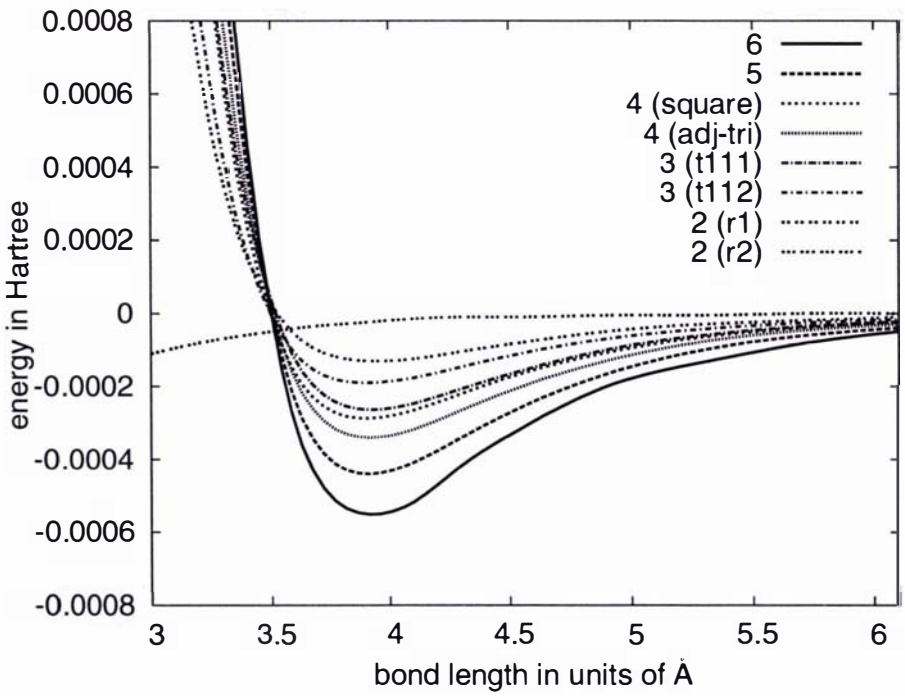

Figure 4.9: Ar_6 DKH-CCSD(T) many-body component binding energies.

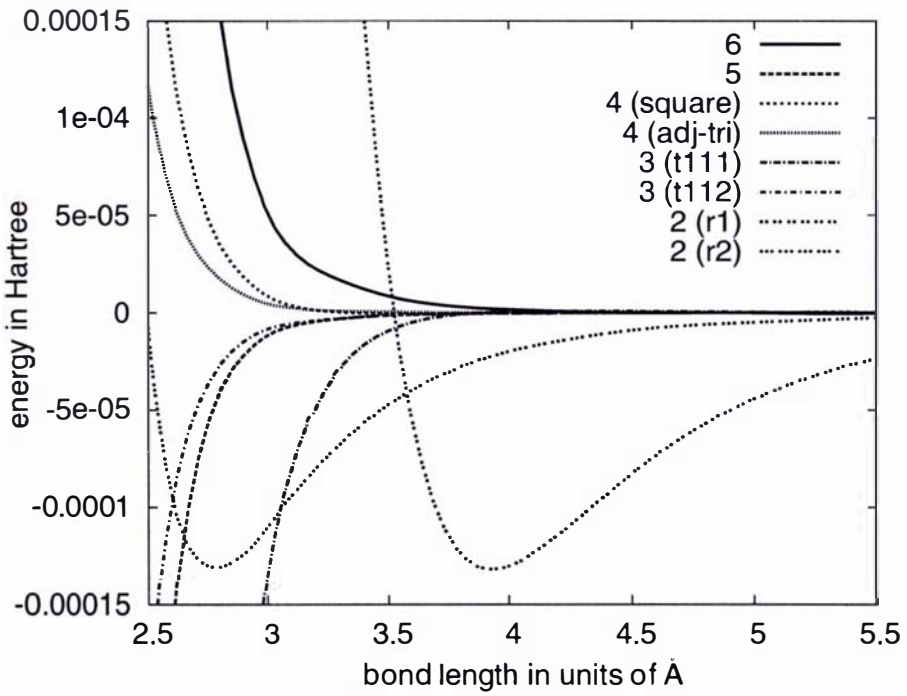

Figure 4.10: Ar_6 DKH-CCSD(T) many-body components.

To demonstrate the relationship between the CCSD(T) results above and the MP2 results obtained for krypton, the binding potential and 2-body potential of Ar_6 are compared in Figures 4.11 and 4.12.

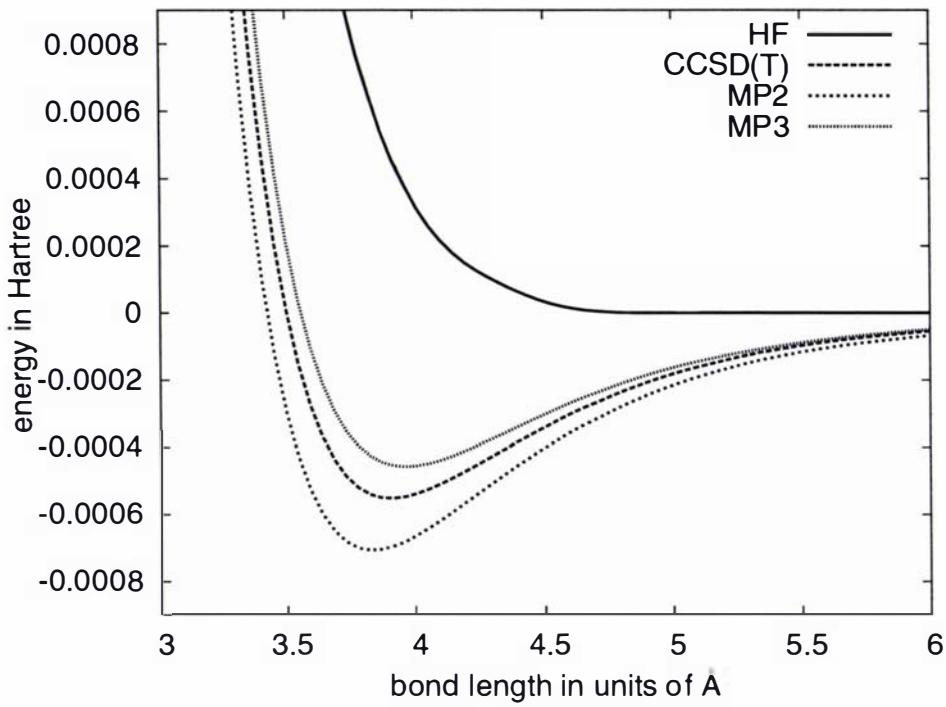

Figure 4.11: Ar_6 comparison of DKH-HF, DKH-MP2, DKH-MP3 and DKH-CCSD(T) binding potentials.

4.2.4 Krypton

The convergence of the many-body series for krypton with respect to the (octahedron) bond-length is shown in Figure 4.13.

The behaviour of the MP2 energy is consistent with the CCSD(T) results obtained above, although the total curve will be overbinding with respect to CCSD(T), the many-body potentials (higher than $n = 2$) should be accurate. The three-body potential diverges below 4.0 Å, and the higher n-body potentials below 3.2 Å. These do not affect the energy of the cluster over the binding portion of the potential.

4.3 Conclusions

There is a clear difference between the behaviour of the many-body potentials calculated for mercury, and those for the noble gases. While studies of noble gas clusters have been carried out successfully using only a two-body potential, for mercury it has been clear that higher-order potentials are required.

These results correlate the importance of the many-body potentials in mercury with the dramatic bond-shortening observed in mercury clusters as the number of atoms is increased. Already at 6 atoms the 3-body potential must be included; in larger clusters and the bulk even higher order terms will be necessary.

That this occurs for mercury and not for the noble clusters may be seen as a direct consequence of the transition from van der Waals to metallic type bonding. However, even at distances of 3.69 Å (the equilibrium bond-length in Hg_2), higher order n-body contributions are not small.

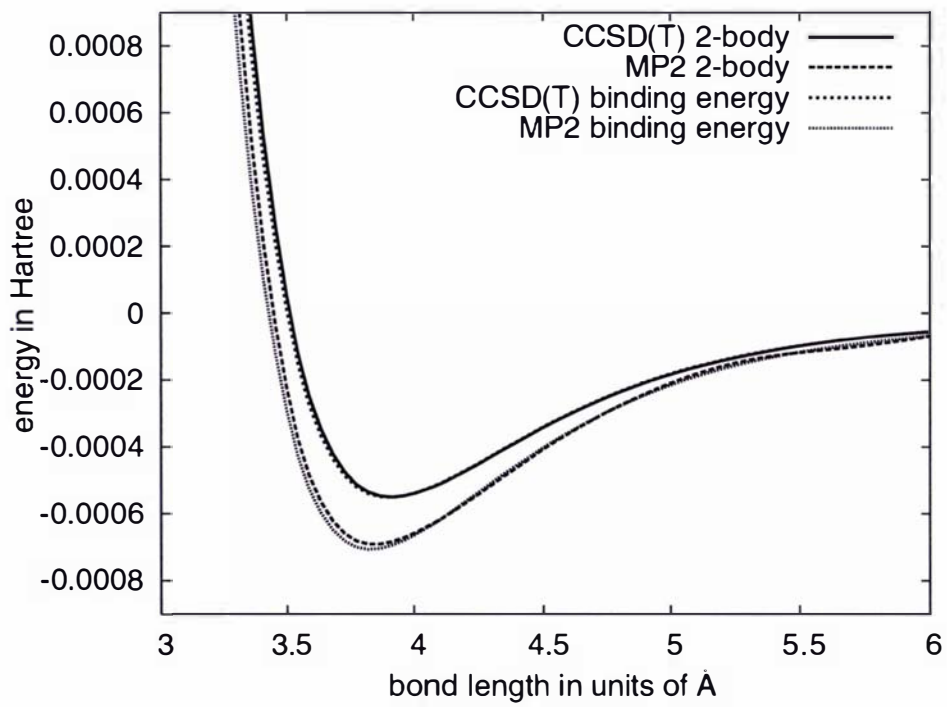

Figure 4.12: Ar_6 comparison of DKH-MP2 and DKH-CCSD(T) binding energies and 2-body potentials.

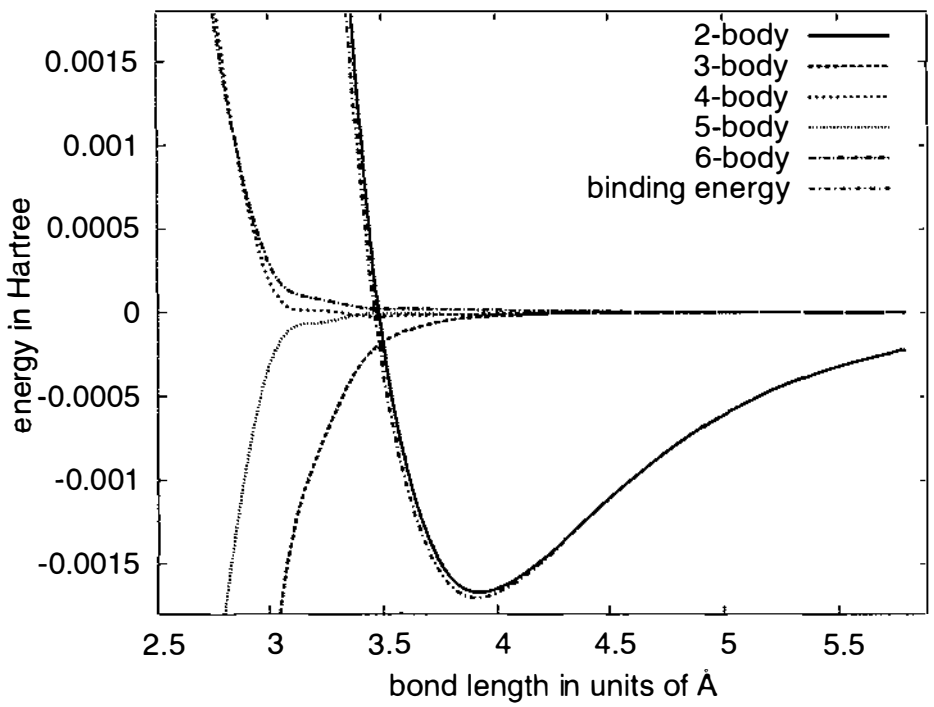

Figure 4.13: Many-body decomposition of the binding energy (per atom) of Kr_6, using DKH-MP2.

Chapter 5

Bulk mercury

The experimentally determined structure of solid mercury has been extensively studied and is well known. Mercury freezes at 233 K, and forms a rhombohedral lattice. This is a variant of the hexagonal close packed lattice, and so has two lattice parameters equivalent $a = b$ and another c with parameters $a = b = 3.47$ Å, and $c = 6.72$ Å. The lattice structure is shown in Figure 5.1 with the rhombohedral primitive cell shown within.

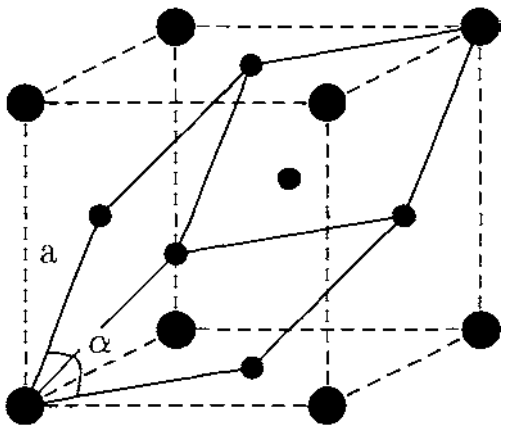

Figure 5.1: The rhombohedral primitive cell is shown with reference to the face-centered cubic (fcc) structure. If the angle α is 60°, it is an ideal fcc close packed structure. This angle is 70° in Hg. If this angle were 90°, then it would be a simple cubic lattice. An angle of 109.28° corresponds to a body-centered cubic (bcc) lattice.

For this structure one may define either a rhombohedral (primitive) unit cell, or a hexagonal one which is non-primitive and contains 3 atoms. The rhombohedral and

hexagonal lattice both belong to the trigonal system. In the hexagonal unit cell (cf. Figure 5.2) the cell is defined according to lattice parameters $a = b \neq c$. Here a is the *second* nearest neighbour distance, and the angle between these lattice vectors is 90°. In the rhombohedral cell (also the primitive cell, see Figure 5.1) $a = b = c$ which equals the nearest neighbour distance, and the angle $\hat{abc} = \alpha = \beta = \gamma$.

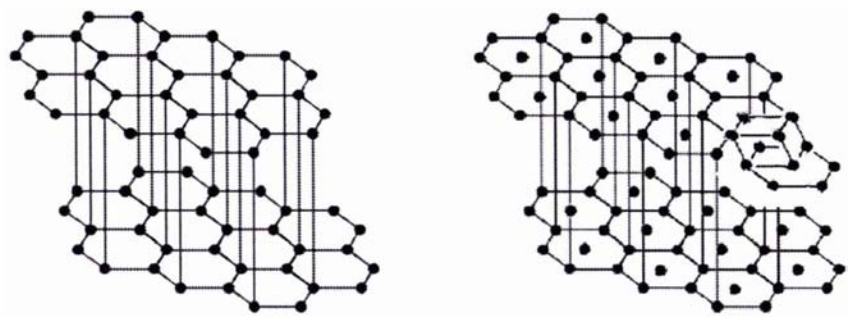

Figure 5.2: In the picture of the hexagonal cell, we can visualise solid mercury (right) as a graphitic structure (left), where short bond lengths a are present along the hexagonal plane, and longer distances c separate the planes. In the mercury structure an intermediate layer (necessary to complete the rhombohedral cell) is missing (remember that the hexagonal cell contains 3 atoms).

Thus for mercury the experimental lattice parameters are $a_R = 3.00$ Å, and $\alpha_R = 70.52$, which equates to hexagonal cell parameters $a_H = 3.47$ Å and $c_H = 6.72$ Å.

The experimental structure is shown in Figure 5.3, for the first 42 neighbours, i.e. the first 6 shells, at distances of 2.99, 3.46, 4.57, 4.87, 5.73, and 5.97 Å from the reference atom at the center.

5.1 Density functional calculations

DFT is generally considered the method of choice for bulk metals. The lack of correlation makes Hartree-Fock repulsive not only for the dimer, but also for the solid, [Paulus and Rościszewski, 2004] and it may be supposed for all cluster sizes in between also. Calculations using DFT, however, produce a surprising variety of numbers. Of these, LDA is undoubtedly the best performing functional for the solid, which is perhaps not surprising since it is based closely on the uniform electron gas as this is a reasonable approximation to metallic bonding.

The program used for all the calculations on extended mercury in this chapter

was CRYSTAL [Saunders et al., 2003] which uses Gaussian basis sets and pseudopotentials, such that a direct comparison can be made with molecular calculations. The program converts the Gaussian basis set given as input to Bloch functions, which are the final wavefunction used in the calculation. This has the consequence that diffuse functions which may be very important for molecular studies are of little practical use and lead inevitably to convergence difficulties when they are included. Furthermore there are currently only s, p, and d-functions implemented in the code. In particular for metallic systems the choice of basis set can be very difficult, due to convergence difficulties.

The most natural basis sets that would construct lattice wavefunctions Ψ (eigenfunctions of the one-electron Hamiltonian) containing the translational symmetry of the lattice;

$$\Psi(\mathbf{k}, \mathbf{r} + \mathbf{g}) = \psi(\mathbf{k}, \mathbf{r}) e^{i\mathbf{k}\cdot\mathbf{g}} \tag{5.1}$$

where $\mathbf{k}$ is the wavevector and $\mathbf{g}$ a lattice vector, are undoubtedly plane waves:

$$\Psi(\mathbf{k}, \mathbf{r}) = \sum_{\kappa} a(\mathbf{k}, \kappa) e^{i(\mathbf{k}+\kappa)\cdot\mathbf{r}} \tag{5.2}$$

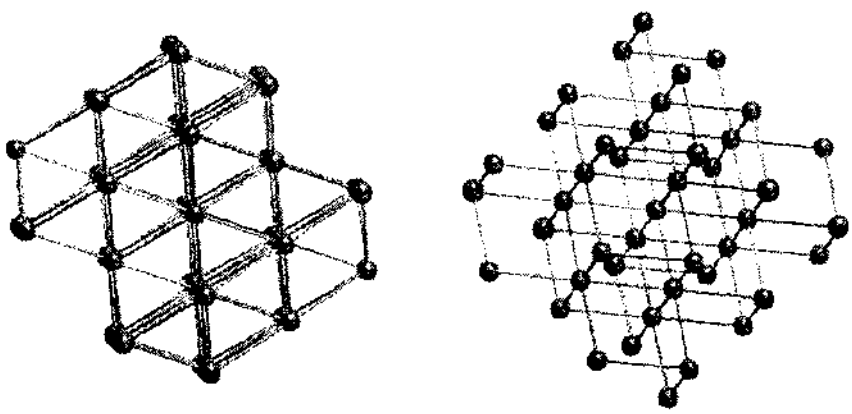

Figure 5.3: The Hg lattice — left: the hexagonal structure; right: the rhombohedral cell.

Here the single-electron wavefunction is a linear combination of plane waves which differ by the reciprocal lattice vector $\boldsymbol{\kappa}$, and are therefore periodic in Fourier space.

Plane waves are the solution of the one-electron equations in the case of the uniform electon gas, which assumes an important limiting role in the description of metallic systems. On the other hand, a very high number of plane waves are typically needed in order to simulate real lattices. This problem is partially circumvented by the use of pseudopotentials to replace the core electrons.

Bloch functions, given by

$$\phi_\mu(\mathbf{k}, \mathbf{r}) = \sum_{\mathbf{g}} \chi_\mu(\mathbf{r} - \mathbf{g}) e^{i\mathbf{k}\cdot\mathbf{g}} \tag{5.3}$$

where the local functions $\chi_\mu(\mathbf{r})$ are centered on the atomic nuclei, allow for an important reduction in the number of basis functions required to construct lattice wavefunctions. The other important advantage is that the atom-centered approach allows the use of standard atomic orbitals (AOs) which may be constructed from the Gaussian basis sets used in molecular calculations.

Disadvantages of this choice of basis set are firstly, that these Bloch functions are often close to being linearly dependent, which requires the deletion of the diffuse functions present in a standard Gaussian basis set. Secondly they are unable to reproduce the correct (plane wave) solution for the ideal case of the uniform electron gas; this makes them less ideal for describing metals (in principle) [Pisani et al., 1988].

A small contracted basis set which was optimised for HF calculations has been used for mercury [Paulus, 2004]. This is shown in Table 5.1. However the convergence properties of DFT are slightly better than HF. Therefore this basis set was improved by an additional diffuse s-function optimised with respect to the dimer potential obtained using a much larger basis set. The PW91 potential curves obtained using both these basis sets are compared in Figure 5.4 to the reference CCSD(T) curve, and PW91 with the large basis of Chapter 2. This basis set (of Table 5.1) was used for all DFT calculations, although the HF calculations were only possible with the original basis (minus the diffuse s-function).[1] The comparison of the 'small' and 'large' basis PW91 potential curves shows that the smaller basis set actually produces a deeper potential. This is in contrast to what one would usually expect, and is due to the large BSSE. As a consequence, even a HF calculation of the dimer with this basis set will find a binding potential. In contrast, in the solid state calculation, an increase

[1]This goes also for B3LYP where the inclusion of HF exchange leads to the same convergence difficulties.

	Exponent	Coefficient
S	20.299700	-0.068441
	12.709700	0.350721
	5.963980	-0.843270
S	20.299700	0.018841
	12.709700	-0.113772
	5.963980	0.312303
S	1.370590	1.00
S	0.570414	1.00
S	0.126000	1.00
S′	0.077	1.00
P	10.559400	0.125368
	6.735380	-0.361046
	1.896870	0.468140
P	1.896870	1.00
P	1.016210	1.00
P	0.499260	1.00
D	11.453300	0.016237
	7.161380	-0.067409
	1.935200	0.305732
	0.897516	0.454688
D	0.386504	1.00
D	0.150435	1.00

Table 5.1: The basis set used for the DFT calculations. The additional *s*-function (labelled S′) could not be included in the HF calculation (or B3LYP).

in size of the small basis set is seen to increase the cohesive energy, as expected.

The binding energies of DFT as calcuated with a range of density functionals at the experimental lattice parameters ($a = 3.47, c = 6.72$) are given in Table 5.2. Table 5.3 shows the DFT energies when the lattice parameters are optimised with respect to this energy (the binding energy of the bulk is known as the cohesive energy, E_{coh}). As well as the hexagonal lattice parameters a and c, the rhombohedral parameters a_R and α_R are given.

The angle α_R indicates the strength of the rhombohedral distortion from cubic symmetry. Like mercury, zinc and cadmium also crystalise in a hexagonal (hcp) structure, however proper close-packing requires an angle α of 60°. The deviation from this angle can alternatively be analysed as an anisotropy due to the ideal 12-membered coordination sphere being divided into two sets of six. One of these sets is at the nearest neighbour distance (also the length parameter a_R in the rhombohedral

Functional	Energy (eV)
B3LYP	0.172
PW91	-0.184
BP86	-0.013
PBE	-0.135
LDA	-1.004
Expt	-0.79

Table 5.2: Calculated binding energies obtained from DFT for bulk mercury at the experimental solid-state structure. Experimental value from [Lide, 2002].

Functional	a	c	a_R	α_R	E_{coh}	a/a_R
B3LYP	3.968	9.658	3.952	60.294	-0.269	1.0051
PW91	3.571	8.632	3.539	60.583	-0.297	1.0085
BP86	3.588	8.578	3.532	61.088	-0.157	1.0170
PBE	3.530	8.658	3.534	59.932	-0.257	0.9990
LDA	3.476	6.661	3.002	71.317	-1.007	1.1667
Expt	3.470	6.719	3.005	70.53	-0.79	1.1533

Table 5.3: Calculated lattice parameters (in Å) and cohesive energies (in eV) for bulk mercury obtained from DFT and compared to experiment [Lide, 2002].

lattice), the second nearest neighbour distance is what is defined as a in the hexagonal cell. Therefore a close packed structure has a ratio a/a_R of 1. The anisotropic ratios for Zn, Cd, and Hg are respectively 1.09, 1.11, and 1.15, and are the highest known for the elemental metals.

It is an interesting question, whether the high anisotropy of bulk mercury is due to the particular stability of long range forces due to the van der Waals interaction. Certainly this behaviour is not captured by any of the density functionals tested here, except for LDA. Exactly what physics is being picked up by LDA and not by the

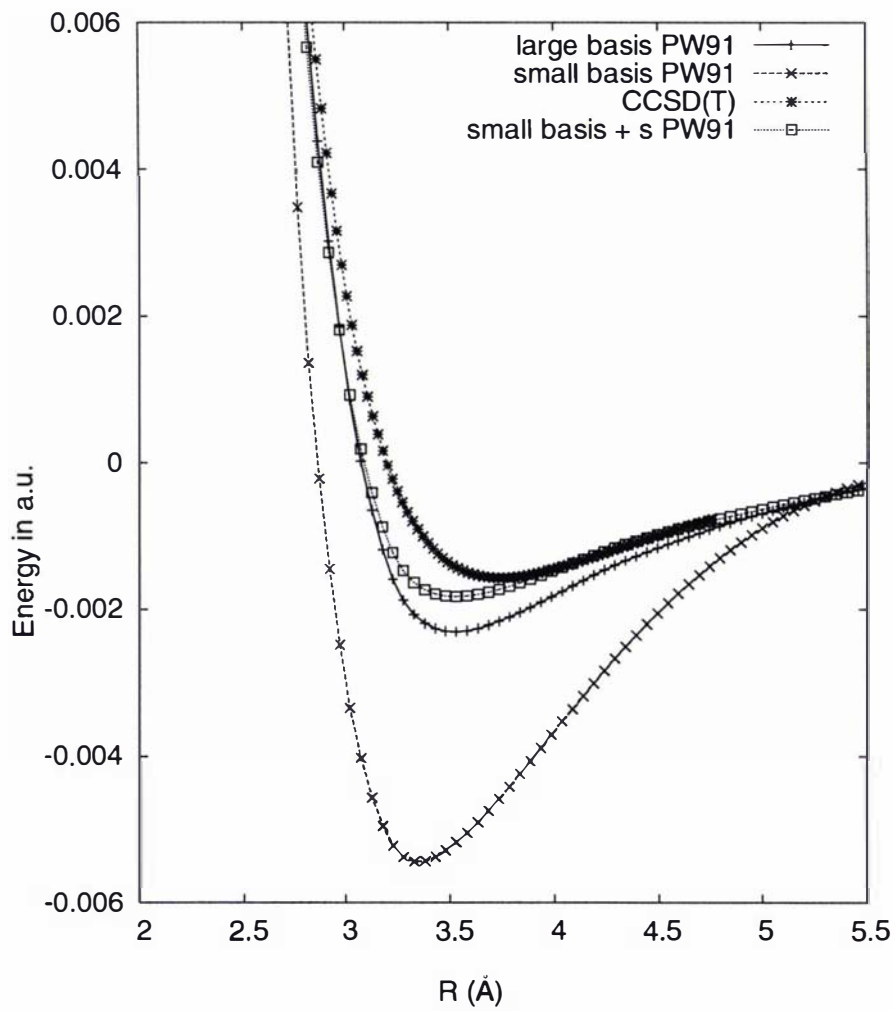

Figure 5.4: A comparison of the PW91 potential curve for Hg_2 with different basis sets. Here the basis denoted "small" is that used in the solid state calculations.

other functionals is hard to ascertain, although the overbinding is characteristic. The importance of many-body effects in the bulk precludes a simple analysis of the solid bonding in terms of the dimer potential, but the high anisotropic ratio is probably related to the relative strengths of short-range and long-range interactions.

5.1.1 Density of states

The density of states (DOS) of bulk mercury is calculated from the energy eigenvalues of the solid and takes into account the relative occupation of these eigenstates. For mercury, the DOS as calculated with HF is compared to various forms of DFT in Figure 5.5. All show the *d*-band below the Fermi level at about -0.50 a.u. (-13.6 eV) with the HF band appearing somewhat broader. This is in general agrecment with other studies (e.g. [Kresse and Hafner, 1997]). While all methods again show some *s*-electron density above the Fermi level, this is a much more pronounced feature for HF, mimicked by B3LYP. These are the two methods for which the solid is unbound at the experimental lattice parameters (cf. Figure 5.2).

The other density functionals show only a little *s*-electron density above the Fermi level, which confirms the conducting nature of the metallic solid.

5.1.2 Band structure

The electronic energy is in fact not uniform throughout the lattice, although the average energy (per cell) is; within each unit cell are positions that are distinct from one another by symmetry. Thus the energy varies as a function of wavevector in reciprocal space, although this variation is periodic. Therefore the electronic states of the lattice are usually plotted for specially chosen points of symmetry in the Brillouin zone, a type of unit cell. The Brillouin zone is defined in reciprocal space, where the primitive vectors of the reciprocal lattice are defined as

$$A = 2\pi \frac{b \times c}{a \cdot b \times c} \tag{5.4}$$

$$B = 2\pi \frac{c \times a}{a \cdot b \times c} \tag{5.5}$$

$$C = 2\pi \frac{a \times b}{a \cdot b \times c} \tag{5.6}$$

$$\tag{5.7}$$

where a, b, and c are the primitive vectors (that define the primitive cell) in real space. The Brillouin zone is the unit cell in reciprocal space which, centered about

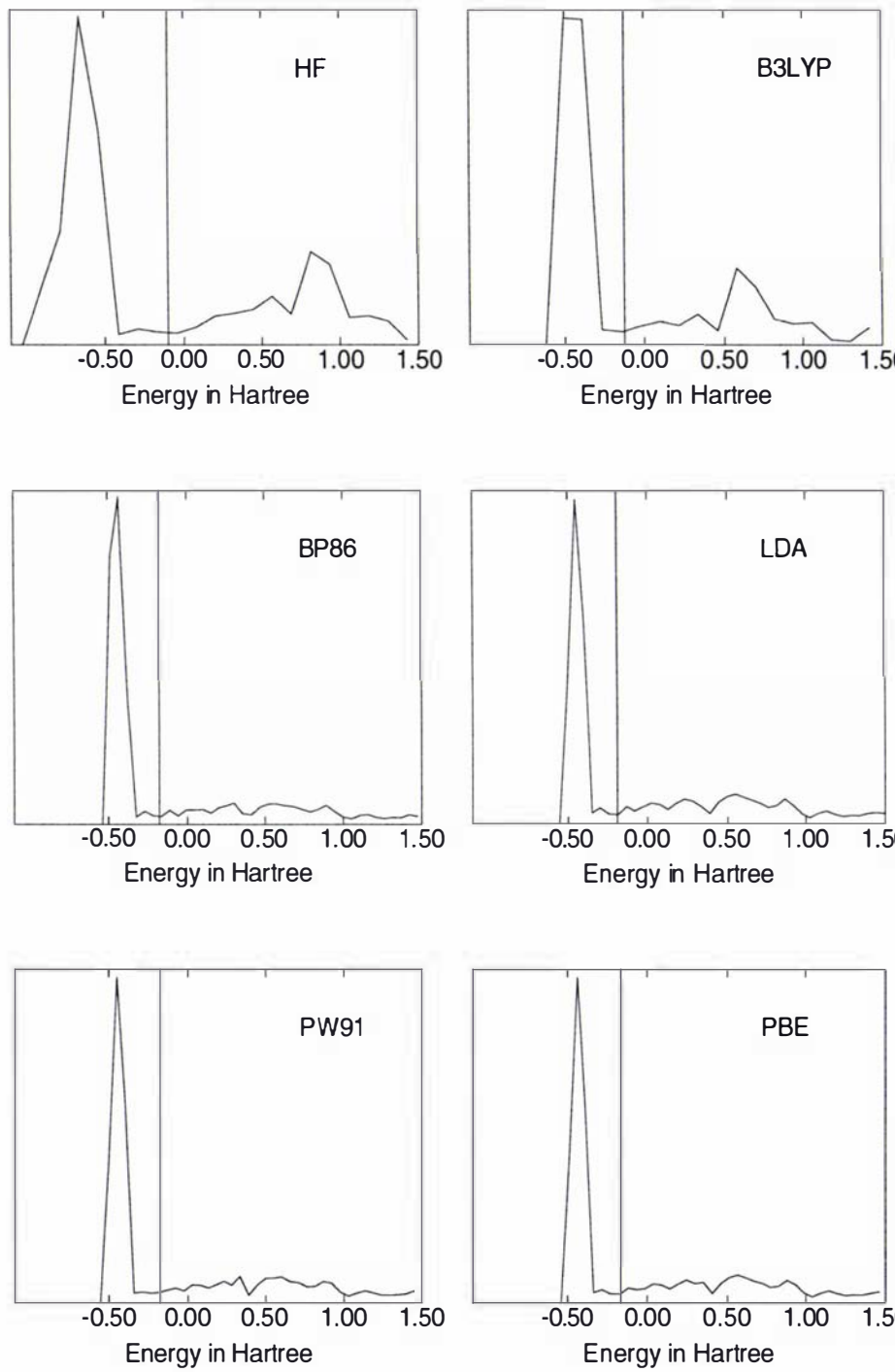

Figure 5.5: The DOS as obtained with HF and DFT. The vertical line indicates the Fermi energy.

an atom (lattice point), contains only points which are closer to this atom than any of its neighbours. It may also be called the first Brillouin zone.

The mercury Brillouin zone is shown in Figure 5.6 with the special symmetry points labelled.

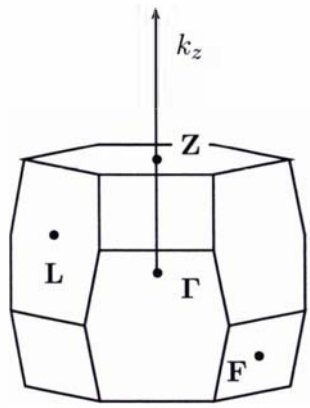

$$\mathbf{\Gamma} = (0,0,0),\ \mathbf{Z} = (1/2,1/2,1/2),\ \mathbf{F} = (1/2,1/2,0),\ \mathbf{L} = (0,1/2,0)$$

Figure 5.6: Brillouin zone of mercury. The high symmetry points at which the band structure is calculated are shown, as defined in [Bradely and Cracknell, 1972].

Figures 5.7 to 5.12 show the band structure of mercury as calculated with HF and a number of density functionals at the experimental lattice parameters. All density functionals agree closely on most aspects of the band structure. The close agreement of all density functionals with respect to the band structure is well known. This is exactly why it had been assumed that DFT should describe such systems well, in contrast with the results of Tables 5.2 and 5.3.

The HF band structure calculated here agrees closely with that previously published [Paulus and Rościszewski, 2004, Deng et al., 1998, Kresse and Hafner, 1997]. In particular, the mixing of the valence *s*-band with the low-lying flat *d*-bands at the Γ point indicate the importance of core-valence interactions. The crossing of the Fermi level between the L and Z points indicates the merging of the valence and conduction bands.

Principal points of difference between the HF and DFT band structures are the behaviour of the conduction bands at the **Γ** point, where the DFT bands are much flatter; also at the **Z** point, the size of the band gap is much larger in HF than the DFT plots.

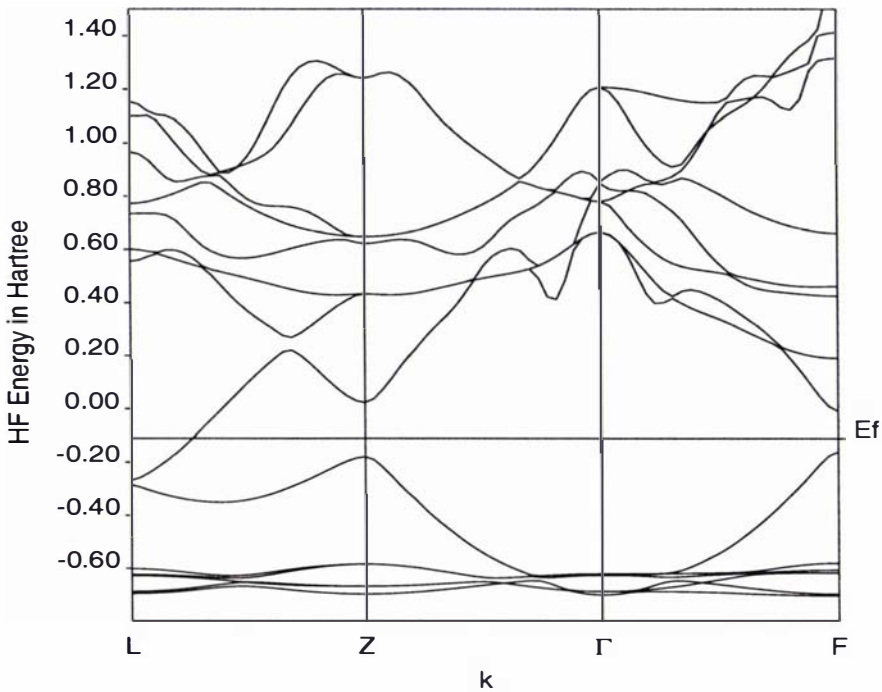

Figure 5.7: The Hartree-Fock band structure of mercury.

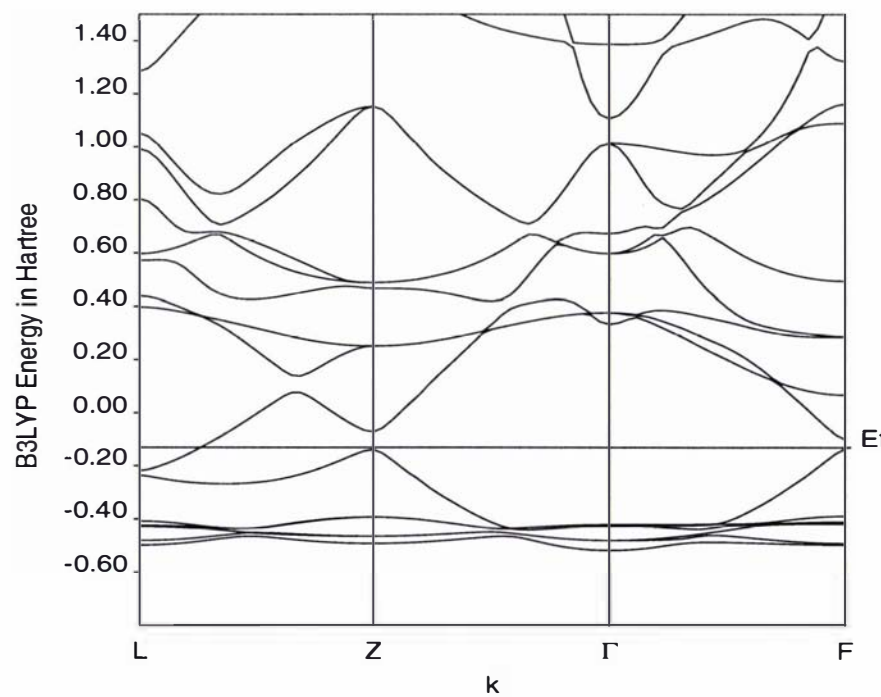

Figure 5.8: The B3LYP band structure of mercury.

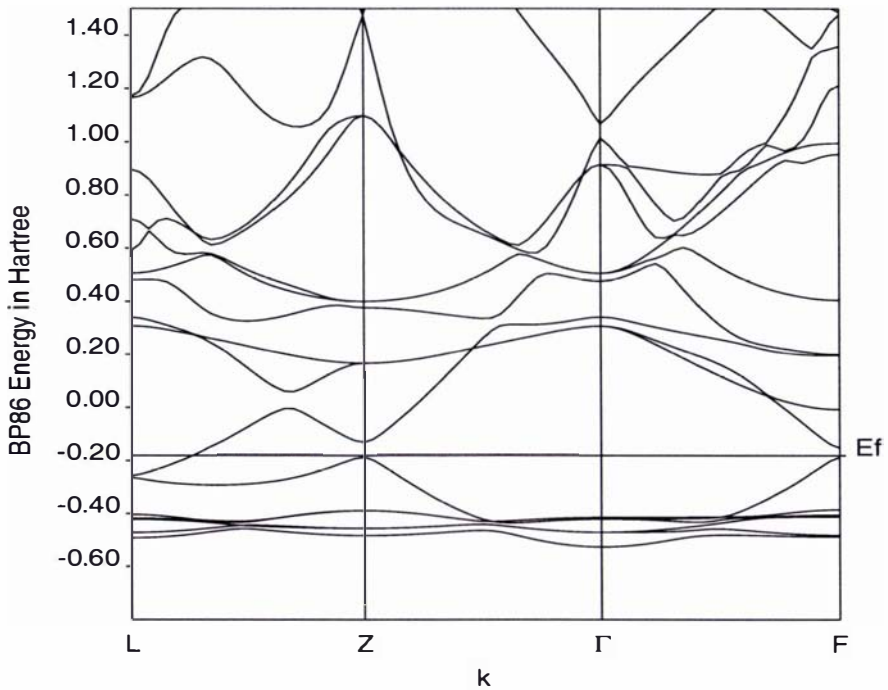

Figure 5.9: The BP86 band structure of mercury.

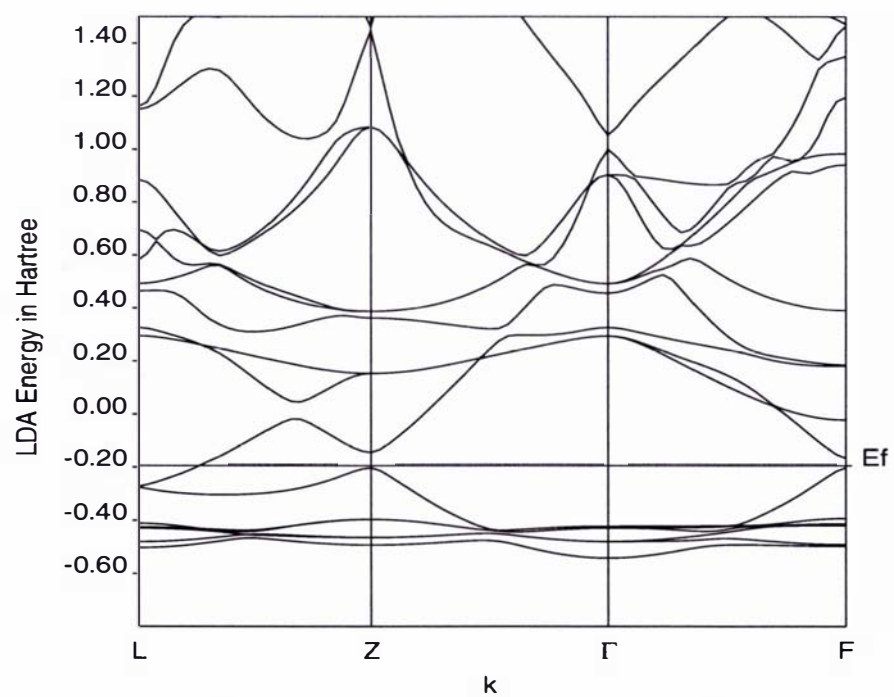

Figure 5.10: The LDA band structure of mercury.

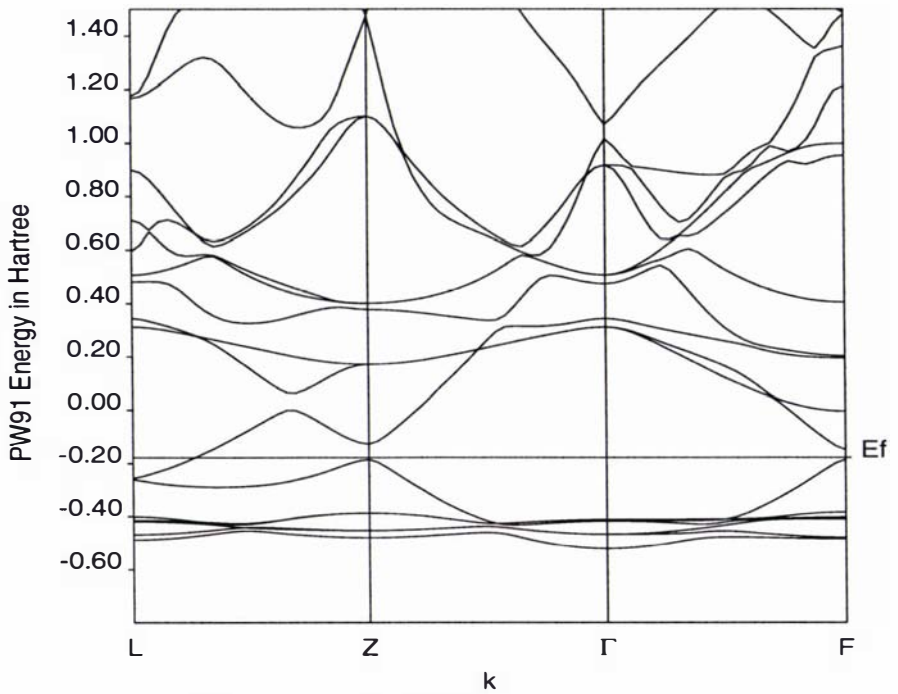

Figure 5.11: The PW91 band structure of mercury.

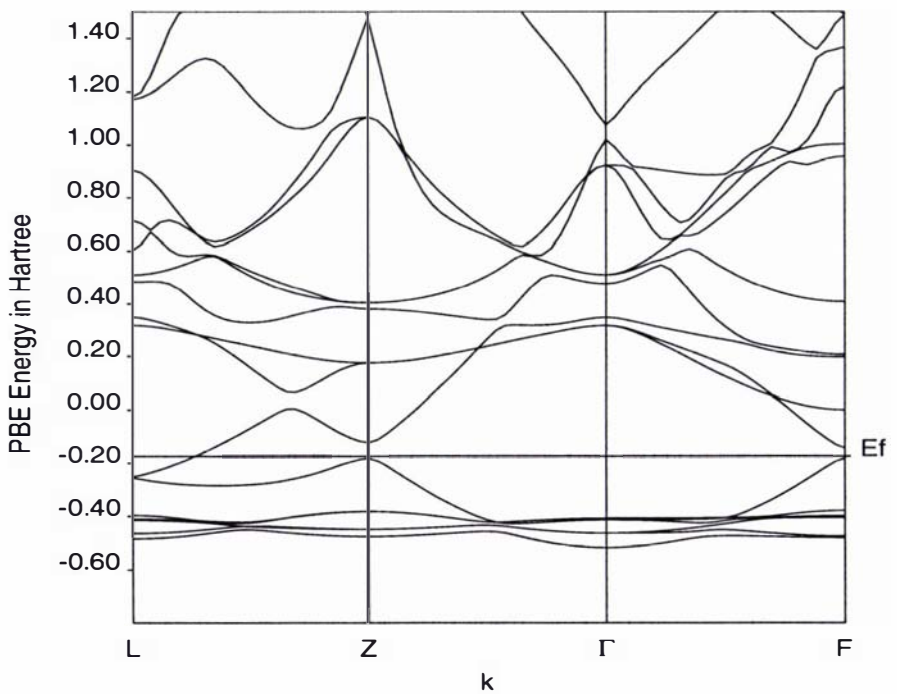

Figure 5.12: The PBE band structure of mercury.

5.1.3 Non-relativistic solid Hg

Calculating the non-relativistic energy of the lattice is the only way in which to assess the importance of relativistic effects directly. By intentionally excluding the effects of relativity from our results, we can gain a better understanding of the way in which these effects are manifested.

In the solid state DFT calculations described above, the effects of relativity are confined to the direct effects of the orbital contraction on orbital energies (e.g. the 6*s*-shell stabilisation) and bond lengths (e.g. the long range van der Waals bonds). These are described simply by the use of a pseudopotential for the core (innermost 60) electrons. Therefore these principal effects may be excluded to model a non-relativistic lattice by using a pseudopotential (and basis set) that have been fitted to non-relativistic calculations of the atom.

The pseudopotential and basis set are given in Tables 5.4 and 5.5. The functional form of the pseudopotential is entirely analogous to the relativistic one and is also from Stuttgart (see http://iris.theochem.uni-stuttgart.de/pseudopotentiale). The basis set has been cut in size from one that was optimised for the non-relativistic atom, i.e. only non-diffuse *s*-, *p*-, and *d*-functions are kept.

	Exponent	Coefficient
S		
	12.959046	434.421962
	6.854898	89.169670
P		
	11.048275	264.386016
	5.376213	46.357124
D		
	8.116369	112.197083
	4.064070	20.746427

Table 5.4: The non-relativistic pseudopotential parameters used for solid mercury.

The non-relativistic dimer potential is plotted in Figure 5.13 both with large and small (solid) basis sets; with MP2 and PW91. The increased binding of the non-relativistic dimer can be rationalised in terms of an increased covalency in the bond due to a weaker inert-pair effect. The effect of the smaller basis is to artificially increase binding due to basis set incompleteness; this is a problem that will be compensated for in the bulk by the transformation to Bloch basis functions.

The resulting non-relativistic optimised lattice parameters and energies are given

	Exponent	Coefficient
S		
	11.054117	1.
	6.1404131	1.
	2.5821409	1.
	1.8761221	1.
	0.8353169	1.
	0.3912778	1.
	0.1593481	1.
P		
	8.7413760	1.
	7.2212840	1.
	3.8484640	1.
	2.0510690	1.
	1.2771010	1.
	0.6530209	1.
	0.2862666	1.
D		
	4.4020520	1.
	1.3716770	1.
	0.6301691	1.
	0.2796754	1.

Table 5.5: The non-relativistic basis set for solid mercury.

in Table 5.6. Clearly the comparison with experiment is far poorer than in the relativistic case, however this should be no surprise. It is clear that without exception the non-relativistic solid is close-packed, and much more strongly bound than relativistically. What is surprising is the very close agreement of the three functionals PW91, BP86, and PBE.

An earlier study, [Singh, 1994], found similarly that the non-relativistic cohesive energy is much larger, 1.607 eV compared to 0.787 eV relativistically. However the non-relativistic lattice parameter was found to be slightly longer than in the relativistic case, in contrast to the DFT results. The values are not directly comparable as the previous calculations used a fcc lattice for the bulk calculation. However in the non-relativistic case it is not clear what the lattice structure should be.

The non-relativistic band structure is shown in Figures 5.14 and 5.15. These show similar features to the relativistic case, in particular the crossing of the Fermi level (E_f) between the L and Z points. Thus non-relativistic mercury is still metallic.

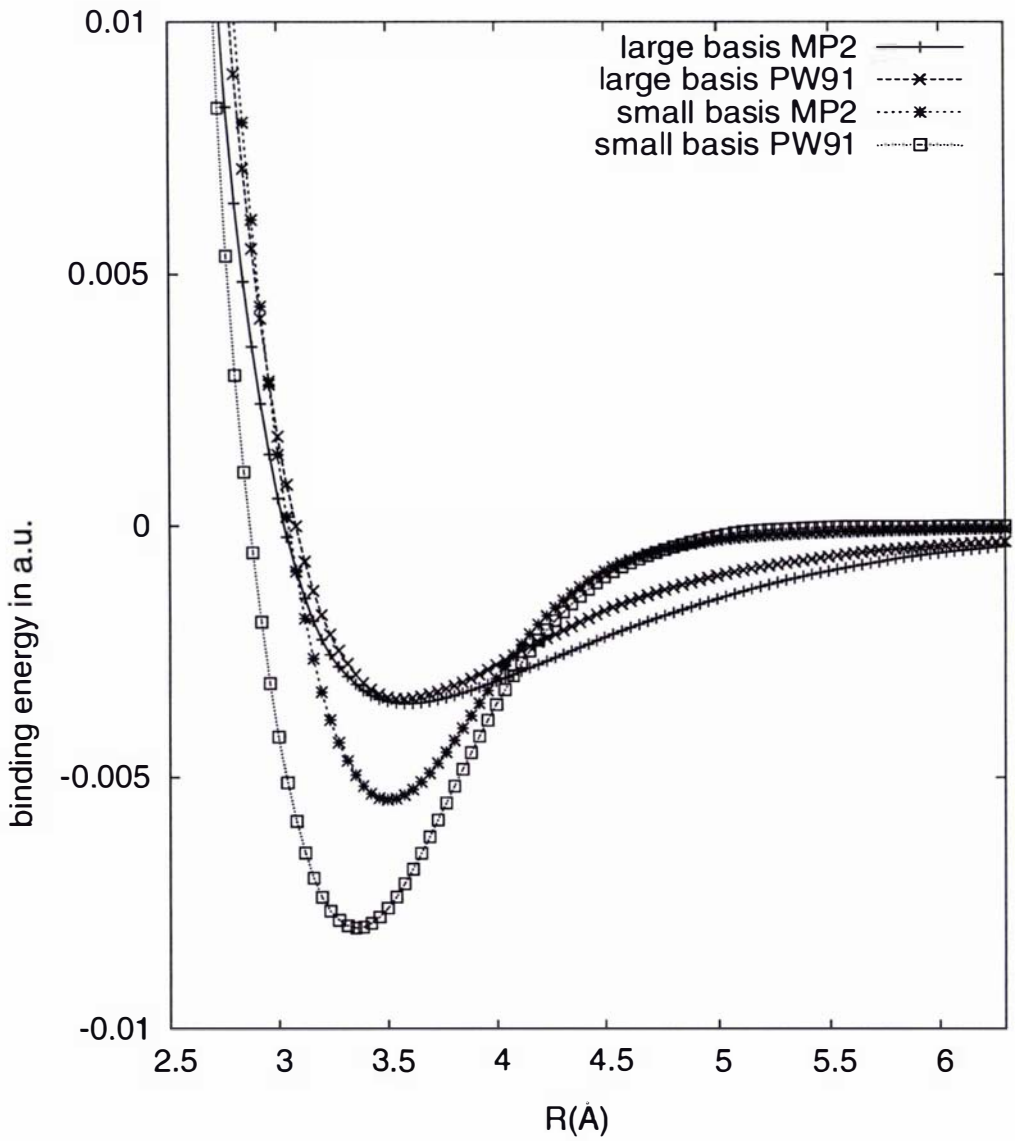

Figure 5.13: The non-relativistic Hg dimer potential.

Functional	a	c	a_R	α_R	E_{coh}	a/a_R
PW91	3.153	7.695	3.143	60.148	-1.836	1.0022
BP86	3.154	7.693	3.143	60.148	-1.553	1.0022
PBE	3.153	7.696	3.143	60.148	-1.800	1.0022
LDA	3.060	7.507	3.064	59.914	-2.654	0.9987
Expt	3.470	6.719	3.005	70.53	-0.79	1.1533

Table 5.6: Non-relativistic lattice parameters (in Å) and cohesive energies (in eV) for bulk mercury obtained from DFT and compared to experiment [Lide, 2002]. The same functionals are used as in the relativistic case, except B3LYP which was omitted due to poor convergence behaviour.

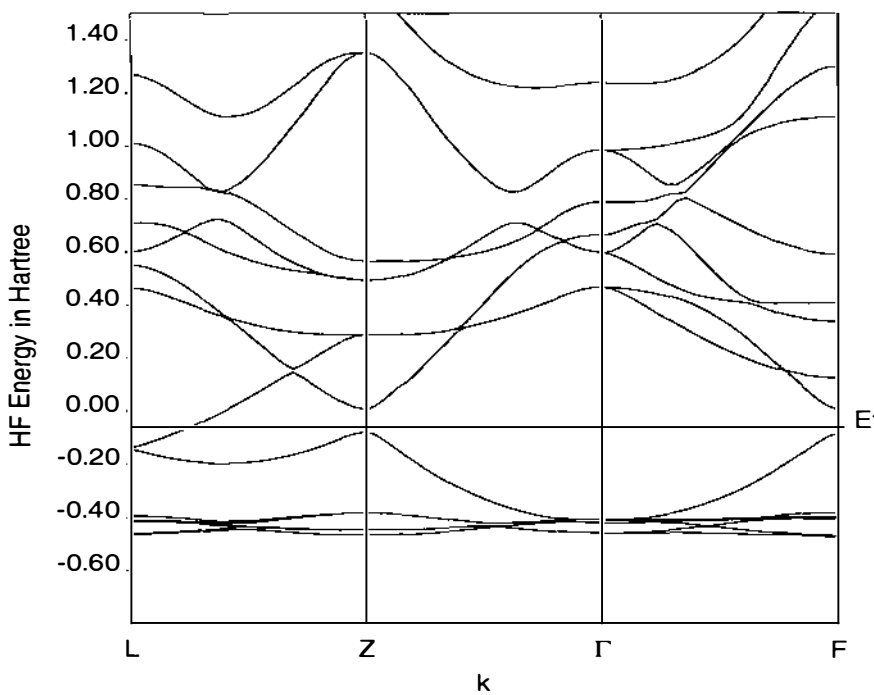

Figure 5.14: The non-relativistic LDA band structure of mercury.

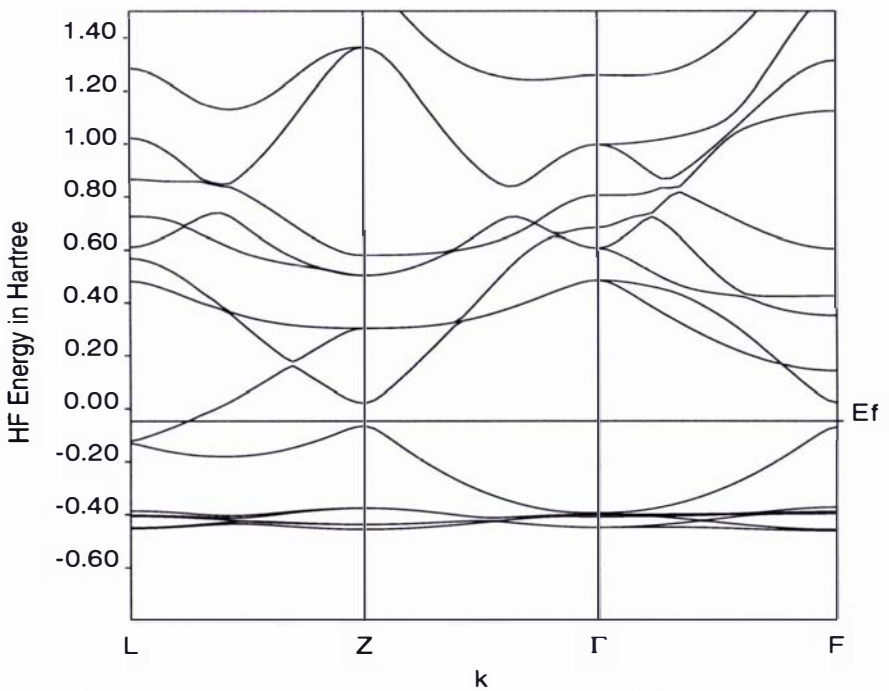

Figure 5.15: The non-relativistic PW91 band structure of mercury.

5.2 Two-body forces and the bulk

The primary difficulty in attempting a simulation of the bulk properties of mercury seems currently to be the inadequacy of a simple two-body potential such as has been used successfully in studies of other systems, such as the noble gases. Due to the poor convergence of the many-body expansion seen even for such a small cluster as Hg_6 (which will be much worse in the bulk due to the observed distance dependence; from Hg_6 to the bulk the change in nearest neighbour distance is still 0.5 Å) there seems little hope of finding a useful two-body potential for mercury. On the other hand, DFT results are unreliable, and the inclusion of many-body potentials increases the cost of the calculation prohibitively for large systems, apart from the problem of convergence.

A possible way to proceed can be suggested based on the results of Chapter 4. When the MP2 energy is split into the Hartree-Fock and correlation components, it is observed that the correlation energy converges much more rapidly, so that higher-body effects can be, for the most part, safely ignored. This is not surprising due to the *local nature* of the correlation interaction.

Therefore the idea is to calculate the energy of the bulk using HF, and then add a two-body correlation energy calculated over all pairs in the lattice. This approach is not only computationally cheap, but is conceptually simple and may in principle be applied to all size ranges between the atom and the bulk.

5.2.1 A two-body correlation potential

In Figure 5.16 are shown the Hartree-Fock curves for the dimer, calculated with our large uncontracted basis set as shown in Table 5.7.

This is compared to the best potential curve for Hg_2, which is the CCSD(T) curve of reference [Schwerdtfeger et al., 2001] including spin-orbit effects and scaled to fit the experimental bond length and energy (3.69 Å, 400 cm^{-1} = 0.0018 a.u.= 0.05 eV). The correlation energy curve is simply the difference between the scaled CCSD(T) (CCSD(T)+Expt) curve and the HF potential. A simple function was fitted to the correlation energy curve which for convenience took the same form as that used for the CCSD(T) Hg_2 potential in reference [Schwerdtfeger et al., 2001]. This is of the form:

$$V(r_{ij}) = \sum_{n=3}^{9} a_{2n}(r_{ij})^{-2n} \tag{5.8}$$

for a potential depending on the distance between two atoms r_{ij}.

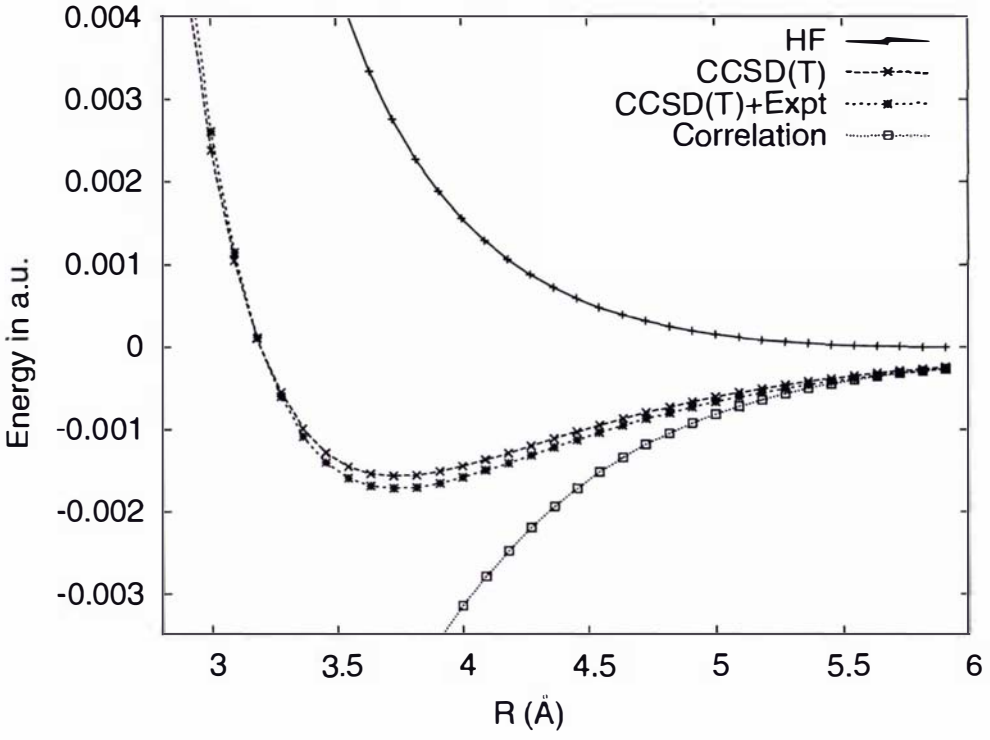

Figure 5.16: The HF and correlation description of Hg_2

Exponent	Exponent	Exponent	Exponent
S	P	D	F
21.808626	9.605107	4.715790	3.600000
11.643380	7.331637	3.111544	1.848018
6.352293	3.574473	1.320395	0.624074
2.579950	2.069620	0.581027	0.250000
1.618329	1.251303	0.241737	G
0.741351	0.662142	0.094501	2.589950
0.263827	0.306699	0.040000	1.192416
0.109004	0.134152	0.015000	0.462617
0.046954	0.056914	0.005000	H
0.020000	0.015000		2.877890
0.005000			1.149796

Table 5.7: Large uncontracted basis set for Hg.

The coefficients a_{2n} are given in Table 5.8. This ansatz was then applied to the

a_6	76.1858917
a_8	-5338.4326255
a_{10}	130050.4713836
a_{12}	-1655953.3064386
a_{14}	11803732.2206329
a_{16}	-44541379.7578471
a_{18}	69236765.3403922

Table 5.8: The coefficients a_{2n} of equation (5.8) used for the correlation potential (energy in a.u., for r in Ångstrøm).

bulk lattice. At the experimental lattice parameters one obtains:

E_{HF}	=	0.508 eV
E_{corr}	=	-1.384 eV
E_{total}	=	-0.876 eV

which compares to an experimental value of -0.79 eV for the bulk. While the correlation correction is slightly too large (or the HF energy too small), this is a better result than obtained with any density funtional yet.

5.3 Optimising the lattice with Hartree-Fock and a correlation correction

We may also look at optimising the lattice parameters with respect to this total (HF + correlation) energy. The optimum values according to this method are then given in Table 5.9.

	a	c	a_R	α_R	E_{coh}	a/a_R
HF + correlation (approximate)	3.26	6.82	2.95	67.04	-0.92	1.1051
Expt	3.47	6.72	3.00	70.53	-0.79	1.1533

Table 5.9: Lattice parameters for bulk mercury obtained from the HF + correlation optimisation and compared to experiment [Lide, 2002].

The difficulty is that the correlation potential appears to be consistently overbinding. Thus the 0.08 eV overbinding at the experimental lattice parameters is accompanied by a preference for shorter bond lengths when the lattice is optimised.

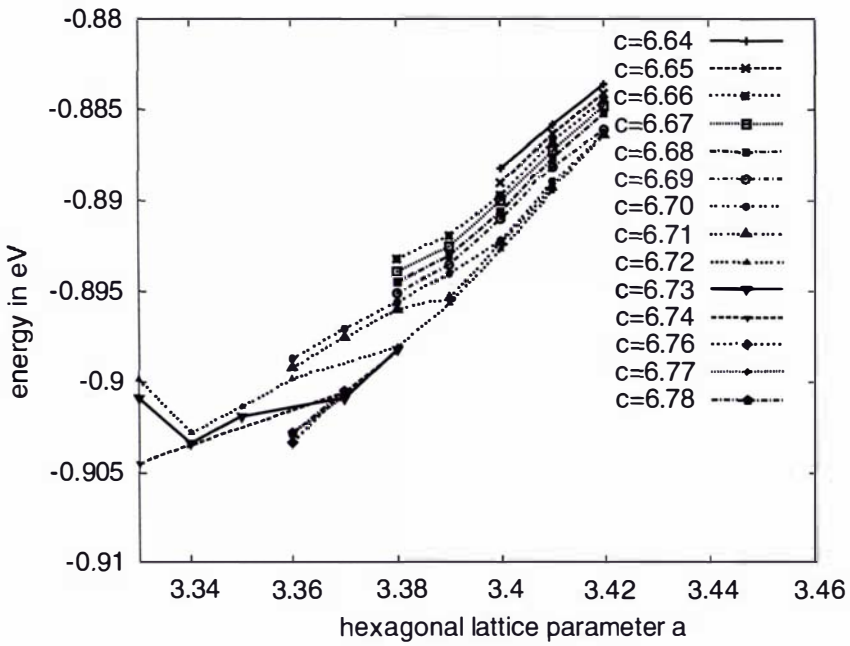

Figure 5.17: The HF and correlation energy optimisation is shown with respect to the lattice parameter a

Unfortunately, as the bulk becomes more compact, the SCF convergence of the HF calculation becomes problematic. It already requires a very small basis set in order to be practical, but as the lattice tightens, this becomes even harder. Therefore the value of a given in Table 5.9 is bounded from below by the convergence of the HF calculation, rather than a true energetic minimum, due to the overbinding correlation potential. This is therefore not physically realistic.

In Figure 5.17 is shown the dependence of the HF+correlation lattice energy on a. Figure 5.18 shows the dependence of the HF+correlation lattice energy on c.

5.3.1 Scaling of the correlation potential

The correlation potential may be written most generally in the form

$$V(r) = af(br - c) \tag{5.9}$$

where the coefficients a, b, and c allow for scaling and shifting the potential energy function f with respect to r. Due to the overbinding nature of the potential when applied to the bulk, this may be an easy way of improving results, and balancing

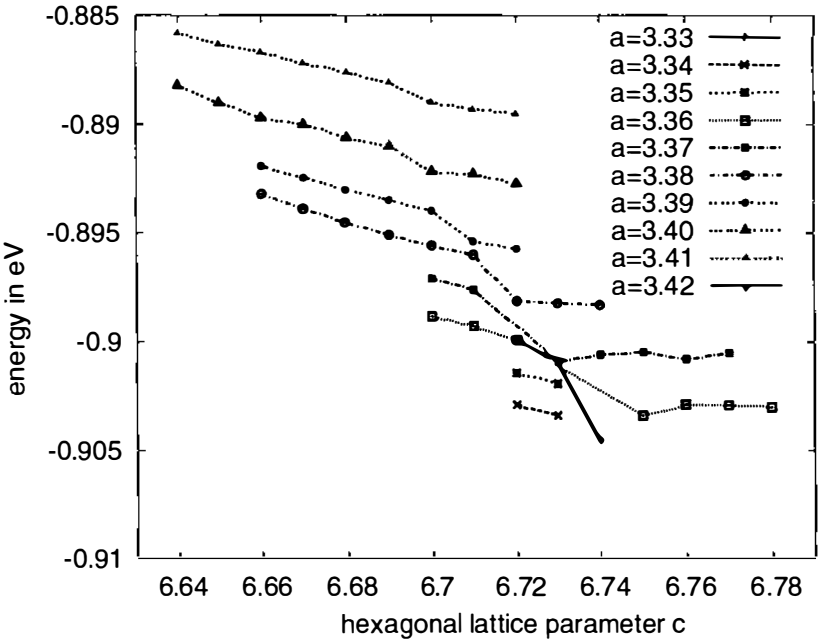

Figure 5.18: The HF and correlation energy optimisation is shown with respect to the lattice parameter c

the basis set deficiencies in the HF calculation. However any 2-body potential may only be applied to the bulk with difficulty, since many-body effects produce three parameters — a, c and the binding energy — that the potential needs to reproduce closely.

If the potential is shifted or scaled along the distance parameter by using $b \neq 1$ or $c \neq 0$, the correct value for a may be easily obtained. However this comes at the price of changing the weight of the correlation potential with respect to the HF energy, and thus the factor a must be used in order to scale the total energy back to a reasonable value. Unfortunately this loses the minimum at $a = 3.47$ Å. Thus fitting such a 2-body potential to even two parameters (a and E) is a non-trivial task when the total energy E is dependent also on the HF potential. This is before the second distance parameter c is even considered.

In fact, if the lattice is not optimised with respect to each of these lattice parameters but only the average bond-length, the correlation potential is spot on. An optimisation which keeps the rhombohedral angle constant and merely expands or contracts the lattice finds a minimum at precisely the experimental parameters. This is shown in Figure 5.19.

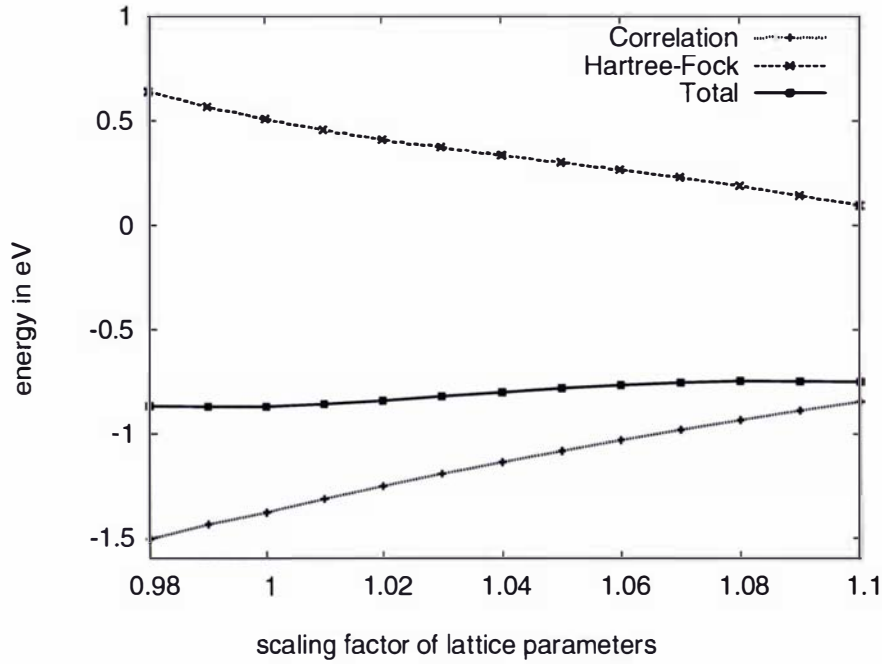

Figure 5.19: The HF and correlation energy optimisation is shown with respect to the factor by which the lattice parameters a and c are scaled. The minimum is at exactly the experimental values.

This is very useful, as this potential may now be expected to work over the total range of clusters from the dimer to the bulk, to give binding energies to 10% accuracy for the extreme case of the solid. It is only applicable to optimisations of bond length within a certain symmetry, as might be expected for a two-body potential.

5.4 Accuracy of the correlation potential

There are a few sources of error to consider. Firstly, the basis set used in the solid state HF calculations is very small, and the effect on the dimer potential due to the BSSE is significant. This means that the solid state HF may be less repulsive than the dimer due to the lack of repulsion between diffuse orbitals, and this makes the dimer correlation curve slightly too binding.

Secondly, information on the repulsive wall of either the CCSD(T)-based or HF curve is limited. When we use the correlation curve to calculate energies at a pair separation of 3 Å, such as found in the bulk, then a very small change in geometry

may have a very large impact. This consideration would also magnify any error due to the first point about the change of basis set. The third consideration is related to the second, namely that the pseudopotentials used (for both molecular and solid calculations) will introduce an error in the repulsive region of the potential which may already be noticeable at 3 Å.

While the agreement with experiment is quite acceptable, it is possible to look at the difference between the basis sets used a little more closely. First the dimer potential was calculated using HF and this small basis. The resulting curves are shown in Figure 5.20.

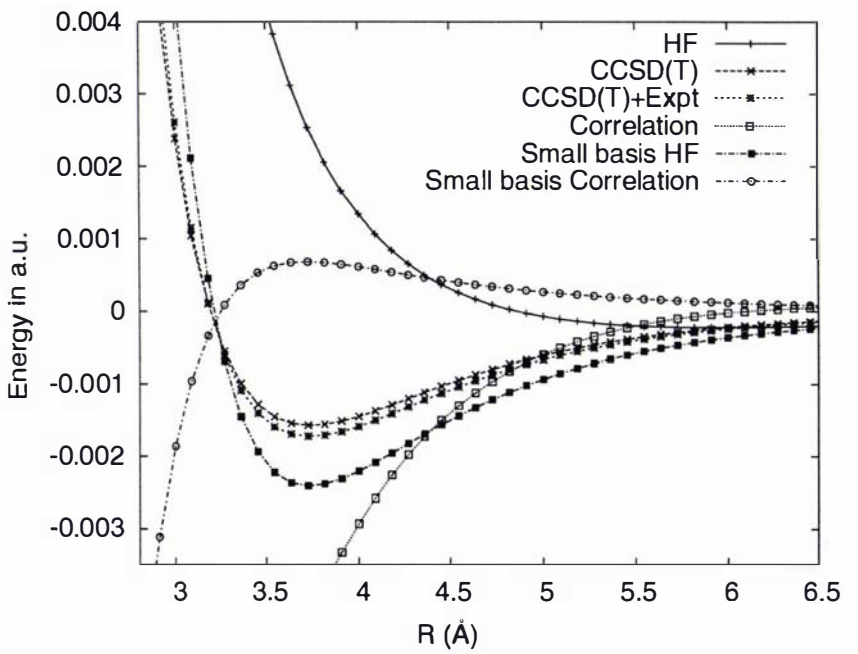

Figure 5.20: The HF potential is shown for both the large and small basis sets, along with their derived effective correlation potentials.

It seems that the BSSE is so large in the small basis set that binding is artificially introduced into the HF description of the Hg dimer, to the extent that it actually becomes overbound. However it is also clear that the correlation potential derived from the small basis set is useless; we know that the solid is not bound in HF theory, and due to the conversion of the basis set to Bloch functions the BSSE seen in the dimer is not apparent in the solid. The small basis correlation potential therefore even has the wrong sign over all the bonding part of the dimer interaction. This is

cause for some concern.

It is perhaps surprising that this small basis set works so well in the bulk, but this is a consequence of the changing physical description required with the shift from dimer to bulk, and the corresponding shift to Bloch basis functions.

The next test then is to assess how well this ansatz of a two-body correlation correction performs for small clusters. In principle this correction should be exact for the dimer, and the question is whether we can expect this approximation to hold for all sizes between the dimer and the bulk. Naturally for the smallest sizes, the use of a large basis set is possible.

5.5 Two-body correlation in small clusters

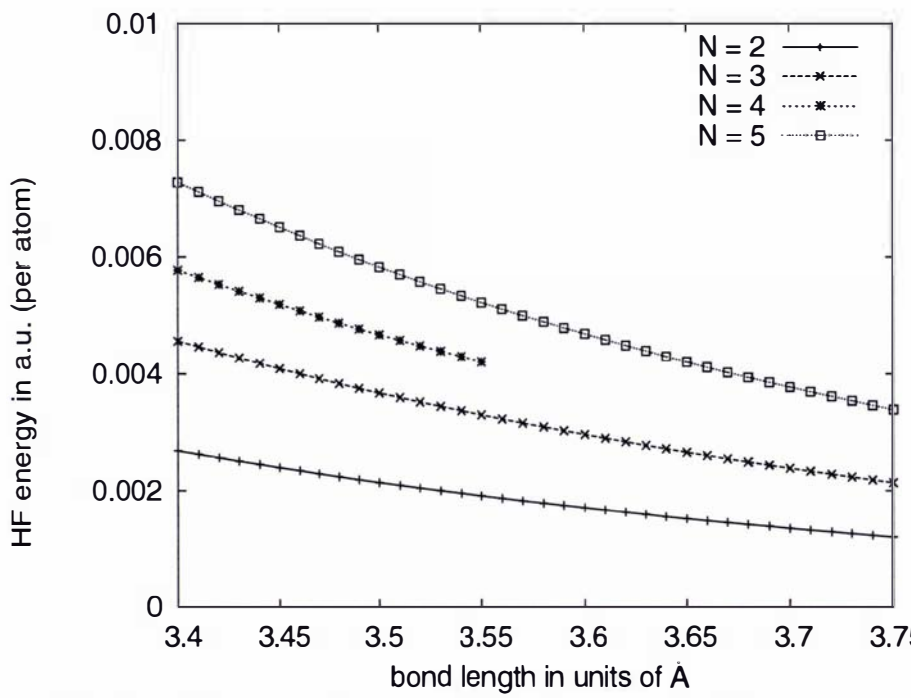

Figure 5.21: The HF potential for each of the clusters with $N = 2 - 5$. Energies are per atom.

For the smallest mercury clusters the HF potential was calculated using the large uncontracted basis set used for the potentials given in Table 5.7, and the two-body correction was calculated using the potential as described above. The sum of these was then taken as the total energy of the cluster, and the structure was optimised

with respect to this energy by varying the bond lengths. The initial coordinates were taken from the MP2 optimised structures described in Chapter 6.

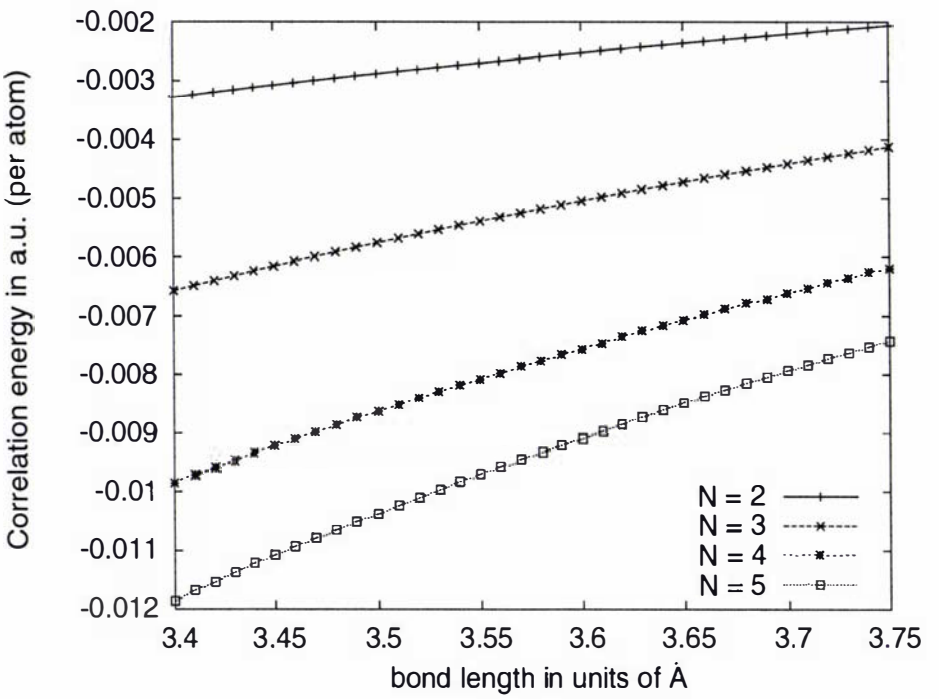

Figure 5.22: The correlation potential for $N = 2 - 5$. Energies are per atom.

The HF and correlation (CCSD(T) - HF) potentials are plotted in Figures 5.21 and 5.22, and the total potential energy is shown in Figure 5.23. The energies given here are the total binding (or non-binding interaction) energy per atom. The consequently optimised bond lengths are given in Table 5.10. No attempt was made to alter the original (LJ) structure of the cluster other than this optimisation with respect to bond lengths.

Some of the trends shown in Figure 5.23 are easily explained. The two-body potential is pairwise additive, such that for a Hg_2 energy $E(r)$ we have for Hg_3 $3E(r)$ and for Hg_4 $6E(r)$. Therefore the per-atom correlation contribution will change from $\frac{E(r)}{2} \rightarrow \frac{3}{3}E(r) \rightarrow \frac{6}{4}R(r)$ for $N = 2 \rightarrow 3 \rightarrow 4$, giving a constant (distance-dependent) difference of $\frac{E(r)}{2}$ between these correlation curves.

The agreement with the CCSD(T) structures of reference [Dolg and Flad, 1997] is very good, as shown in Table 5.10. Clearly this simple ansatz of a two-body correlation potential can be expected to have wide applicability for mercury clusters and for the simulation of solid to liquid phase transitions.

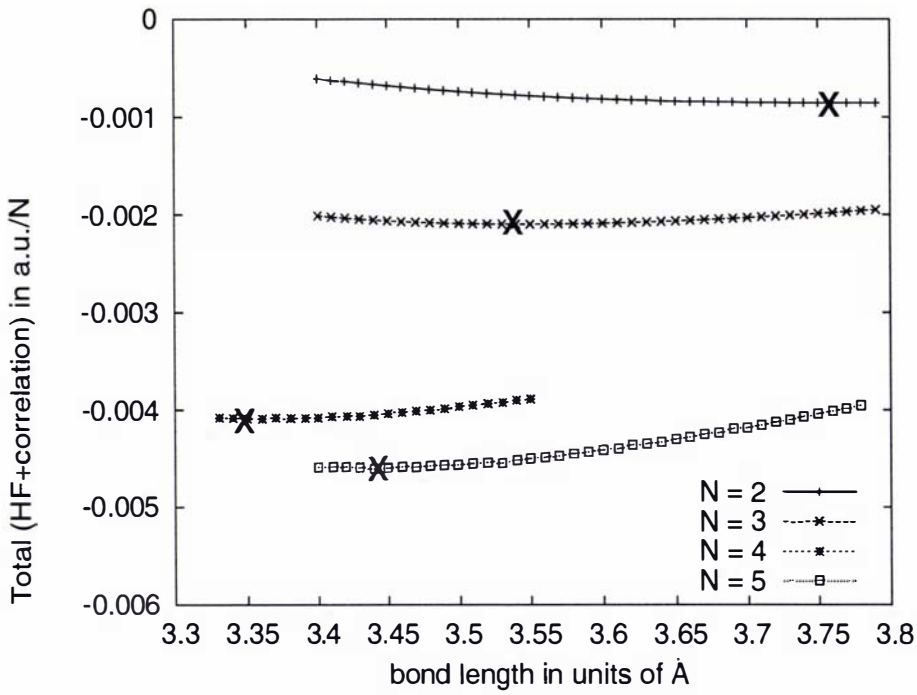

Figure 5.23: The total (HF + correlation) potential for each of the clusters with $N = 2 - 5$. Energies are per atom, and the optimum bond length is marked with a cross.

	HF + correlation			CCSD(T) [Dolg and Flad, 1997]	
N	r(Å)	BE (a.u.)	BE (eV)	r(Å)	BE (eV)
2	3.762	-0.0017	-0.0467	3.75	-0.046
3	3.542	-0.0063	-0.1712	3.51	-0.183
4	3.359	-0.0164	-0.4457	3.35	-0.472
5	3.438	-0.0230	-0.6254	3.44	-0.695
6	3.501	-0.0282	-0.7684	3.52	-0.792

Table 5.10: The HF + correlation optimised clusters $N = 2 - 6$, based on LJ geometries which represent the global minimum. The CCSD(T) results are those of reference [Dolg and Flad, 1997]. For Hg_5 the bond length given is that of the axial-equatorial bond of the trigonal bipyramid (which are more numerous (6 pairs) than the longer axial-axial (1) or shorter equatorial-equatorial (3) bonds). For Hg_6 the shortest bond is given.

5.6 Conclusions

From an analysis of the situation so far, e.g. the behaviour of density functionals in the dimer as compared to in the bulk; the inadequacy of the two-body potential alone; also the good description of correlation by a two-body potential, it is clear that the study of mercury clusters requires a number of different approaches. For the smallest sizes a rigorous quantum chemical method has to be preferred, such as CCSD(T) when possible or MP2. In the case of DFT the choice of functional plays an enormous role; PW91 seems to describe the bonding of small systems best.

The use of a 2-body potential to correct Hartree-Fock for correlation is promising, although the behaviour of the optimised bulk stucture is a little disappointing, due to the poor convergence behaviour at short bond lengths. The solid state HF calculation is problematic at this stage due to the small basis sets required. Both for the clusters and for the bulk, the two-body correction is very accurate in finding the minimum bond-length (for fixed angles).

In general all possible methods should be used in order to compare their performance and applicability; this will certainly be the approach for the small neutral mercury clusters to begin with.

Chapter 6

Neutral Clusters

In this chapter I will address the question of structure for the neutral mercury clusters, and subsequently calculate vibrational frequencies and polarisabilities. The structures of mercury clusters are of interest for many reasons. Firstly because the relativistic stabilisation of the valence $s-$shell in mercury allows an interesting comparison to be made with the noble gas clusters, which have been thoroughly studied. A second question is posed by the unique behaviour of bulk mercury, most notably the low melting point (compared to other metals). Also, as in most (metal) cluster physics the issue of a metal to non-metal transition is of interest. Such a transition can only be investigated by examining the size dependence of an associated property. This leads back to the structure, as many properties cannot be obtained without first determining the molecular nuclear arrangement and the electronic energy.

6.1 Isomers

For the noble gases the minimum energy structures are (primarily — and for all the clusters in the size range here) the highly symmetric icosahedra that are obtained for example using a simple Lennard-Jones type model. These result from the essentially isotropic forces due to the van der Waals bonding and lack of covalency, and so have been commonly assumed to apply to the small mercurry clusters also.

A limited comparison with other structures has been done; in a recent paper Hartke *et al* proposed several unusual low-symmetry structures as the global minima for Hg clusters [Hartke et al., 2001]. These have therefore been compared to the Lennard-Jones (LJ) or noble gas-type clusters, and a vibrational analysis performed in order to test their stability. The LDA and MP2 calculations were carried out with

Gaussian 03 [Frisch et al., 2003], and the coupled cluster calculations were performed using Molpro [Werner et al., 2003].

6.1.1 Structural optimisation

The optimisation of the structure of a molecule with respect to its energy is one of the most common problems addressed in quantum chemistry. For the case of two atoms, or indeed any molecule of known symmetry where the number of parameters is low, it is a simple problem. However in the general case where there are N atoms and $3N - 6$ degrees of freedom, it becomes quickly more demanding.

If the energy at a point on the potential energy surface (given in terms of the nuclear coordinates R_i as $\mathbf{r} = (R_1, R_2, \ldots, R_{3N})$, where the subscript labels the nuclear positions) is expanded in a Taylor series

$$E(\mathbf{r}') = E(\mathbf{r}) + (\mathbf{r}' - \mathbf{r})^{\dagger} f(\mathbf{r}) + \frac{1}{2}(\mathbf{r}' - \mathbf{r})^{\dagger} H(\mathbf{r})(\mathbf{r}' - \mathbf{r}) \tag{6.1}$$

then the gradient is

$$f_i = \left.\frac{\partial E(\mathbf{r})}{\partial X_i}\right|_{r'} \tag{6.2}$$

and the Hessian

$$H_{ij} = \left.\frac{\partial^2 E(\mathbf{r})}{\partial X_i \partial X_j}\right|_{r'} . \tag{6.3}$$

These derivatives can be calculated either numerically from a set of $\mathbf{r}$-dependent energies, or analytically with respect to the molecular orbital coefficients, where the form of the equations must depend on the method used for the energy calculation [Yamaguchi et al., 1994].

There are a number of different methods that might be used for the structural optimisation based on these derivatives once they are obtained.

A transition state (higher order critical point) occurs when at a stationary point $f(r) = 0$ one (or more) of the eigenvalues of $H(r)$ is negative. Therefore an analysis of the frequencies of vibration is always done (where the cost of the method allows; e.g. for DFT and MP2) to check that the calculated structures are in fact stable and not just stationary points on the potential energy surface.

6.1.2 Lennard-Jones isomers

The LJ type clusters are based on the principle of maximising the number of van der Waals interactions between the atoms, which are non-covalent and therefore isotropic.

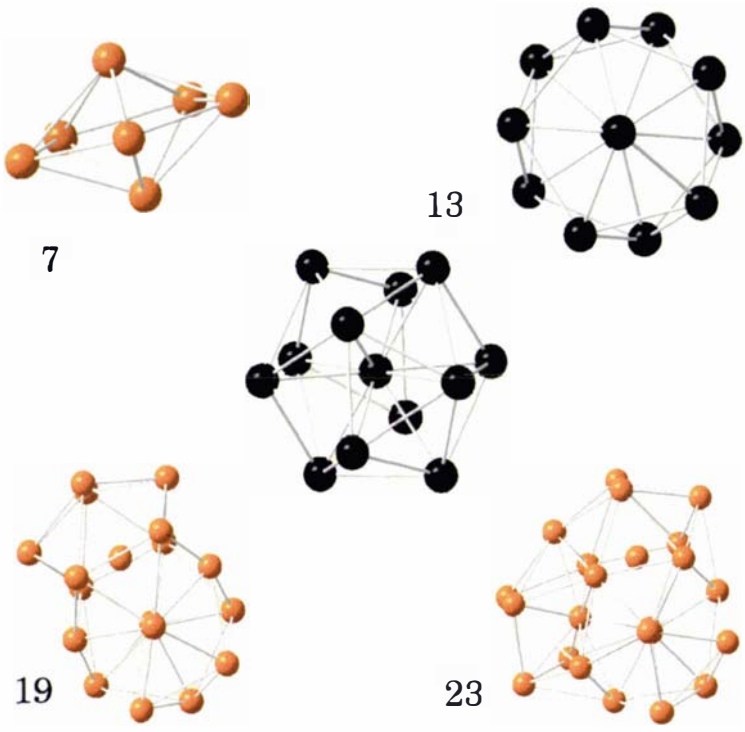

Figure 6.1: Structures of 'magic' Lennard-Jones clusters. The icosahedron is shown twice (in black), at top right the view shows the symmetry clearly, while the centre depiction shows the relationship to the pentagonal bipyramid (shown at top left).

Therefore the lowest energy structures are of high symmetry, and as close to spherical as can be managed to minimise surface effects. The optimised structures of the Lennard-Jones and related clusters can be found at the Cambridge Cluster Database and in the following all mercury LJ-type clusters have been optimised from coordinates taken from that database [Wales et al., 2004].

The LJ clusters were optimised using a correlation consistent basis set that was optimised for the MP2 energy of the atom. In DFT two functionals were chosen: LDA because it performs astoundingly well for solid mercury, and PW91[1] because it

[1]PW91 refers always in this thesis to what is known in Gaussian as PW91PW91 (PW91 for both exchange and correlation).

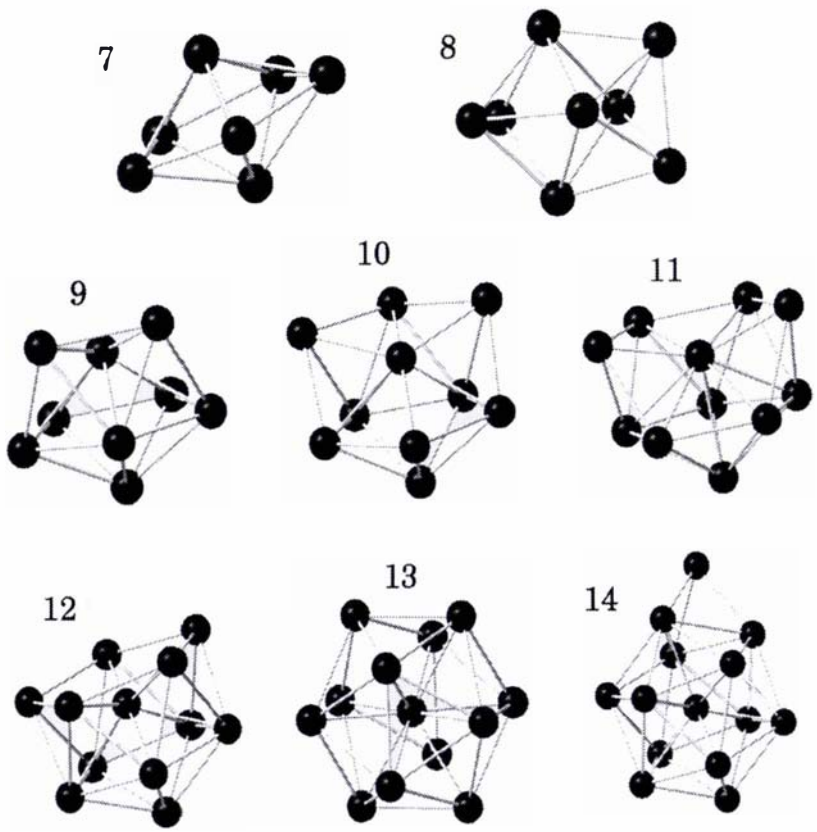

Figure 6.2: Structures of small Hg Lennard-Jones type clusters

best approximates the binding potential of the dimer.

The MP2 clusters should be considerably more reliable than the DFT results; however even MP2 calculations could only be carried out to the limited size of 9 atoms. The CCSD(T) results are undoubtedly the most accurate, however the BSSE correction (discussed later) becomes a much larger problem here than in DFT. CCSD(T) calculations were only feasible up to a size of 7 atoms. These calculations were performed with a full active orbital space, i.e. 20 electrons per atom to be correlated, which meant 140 electrons in total.

The structures of these optimised isomers are summarised in Table 6.1. The coordinates of the isomers are given in the appendix.

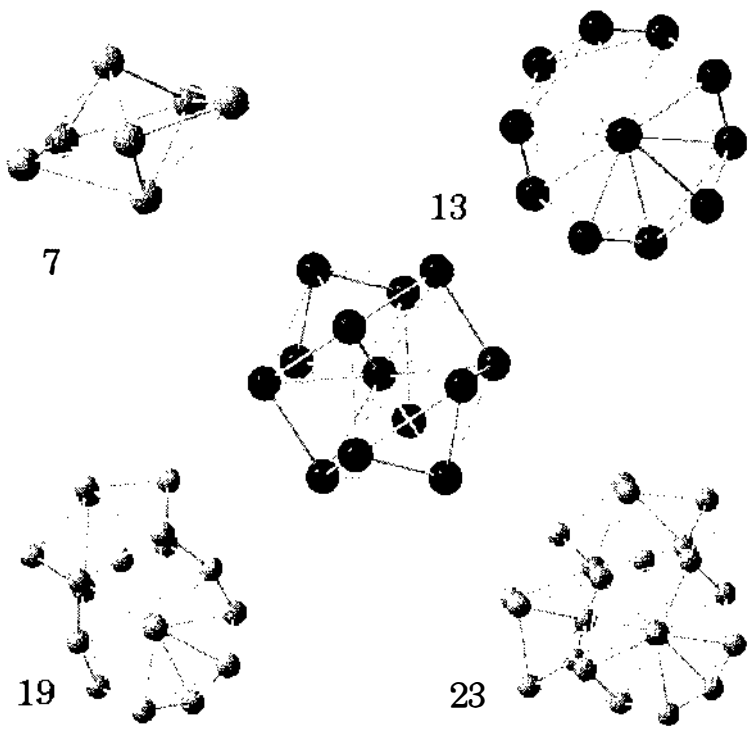

Figure 6.1: Structures of 'magic' Lennard-Jones clusters. The icosahedron is shown twice (in black), at top right the view shows the symmetry clearly, while the centre depiction shows the relationship to the pentagonal bipyramid (shown at top left).

Therefore the lowest energy structures are of high symmetry, and as close to spherical as can be managed to minimise surface effects. The optimised structures of the Lennard-Jones and related clusters can be found at the Cambridge Cluster Database and in the following all mercury LJ-type clusters have been optimised from coordinates taken from that database [Wales et al., 2004].

The LJ clusters were optimised using a correlation consistent basis set that was optimised for the MP2 energy of the atom. In DFT two functionals were chosen: LDA because it performs astoundingly well for solid mercury, and PW91[1] because it

[1]PW91 refers always in this thesis to what is known in Gaussian as PW91PW91 (PW91 for both exchange and correlation).

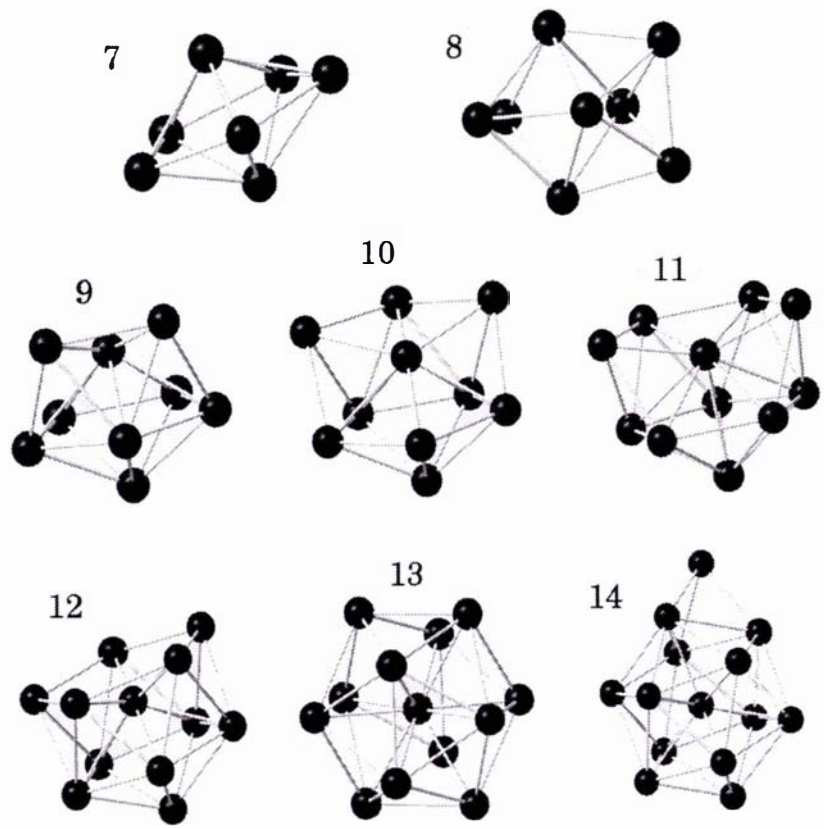

Figure 6.2: Structures of small Hg Lennard-Jones type clusters

best approximates the binding potential of the dimer.

The MP2 clusters should be considerably more reliable than the DFT results; however even MP2 calculations could only be carried out to the limited size of 9 atoms. The CCSD(T) results are undoubtedly the most accurate, however the BSSE correction (discussed later) becomes a much larger problem here than in DFT. CCSD(T) calculations were only feasible up to a size of 7 atoms. These calculations were performed with a full active orbital space, i.e. 20 electrons per atom to be correlated, which meant 140 electrons in total.

The structures of these optimised isomers are summarised in Table 6.1. The coordinates of the isomers are given in the appendix.

6.1.3 Low symmetry isomers

The structures proposed by Hartke *et al* covered the size range of 7 to 14 atoms. The minimum energy structures are pictured in Figure 6.3. The results of Hartke *et*

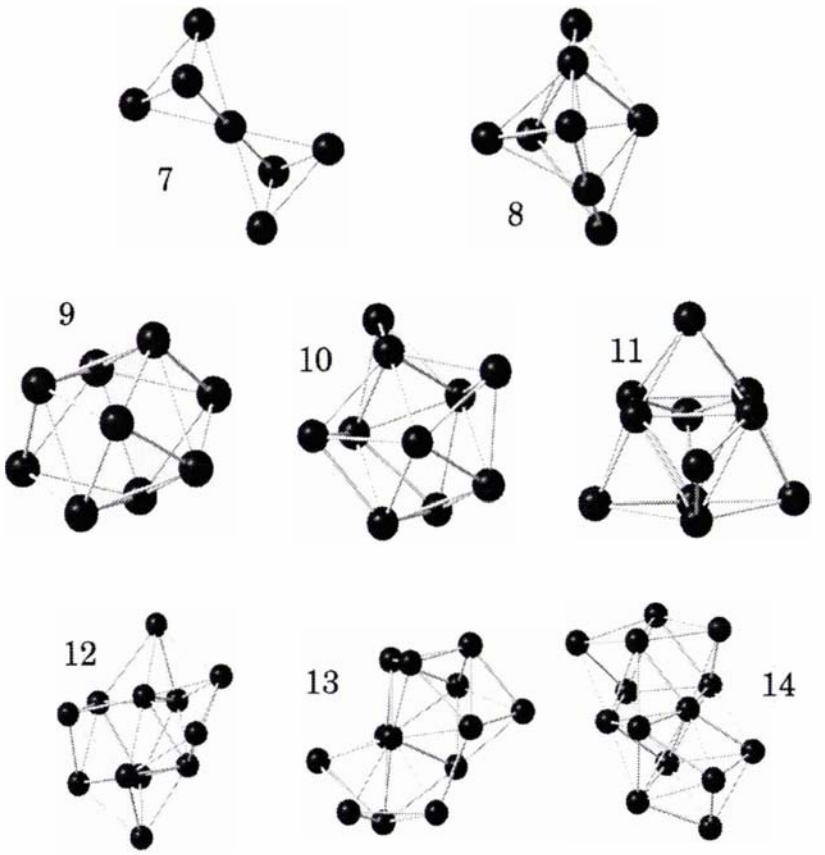

Figure 6.3: LDA optimised structures of Hartke clusters

al. are remarkable for their complete failure to agree with Lennard-Jones or Morse type clusters. The model used is that of an effective dispersion potential based on accurate calculations of the dimer, and added to the HF energy to include correlation effects [Wang et al., 2000]. In comparison there are simulated annealing results from the (2 + 3n)-body approach of Moyano *et al.* [Moyano et al., 2002] which used two- and three-body potentials constructed from relativistic coupled cluster and second-order many-body perturbation theory. These show behavior in agreement with the

LJ potential, and have the familiar 'magic numbers' at $N = 6$, 13, 19, 23, 26, and 29 atoms. Due to the different methods used, it is not very useful to compare the energies obtained by Hartke or by Moyano with those calculated here. The best that one can compare is the geometry of the minimum energy isomer found by each method. Therefore in assessing the relative energies of both LJ and Hartke isomers using three different methods, the hope is to find some degree of mutual corroboration between them. CCSD(T) calculations, though reliable, are certainly not feasible up to the sizes explored by Hartke; however the DFT calculations may be benchmarked against the small CCSD(T) clusters. The results for the optimised Hartke clusters

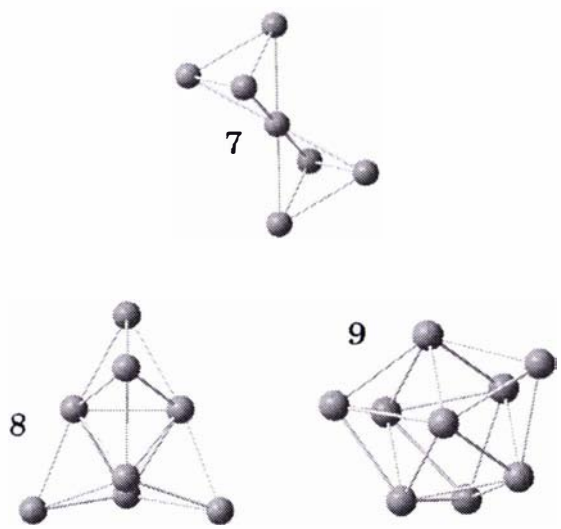

Figure 6.4: MP2 optimised structures of the Hartke clusters

are given in Table 6.2. The methods are the same as described above for the LJ isomers.

N	Symmetry	BE	BE/N	r_{min}
DFT (LDA)				
2	$C_{\infty h}$	-0.007833	-0.003916	3.1068
3	D_{3h}	-0.022583	-0.007528	3.1000
4	T_d	-0.044205	-0.011051	3.1023
5	D_{3h}	-0.062660	-0.012532	3.1094
6	O_h	-0.080514	-0.013419	3.1725
7	D_{5h}	-0.104977	-0.014997	3.1618
8	D_{2d}	-0.125654	-0.015707	3.1091
9	C_{2v}	-0.151237	-0.016804	3.0938
10	C_{3v}	-0.176152	-0.017615	3.0999
11	C_{2v}	-0.200228	-0.018203	3.0554
12	C_{5v}	-0.225873	-0.018823	3.0455
13	I_h	-0.254774	-0.019598	3.1114
14	C_{3v}	-0.277637	-0.019831	3.0969
DFT (PW91)				
2	$D_{\infty h}$	-0.002263	-0.001132	3.5079
3	D_{3h}	-0.006437	-0.002146	3.4913
4	T_d	-0.012726	-0.003182	3.4569
5	D_{3h}	-0.018492	-0.003698	3.4380
6	O_h	-0.023511	-0.003918	3.5046
7	D_{5h}	-0.031509	-0.004501	3.4788
8	D_{2d}	-0.036255	-0.004532	3.4702
9	C_{2v}	-0.045266	-0.005030	3.4349
10	C_{3v}	-0.052829	-0.005283	3.4064
11	C_{2v}	-0.060374	-0.005489	3.3948
12	C_{5v}	-0.068899	-0.005742	3.3725
13	$\mathbf{I_h}$	-0.078687	-0.006053	3.3922
14	C_{3v}	-0.085202	-0.006086	3.3852
MP2				
2	$C_{\infty h}$	-0.0011820	-0.0005910	3.7842
3	D_{3h}	-0.0040108	-0.0013369	3.6839
4	T_d	-0.0093139	-0.0023285	3.5555
5	D_{3h}	-0.0148612	-0.0029722	3.4791
6	T_h	-0.0200928	-0.0033488	3.5521
7	D_{5h}	-0.0287650	-0.0041097	3.4869
8	C_{2v}	-0.0340842	-0.0042619	3.3861
9	C_{2v}	-0.0450054	-0.0050006	3.3607
CCSD(T)				
2	D_{2h}	-0.0004868	-0.0002435	4.0578
3	C_s	-0.0015751	-0.0005251	3.9963
4	C_{2v}	-0.0034555	-0.0008639	3.9188
5	C_{2v}	-0.0054159	-0.0010832	3.8944
6	D_{2h}	-0.0073508	-0.0012251	3.8996
7	D_{5h}	-0.0103723	-0.0014818	3.7620

Table 6.1: LJ isomers, optimised with DFT (LDA, PW91), MP2 and CCSD(T) methods. The binding energy (BE) and binding energy per atom (BE/N) are in a.u., the shortest bond length in the cluster (r_{min}) is given in Ångstrøm. The symmetry given is that used in the calculation.

DFT (LDA)

N	Symmetry	BE	BE/N	r_{min}
7	C_i	-0.092016	-0.013145	3.0496
8	C_1	-0.119689	-0.014961	3.1516
9	C_1	-0.151365	-0.016818	3.0943
10	C_{3v}	-0.174153	-0.017415	3.0860
11	C_1	-0.195852	-0.017805	3.0804
12	C_1	-0.220430	-0.018369	3.0595
13	C_1	-0.248268	-0.019098	3.0461
14	C_1	-0.270249	-0.019303	3.0210

DFT (PW91)

N	Symmetry	BE	BE/N	r_{min}
7	C_i	-0.026700	-0.003814	3.3841
8	C_s	-0.035842	-0.004480	3.4680
9	C_1	-0.043126	-0.004792	3.4524
10	C_{3v}	-0.049925	-0.004993	3.4369
11	C_1	-0.056649	-0.005150	3.4146
12	C_1	-0.064143	-0.005345	3.3460
13	C_1	-0.071283	-0.005483	3.3129
14	C_1	-0.078837	-0.005631	3.3515

MP2

N	Symmetry	BE	BE/N	r_{min}
7	C_i	-0.021095	-0.003014	3.4847
8	C_i	-0.033608	-0.004201	3.4135
9	C_i	-0.040254	-0.004473	3.4231

CCSD(T)

N	Symmetry	BE	BE/N	r_{min}
7	D_{3d}	-0.007508	-0.001073	3.835

Table 6.2: Low symmetry (Hartke) isomers, optimised with DFT (LDA, PW91), MP2 and CCSD(T) methods. The binding energy (BE) and binding energy per atom (BE/N) are in a.u., the shortest bond length in the cluster (r_{min}) is given in Ångstrøm. The symmetry given is that used in the calculation.

The coordinates of these clusters are given in appendix A. A comparison of the performance of the different methods is given in section 6.2.

6.1.4 Hg_7

The only size for which a comparison of the LJ and Hartke isomers at the CCSD(T) level was feasible was for 7 atoms. The results are consistent with the LDA, PW91 and MP2 calculations, although the bonding of the CCSD(T) calculations is characteristically weaker. The CCSD(T) optimisations were done in the maximum symmetry for the isomer, which in Molpro is restricted to D_{4h} and lower symmetry point groups. Thus the LJ isomer (D_{5h} symmetry) was calculated in C_{2v} symmetry, and the D_{3d} Hartke isomer in C_{2h} symmetry. Due to symmetry, both isomers have only two parameters to be optimised. These may be defined either as two bond-lengths, R_1 and R_2, or a bond length R_1 and an angle A_1. These structures are compared in Figure 6.5, with the variable bonds and angles labelled.

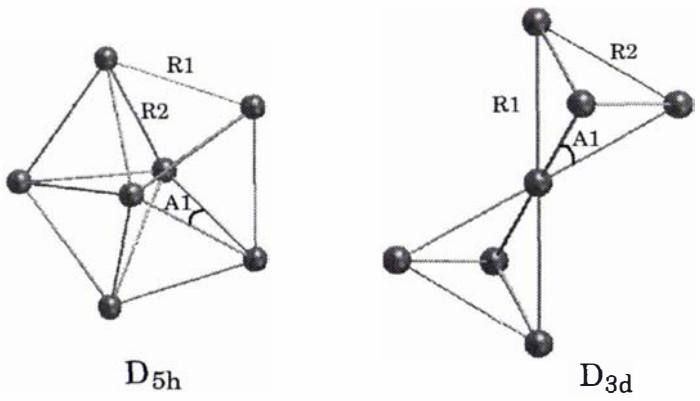

Figure 6.5: The lowest energy structures of the two Hg_7 isomers.

The coordinates for these isomers as optimised with CCSD(T) are given in the appendix. The variable parameters not dependent on symmetry are given in Table 6.3.

The LJ (D_{5h}) isomer is more stable at every level of calculation. The CCSD(T) calculation finds it to be more stable by a difference of -0.002864 a.u. Moreover both the DFT and MP2 calculations found that the Hartke structure is a higher-order

Parameter	D_{5h}	D_{3d}
R_1	3.938	3.835
R_2	3.833	4.096
A_1	58.159	64.556

Table 6.3: CCSD(T) optimised parameters for the Hg_7 isomers, the LJ isomer (D_{5h}) and the 'low-symmetry' Hartke isomer (D_{3d}). Only two of the three tabulated parameters are needed to define the structure. Bond lengths R_1 and R_2 are in Å, angles A_1 in degrees.

saddle point, with 2 and 3 negative frequencies respectively.

6.1.5 Tetrahedral isomers

It has recently been proposed [Johansson and Pyykkö, 2004] that at certain sizes where perfect tetrahedra may be formed ($N = 4, 10, 20, 35, 56 \ldots$), that these magic tetrahedra may in some cases be lower in energy than the corresponding LJ structure. The case of $N = 4$ is of no interest as the tetrahedron is the LJ structure. However it is of interest to examine the case of $N = 10$ for mercury. The structure is pictured in Figure 6.6.

The structure was optimised using PW91 and the stability examined by a frequency analysis. The starting coordinates were taken from the supplementary data of [Johansson and Pyykkö, 2004]. The resulting structure is compared with other isomers for $N = 10$ in Table 6.4.

The zero point vibrational energy (ZPVE) correction is reasonably large relative to the total binding energy, however, it has no effect on the relative energies of the different isomers. While the tetrahedral isomer is a local minimum and exhibits no negative frequencies, it is also clearly less stable than the LJ isomer. It is however more stable than the Hartke structure. In contrast to the case for cadmium [Johansson and Pyykkö, 2004], the relative stabilities of the tetrahedral and Lennard-Jones isomers can not be related to the strong anisotropy of the bulk lattice, as this ratio is in fact larger for Hg than for Cd. However this could be explained by the earlier onset of metallicity in Cd clusters than in Hg ones, which means the physics of small Cd clusters may be closer to that of the bulk than is observed for

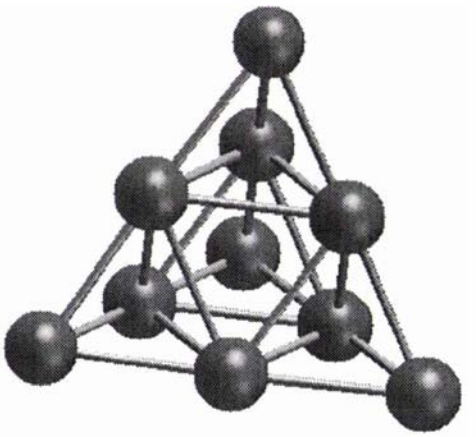

Figure 6.6: Tetrahedral Hg_{10}.

Isomer	BE	BE + ZPVE	r_{min}
Tetrahedral	-0.0502	-0.0487	3.4066
Lennard-Jones	-0.0528	-0.0513	3.4064
D_{3d} (from [Hartke et al., 2001])	-0.0499	-0.0484	3.4369

Table 6.4: A comparison of the PW91 structures for Hg_{10}. The binding energy (BE) and the binding energy with a zero-point vibrational correction (BE + ZPVE) are in a.u. and the minimum bond length (r_{min}) is in Ångstrøm.

Hg. Of course, the possibility remains that the true ground state for Cd_{10} may not have been found.

6.2 Energies

The energies of the small LJ clusters are plotted in Figures 6.7 and 6.8.

The LDA energies are as expected consistently overbinding, and show a much quicker convergence towards the bulk. The MP2 energies are of course better than DFT, but as for the dimer are expected to still be overbinding. The CCSD(T) values

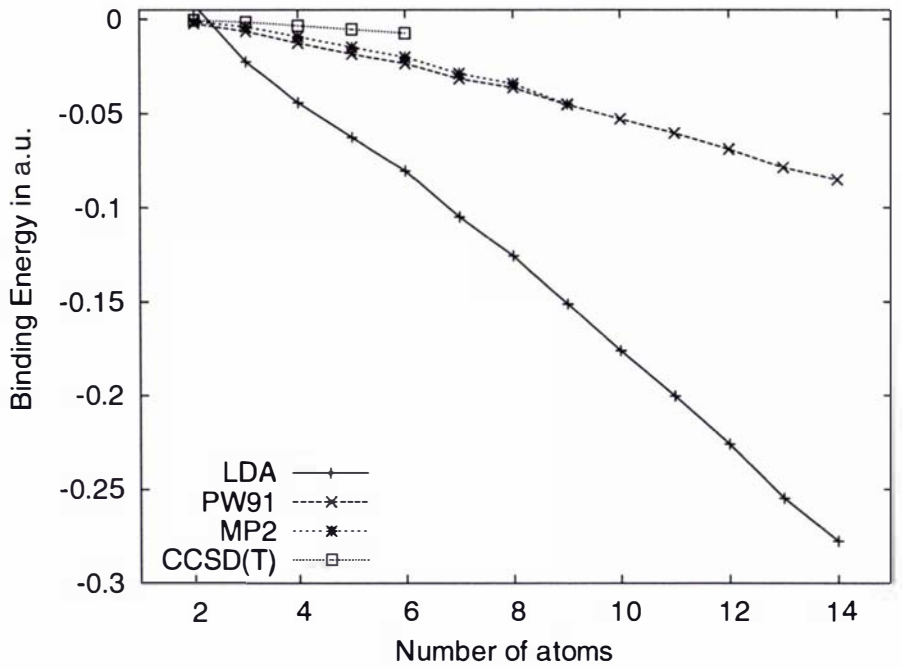

Figure 6.7: Total binding energy of LJ clusters.

are the most realistic. It is apparent that the binding in these clusters is much weaker, and only a slow progression towards stronger binding is observed for the small sizes calculated.

The isomers found by Hartke *et al* are compared with the standard LJ isomers in Figures 6.9 and 6.10. Although these isomers have been found not to be minima at $N = 7, 14$, the energies are included for reference. Figure 6.9 shows the evolution of the total binding energy with cluster size for each method. Figure 6.10 shows the energy difference between isomers. In all cases, the energy of the LJ isomer is lower, however there are a few cases (notably $N = 8$ and 9) where the energies are quite close. However for these sizes both structures are realistic possibilities for the ground state, of high symmetry. With the inclusion of a zero-point vibrational energy correction, the difference between the isomers remains essentially the same.

The qualitative agreement between methods (DFT, MP2, and CCSD(T)) is good. It is reassuring that despite the large differences shown here quantitatively in the energies produced by different methods, the optimised stuctures are consistently reproduced with a bond length scaled according to a characteristic bond length of the

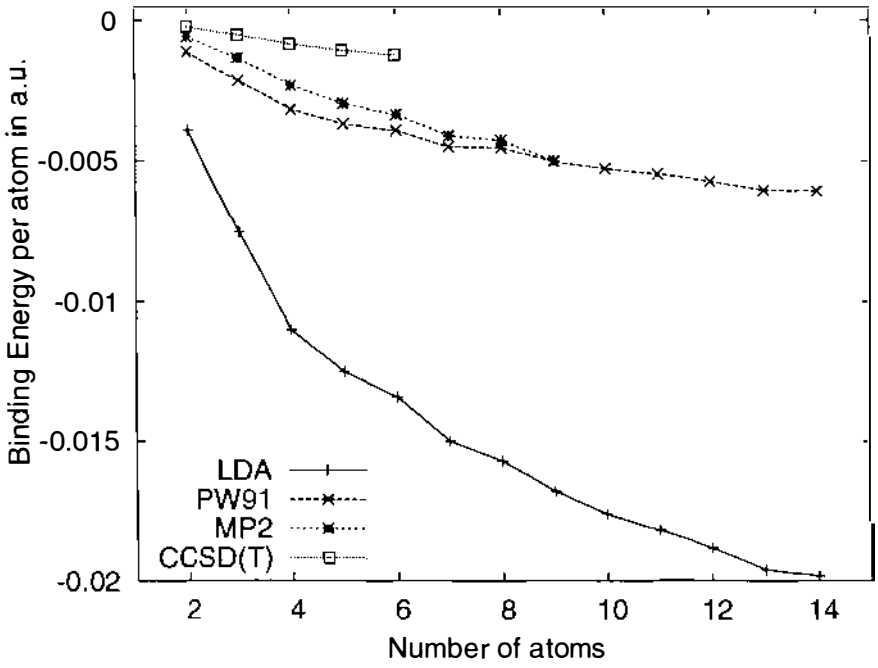

Figure 6.8: Binding energy of LJ clusters per atom.

method. This is shown in Figure 6.11, for the non-BSSE corrected calculations.

Figure 6.12 shows the correlation of energy with bond length for the LJ clusters up to $N = 14$. The LDA clusters all have close to a constant bond length, ranging between 3.0 and 3.2 Å. The PW91 and MP2 calculations find longer bond lengths than LDA, ranging between 3.3 and 3.8 Å for the range studied. The bond length decreases with N, as expected as the binding energy per atom is also increased. This decrease is much faster for MP2 than for PW91 though, such that these lines cross. The CCSD(T) calculations show the same trend of a sharp decrease in bond length, which levels out between 5 and 6 atoms. This is to be expected as the 5- and 6-atom clusters are the first which contain a second bond length within the cluster, which is necessarily larger than r_{min} and thus the average bond length is approximately maintained. The CCSD(T) bond lengths range from 3.9 to 4.1 Å for the clusters with $N < 7$.

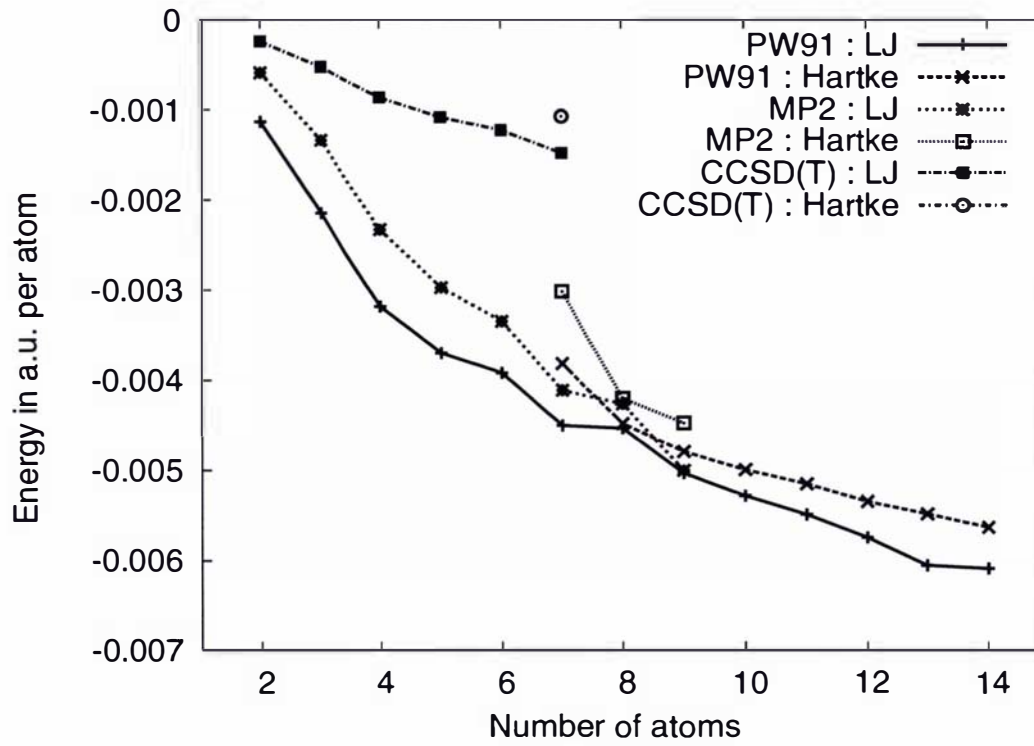

Figure 6.9: Binding energy (per atom) of LJ clusters compared with the Hartke low-symmetry isomers.

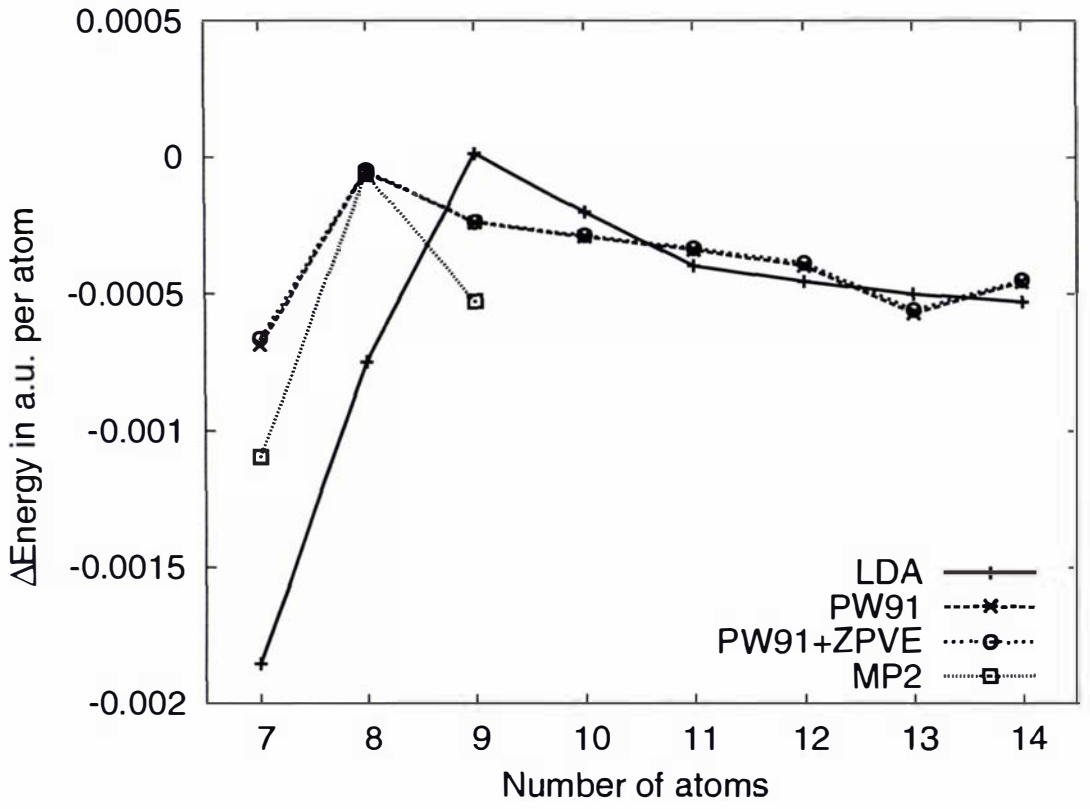

Figure 6.10: Binding energy difference between LJ clusters and Hartke isomers in a.u. per atom. A zero-point vibrational energy (ZPVE) correction is added to the PW91 energies for comparison, calculated in the harmonic approximation as $\sum_i \hbar\omega_i/2$. A negative energy difference means that LJ is the most stable arrangement.

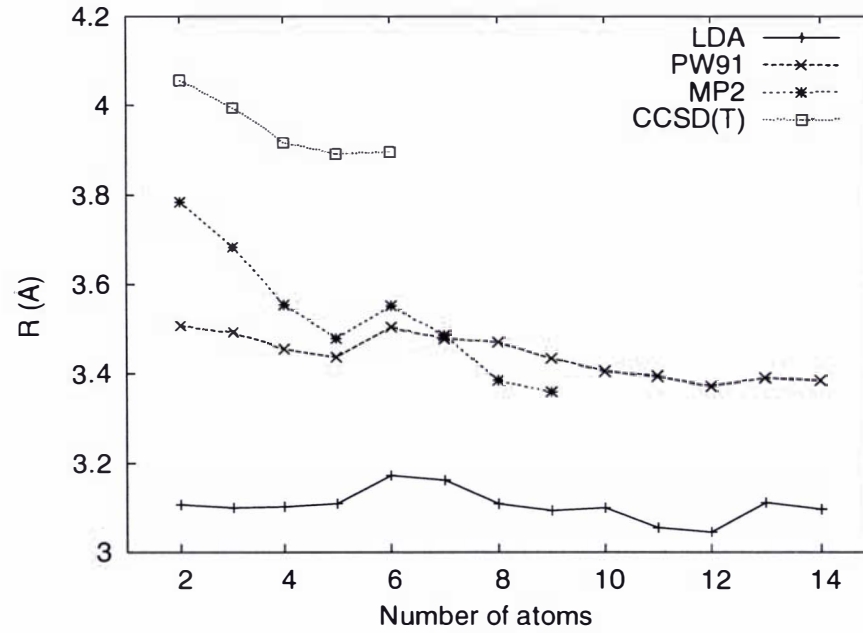

Figure 6.11: The dependence of the minimum bond length of LJ clusters on N.

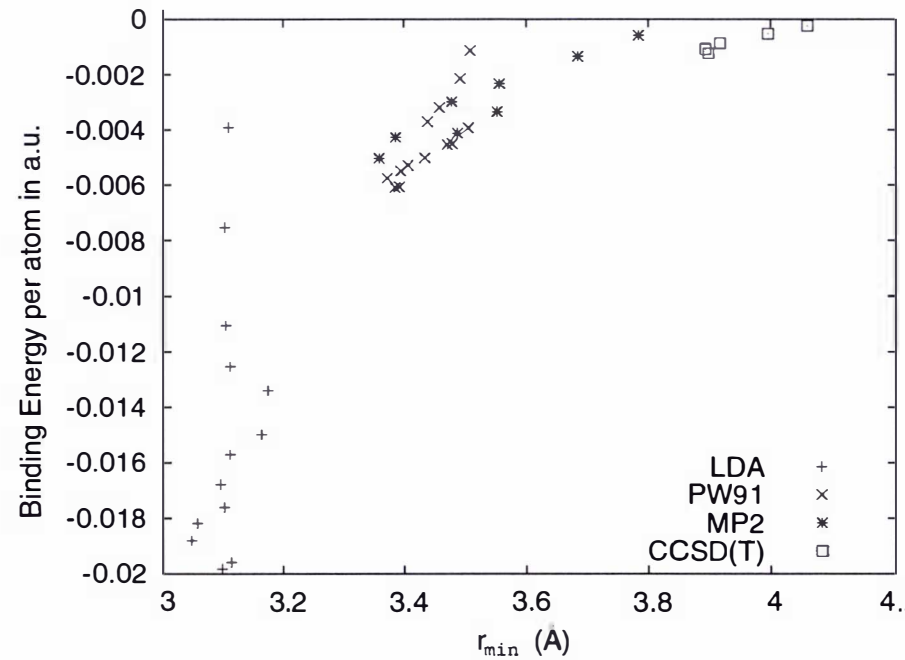

Figure 6.12: Binding energy per atom of LJ clusters correlated with the minimum bond length.

6.3 Frequencies

The vibrational frequencies were calculated for each isomer using both DFT methods (LDA and PW91), and also MP2. They are listed in the appendix C for the optimised isomers given above. Negative frequencies correspond to imaginary solutions, and so indicate the presence of a saddle point (at a specific level of theory) of the order of the number of negative vibrations. In physical terms this corresponds to an unstable molecule. All the Hartke isomers were optimised in either LDA or MP2 first, and then the frequencies were calculated at this stationary point. All the LJ isomers were found to be minima on the potential energy surface, with no unphysical frequencies of vibration. However of the Hartke isomers calculated, Hg_7 had 2 negative frequencies according to the LDA or PW91 calculation, and three according to MP2 (or two, one of which is doubly degenerate). For $N = 12$ and 13 also, the PW91 calculation found the Hartke isomers to be transition states. The others were all local minima. Therefore it seems reasonably clear that the true minimum energy structures are indeed the LJ isomers, although the alternative isomers are close in energy for the cases of $N = 8$ and $N = 9$.

There is more information than just the nature of a stationary point to be obtained from the calculated frequencies however. For example, the Debye temperature of a solid, Θ_D, is related to the cut off frequency in the Debye model ω_D by

$$\Theta_D = \frac{h}{k\omega_D} \tag{6.4}$$

and from it may be obtained the zero-point vibrational energy of a solid as

$$E_{\mathrm{ZPVE}} = \frac{9}{8} k\Theta_D. \tag{6.5}$$

Θ_D can be obtained by a measurement of the specific heat of a solid at very low temperature. The experimentally determined Debye temperature of mercury is 71.9 K. [van der Hoeven and Keesom, 1964] This gives a value of $E_{\mathrm{ZPVE}} = 56.2\ cm^{-1}$.

By summing over the vibrational frequencies obtained for each mercury cluster, the analogous quantity is obtained for finite sizes of mercury. Then by plotting against $N^{-1/3}$ we obtain a linear fit that gives the bulk limit at $\lim_{N\to\infty} N^{-1/3} = 0$. This is shown in Figure 6.13. It is clear that finite size effects are greatest for the smallest molecules, and the magic numbers show up again as peaks such as $N = 13$. By excluding $N < 14$, agreement with experiment is improved considerably, from 78.4 cm^{-1} to 67.3 cm^{-1}. If we take only the largest clusters with $N > 24$, remarkable

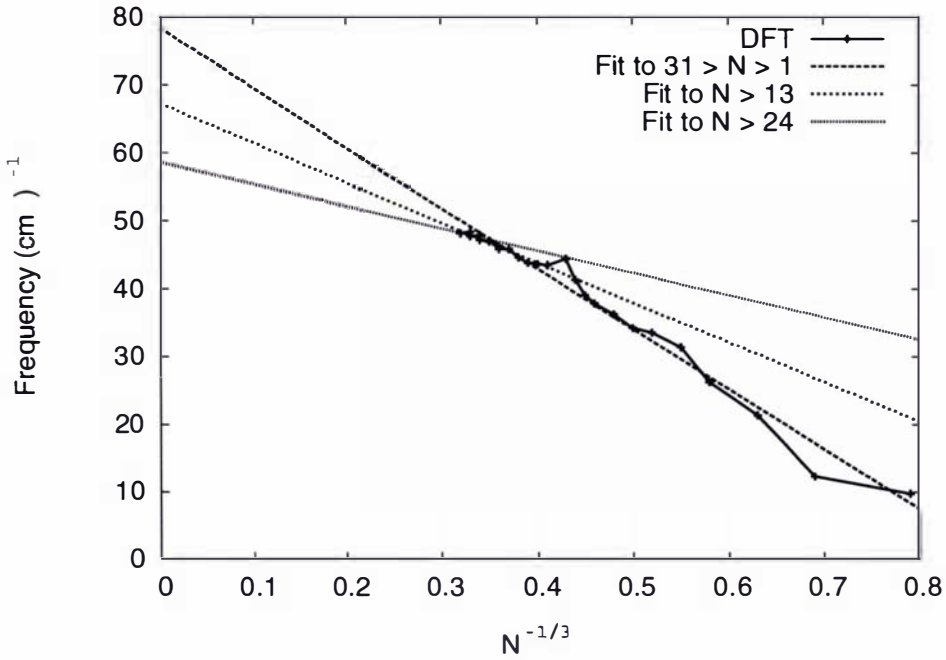

Figure 6.13: Extrapolation to the bulk limit E_{ZPVE}. The fit to $1 < N \leq 30$ gives $E_{\mathrm{ZPVE}} = 78.4\ cm^{-1}$, $13 < N \leq 30$ gives $E_{\mathrm{ZPVE}} = 67.3\ cm^{-1}$, and $24 < N \leq 30$ gives $E_{\mathrm{ZPVE}} = 58.7\ cm^{-1}$.

agreement with experiment is obtained ($E_{\mathrm{ZPVE}} = 58.7\ cm^{-1}$). Hence, the ZPVE can be successfully estimated from calculations of small to medium sized clusters.

6.4 Optimised structures and the basis set superposition error

As expected in analogy with noble gas clusters, the most stable isomers for small sizes of mercury cluster are the symmetric, LJ-type. The best description of their structure and energy is obtained using coupled cluster methods. However due to the limited size of the basis set available to CCSD(T) calculations, it is to be expected that the basis set superposition error (BSSE) is non-negligible. An estimate of the BSSE for the CCSD(T) clusters (2-6) was obtained by calculating the sum of the error in each pair interaction, according to the BSSE calculated for the dimer. The subsequent binding energies are given in Table 6.5, as is the BSSE correction. Another slightly smaller contribution to the binding energy is the spin-orbit (SO)

interaction, which has been approximated according to the equation in reference [Schwerdtfeger et al., 2001] taken from reference [Dolg and Flad, 1996] as

$$V_{SO} = -45.77254r^{-4.26957}e^{-0.67264r}. \tag{6.6}$$

Then the total energy (CCSD(T) energy + BSSE + SO) was optimised locally to give the best approximation of the actual binding of each cluster. The BSSE correction

N	r'	BE	BSSE	SO	BE(+ BSSE + SO)
2	4.352	-0.000418	-0.000276	-0.000022	-0.000165
3	4.289	-0.001360	-0.000911	-0.000078	-0.000527
4	4.289	-0.002800	-0.002068	-0.000189	-0.000921
5	4.173	-0.004670	-0.003251	-0.000304	-0.001722
6	4.158	-0.006483	-0.004508	-0.000421	-0.002396

Table 6.5: The effect of the basis set superposition error and spin-orbit interaction, estimated for $N = 2-6$. r' is the bond length obtained when the cluster is optimised with respect to the total (CCSD(T)+BSSE+SO) energy, and is in Å. All energies are in a.u.

worsens the agreement with experiment for the dimer, making the bond lengths considerably too long. However it may be taken as an upper bound on the error induced by this basis set. This does mean that the errors in both bond lengths and energies are somewhat greater than desired. However it does not indicate any reason to doubt the relative ordering of different isomers.

A final comparison of the energies and bond lengths of mercury clusters (N = 2-6) obtained with different methods is given in Table 6.6. It is interesting that the ansatz of Hartree-Fock plus two-body correlation potential compares well with the best known results to date, which are those of Dolg. In contrast the CCSD(T) results presented here suffer from the restricted size of the basis set used and are under-bound.

6.5 Polarisabilities

Polarisabilities are perhaps one useful experimental means of distinguishing between different isomers. The choice of basis set is particularly sensitive for polarisability calculations, but in order to extend these calculations to larger cluster sizes, the size of the basis set still had to be kept minimal. The various basis sets discussed in Chapter 2 give widely differing results. The PW91 values are given in Table 6.7. The experi-

N	r_e				BE			
	CC′	Dolg	HFC	2+3n	CC′	Dolg	HFC	2+3n
2	4.352	3.75	3.762	3.690	-0.00042	-0.00169	-0.00170	-0.00165
3	4.289	3.51	3.542	3.612	-0.00136	-0.00673	-0.00630	-0.00636
4	4.289	3.35	3.359	3.398	-0.00380	-0.01735	-0.01640	-0.01481
5	4.173	3.44	3.438	3.361	-0.00467	-0.02554	-0.02300	-0.02308
6	4.158	3.52	3.501		-0.00648	-0.02911	-0.02820	

Table 6.6: Binding energies (BE) in a.u. and bond lengths (r_e) in Å of mercury clusters (N = 2-6) obtained with different methods. The CC′ results are the CCSD(T)+BSSE+SO results of Table 6.5, the Dolg results are the CCSD(T) results of [Dolg and Flad, 1997], the HFC results are the Hartree-Fock + 2-body correlation results of Chapter 5, and the 2+3n results are the simulated annealing results of [Moyano et al., 2002].

small	large	small+spf	solid	expt
15.51	34.61	32.99	26.63	33.92

Table 6.7: The PW91 atomic polarisability for Hg as obtained using varying basis sets. Small+spf refers to the basis set given in Table 6.8. The large and small basis sets are given in Chapter 2, and the experimental value is from [Goebel and Hohm, 1996].

mental atomic polarisability of Hg is 33.92 a.u., taken from [Goebel and Hohm, 1996].

The small correlation consistent basis set optimised for the CCSD(T) calculations was improved for polarisability calculations by the addition of diffuse s- and p-functions, and an extra f-function. This is given in Table 6.8. The size of this basis set, coupled with its good performance with respect to the atomic polarisability means that these calculations can be extended to reasonably large sizes. Figure 6.14 confirms that there is reasonable agreement between the clusters with $N = 2 - 6$ when the optimisation is done using the large basis set, and with the small basis set so long as the polarisability is subsequently calculated with the small+spf basis set. The polarisabilities shown are the isotropic (spherically averaged) polarisabilities. It should be noted that at the atomic level the large basis overestimates the polarisability by 0.6 a.u., the small+spf basis underestimates it by 1 a.u., and thus the errors are of comparable magnitude.

Figure 6.15 compares the polarisability per atom of each of the Hartke isomers with the corresponding LJ isomer. Clearly the average polarisability per atom of the

	Exponent	Coefficient
S		
	19.457400988	-0.055290570
	11.698223047	0.396066986
	6.249682087	-0.858130000
	0.609577831	1.000000000
	1.349764795	1.000000000
	0.10864663	1.000000000
	0.02800000	1.000000000
P		
	14.68454311	0.024149244
	5.63966466	-0.207870000
	1.86439764	1.000000000
	0.77734565	1.000000000
	0.22728859	1.000000000
	0.06500000	1.000000000
D		
	5.67006804	-0.065949240
	1.91272470	0.389200000
	0.76681308	1.000000000
	0.25285570	1.000000000
F		
	1.13765269	0.050000000
	1.90000000	0.295000000

Table 6.8: The polarisability basis set for Hg (small+spf).

Hartke structures is higher, due to the lower symmetry and less compact arrangement. The difference is consistently about 1 a.u. per atom, with the exceptions of $N = 10$, where the isomers have almost exactly equal polarisabilities per atom, and $N = 13$, where the difference is almost 2.5 a.u. per atom. This maximum difference seen for $N = 13$ is due to the particularly high symmetry of the icosahedral LJ cluster, which results in a lower than otherwise expected polarisability. However even this difference is still only approximately 30 a.u., i.e. about 7% of the total polarisability value for $N = 13$.

In Figure 6.16 are plotted the polarisability per atom of all clusters $N = 1 - 24$ where the structures are all optimised using PW91 from the LJ minimum energy structure. Clear 'magic numbers' are seen at $N = 6, 8, 13, 19, 23$. These correspond to the most symmetric structures, the $N = 6$ octahedron, $N = 8$ D_{2d} structure (based on the octahedron), and the icosahedral structures for $N = 13, 19$ and 23. This is in

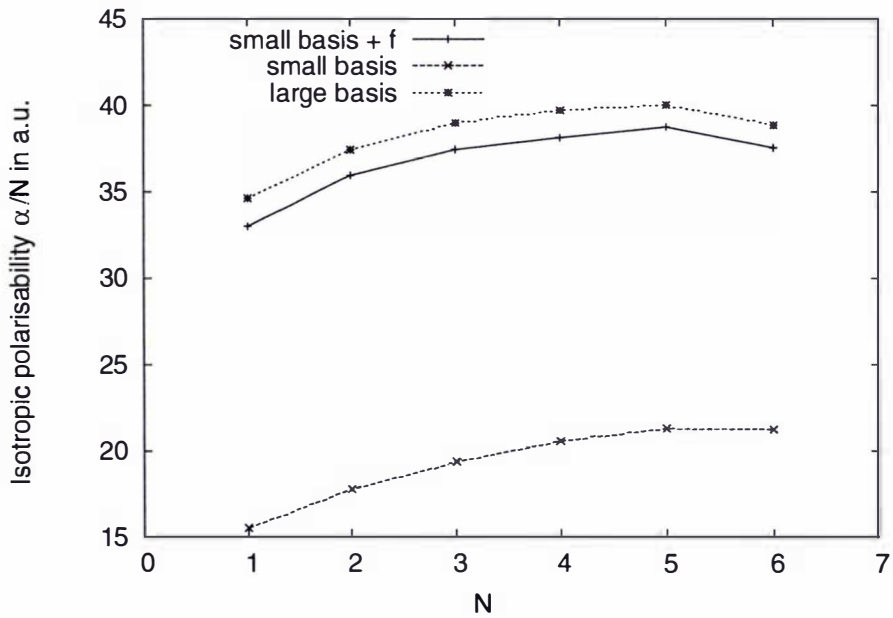

Figure 6.14: A comparison of the PW91 polarisabilities per atom for $N = 1 - 6$ calculated with different basis sets.

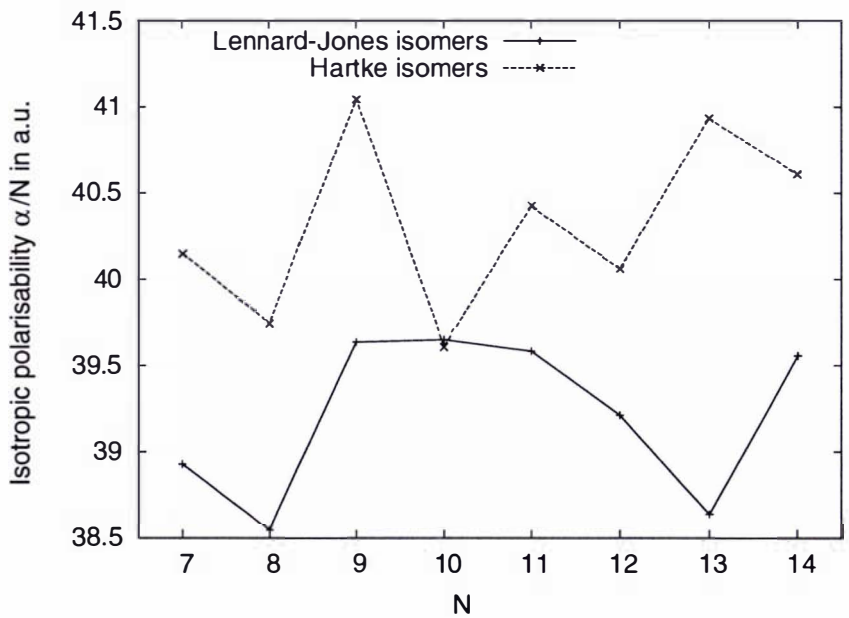

Figure 6.15: A comparison of the PW91 polarisabilities per atom of different isomers for $N = 7 - 14$.

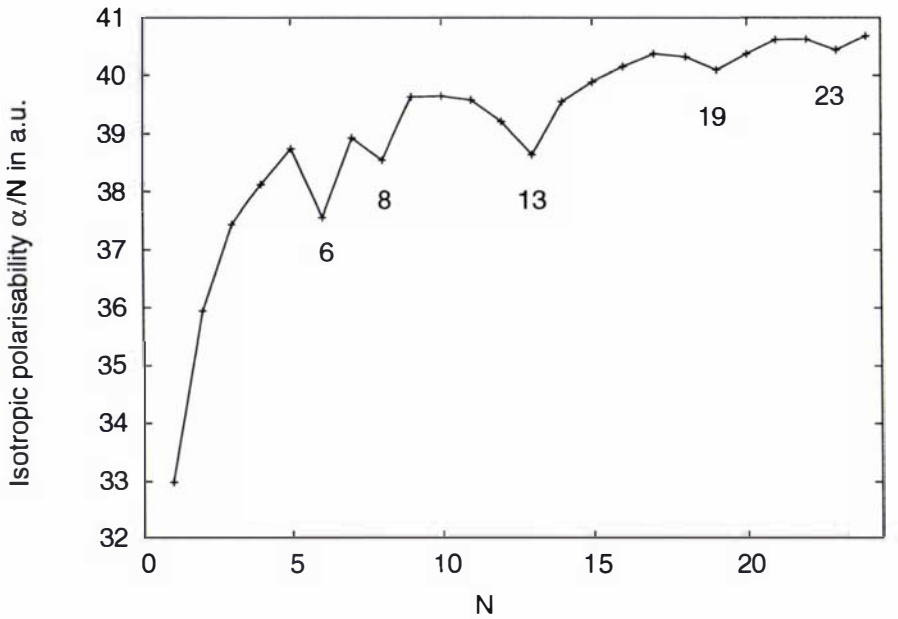

Figure 6.16: The isotropic polarisabilities (per atom) of LJ clusters, calculated with PW91. The 'magic numbers' corresponding to highly symmetric structures are marked.

precise agrement with the 'magic numbers' found previously [Moyano et al., 2002]. These numbers are even more pronounced in the plot of the change in polarisability from $N \rightarrow N + 1$. In Figure 6.17 are shown these changes for the Lennard-Jones isomers. In Figure 6.18 are shown the same changes for the Hartke isomers. Here a large difference is seen, especially at $N = 7$ where the Hartke isomer is strangely non-compact, and at $N = 10$ and 13 where the symmetric, compact LJ structures are in particular contrast to the disordered Hartke structures. For $N = 8$ and 9, the Hartke structures are reasonably symmetric and compact and thus agree approximately with the LJ structures. However the overall trend is clearly quite different.

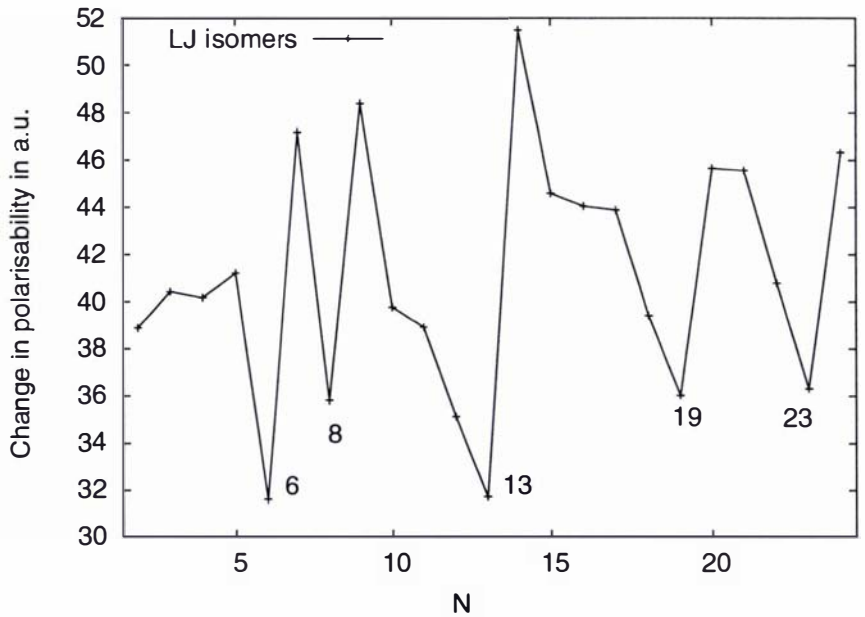

Figure 6.17: The change in polarisability as $\alpha(N) - \alpha(N-1)$ of LJ clusters, calculated with PW91. The 'magic numbers' corresponding to highly symmetric structures are marked.

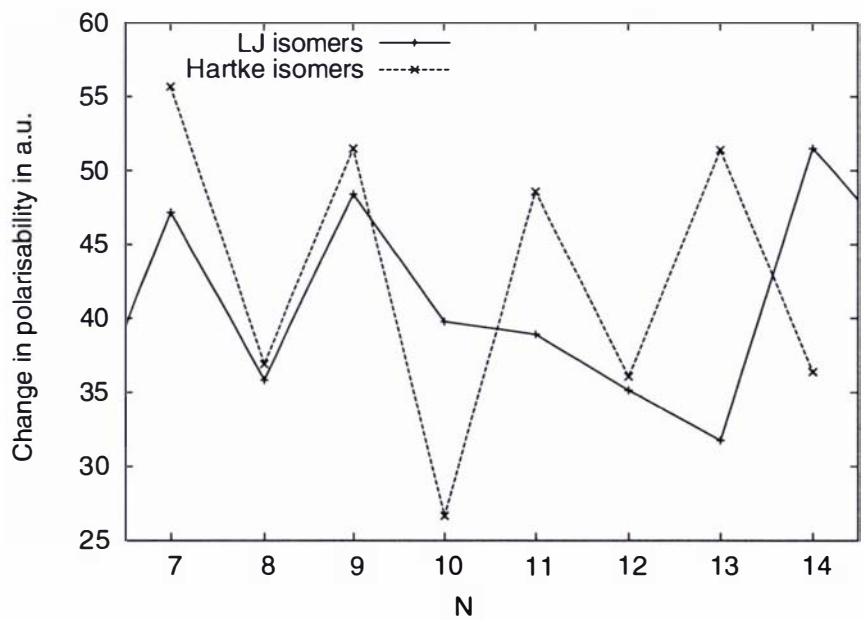

Figure 6.18: The change in polarisability as $\alpha(N) - \alpha(N-1)$ of Hartke clusters compared to the LJ clusters. The calculations were done using PW91.

Chapter 7

Cationic Clusters

The effect of a positive or negative charge on a cluster can be very important. The geometric structure may change completely, and especially in the case of mercury and other closed-shell atoms, there is a large difference due to the switch from van der Waals to covalent and ionic bonding due to charge-induced dipole interactions. The absorption spectra and fragmentation of mass-selected cationic clusters of noble gas and mercury atoms have been measured by Bernd von Issendorff [von Issendorff, 1994, Haberland et al., 1992]. The photofragmentation spectra show

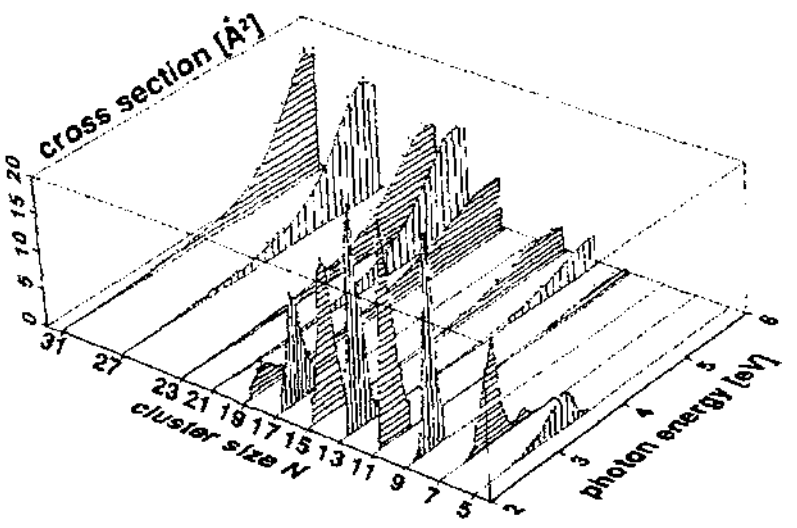

Figure 7.1: The photoabsorption spectra of doubly charged mercury clusters (reproduced from reference [Haberland et al., 1992]).

a transition between the size range $N = 3 - 6$ and $N = 7 - 30$ for the singly charged cations and at a larger size for the doubly charged cations as shown in Figure 7.1.

The small sizes show a strong absorption consisting of several individual peaks between 3-4 eV; the energy decreases with size. This is assigned by the experiment to the *s-p* transition. From $N = 5$ a second absorption is observed at higher energy, which eventually (at $N = 7, 8$) becomes dominant. This absorption is essentially size-independent, and from $N = 5$ to the largest sizes considered has a peak at constant energy within experimental error (5.75 eV).

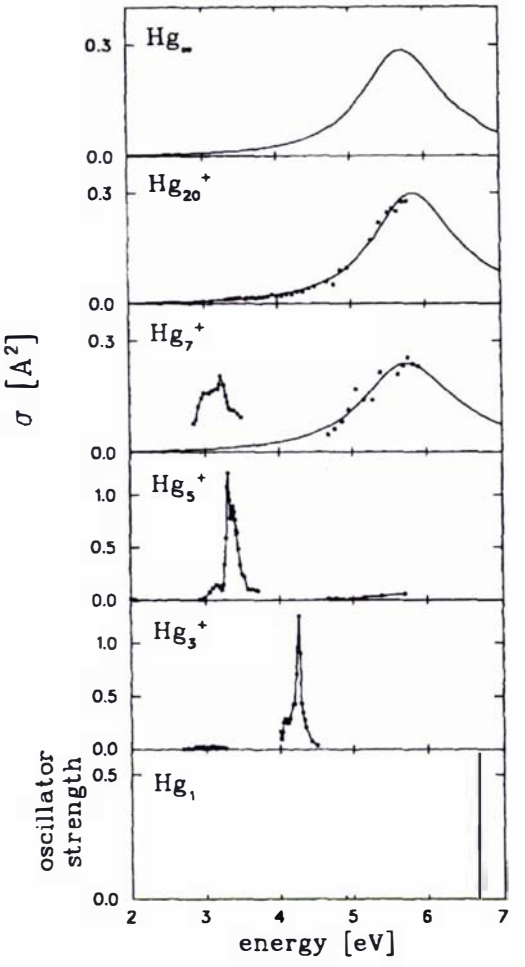

Figure 7.2: The photoabsorption spectra of selected singly charged charged mercury clusters compared to the calculated bulk plasmon (top) (reproduced from reference [Haberland et al., 1992]

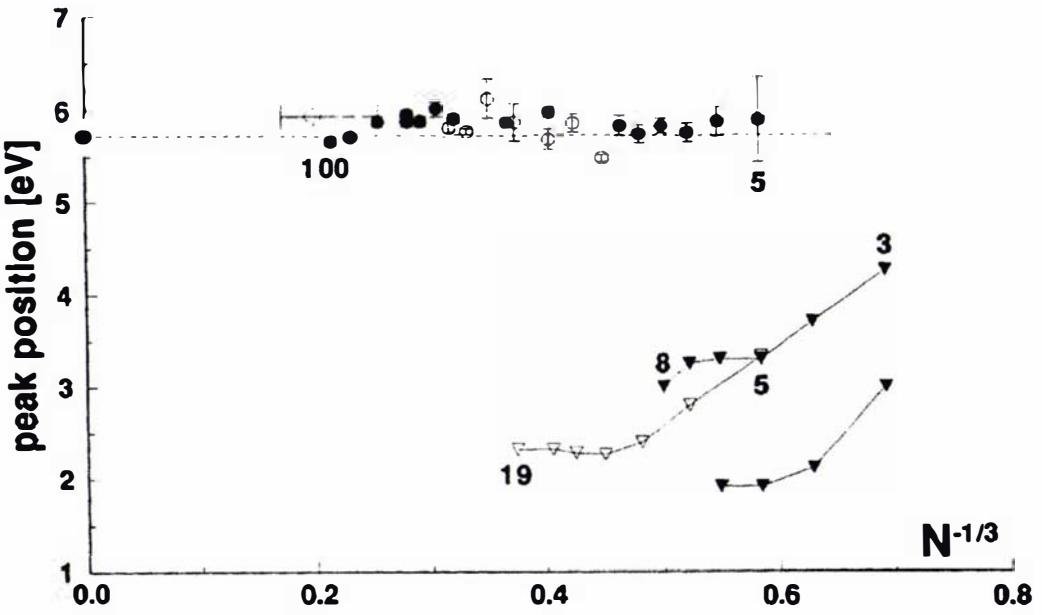

Figure 7.3: The photoabsorption energies of charged mercury clusters (reproduced from reference [Haberland et al., 1992]. The closed symbols are the singly charged clusters and the open symbols are the doubly charged clusters. The triangles are the low energy absorption assigned to the *s-p* excitations, and the circles represent the plasmon-like size-independent transition.

The question is whether this results from a structural transition at these sizes, or is a more complicated manifestation of the underlying electronic structure.

The structures of the small cationic clusters of mercury have been optimised, completely analogously to the neutral clusters, i.e. using the same basis sets and methodologies.

7.1 Isomers and relative stabilities

The structures of the Hg cationic clusters were optimised using DFT (LDA and PW91), and MP2. The global minimum structures obtained with LDA, PW91 and MP2 are pictured in Figure 7.4.

The associated binding energies and minimum bond lengths are given in Tables 7.1, 7.2, and 7.3. The PW91 and LDA functionals give similar results for most sizes in this range. LDA gives typically shorter bond-lengths, but they both find planar

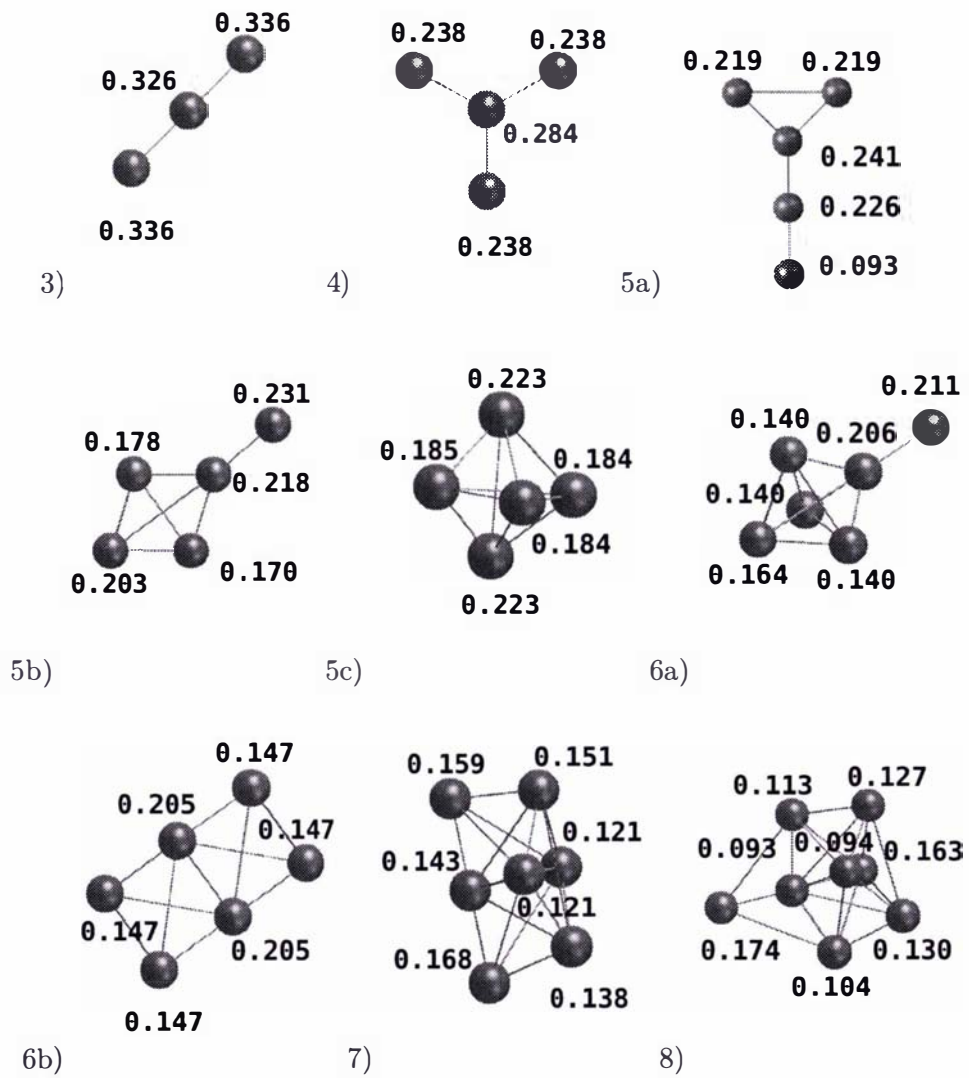

Figure 7.4: The cation structures obtained with DFT (LDA, PW91) and MP2. For $N = 5$ and 6 the global minimum depends on the method used. 5a) is found by PW91 and MP2, while 5b) is preferred by LDA. 6a) is the global minimum for LDA and MP2, while 6b) is more stable in the PW91 calculation. The Mulliken charges obtained from the PW91 calculation are printed next to each atom. The figure continues on the next page.

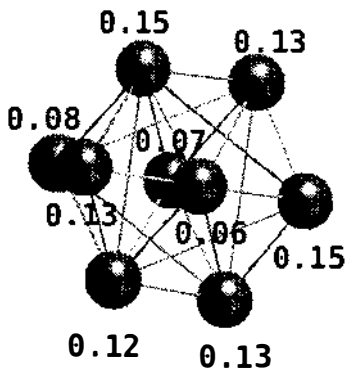

9)

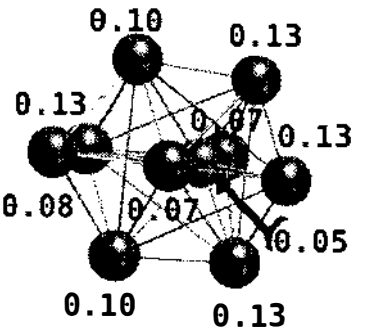

10)

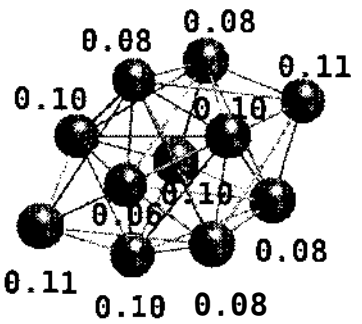

11)

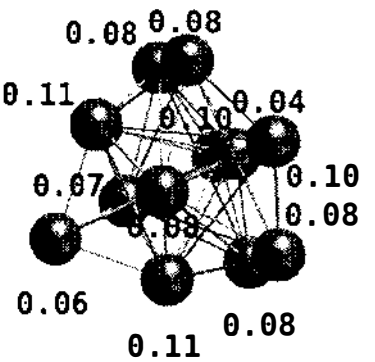

12)

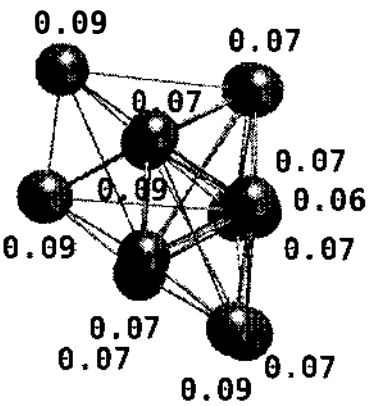

13)

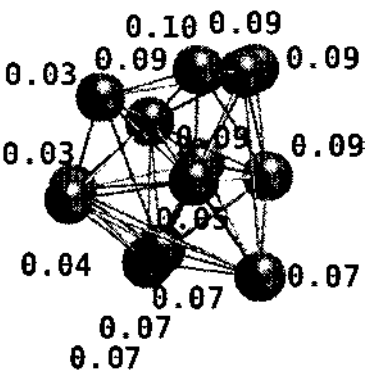

14)

N	Symmetry	Binding Energy	BE/N	r_{min}
2	$D_{\infty h}$	-0.0789164	-0.0394582	2.7463
3	$D_{\infty h}$	-0.1277453	-0.0425818	2.7562
4	D_{3h}	-0.1521128	-0.0380282	2.8062
5	C_{2v}	-0.1831797	-0.0366359	2.8079
6	C_s	-0.2104255	-0.0350709	2.8895
7	C_s	-0.2390643	-0.0341520	2.9041
8	C_1	-0.2604754	-0.0325594	2.8287
9	C_1	-0.2939036	-0.0326560	2.9677
10	C_1	-0.3102501	-0.0310250	2.8935
11	C_1	-0.3481526	-0.0316502	2.9626
12	C_1	-0.3761826	-0.0313485	2.9675
13	C_1	-0.3981801	-0.0306292	2.9630
14	C_1	-0.4299537	-0.0307110	2.9020

Table 7.1: LDA optimised Hg cations.

N	Symmetry	Binding Energy	BE/N	r_{min}
2	$D_{\infty h}$	-0.0671484	-0.0335742	2.8683
3	$D_{\infty h}$	-0.1044206	-0.0348069	2.8830
4	D_{3h}	-0.1202255	-0.0300564	2.9490
5	C_{2v}	-0.1386702	-0.0277340	2.8808
6	C_s	-0.1495853	-0.0249309	3.0755
7	C_s	-0.1592170	-0.0227453	3.0903
8	C_1	-0.1689243	-0.0211155	3.0302
9	C_1	-0.1788258	-0.0198695	3.1363
10	C_1	-0.1865467	-0.0186547	3.0785
11	C_1	-0.2021164	-0.0183742	3.1740
12	C_1	-0.2096254	-0.0174688	3.1780
13	C_1	-0.2193009	-0.0168693	3.2078
14	C_1	-0.2286439	-0.0163317	3.1342

Table 7.2: PW91 optimised Hg cations.

structures for the smallest sizes, and switch to 3d structures as the number of atoms increases. However for $N = 5$ they disagree on the exact structure found, PW91 finding the isomer of Hg_4^+ with the extra atom bound to one of the outer atoms, while LDA prefers the isomer where the new atom bridges two of the outer atoms. For $N = 6$ also, LDA finds that a three dimensional structure is more stable, whereas PW91 still prefers a planar isomer. From $N = 7$ onwards, there is agreement at least on the three-dimensional nature of the preferred isomers. The same structural motifs

are observed for all methods, and although for the larger sizes it is of course much less certain that these are the true minimum energy structures, these are at least local minima and probably closely related to the true ground state.

MP2 calculations do not support either of the density functionals used over the other. For $N = 5$ MP2 favours the same isomer as PW91, over the LDA isomer and a three dimensional structure. However for $N = 6$, MP2 agrees with LDA and finds the 3 dimensional isomer to be the most stable. As N increases and the system approaches the metallic state, single reference MP2 will eventually fail.

N	Symmetry	Binding Energy	BE/N	r_{min}
2	$D_{\infty h}$	-0.0521886	-0.0260943	2.7528
3	$D_{\infty h}$	-0.0811579	-0.0270526	2.7858
4	D_{3h}	-0.0929304	-0.0232326	2.8596
5	C_{2v}	-0.1069348	-0.0213869	2.7561
6	C_s	-0.1178667	-0.0196444	2.8781
7	C_1	-0.1293034	-0.0184719	3.0041
8	C_s	-0.1410310	-0.0176289	2.9261
9	C_1	-0.1533622	-0.0170402	3.0448

Table 7.3: MP2 optimised Hg cations.

The energy differences between isomers are on the milli-Hartree scale ($\simeq$ 0.03 meV). The binding energies of the different isomers found for Hg_5^+ are shown in Table 7.4.

Isomer	LDA	PW91	MP2
a	-0.1820	-0.1387	-0.1069
b	-0.1832	-0.1362	-0.1044
c	-0.1831	-0.1313	-0.1038

Table 7.4: A comparison of binding energies for the different Hg_5^+ isomers. The labelling is as in Figure 7.4, binding energies are in a.u.

Classically one would expect the charge on a metallic cluster to sit on the outside, although perhaps a classical electrostatic model is not the best model for the planar clusters shown here. In particular, the isomers 4 and 5a contain most of the charge on the central atom, according to the Mulliken charge analysis. This implies that this configuration maximises the charge-induced dipole interactions which bind these clusters. It also indicates that perhaps a classical electrostatic model is inappropriate for these small, planar clusters, although it works better for the larger sizes, such as

Hg_{14}^{+}, where indeed the atoms containing the most charge are sitting on the outside of the cluster.

7.2 Absorption spectra and CIS(D) calculations.

CIS(D) calculations are able to determine not only the energies associated with the electronic transitions within the molecule, but also which of these will be observed, by calculation the oscillator strength of each excitation. More detail is given in reference [Head-Gordon et al., 1994], and only a brief sketch of the method is given here.

Configuration interaction (CI) calculations include all excited states in the wavefunction by taking the linear combination of all possible N-electron Slater determinants,

$$|\Psi\rangle = c_0 |\Phi_0\rangle + \sum_{ra} c_a^r |\Phi_a^r\rangle + \sum_{\substack{a<b \\ r<s}} c_{ab}^{rs} |\Phi_{ab}^{rs}\rangle + \sum_{\substack{a<b<c \\ r<s<t}} c_{abc}^{rst} |\Phi_{abc}^{rst}\rangle + \dots \tag{7.1}$$

where r, s, t label ground state occupied orbitals from which electrons may be excited to virtual orbitals labelled a, b, c. In a complete basis, the complete series found by continuing equation (7.1) up to the maximum number of possible excitations will be exact. Brillouin's theorem states that there is no direct interaction between the single excitations and the ground state, meaning that all terms of the form

$$\langle \Phi_0 | \hat{H} | \Phi_a^r \rangle = 0. \tag{7.2}$$

Therefore truncating the CI expansion after single excitations leaves only the matrix elements

$$\langle \Phi_0 | \hat{H} | \Phi_0 \rangle \tag{7.3}$$

and

$$\langle \Phi_a^r | \hat{H} | \Phi_a^r \rangle \tag{7.4}$$

remaining.

While the single excitations have very little effect on the energy of the ground state and are basically of HF quality, they are the main contributors to the observed excited states. However for an accurate description of the transition energies double

excitations should also be included. Then the CI matrix is:

$$\begin{bmatrix} \langle\Phi_0|\hat{H}|\Phi_0\rangle & 0 & \langle\Phi_0|\hat{H}|\Phi_{ab}^{rs}\rangle \\ 0 & \langle\Phi_a^r|\hat{H}|\Phi_a^r\rangle & \langle\Phi_a^r|\hat{H}|\Phi_{ab}^{rs}\rangle \\ \langle\Phi_{ab}^{rs}|\hat{H}|\Phi_0\rangle & \langle\Phi_{ab}^{rs}|\hat{H}|\Phi_a^r\rangle & \langle\Phi_{ab}^{rs}|\hat{H}|\Phi_{ab}^{rs}\rangle \end{bmatrix} \tag{7.5}$$

7.2.1 Basis set effects

In Table 7.5 are given the CIS excitation energies and oscillator strengths of Hg_3^+ as calculated with two different basis sets. The 'small' basis set is the correlation consistent small basis set given in Chapter 2; the 'small+spf' basis is the same basis with additional s, p, and f-functions that was used for the polarisability calculations in Chapter 6. It is clear from this simple comparison that the diffuse functions

	small basis set		small+spf basis set	
	CIS Energy (eV)	Osc. Str.	CIS Energy (eV)	Osc. Str.
1	3.2366	0.3704	2.9387	0.0018
2	5.0091	0.0000	3.2841	0.0028
3	5.9509	1.8092	3.2841	0.0028
4	7.4201	0.0005	4.1369	1.9648
5	7.4201	0.0005	4.3100	0.0000
6	7.7414	0.0000	4.3100	0.0000
7	8.2803	0.0000	4.6573	0.0000
8	8.2803	0.0000	5.1508	0.0349
9	8.5750	0.0000	5.1508	0.0349
10	8.7906	0.0367	5.4936	0.0000
11	8.7906	0.0367	5.4936	0.0000
12	9.0183	0.0000	6.1098	0.0000

Table 7.5: The excitation energies and oscillator strengths of Hg_3^+, as calculated with two different basis sets.

are very important, and lower the energy of the excitation spectrum considerably. Moreover the oscillation strengths are severely affected, although the overall pattern of a strong excitation at low energies and a very weak excitation at higher energies is reproduced for Hg_3^+. Therefore the small+spf basis was used for all the CIS, CIS(D)

and SAC-CI results in this Chapter.

7.2.2 Excitation energies

All calculated excitation energies were based on the global minimum structure found in the MP2 calculations. Thus Hg_5^+ is assumed to be planar (structure a) and Hg_6^+ is 3-dimensional. In Tables 7.6, 7.7, and 7.8 are given the CIS and CIS(D) excitation energies and the oscillator strengths for Hg_3^+, Hg_4^+, and Hg_5^+. These are the minimum energy (planar) isomers. The excitation energies were calculated for each size over the range for which excitations were experimentally observed. For $N > 4$, this means up to 5.8 eV.

For the 3-dimensional Hg_6^+, Hg_7^+ and Hg_8^+, the excitation energies are given in Tables 7.9 and 7.10. For $N = 7$ and 8 only the CIS calculation was performed.

	CIS Energy (eV)	CIS(D) Energy (eV)	Oscillator Strength
1	2.939	2.816	0.002
2	3.284	3.704	0.003
3	3.284	3.704	0.003
4	4.137	4.290	1.965
5	4.310	4.912	0.000
6	4.310	4.912	0.000
7	4.657	4.616	0.000
8	5.151	5.869	0.035
9	5.151	5.869	0.035
10	5.494	5.849	0.000
11	5.494	5.849	0.000
12	6.110	5.887	0.000

Table 7.6: The excitation energies and oscillator strengths of Hg_3^+.

	CIS Energy (eV)	CIS(D) Energy (eV)	Oscillator Strength
1	2.767′	2.862	0.000
2	2.843	3.237	0.006
3	3.468′	3.597	0.409
4	4.070′	4.738	0.000
5	4.291	4.664	0.000
6	4.292	4.992	0.000
7	4.437′	4.927	0.515
8	4.896	5.676	0.013

Table 7.7: The excitation energies and oscillator strengths of Hg_4^+. A ′ denotes a 2-fold degeneracy in the excitation.

	CIS Energy (eV)	CIS(D) Energy (eV)	Oscillator Strength
1	2.521	2.924	0.001
2	2.525	2.611	0.054
3	2.597	2.925	0.000
4	2.989	3.161	0.091
5	3.355	3.409	1.598
6	3.426	3.966	0.005
7	3.685	4.177	0.068
8	3.759	4.494	0.000
9	3.781	4.221	0.011
10	4.013	4.480	0.791
11	4.099	4.801	0.035
12	4.254	4.993	0.000
13	4.486	4.802	0.010
14	4.559	5.161	0.126
15	4.806	5.065	0.039
16	4.834	5.594	0.015
17	4.839	4.824	0.003
18	4.909	5.248	0.000
19	5.308	5.629	0.332
20	5.486	5.724	0.425
21	5.558	5.407	0.114
22	5.654	5.615	0.000
23	5.694	5.814	0.160
24	5.722	5.824	0.000

Table 7.8: The excitation energies and oscillator strengths of Hg_5^+.

	CIS Energy (eV)	CIS(D) Energy (eV)	Oscillator Strength
1	2.433	2.420	0.005
2	2.495	2.842	0.000
3	2.495	2.843	0.000
4	2.666	2.740	0.184
5	2.878	2.926	0.028
6	2.878	2.927	0.028
7	3.182	3.611	0.015
8	3.182	3.611	0.015
9	3.518	4.071	0.280
10	3.763	4.354	0.004
11	3.763	4.354	0.004
12	3.880	4.196	0.041
13	3.950	4.728	0.000
14	4.168	4.648	0.053
15	4.168	4.648	0.053
16	4.208	4.374	0.505
17	4.325	4.835	0.018
18	4.326	4.835	0.018
19	4.502	4.716	0.026
20	4.502	4.716	0.027
21	4.777	5.170	0.011
22	4.777	5.170	0.011
23	4.794	4.976	0.940
24	4.885	5.013	0.002
25	4.885	5.013	0.002
26	4.974	5.276	0.001
27	5.187	5.520	0.000
28	5.303	5.306	0.004
29	5.303	5.306	0.004
30	5.305	4.889	0.104
31	5.332	5.472	0.000
32	5.396	5.521	0.312
33	5.396	5.521	0.313
34	5.483	5.458	0.060
35	5.483	5.458	0.060
36	5.543	5.488	0.528
37	5.691	5.384	0.016
38	5.691	5.383	0.016
39	5.813	5.464	0.000
40	5.860	5.681	0.003
41	5.861	5.681	0.002
42	5.875	5.557	0.433

Table 7.9: The excitation energies and oscillator strengths of Hg_6^+.

	CIS Energy (eV)	Osc. Str.		CIS Energy (eV)	Osc. Str.
1	2.121	0.000	31	4.692	0.000
2	2.262	0.058	32	4.753	0.075
3	2.282	0.038	33	4.849	0.014
4	2.377	0.070	34	4.944	0.003
5	2.379	0.028	35	4.996	0.047
6	2.486	0.000	36	5.067	0.447
7	2.627	0.003	37	5.081	0.003
8	2.916	0.026	38	5.101	0.006
9	3.071	0.001	39	5.163	1.262
10	3.278	0.000	40	5.207	0.210
11	3.359	0.043	41	5.312	0.006
12	3.400	0.000	42	5.343	0.029
13	3.488	0.000	43	5.344	0.001
14	3.646	0.000	44	5.358	0.308
15	3.766	0.039	45	5.434	0.099
16	3.942	0.002	46	5.491	0.175
17	3.952	0.003	47	5.572	0.000
18	4.067	0.025	48	5.597	1.092
19	4.110	0.014	49	5.656	0.102
20	4.134	0.000	50	5.730	0.109
21	4.189	0.000	51	5.735	0.000
22	4.277	0.012	52	5.754	0.258
23	4.392	0.023	53	5.837	0.099
24	4.411	0.022	54	5.864	0.004
25	4.431	0.000	55	5.923	0.002
26	4.460	0.000	56	6.028	0.000
27	4.466	0.083	57	6.092	1.594
28	4.555	0.003	58	6.196	0.062
29	4.584	0.000	59	6.224	0.105
30	4.663	0.023	60	6.315	0.000

Table 7.10: The excitation energies and oscillator strengths of Hg_7^+.

	CIS Energy (eV)	Osc. Str.		CIS Energy (eV)	Osc. Str.
1	2.1400	0.0003	41	4.9517	0.1824
2	2.1887	0.0134	42	5.0393	0.1042
3	2.3477	0.0049	43	5.1410	0.0436
4	2.4583	0.0463	44	5.1479	0.6716
5	2.6041	0.0000	45	5.1730	0.0000
6	2.6562	0.0864	46	5.2045	0.2736
7	2.6987	0.0341	47	5.2222	0.1050
8	2.8227	0.1068	48	5.2717	0.4969
9	2.8886	0.0198	49	5.2810	0.3722
10	3.0844	0.0279	50	5.2941	0.3895
11	3.2639	0.0005	51	5.3007	0.1056
12	3.4195	0.0000	52	5.3413	0.2071
13	3.4509	0.0269	53	5.4261	0.0000
14	3.5378	0.1619	54	5.4711	0.0350
15	3.6782	0.0001	55	5.5277	0.1705
16	3.7534	0.0002	56	5.5754	0.0524
17	3.7991	0.0481	57	5.6082	0.0641
18	3.8878	0.0824	58	5.6299	0.0000
19	4.0221	0.0249	59	5.6550	0.1067
20	4.0636	0.0000	60	5.7362	0.0207
21	4.0933	0.0320	61	5.7642	0.9146
22	4.1021	0.0000	62	5.7787	0.0000
23	4.1154	0.0237	63	5.8323	0.0069
24	4.2255	0.0176	64	5.8339	0.0294
25	4.2321	0.0123	65	5.8747	0.1506
26	4.2507	0.0233	66	5.9391	0.2611
27	4.2991	0.0000	67	5.9810	0.3423
28	4.3142	0.0002	68	5.9989	0.3245
29	4.4497	0.0058	69	6.1008	1.4730
30	4.4569	0.0015	70	6.1176	0.0000
31	4.5516	0.0000	71	6.1523	0.3734
32	4.5796	0.0274	72	6.1596	0.8056
33	4.6193	0.1544	73	6.2397	0.0000
34	4.6385	0.0076	74	6.2867	0.0312
35	4.6645	0.0038	75	6.3953	0.0145
36	4.7936	0.0018	76	6.4179	0.0000
37	4.8211	0.0005	77	6.4195	0.0189
38	4.8507	0.0001	78	6.5639	0.0626
39	4.8542	0.0002	79	6.5742	0.0415
40	4.9283	0.7337	80	6.6608	0.0648

Table 7.11: The excitation energies and oscillator strengths of Hg_8^+.

In order to make a comparison with experiment, those transitions with the largest oscillator strengths from the tabulated CIS and CIS(D) energies were first selected. Then these were plotted alongside the experimental data in Figure 7.5. Both CIS and

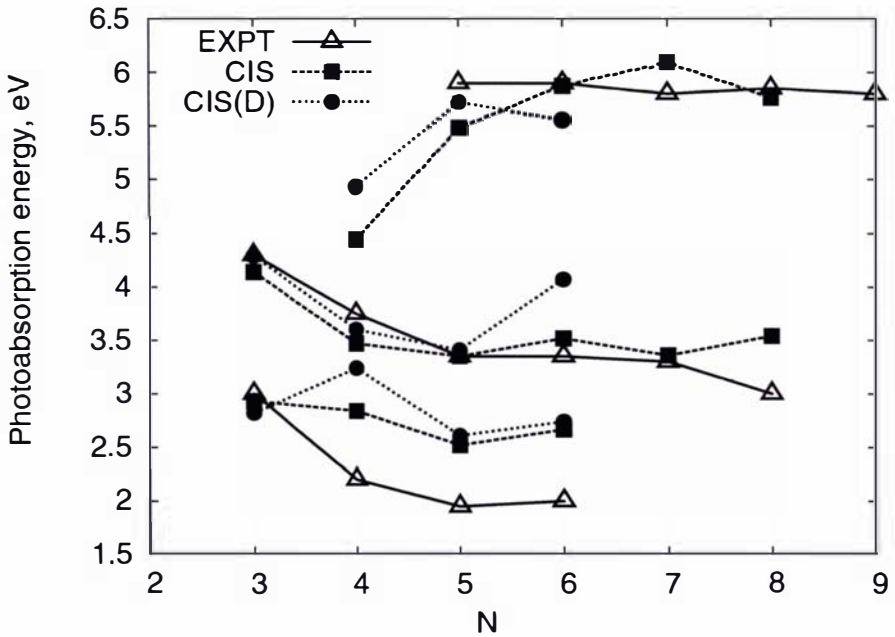

Figure 7.5: The CIS and CIS(D) results compared to experiment. The values plotted are the excitations with the largest calculated oscillator strength.

CIS(D) overestimate the lowest energy transition, for $N = 3-6$. This error, of 0.5-1.0 eV, may be partly due to deficiencies in the basis set, according to the effects of the basis set discussed earlier. It is however a typical error range for the CIS calculation, as has been shown previously [Maurice and Head-Gordon, 1996]. However the higher energy transitions are much more closely reproduced. For $N = 3 - 5$, both CIS and CIS(D) find the second *s-p* transition to much better accuracy. For $N = 6$ the CIS(D) is overestimated considerably, although the CIS calculation remains close to experiment.

An analysis of the states contributing to the low energy transitions agrees with the experimental explanation of these as *s-p* transitions. In Figure 7.6 are shown the molecular orbitals between which the strongest excitations are observed, for $N = 4$ and $N = 8$. The largest oscillator strengths correspond to the most favourable transitions, and this can be partly explained by an analysis of the nature of the

occupied s and virtual p orbitals seen in Figure 7.6. The MO pictures illustrate the

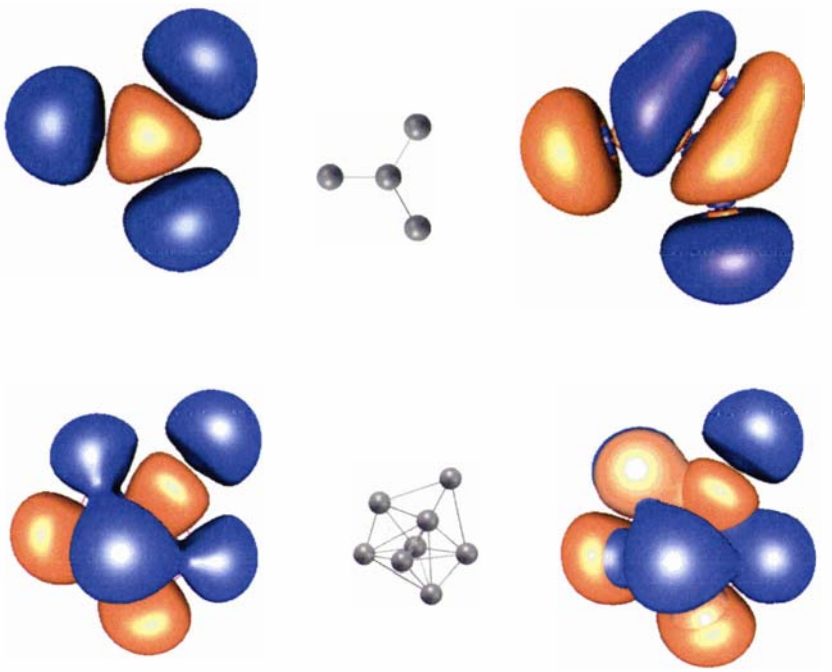

Figure 7.6: Molecular orbitals for the strongest excitations seen for Hg_4^+ (top) and Hg_8^+ (bottom). On the left are the occupied (HOMO s) orbitals, on the right the virtual orbitals.

parity change (going from left to right) and also the favourable overlap of orbitals, as the spatial extension of each pair is similar. The Hg_4^+ absorption is an example of the $6s \rightarrow 6p$ type transition which shifts to lower energy with cluster size. The observed 'plasmon-like' absorption for Hg_8^+ is from the $6s$- to approximately the centre of the $6p$-band, and thus remains more or less constant with cluster size.

7.2.3 SAC-CI calculations

Symmetry-Adapted-Cluster CI (SAC-CI) calculations [Nakatsuji et al., 2002] are a recent modification of the CI procedure which has been implemented in Gaussian03.

The symmetry-adapted cluster expansion is defined as

$$|\Psi_g\rangle = e^{\sum_i c_i s_i} |0\rangle \tag{7.6}$$

$$= \left(1 + \sum_i c_i s_i + \frac{1}{2} \sum_{i,j} c_i c_j s_i s_j + \ldots\right) |0\rangle \tag{7.7}$$

where $|0\rangle$ is the ground state (closed shell) HF wavefunction and s_i is a symmetry-adapted excitation operator. These include both single and double excitations.

The SAC-CI wavefunction is then for excited or ionised states

$$|\Psi_e\rangle = \sum_k d_k |\Phi_k\rangle \tag{7.8}$$

$$= \left(\sum_k d_k R_k + \sum_{k,l} d_k c_l R_k s_l + \ldots\right) |0\rangle - \sum_k d_k s_{gk} |\Psi_g\rangle \tag{7.9}$$

where

$$s_{gk} = \langle \Psi_g | R_k | \Psi_g \rangle . \tag{7.10}$$

The operators R_k are single and double excitation operators, and in the case of calculations on ionised species they will include the ionisation operator (electron annihilation or creation).

For SAC-CI calculations on Hg_n^+ cations, therefore, the SAC calculation is done for the neutral closed shell cluster and the subsequent CI calculation first ionises the cluster and then calculates excited states.

7.2.4 SAC-CI for Hg_3^+ and Hg_4^+.

The SAC-CI calculations were performed for the smallest sizes only to enable a comparison with the CIS(D) results. Many fewer low-energy states are found with the SAC-CI calculation. However, the lowest energy excitation (between 2-3 eV) is more clearly reproduced in the SAC-CI excitations. Unfortunately, the overall accuracy seems to be less as the second excitation is not reproduced as well as with CIS(D), when compared with the experimental energies.

	SAC-CI Energy (eV)	Oscillator Strength	Symmetry
1	2.7350	0.0978	Σ_u^+
2	4.4697	0.0000	Σ_g^+
3	5.1124	2.2150	Σ_u^+
4	6.6029	0.0541	Π_u
5	7.3781	0.0000	Σ_g^+
6	7.6169	0.0000	Π_g
7	8.0121	0.0000	Π_u
8	8.0514	0.0000	Δ_g
9	8.0514	0.0000	Σ_u^+
10	8.0774	0.1885	Σ_u^+

Table 7.12: SAC-CI excitation energies and oscillator strengths of Hg_3^+. The experimentally observed energies are at 3.0 and 4.3 eV.

	SAC-CI Energy (eV)	Oscillator Strength	Symmetry
1	2.6637	0.0857	E′
2	4.7820	0.0000	A_1'
3	5.1796	0.0000	A_1''
4	6.4103	0.0199	A_2''
5	6.7832	0.0000	A_2''
6	7.1037	0.0004	A_2'
7	7.3414	0.0012	A_2'
8	7.4180	1.2808	E′
9	7.4258	0.0000	A_1'
10	7.5362	0.0000	A_2''
11	7.6242	0.0000	A_1'
12	8.1392	0.0000	E″
13	8.6405	0.0000	A_1''
14	8.7006	0.0000	A_1''
15	8.7653	0.0000	A_1''

Table 7.13: SAC-CI excitation energies and oscillator strengths of Hg_4^+. The experimentally observed transitions are at 2.2 and 3.7 eV.

In Figure 7.7 are shown the simulated spectra for $N = 3-8$ using the CIS, CIS(D), and SAC-CI excitation energies and oscillators strengths. These were obtained using

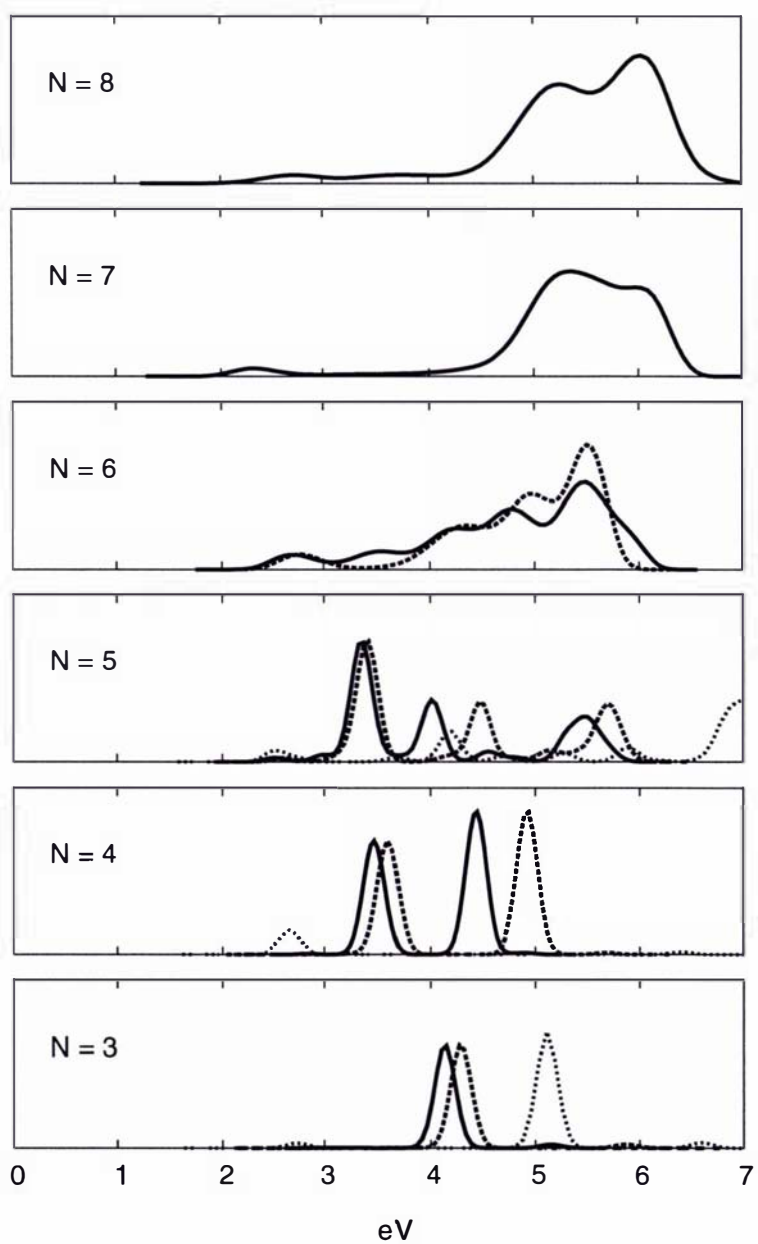

Figure 7.7: The simulated spectra for Hg_n^+, $N = 3 - 8$. The CIS (solid line), CIS(D) (dashed line, $N = 3 - 6$) and SAC-CI (dotted line, $N = 3 - 5$) results are given. Y-axis units are arbitrary as the intensities are normalised to fit the graph.

simple line broadening with a Gaussian function. The overall experimental observation of a shift from low to high energy absorptions at $N = 5$ is reproduced nicely.

In Figure 7.8 are shown the CIS spectra for $N = 3 - 8$, as a 3-dimensional projection. The overall trend seen in Figure 7.1 is reproduced clearly, although the actual positions of the peaks are shifted up to 1 eV.

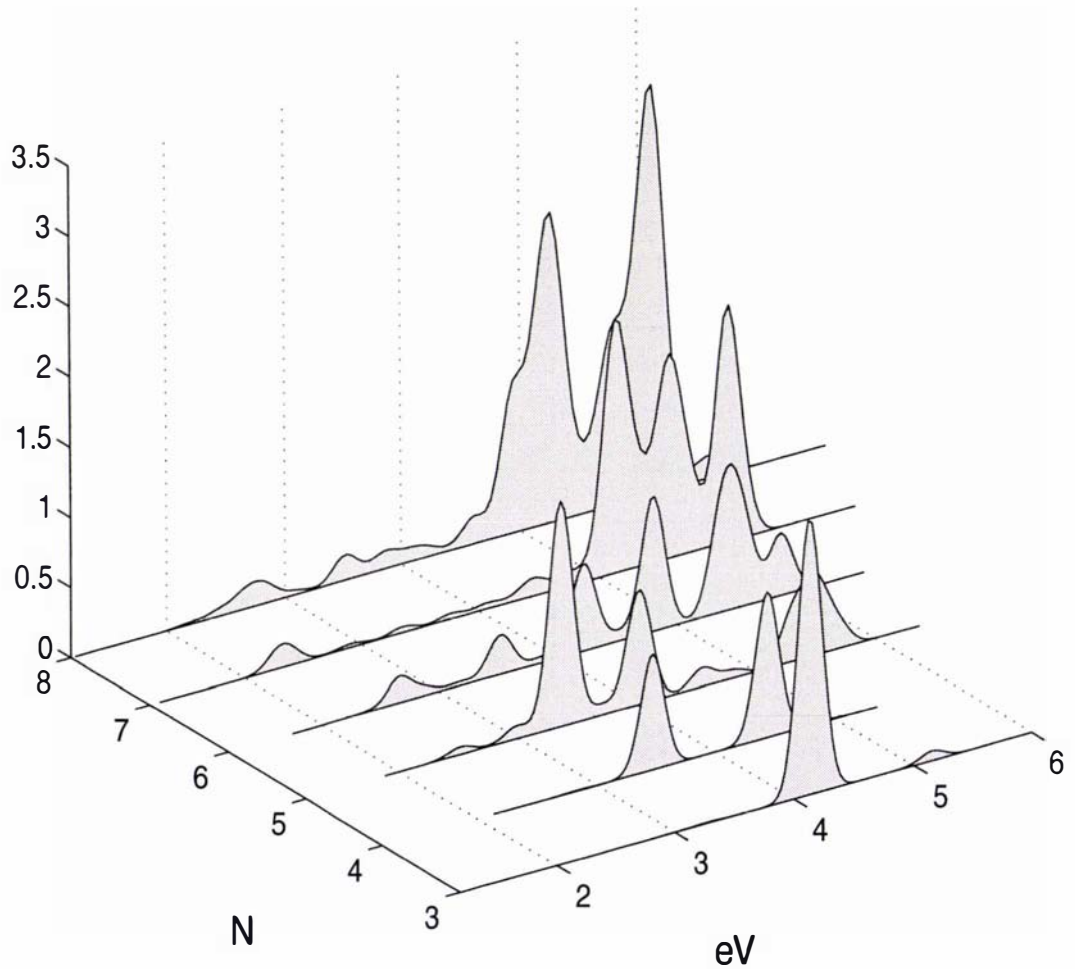

Figure 7.8: The simulated spectra for Hg_n^+, $N = 3 - 8$, from the CIS results.

7.2.5 A CIS comparison with other isomers

Because the absorption spectra in the size range $N = 5-7$ show both low energy (s-p) and high energy (plasmon-like) features, it raises the question of whether both types of isomers, planar and 3-dimensional, may be present under experimental conditions.

Conversely, a more indirect correlation between structure and absorption spectra may exist.

A comparison of the CIS calculations for the different isomers for $N = 5$ and $N = 6$ may be expected to shed some light on the question of to what degree the spectra are structure dependent.

In Tables 7.14 and 7.15 are given the CIS excitation energies for both planar and 3-dimensional isomers. The transitions closest to the experimental energies are highlighted in bold. From the comparison for Hg_5^+ it does seem that the planar isomers give somewhat similar results, when compared to the 3-dimensional isomer. For both $N = 5$ and 6 the planar isomers seem to have stronger (large oscillator strength) low energy transitions than the 3-dimensional isomers. In particular the 3-dimensiontal isomer for $N = 5$ has no low energy excitations with appreciable oscillator strength. Therefore while no isomer reproduces all experimentally observed transitions accurately, there is a correlation between the shift to 3-dimensional structures seen for these sizes, and the experimentally observed disappearance of low energy *s-p* excitations.

7.3 Conclusions

The optimised cationic clusters show a clear structural transition at precisely the sizes at which the experimental shift from a low (*s-p*) to high energy transition was observed. The emergence of the plasmon-like size-independent absorption at $N = 5 - 7$ correlates with the first appearance of a 3-dimensional isomer ($N = 5$) and the disappearance of a low lying planar isomer ($N = 7$). The CIS, CIS(D), and SAC-CI calculations performed reproduce some aspects of the experiment clearly, but not all. In particular, it is difficult to determine whether the combination of low and high energy absorptions between $N = 5 - 7$ is due to the presence of multiple (both planar and 3d) isomers, or whether the correspondence between a shift in isomeric preference and absorption energy is more indirect.

CIS calculations of the excitation energies and oscillator strengths of the non-ground state isomers show that the 3-dimensional isomers for $N = 5$ and 6 also lack the low energy *s-p* excitations seen for the planar isomers. The variation between the calculated and experimental energies is high; this is not surprising when the CIS(D) corrections can shift the CIS energies considerably, often by 0.5 eV and up to 0.8 eV.

	Planar isomer (a)		Planar isomer (b)		3d (D_{3h}) isomer (c)	
	CIS (eV)	Osc. Str.	CIS (eV)	Osc. Str.	CIS (eV)	Osc. Str.
1	2.5214	0.0007	2.3909	0.0005	2.5211	0.0361
2	2.5246	0.0538	2.4846	0.0494	2.6744	0.0360
3	2.5973	0.0004	2.4848	0.0011	2.6764	0.0361
4	2.9888	0.0907	2.7631	0.0512	2.6905	0.0001
5	**3.3547**	**1.5979**	2.8277	0.1937	2.8638	0.0000
6	3.4261	0.0047	3.4029	0.0011	2.8688	0.0000
7	3.6853	0.0674	3.4327	0.0002	3.2394	0.0537
8	3.7590	0.0000	**3.5087**	**0.3840**	3.2412	0.0540
9	3.7806	0.0106	3.5822	0.0000	3.6965	0.0138
10	4.0133	0.7909	4.0121	0.0705	4.0387	0.0098
11	4.0993	0.0348	4.1221	0.0030	4.0402	0.0100
12	4.2538	0.0002	4.1776	0.8062	4.0761	0.0000
13	4.4861	0.0098	4.1888	0.0172	4.4120	0.0472
14	4.5594	0.1257	4.2731	0.0041	4.5470	0.0079
15	4.8058	0.0390	4.4129	0.0819	4.5497	0.0739
16	4.8337	0.0150	4.6930	0.0000	4.5501	0.0629
17	4.8395	0.0028	4.7744	0.0086	4.5507	0.0108
18	4.9089	0.0000	4.7776	0.0318	4.9693	0.0000
19	5.3085	0.3318	4.9169	0.9424	5.0878	0.0001
20	5.4862	0.4253	5.3393	0.3206	5.0903	0.0001
21	5.5582	0.1143	5.3986	0.3414	5.1668	0.0000
22	5.6539	0.0003	5.4559	0.0118	5.1709	0.0000
23	5.6941	0.1599	5.4848	0.0000	5.2439	0.2604
24	5.7223	0.0002	5.6142	0.0021	5.3690	0.0000
25	5.7540	0.0000	5.6312	0.0000	5.3975	0.3804
26	5.8226	0.1981	**5.6906**	**0.7971**	5.4000	0.3794
27	5.8980	0.0442	5.7329	0.0005	5.4173	0.0000
28	6.1062	0.0017	5.7692	0.2771	5.6855	0.0000
29	**6.1501**	**0.7809**	6.0657	0.0022	5.6866	0.0000
30	6.2563	0.0136	6.0668	0.4446	5.8421	0.1882
31	6.3868	0.0026	6.2120	0.0524	5.9208	0.0640
32	6.4084	0.0069	6.3658	0.0000	5.9216	0.0731
33	6.4566	0.0000	6.3932	0.0021	**6.0439**	**0.5535**
34	6.5953	0.0081	6.4317	0.0159	**6.0483**	**0.5633**
35	6.6152	0.0117	6.5790	0.0000	6.1273	0.0001
36	6.8043	0.1536	6.6529	0.0008	6.1533	0.0000
37	6.8905	0.0006	6.6772	0.0355	6.1553	0.0000
38	6.8918	0.0232	6.7240	0.4949	6.2524	0.0000
39	6.9619	0.2358	6.8070	0.2205	6.3600	0.0002
40	6.9985	0.0293	6.8640	0.9714	6.3870	1.3284

Table 7.14: A comparison of the CIS excitation energies and oscillator strengths for the different isomers for Hg_5^+. The experimental transitions are observed at 1.95, 3.35, and 5.90 eV, and the closest corresponding calculated transitions (those with the largest oscillator strength) are marked in bold.

	3d isomer		Planar isomer	
	CIS Energy (eV)	Osc. Strength	CIS Energy (eV)	Osc. Strength
1	2.4331	0.0054	2.0925	0.0000
2	2.4946	0.0002	2.1194	0.0000
3	2.4946	0.0002	2.1758	0.0000
4	**2.6664**	**0.1843**	2.2207	0.0838
5	2.8780	0.0284	**2.4204**	**0.1300**
6	2.8784	0.0284	3.0802	0.0000
7	3.1825	0.0151	3.1018	0.0000
8	3.1825	0.0151	3.1108	0.0608
9	**3.5180**	**0.2797**	3.1307	0.0000
10	3.7630	0.0036	3.3061	0.0000
11	3.7631	0.0036	3.5142	0.0044
12	3.8797	0.0411	3.8257	0.0000
13	3.9496	0.0000	3.8833	0.0016
14	4.1684	0.0533	3.8923	0.0985
15	4.1685	0.0532	3.9045	0.0090
16	4.2082	0.5054	3.9217	0.0000
17	4.3254	0.0175	3.9518	0.0000
18	4.3255	0.0175	3.9775	0.0000
19	4.5019	0.0264	4.4117	0.0000
20	4.5023	0.0265	4.5678	0.0049
21	4.7773	0.0113	4.5968	0.9528
22	4.7774	0.0113	4.6749	0.0055
23	4.7940	0.9398	4.8257	0.0000
24	4.8849	0.0015	**4.9491**	**1.8825**
25	4.8850	0.0015	5.0131	0.0000
26	4.9738	0.0012	5.0846	0.0004
27	5.1865	0.0000	5.0994	0.0000
28	5.3026	0.0038	5.1420	0.0003
29	5.3027	0.0038	5.1426	0.0000
30	5.3051	0.1035	**5.2093**	**1.6894**
31	5.3321	0.0000	5.2819	0.0000
32	5.3960	0.3117	5.4037	0.0000
33	5.3962	0.3125	5.4196	0.0000
34	5.4832	0.0601	5.5618	0.0000
35	5.4833	0.0595	**5.6619**	**0.9594**
36	5.5426	0.5279	5.7592	0.0145
37	5.6915	0.0160	5.7825	0.0000
38	5.6915	0.0161	5.8750	0.2450
39	5.8132	0.0000	5.9677	0.0000
40	5.8605	0.0025	5.9715	0.0000
41	5.8606	0.0024	5.9927	0.0000
42	**5.8754**	**0.4332**	6.0946	0.0170

Table 7.15: A comparison of the CIS electronic excitation energies for different isomers for Hg_6^+. The experimentally observed energies are 2.0, 3.3, and 5.9 eV, and the closest corresponding calculated transitions are marked in bold.

Chapter 8

The photoelectron spectra of anionic Zn clusters

In this chapter I will consider the simulation of the photoelectron spectra of anionic Zn clusters. It is necessary to test the methods used in this thesis by comparison of calculated results with experimental data, and as appropriate data for mercury clusters is not always available, an inspection of its lightest homologue Zn may be useful.

8.1 Metal clusters and the jellium model

Research into metal clusters has been dominated by the simple s-metals (Na,K) due to the natural way in which they are described by the jellium model (JM). [de Heer, 1993] Divalent systems such as Mg have also been successfully explained by the JM with only small perturbations seen at certain cluster sizes. [Akola et al., 2001] An open question is however, the influence of the *d*-band in such systems. Recent studies of the coinage metals have found that *s*-*d* hybridisation can play an important role in determining cluster structure, and combined with experimental data ground state structures have been assigned for the smaller cluster sizes. [Häkkinen et al., 2002, Furche et al., 2002]

Zinc is the first *d*-metal which with its $4s^2$ valence electrons is iso-electronic with Mg, and can therefore be expected to be a suitable test of *d*-electron influence. The inclusion of the *d*-electrons in the calculation increases the computational requirements considerably, and as a consequence only the clusters with up to 12 atoms are studied.

Photoelectron spectroscopy has been widely used in the study of metal clusters to obtain electronic binding energies which, in combination with either the JM or *ab initio* calculations can give clear information about strucure and isomerisation. [Moseler et al., 2003] [Akola et al., 2001]

8.2 Plane wave DFT and clusters

The calculated structures are obtained using the BO-LSD-MD (Born-Oppenheimer local-spin-density molecular dynamics) program code written by Barnett and Landman. [Landman and Barnett, 1993] A soft-core pseudopotential is used for the core electrons, and for Zn the outer $3d$ and $4s$ electrons are explicitly described in a plane wave basis by the PBE density functional.[1] The DFT Kohn-Sham equations are solved for the 12 explicit electrons. For the atom the ionisation potential is 9.557 eV (expt = 9.395 eV), for the (neutral) dimer there is a bond length of 4.200 Å(expt = 4.19 Å), and a binding energy of 0.026 eV (expt = 0.034 eV). [Czajkowski and Koperski, 1999] This is reasonable as the Zn dimer is a van der Waals molecule for which gradient corrected (GGA)-DFT often underbinds. A comparison of the performance of DFT with the *ab initio* methods in Chapter 2 in encouraging, the CCSD(T) calculation gives a bond length of 4.215 Å, and a binding energy of 0.038 eV. The structural optimisation is provided by a Langevin MD procedure at finite temperature starting from an arbitrary initial configuration. Due to the complicated potential energy surface characteristic of most metal clusters, the optimisation was only aimed at finding a local minimum based more or less loosely on the initial configuration. Thus isomers of a different symmetry can be compared, with the initial coordinates taken from the results of, for example, a Mg cluster optimisation and appropriately scaled. The search for the minimum energy isomer is based on the assumption that experimental conditions allow thermodynamic equilibrium. While other considerations are sometimes important, such as the mechanism of formation, [Kronik et al., 2002] the DOS for the higher energy isomers is found in all cases to fit less well than the ground state isomer. Due to the many possible candidate structures and also the increased calculation cost for larger cluster sizes, the most important factor in the search for the ground state isomer is certainly the selection of the starting geometry. For some cluster sizes isomers based on the same underlying symmetry (i.e. tetrahedral packing) are often close in energy. However

[1] See reference [Trouillier and Martins, 1991]. The plane wave cutoff energy is 1.22 keV. The pseudopotential uses s-nonlocal and p- and d-local components which have cutoff radii of 2.2, 2.3, and 2.0 a_0 respectively.

the calculated DOS is very sensitive to small changes in structure, which makes the comparison with experimental spectra of particular importance.

In order to compare the calculated Kohn-Sham spectrum with the DOS from photoelectron spectra, the Kohn-Sham energies are first shifted by the vertical detachment energy (VDE) calculated for the isomer. This is straightforwardly obtained as the difference in energy between the anion and the neutral cluster calculated in the geometry of the anion. Gaussian broadening is then used on the occupied KS states to approximate the experimental spectrum.

8.3 Photoelectron spectra and the calculated density of states

As has been noted previously, [Akola et al., 2001] for the smallest anions the LDA-GGA model is unable to describe binding. The trimer and tetramer are not stable, and for the sizes up to $N = 6$ no experimental data is available. Even previous coupled cluster calculations have found the trimer anion to be unstable (with respect to electron detachment). [Flad et al., 1999] For $N = 7$, the smallest size for which experimental results exist, the agreement with the experimental spectrum is least convincing.

8.3.1 Isomers

In Figure 8.1 the binding energies of the ground state isomers are plotted, the calculated VDEs and also the average bond length in each of the clusters Zn_n^- are also shown. The corresponding structures are shown in Figure 8.2. The smallest size shown, Zn_5^-, is the smallest size for which DFT is able to bind an electron. However as the experimental spectra have only been observed from a minimum size of 7 atoms, it is not clear whether Zn_5^- is truly stable or whether this is an artifact caused by DFT.

The relationship of the ground state isomers for $N = 8, 10, 12$ to the highly symmetrical D_{3d} structure for $N = 9$ is shown in Figure 8.3. The high symmetry of the $N = 9$ structure is accompanied by a particularly high stability, such that the 8-atom cluster is related by the deletion of one atom, and the larger 10- and 12-atom clusters have a 9-atom core with weakly bound atoms bound to the outside. The close relationship of the two degenerate isomers for $N = 9$, 9a and 9b, is also shown in Figure 8.3. 9a is the D_{3d} structure, but the closely related isomer 9b is of only

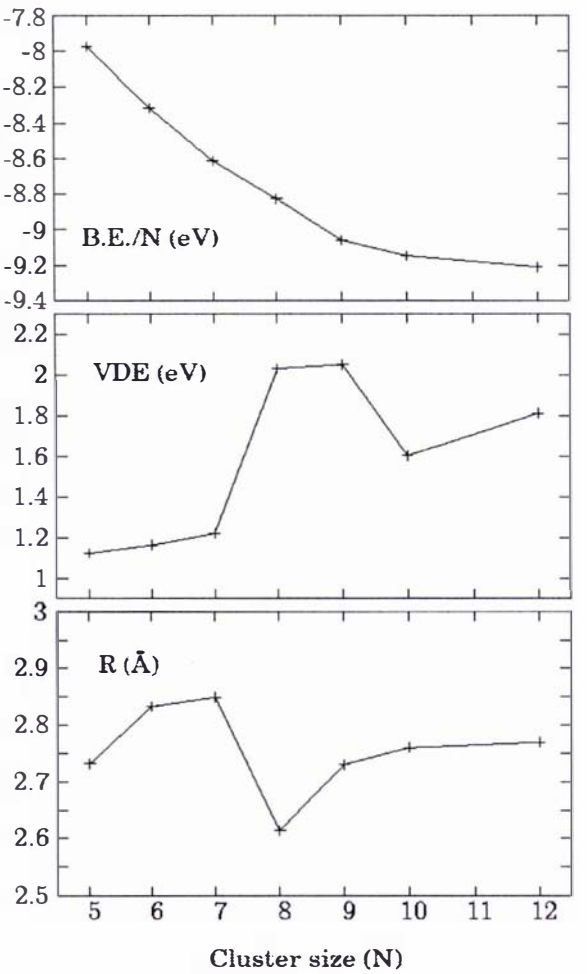

Figure 8.1: From top: Calculated binding energies, vertical detatchment energies (VDE) and average bond lengths in Zn clusters. The average bond length is calculated over all bonded atoms, taken as the average of all pairs within a cutoff radius.

slightly lower symmetry.

For $N = 8 - 12$ a trigonal prism based structure such as those found for Mg_n^- are the ground state isomers, but in the case of $N = 7$ an unexpected structure is observed which consists of two tetrahedra sharing a tip, and twisted towards each other such that a third tetrahedron is formed between them. Surprisingly this structure is 0.15 eV lower in energy than that of the pentagonal bi-pyramidal (pbp) structure, and 0.38 eV more stable than the structure found to be the ground state for Mg_7^- by

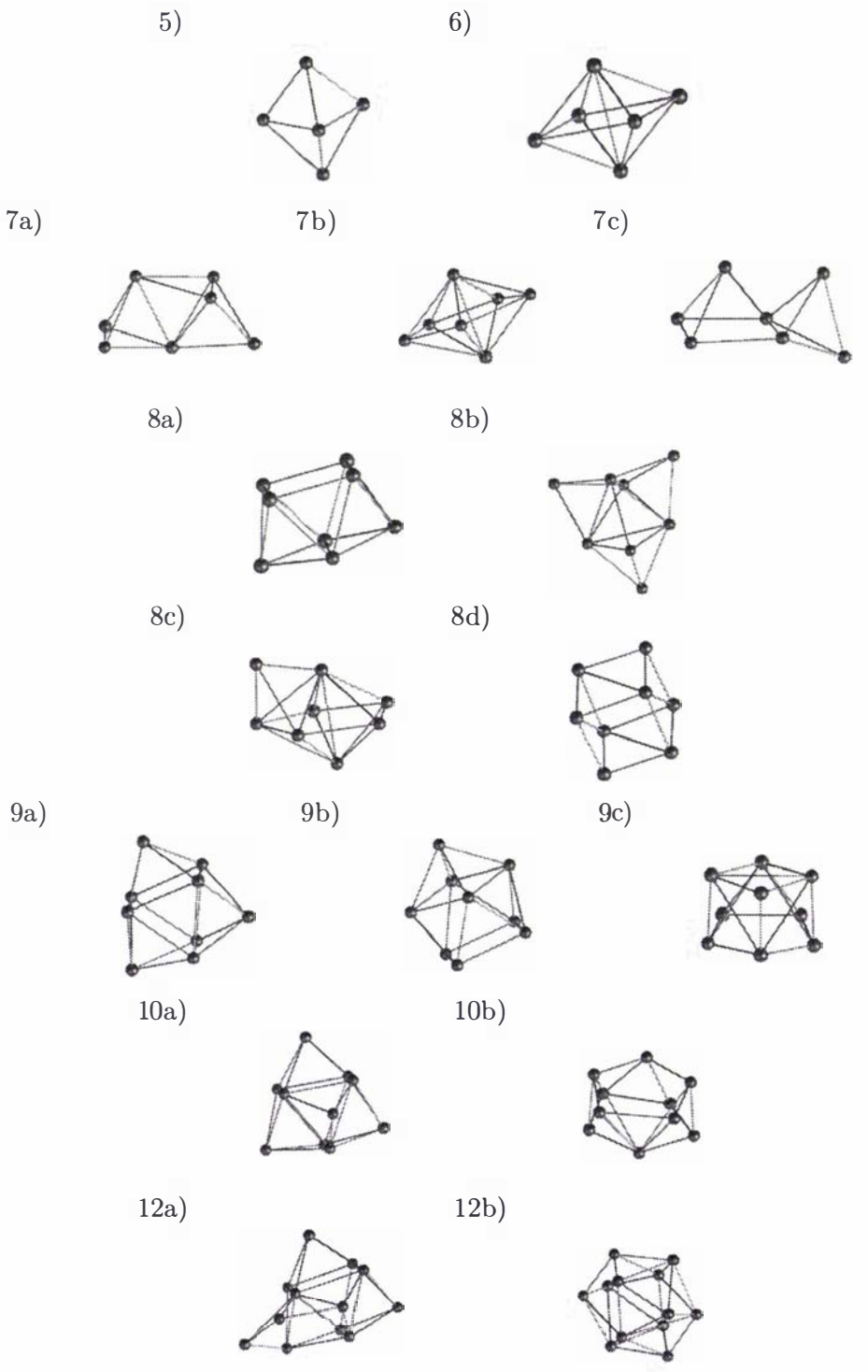

Figure 8.2: The optimised isomers for Zn_n^- clusters, $N = 5, \ldots, 10, 12$.

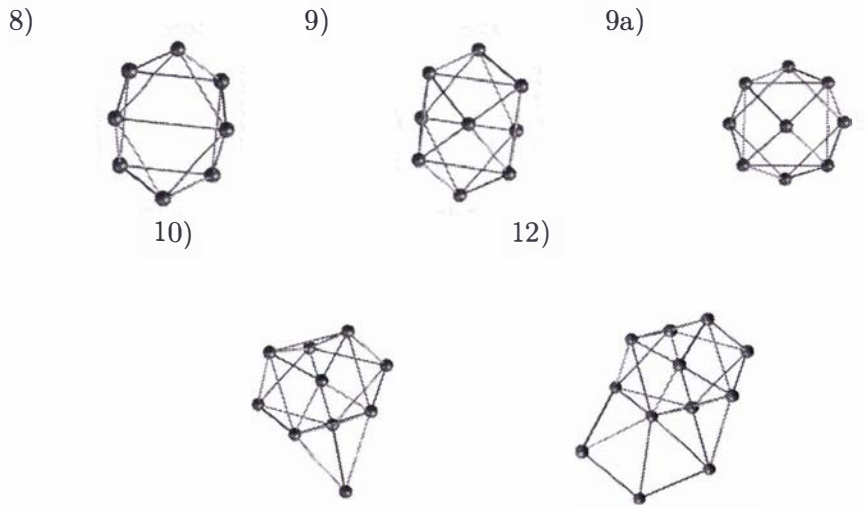

Figure 8.3: Ground state Zn_n^- clusters based on the D_{3d} structure for $N = 9$.

Jellinek *et* al, which is a trigonal prism with two atoms sited on a triangular face and the adjoining edge of the square. [Jellinek and Acioli, 2002] What makes the tetrahedron based structure more stable is not clear, although it corresponds loosely to the structure of Zn_8^- missing one atom, but somewhat distorted.

For Zn_8^- the structure shown as 8a in Figure 8.2 (8 in Figure 8.3) was found to be the ground state by an energy difference of 0.12 eV as compared to the structures based on the Mg ground state (8b). This is a cube with the upper plane rotated by 45 degrees with respect to the lower, and distorted to form two trigonal prisms. In fact this corresponds closely to the structure of $N = 9$ without its capping atom, which allows the structure to be quite compact. As the cap is added to form Zn_9^-, the structure must stretch to accommodate this atom, thereby lengthening the bond distance as is seen. This structure is the basis for both Zn_{10}^- and Zn_{12}^-, which fit successive atoms around the surface of the 9-atom subunit. In fact isomers 9a and 9b are degenerate, 9a being D_{3d} symmetry, as in ref [Jellinek and Acioli, 2002], and 9b differs only in that the 4 atoms forming the base (if the capping atom is on top) are in a square, not a diamond (which is required in 9a for the higher symmetry). The absolute degeneracy of these two isomers is echoed in the DOS, which are effectively identical. Even in those cases where the ground state is closely related to the trigonal prism based Mg structures, they are by no means identical, and the resulting DOS can be quite different. The DOS of each isomer given in 8.2 are shown in Figure 8.4.

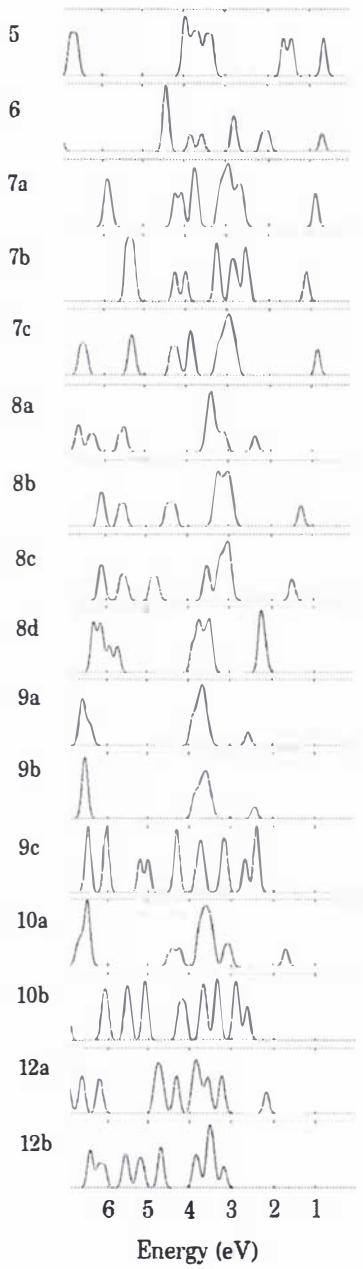

Figure 8.4: The DOS of optimised isomers for Zn clusters, $N = 5 - 10, 12$.

Except for the two degenerate isomers 9a and 9b (which are closely structurally related), it is clear that the DOS depends sensitively on the cluster structure. Thus a match between the experimental spectrum and the DOS of the calculated ground

state isomer confirms the correct structure has been found. In the case of $N = 7$, neither the ground state nor the pentagonal bipyramid (7b) nor the trigonal prism based isomer (7c) provide a DOS in very close agreement with the photoelectron spectrum. In this case the error seems to be primarily in the calculated VDE by which the spectrum is shifted. A VDE 0.5 eV greater would provide good agreement for the ground state isomer. However it is hard to make a definitive assignment for this size.

8.3.2 Comparison with experiment

In Figure 8.5 are shown the DOS for each of the clusters which are comparable to experiment, which are those with $N = 7, 8, 9, 10, 12$. The angular momentum character of each orbital is shown, the analysis has been done both for the centre of mass, which corresponds to a jellium model decomposition, and also for the ions, corresponding to a LCAO (linear combination of atomic orbitals) model. It should be noted that the d-electron states have been scaled down by a factor of 10 to allow a comparison.

The total DOS is in reasonable agreement with the experimental spectrum. In the atomic (LCAO) decomposition, the atomic s-, p-, and d-electrons are clearly distinguished in all plots. In the JM decomposition, for $N = 7$ the HOMO (Highest Occupied Molecular Orbital) shows strong d-character, and only a little less s. This is followed in the next series of states by d- and then p-character. For $N = 8$, the HOMO is more strongly s than d, but otherwise the same picture holds. The lowest states (due to the atomic d-electrons) are unable to be clearly decomposed, but there is at least some evidence of the JM $1s$-orbital visible. The picture for Zn_9^- is very similar. With 19 electrons however it has a JM $2s$ HOMO orbital; this is clearly visible. For Zn_{10}^- in the HOMO an increased atomic s-character begins to be visible, which may indicate mixing of the s- and p-bands. In the JM decomposition this is indicated by strong mixing rather than a clear $1f$ state; likely due to the perturbation of the electronic states by the ionic cores. In Zn_{12}^- the JM f-contribution starts to be seen clearly, both in the HOMO and in the next lowest states.

Based on the analysis of the s- and p- character of the atomic-type orbitals, as well as the difference in energy between the HOMO orbital and the lower states, it is difficult to place the onset of metallicity. There seems to be increased hybridisation of the HOMO for Zn_{10}^- than is visible for $N = 8, 9$, however conversely this is also the size for which the gap between the HOMO and the lower states is largest.

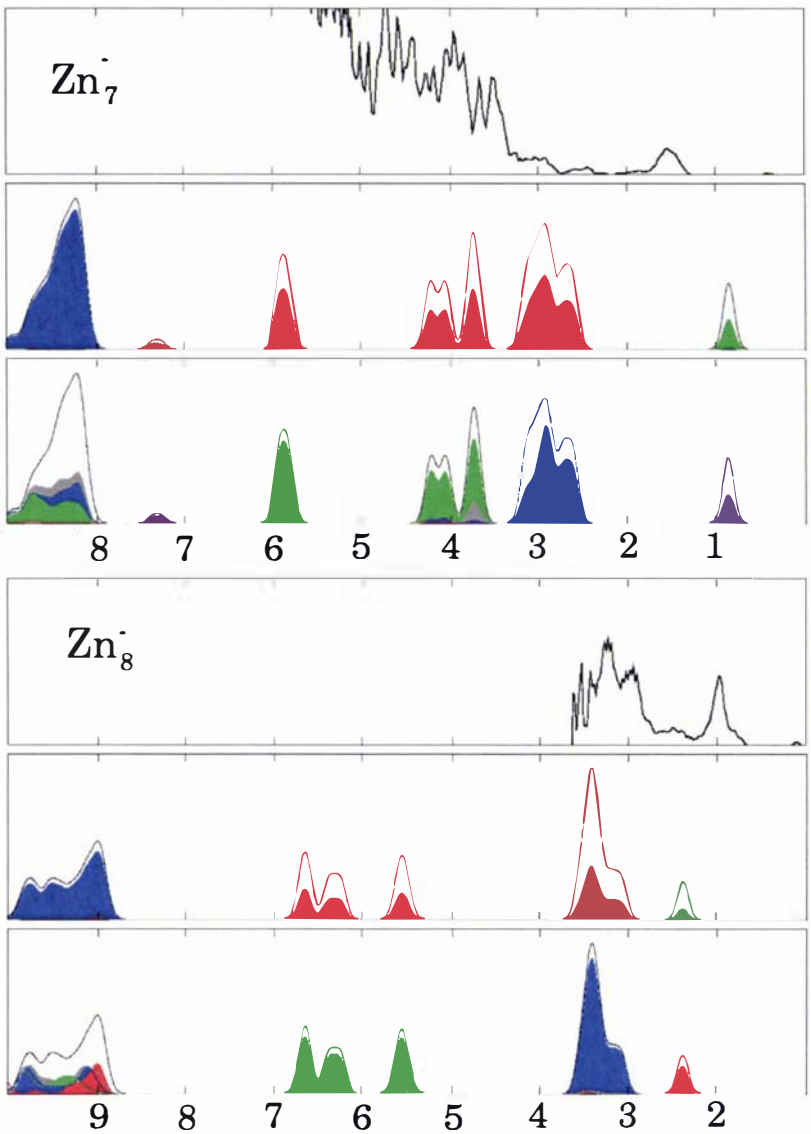

Figure 8.5: The density of states compared to the experimental spectrum for $N = 7, 8, 9, 10, 12$. The s-component of the wavefunctions is shown in red, p in green, d in blue, f in grey, and the total in black. The energy scale is binding energy in eV. The d-electron states (above 6 eV) have been scaled by 0.1 for visibility, however the JM decomposition of these states has been left at the original intensity in order to be distinguishable. (Figure continued on the following page).

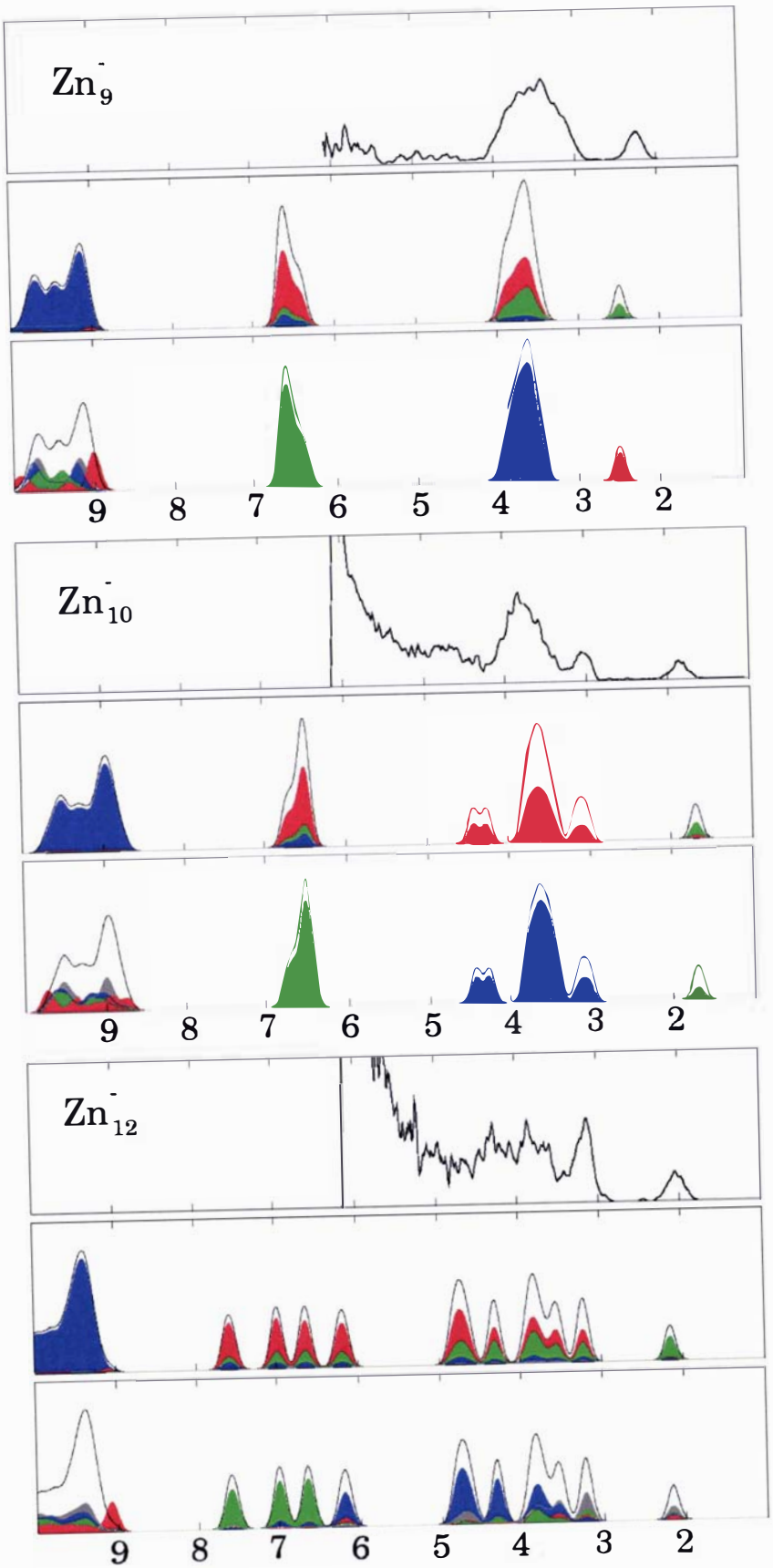
Zn_9^-
9 8 7 6 5 4 3 2
Zn_{10}^-
9 8 7 6 5 4 3 2
Zn_{12}^-
9 8 7 6 5 4 3 2

A clear visualisation of the JM nature of the HOMO, LUMO, and other valence orbitals is provided by the overall electron density. In Figure 8.6 the HOMO and LUMO $1f$ orbitals are shown for Zn_{10}^-, as well as the HOMO-1 ($2s$) and a representative core molecular orbital where the atom-based d-orbitals are clearly visible. The contrast between the two models is very clear, and shows that the presence of the d-electrons had very little effect on the applicability of the JM to the s-electrons.

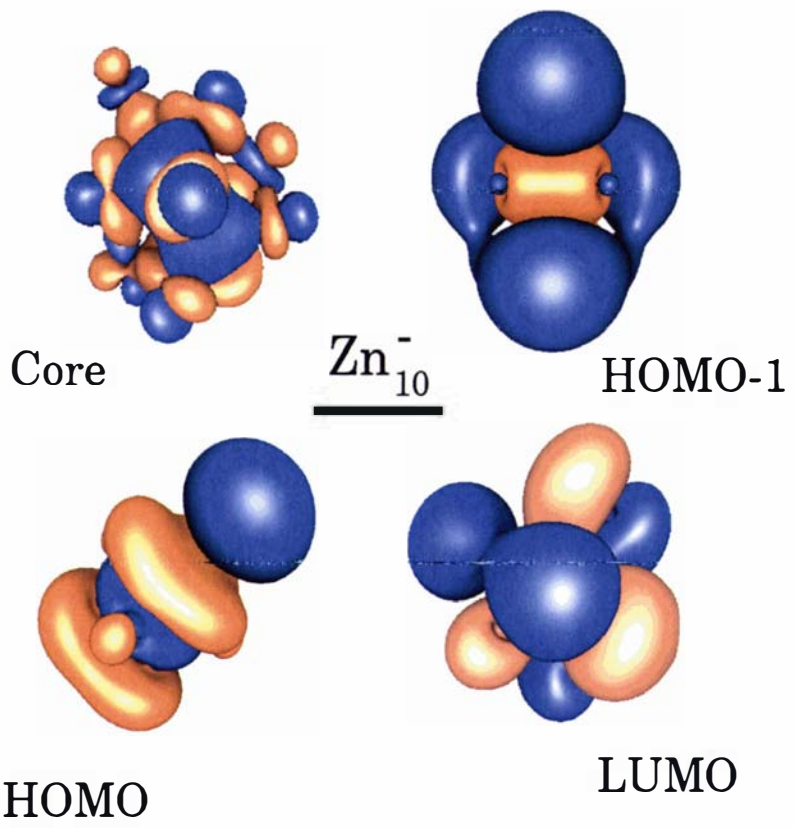

Figure 8.6: A comparison of core (LCAO-like) and valence (JM) orbitals for Zn_{10}^-. The HOMO (highest occupied molecular orbital) and LUMO (lowest unoccupied molecular orbital) are both JM $1f$ states; the HOMO-1 is $2s$, and the core molecular orbital is composed of atomic d-states.

8.4 Conclusions

There is still a need for further studies to demonstrate how well the JM may be adapted to work for more complex metals, and what its limitations are. It is clear that over a limited size range, up to $N = 12$, the Zn anionic clusters are closely related to those of Mg, showing the same structural trends. This would indicate that the *d*-electrons in Zn have a limited impact on the structure of the clusters. However, the JM is unable to explain some of the details of structure, due primarily to the effects of the strongly perturbing ionic cores. Good agreement is obtained between the photoelectron spectrum and the calculated DOS, especially for the larger cluster sizes. The agreement is less good for example for $N = 7$; however this may be due to some extent to a deficiency in the GGA-DFT model, as has been remarked previously.

Chapter 9

Conclusion

The long-term goal of modelling large clusters of many hundreds of atoms, and thus approaching the physics of the bulk (melting and metal-non-metal transitions) is being slowly approached. Advances in computing power and algorithms for cheaper calculations help to reduce the size of the problem. However the real step needs to be taken on a lower level, and the poor convergence of the many-body expansion is clearly a real stumbling block.

This thesis has investigated mercury clusters from numerous perspectives, using quantum chemical methods (DFT, MP2, CCSD(T)) to calculate structures, assess stabilities, and compare isomers. An effort has also been made to analyse more closely the many-body expansion, and the poor performance of the two-body approximation to the total binding energy when compared to the noble gases is clearly due to the variation in bond lengths observed between 3.7 Å in the dimer and 3.0 Å in the bulk. Therefore the metal to non-metal transition is shown to be a result of the bond shortening.

Despite the poor performance of DFT in describing the mercury dimer (and the bulk with the exception of LDA) the comparison of response theory polarisabilities with experimental values shows a great deal of promise for this approach in dealing with a range of electric and magnetic properties for small mercury clusters. The use of the four-component relativistic formalism admits spin-orbit coupling and its effects into the problem in a simple fashion, thereby widening the applicability of this approach markedly.

It is however disappointing that the more expensive CCSD(T) calculations are restricted both by the size of the mercury atom and by the small basis sets required to calculate even a 7-atom cluster. While this was accepted here in order to make

the comparison of two published isomers for Hg_7 possible, it is not by any means a solution to the problem of larger clusters. For bigger systems the two-body correlation potential seems to be the best approach. The Hartree-Fock treatment of mercury clusters is consistent from the smallest sizes up to the bulk, and the convergent nature of the correlation energy makes this a useful correction. However this approach is currently limited by the size of the basis set used for the HF calculations, with 222 primitive basis functions per atom. Moreover, while the binding energies and bond lengths obtained are in very close agreement with the best values available, the two-body nature of the potential means that it may not contain enough information to optimise all lattice parameters correctly, although it does pinpoint the correct bond-length for fixed angles, and provides a convincing cohesive energy at the experimental parameters. Conversely, as HF does not produce a physically bound lattice it may well introduce other errors.

This is precisely the same situation as is observed for the clusters, where we are only able to optimise each symmetry constrained cluster in terms of an overall contraction or expansion of bond length. The need for a pre-ordained structure will limit the applicability of this method for larger sizes where the number of competing isomers is much larger. If a computationally less demanding method is to be successful in simulating large systems of mercury, the approach of splitting the energy into HF and 2-body correlation parts is the best basis for a two-body potential so far.

In the ionic clusters (Hg_n^+ and Zn_n^-) studied, the contrast between the neutral Hg_n clusters and the usual behaviour of metallic clusters is clearly highlighted. The cationic mercury clusters exhibit planar structures at small sizes, such as are known for gold; the anionic zinc clusters are very similar to anionic magnesium clusters in many respects. However while these charged structures may be easier to deal with than the difficult case of neutral mercury, the attempt made here to elucidate the photoabsorption spectra of Hg_n^+ shows that difficulties remain in bridging the gap between theoretical structures and experimental properties.

Appendix A

Basis sets

A.1 Noble gases

Here are given the noble gas basis sets used in Chapter 4. They are the Douglas-Kroll basis sets (cc-pVQZ-DK from www.emsl.pnl.gov), but for neon and argon the hardest d, f and g functions were removed.

See [T. H. Dunning, 1989, Woon and T. H. Dunning, 1993, Wilson et al., 1999].

	Exponent	Coefficient
S		
	528.50000000	0.0009592
	79.31000000	0.0072329
	18.05000000	0.0360060
	5.08500000	0.1278065
S		
	1.6090000	1.0000000
S		
	0.5363000	1.0000000
S		
	0.1833000	1.0000000
P		
	5.9940000	1.0000000
P		
	1.7450000	1.0000000
P		
	0.5600000	1.0000000
D		
	4.2990000	1.0000000
D		
	1.2230000	1.0000000
F		
	2.6800000	1.0000000

Table A.1: Basis set used for helium

	Exponent	Coefficient
S		
	99920.0000000	0.0002309
	14960.0000000	0.0009487
	3399.0000000	0.0039528
	958.9000000	0.0152737
	311.2000000	0.0517892
	111.7000000	0.1445869
	43.3200000	0.3048408
	17.8000000	0.3992901
	7.5030000	0.2177599
S		
	99920.0000000	-0.0000543
	14960.0000000	-0.0002242
	3399.0000000	-0.0009299
	958.9000000	-0.0036578
	311.2000000	-0.0124756
	111.7000000	-0.0373656
	43.3200000	-0.0864225
	17.8000000	-0.1585073
	7.5030000	-0.1131074
S		
	2.3370000	1.0000000
S		
	0.9001000	1.0000000
S		
	0.3301000	1.0000000
P		
	99.6800000	0.0066835
	23.1500000	0.0461632
	7.1080000	0.1735949
P		
	2.4410000	1.0000000
P		
	0.8339000	1.0000000
P		
	0.2662000	1.0000000
D		
	2.2130000	1.0000000
D		
	0.7470000	1.0000000
F		
	1.5240000	1.0000000

Table A.2: Basis set used for neon

	Exponent	Coefficient		Exponent	Coefficient
S			P		
	950600.0000000	0.0001729		1890.0000000	0.0006345
	142300.0000000	0.0005491		447.8000000	0.0045580
	32360.0000000	0.0017106		144.6000000	0.0229891
	9145.0000000	0.0052236		54.4600000	0.0840762
	2970.0000000	0.0160867		22.5100000	0.2179697
	1064.0000000	0.0473162		9.7740000	0.3744141
	410.8000000	0.1237533		4.3680000	0.3654219
	168.0000000	0.2620152		1.9590000	0.1286601
	71.9900000	0.3794265	P		
	31.6700000	0.2726419		1890.0000000	-0.0001777
	12.8900000	0.0496374		447.8000000	-0.0012754
	5.9290000	-0.0035227		144.6000000	-0.0065156
	2.6780000	0.0021435		54.4600000	-0.0241765
S				22.5100000	-0.0651679
	950600.0000000	-0.0000494		9.7740000	-0.1153641
	142300.0000000	-0.0001572		4.3680000	-0.1230461
	32360.0000000	-0.0004909		1.9590000	0.0657576
	9145.0000000	-0.0015035	P		
	2970.0000000	-0.0046766		0.8260000	1.0000000
	1064.0000000	-0.0140154	P		
	410.8000000	-0.0385750		0.3297000	1.0000000
	168.0000000	-0.0908526	P		
	71.9900000	-0.1685476		0.1242000	1.0000000
	31.6700000	-0.1762288	D		
	12.8900000	0.1095078		0.3110000	1.0000000
	5.9290000	0.5638908	D		
	2.6780000	0.4444235		0.7630000	1.0000000
S			F		
	950600.0000000	0.0000155		0.5430000	1.0000000
	142300.0000000	0.0000491			
	32360.0000000	0.0001536			
	9145.0000000	0.0004697			
	2970.0000000	0.0014670			
	1064.0000000	0.0043862			
	410.8000000	0.0121987			
	168.0000000	0.0288360			
	71.9900000	0.0554744			
	31.6700000	0.0594865			
	12.8900000	-0.0387248			
	5.9290000	-0.2779522			
	2.6780000	-0.3580799			
S					
	0.9416000	1.0000000			
S					
	0.4239000	1.0000000			
S					
	0.1714000	1.0000000			

Table A.3: Basis set used for argon

	Exponent	Coefficient		Exponent	Coefficient
S			S		
	18226108.0000000	0.0001346		18226108.0000000	0.0000176
	2728802.5000000	0.0003699		2728802.5000000	0.0000483
	620997.7100000	0.0009532		620997.7100000	0.0001248
	175899.5800000	0.0022414		175899.5800000	0.0002943
	57387.4970000	0.0051564		57387.4970000	0.0006806
	20717.1810000	0.0117831		20717.1810000	0.0015702
	8078.8899000	0.0271181		8078.8899000	0.0036720
	3349.5170000	0.0617018		3349.5170000	0.0086288
	1459.7812000	0.1320938		1459.7812000	0.0196348
	662.8939100	0.2433513		662.8939100	0.0410530
	311.3921500	0.3342231		311.3921500	0.0717503
	149.9375100	0.2660010		149.9375100	0.0830652
	72.4982490	0.0783391		72.4982490	-0.0147751
	35.5693540	0.0022830		35.5693540	-0.3060106
	17.7666330	0.0012440		17.7666330	-0.4924458
	8.7123830	-0.0006064		8.7123830	0.0173704
	4.1449710	0.0002445		4.1449710	0.7241199
	1.9696490	-0.0001311		1.9696490	0.4816145
S			S		
	18226108.0000000	-0.0000436		18226108.0000000	-0.0000056
	2728802.5000000	-0.0001200		2728802.5000000	-0.0000154
	620997.7100000	-0.0003098		620997.7100000	-0.0000398
	175899.5800000	-0.0007306		175899.5800000	-0.0000939
	57387.4970000	-0.0016882		57387.4970000	-0.0002175
	20717.1810000	-0.0038910		20717.1810000	-0.0005010
	8078.8899000	-0.0090818		8078.8899000	-0.0011749
	3349.5170000	-0.0212637		3349.5170000	-0.0027527
	1459.7812000	-0.0480311		1459.7812000	-0.0063013
	662.8939100	-0.0989321		662.8939100	-0.0131196
	311.3921500	-0.1676847		311.3921500	-0.0232625
	149.9375100	-0.1842099		149.9375100	-0.0266687
	72.4982490	0.0259546		72.4982490	0.0041194
	35.5693540	0.4697271		35.5693540	0.1076512
	17.7666330	0.5159235		17.7666330	0.1764312
	8.7123830	0.1369852		8.7123830	-0.0044879
	4.1449710	0.0048179		4.1449710	-0.3791695
	1.9696490	0.0015158		1.9696490	-0.4281149
			S		
				0.6799520	1.0000000
			S		
				0.3245020	1.0000000
			S		
				0.1374410	1.0000000

Table A.4: Basis set used for krypton - *s*-functions

	Exponent	Coefficient		Exponent	Coefficient
P			D		
	28600.8310000	0.0002534		1437.7792000	0.0001457
	6770.9912000	0.0010131		434.2684600	0.0011947
	2199.0489000	0.0042729		168.9269900	0.0066778
	841.1795700	0.0158146		74.7775350	0.0265666
	356.7663300	0.0511469		35.5160240	0.0788804
	162.6362000	0.1347035		17.6710510	0.1764128
	77.9660350	0.2695313		9.0046110	0.2825681
	38.6614890	0.3656351		4.5947730	0.3287200
	19.5767910	0.2680330		2.3264860	0.2596116
	9.7917610	0.0758652	D		
	4.8353830	0.0047626		1.1332470	1.0000000
	2.3681250	0.0011771	D		
	1.0899960	-0.0002294		0.4813070	1.0000000
P			D		
	28600.8310000	-0.0001036		0.2053000	1.0000000
	6770.9912000	-0.0004157	F		
	2199.0489000	-0.0017585		0.4130000	1.0000000
	841.1795700	-0.0065757	F		
	356.7663300	-0.0216222		0.9557000	1.0000000
	162.6362000	-0.0590317	G		
	77.9660350	-0.1235313		0.7395000	1.0000000
	38.6614890	-0.1782107			
	19.5767910	-0.0889368			
	9.7917610	0.2246505			
	4.8353830	0.4903919			
	2.3681250	0.3649839			
	1.0899960	0.0721021			
P					
	28600.8310000	0.0000281			
	6770.9912000	0.0001129			
	2199.0489000	0.0004774			
	841.1795700	0.0017895			
	356.7663300	0.0058901			
	162.6362000	0.0161827			
	77.9660350	0.0340172			
	38.6614890	0.0497318			
	19.5767910	0.0220555			
	9.7917610	-0.0778025			
	4.8353830	-0.1765263			
	2.3681250	-0.1520689			
	1.0899960	0.1361487			
P					
	0.5045880	1.0000000			
P					
	0.2184550	1.0000000			
P					
	0.0899590	1.0000000			

Table A.5: Basis set used for krypton - p, d, f, g-functions

Appendix B

Cartesian Coordinates

All coordinates given are in Ångstrøm.

B.1 Lennard-Jones type Mercury clusters

N	x	y	z
2	0.000000	0.000000	1.553406
	0.000000	0.000000	-1.553406
3	0.000000	1.789786	0.000000
	1.550000	-0.894893	0.000000
	-1.550000	-0.894893	0.000000
4	1.096835	1.096835	1.096835
	-1.096835	-1.096835	1.096835
	-1.096835	1.096835	-1.096835
	1.096835	-1.096835	-1.096835
5	0.000000	0.000000	2.599569
	0.000000	1.795233	0.000000
	1.554717	-0.897616	0.000000
	0.000000	0.000000	-2.599569
	-1.554717	-0.897616	0.000000
6	0.000000	0.000000	2.243290
	0.000000	2.243290	0.000000
	-2.243290	0.000000	0.000000
	0.000000	0.000000	-2.243290
	0.000000	-2.243290	0.000000
	2.243290	0.000000	0.000000

Table B.1: Coordinates of atoms in the LDA optimised LJ isomers. (N = 1 - 6)

N	x	y	z
7	0.000000	2.721726	0.000000
	2.588515	0.841060	0.000000
	-2.588515	0.841060	0.000000
	1.599790	-2.201922	0.000000
	-1.599790	-2.201922	0.000000
	0.000000	0.000000	1.609166
	0.000000	0.000000	-1.609166
8	0.000000	2.057855	0.666438
	2.057855	0.000000	-0.666438
	0.000000	1.554540	-2.436426
	-2.057856	0.000000	-0.666438
	0.000000	-1.554540	-2.436426
	-1.554540	0.000000	2.436426
	0.000000	-2.057855	0.666438
	1.554540	0.000000	2.436426
9	-2.609353	1.592022	0.840895
	2.609353	1.592022	0.840895
	-2.609353	-1.592022	0.840895
	2.609353	-1.592022	0.840895
	0.000000	2.558658	-0.687853
	0.000000	-2.558658	-0.687853
	-1.591029	0.000000	-1.653316
	1.591029	0.000000	-1.653316
	0.000000	0.000000	1.318759
10	-2.684131	1.549684	1.156446
	2.684131	1.549684	1.156446
	0.000000	-3.099367	1.156446
	0.000000	2.940985	0.130137
	2.546968	-1.470493	0.130137
	-2.546968	-1.470493	0.130137
	1.579520	0.911937	-1.692860
	0.000000	-1.823873	-1.692860
	-1.579520	0.911937	-1.692860
	0.000000	0.000000	1.218830

Table B.2: Coordinates of atoms in the LDA optimised LJ isomers. (N = 7 - 10)

N	x	y	z
11	2.591432	1.618594	0.417914
	0.000000	-2.893044	1.941532
	-1.587572	0.000000	-2.111187
	0.000000	2.535453	-1.145623
	0.000000	-2.535453	-1.145623
	0.000000	2.893044	1.941532
	-2.591432	-1.618594	0.417914
	0.000000	0.000000	0.958901
	1.587572	0.000000	-2.111187
	2.591432	-1.618594	0.417914
	-2.591432	1.618594	0.417914
12	0.000000	2.714627	1.122520
	2.743978	-0.891572	-1.562582
	0.000000	0.000000	2.787788
	-2.743978	-0.891572	-1.562582
	1.695871	2.334167	-1.562582
	-1.595618	-2.196179	1.122520
	2.581764	0.838866	1.122520
	-2.581764	0.838866	1.122520
	0.000000	0.000000	-0.587479
	0.000000	-2.885189	-1.562582
	1.595618	-2.196179	1.122520
	-1.695871	2.334167	-1.562582

Table B.3: Coordinates of atoms in the LDA optimised LJ isomers. (N = 11 - 12)

N	x	y	z
13	0.000000	0.000000	3.111411
	1.635766	-2.251438	1.391465
	2.646724	0.859973	1.391465
	0.000000	2.782931	1.391465
	-1.635766	-2.251438	1.391465
	-2.646724	0.859973	1.391465
	0.000000	0.000000	-3.111411
	2.646724	-0.859973	-1.391465
	0.000000	-2.782931	-1.391465
	1.635766	2.251438	-1.391465
	-1.635766	2.251438	-1.391465
	-2.646724	-0.859973	-1.391465
	0.000000	0.000000	0.000000
14	0.000000	0.000000	4.502411
	0.000000	1.855950	-2.840057
	-1.607300	-0.927975	-2.840057
	1.607300	-0.927975	-2.840057
	2.636349	1.522097	-0.881035
	0.000000	-3.044194	-0.881035
	-2.636349	1.522097	-0.881035
	0.000000	3.055810	0.202531
	-2.646409	-1.527905	0.202531
	2.646409	-1.527905	0.202531
	1.685648	0.973210	2.121881
	0.000000	-1.946419	2.121881
	-1.685648	0.973210	2.121881
	0.000000	0.000000	-0.312371

Table B.4: Coordinates of atoms in the LDA optimised LJ isomers. (N = 11 - 12)

N	x	y	z
2	0.000000	0.000000	1.892103
	0.000000	0.000000	-1.892103
3	0.000000	2.126897	0.000000
	1.841947	-1.063448	0.000000
	-1.841947	-1.063448	0.000000
4	1.264280	1.264280	1.264280
	-1.264280	-1.264280	1.264280
	-1.264280	1.264280	-1.264280
	1.264280	-1.264280	-1.264280
5	0.000000	0.000000	2.948350
	0.000000	2.008653	0.000000
	1.739545	-1.004327	0.000000
	0.000000	0.000000	-2.948350
	-1.739545	-1.004327	0.000000
6	0.000000	0.000000	2.511715
	0.000000	2.511715	0.000000
	-2.511715	0.000000	0.000000
	0.000000	0.000000	-2.511715
	0.000000	-2.511715	0.000000
	2.511715	0.000000	0.000000

Table B.5: Coordinates of atoms in the MP2 optimised LJ isomers. (N = 2 - 6)

N	x	y	z
7	0.000000	0.000000	1.770217
	0.000000	3.004084	0.000000
	-2.857054	0.928313	0.000000
	2.857054	0.928313	0.000000
	-1.765756	-2.430355	0.000000
	1.765756	-2.430355	0.000000
	0.000000	0.000000	-1.770217
8	0.000000	1.747706	0.672790
	2.530818	0.000000	-0.827050
	0.000000	1.731622	-2.735371
	-2.530818	0.000000	-0.827050
	0.000000	-1.731622	-2.735371
	-1.869960	0.000000	2.889631
	0.000000	-1.747706	0.672790
	1.869960	0.000000	2.889631
9	-2.887624	1.777037	0.985899
	2.887624	1.777037	0.985899
	-2.887624	-1.777037	0.985899
	2.887624	-1.777037	0.985899
	0.000000	2.843980	-0.773751
	0.000000	-2.843980	-0.773751
	-1.743417	0.000000	-1.756423
	1.743417	0.000000	-1.756423
	0.000000	0.000000	1.116751

Table B.6: Coordinates of atoms in the MP2 optimised LJ isomers. (N = 7 - 9)

N	x	y	z
2	0.000000	0.000000	-2.031322
	0.000000	0.000000	2.031322
3	2.307676	0.000000	0.000000
	-1.153838	-1.998506	0.000000
	-1.153838	1.998506	0.000000
4	1.960038	0.000000	1.385956
	-1.960038	0.000000	1.385956
	0.000000	-1.960038	-1.385956
	0.000000	1.960038	-1.385956
5	0.000000	0.000000	-3.183968
	0.000000	0.000000	3.183968
	2.251405	0.000000	0.000000
	-1.125703	1.949774	0.000000
	-1.125703	-1.949774	0.000000
6	0.000000	0.000000	2.757711
	0.000000	0.000000	-2.757711
	2.757711	0.000000	0.000000
	-2.757711	0.000000	0.000000
	0.000000	-2.757711	0.000000
	0.000000	2.757711	0.000000
7	3.349612	0.000000	0.000000
	1.035087	-3.185671	0.000000
	1.035087	3.185671	0.000000
	-2.709893	-1.968853	0.000000
	-2.709893	1.968853	0.000000
	0.000000	0.000000	-1.859785
	0.000000	0.000000	1.859785

Table B.7: Coordinates of atoms in the CCSD(T) optimiscd LJ isomers.

N	x	y	z
2	0.000000	0.000000	1.753926
	0.000000	0.000000	-1.753926
3	0.000000	2.015731	0.000000
	1.745674	-1.007866	0.000000
	-1.745674	-1.007866	0.000000
4	1.222200	1.222200	1.222200
	-1.222200	-1.222200	1.222200
	1.222200	-1.222200	-1.222200
	-1.222200	1.222200	-1.222200
5	0.000000	0.000000	2.884055
	0.000000	1.984946	0.000000
	1.719014	-0.992473	0.000000
	0.000000	0.000000	-2.884055
	-1.719014	-0.992473	0.000000
6	0.000000	0.000000	2.478100
	0.000000	2.478100	0.000000
	-2.478100	0.000000	0.000000
	0.000000	0.000000	-2.478100
	0.000000	-2.478100	0.000000
	2.478100	0.000000	0.000000

Table B.8: Coordinates of atoms in the PW91 optimised small mercury clusters.

N	x	y	z
7	0.000000	3.008045	0.000000
	2.860821	0.929537	0.000000
	-2.860821	0.929537	0.000000
	1.768085	-2.433560	0.000000
	-1.768085	-2.433560	0.000000
	0.000000	0.000000	1.747542
	0.000000	0.000000	-1.747542
8	-0.111553	-0.025315	-0.119427
	-0.102779	-0.050214	3.380653
	-0.764172	2.903576	1.683634
	2.441917	2.284745	0.508802
	1.905414	2.730263	3.908195
	3.196151	-0.932500	-0.646969
	3.334815	-0.249057	2.752424
	1.225008	-2.741180	1.577592
9	-2.923720	1.775375	0.945048
	2.923720	1.775375	0.945048
	-2.923720	-1.775375	0.945048
	2.923720	-1.775375	0.945048
	0.000000	2.840609	-0.733461
	0.000000	-2.840609	-0.733461
	-1.755715	0.000000	-1.785999
	1.755715	0.000000	-1.785999
	0.000000	0.000000	1.258727
10	-2.935031	1.694541	1.358989
	2.935031	1.694541	1.358989
	0.000000	-3.389082	1.358989
	0.000000	3.310556	0.136162
	2.867026	-1.655278	0.136162
	-2.867026	-1.655278	0.136162
	1.756879	1.014335	-1.833670
	0.000000	-2.028670	-1.833670
	-1.756879	1.014335	-1.833670
	0.000000	0.000000	1.015557

Table B.9: Coordinates of atoms in the PW91 optimised small mercury clusters $N = 7 - 10$.

N	x	y	z
11	2.872061	1.792509	0.493978
	0.000000	-3.070946	2.198174
	-1.766166	0.000000	-2.310195
	0.000000	2.826431	-1.248125
	0.000000	-2.826431	-1.248125
	0.000000	3.070946	2.198174
	-2.872061	-1.792509	0.493978
	0.000000	0.000000	0.744382
	1.766166	0.000000	-2.310195
	2.872061	-1.792509	0.493978
	-2.872061	1.792509	0.493978
12	0.000000	3.021306	1.232784
	2.900043	-0.942281	-1.781754
	0.000000	0.000000	3.085800
	-2.900043	-0.942281	-1.781754
	1.792325	2.466924	-1.781754
	-1.775879	-2.444288	1.232784
	2.873433	0.933635	1.232784
	-2.873433	0.933635	1.232784
	0.000000	0.000000	-0.340947
	0.000000	-3.049285	-1.781754
	1.775879	-2.444288	1.232784
	-1.792325	2.466924	-1.781754

Table B.10: Coordinates of atoms in the PW91 optimised small mercury clusters $N = 11 - 12$.

N	x	y	z
13	0.000000	0.000000	3.392247
	1.783410	-2.454653	1.517059
	2.885618	0.937594	1.517059
	0.000000	3.034118	1.517059
	-1.783410	-2.454653	1.517059
	-2.885618	0.937594	1.517059
	0.000000	0.000000	-3.392247
	2.885618	-0.937594	-1.517059
	0.000000	-3.034118	-1.517059
	1.783410	2.454653	-1.517059
	-1.783410	2.454653	-1.517059
	-2.885618	-0.937594	-1.517059
	0.000000	0.000000	0.000000
14	0.000000	0.000000	5.076546
	0.000000	2.056462	-3.085389
	-1.780948	-1.028231	-3.085389
	1.780948	-1.028231	-3.085389
	2.884846	1.665566	-1.021803
	0.000000	-3.331133	-1.021803
	-2.884846	1.665566	-1.021803
	0.000000	3.330252	0.253298
	-2.884082	-1.665126	0.253298
	2.884082	-1.665126	0.253298
	1.780609	1.028035	2.293589
	0.000000	-2.056070	2.293589
	-1.780609	1.028035	2.293589
	0.000000	0.000000	-0.395632

Table B.11: Coordinates of atoms in the PW91 optimised small mercury clusters $N = 13 - 14$.

B.2 Hartke isomers

N	x	y	z
7	0.000000	0.000000	0.000000
	-0.034010	0.023963	3.049319
	2.663297	0.021769	1.499261
	0.866785	-2.516842	1.498610
	0.034010	-0.023963	-3.049319
	-2.663297	-0.021769	-1.499261
	-0.866785	2.516842	-1.498610
8	0.000000	1.855830	0.651695
	1.600232	-0.927867	0.655526
	-1.600232	-0.927867	0.655526
	0.000000	0.007805	3.211207
	0.000000	0.005153	-1.967035
	2.626454	1.505031	-1.064992
	-2.626454	1.505031	-1.064992
	0.000000	-3.023115	-1.076935
9	-0.903976	1.564498	1.582096
	-0.903216	-1.571482	1.579520
	-3.058487	-0.000426	0.002178
	1.808953	0.000886	1.581075
	1.529236	2.647737	0.000761
	-0.907646	1.568602	-1.579470
	-0.905670	-1.568714	-1.580206
	1.535366	-2.644852	-0.003097
	1.805440	0.003751	-1.582858
10	0.000000	-1.812292	1.149260
	1.569491	0.906146	1.149260
	-1.569491	0.906146	1.149260
	0.000000	-1.804321	-1.947143
	1.562588	0.902160	-1.947143
	-1.562588	0.902160	-1.947143
	0.000000	3.105824	-0.417816
	-2.689722	-1.552912	-0.417816
	2.689722	-1.552912	-0.417816
	0.000000	0.000000	3.647097

Table B.12: Coordinates of atoms in the LDA optimised Hartke isomers. (N = 7 - 10)

N	x	y	z
11	-1.539867	1.378228	1.166717
	-1.540897	0.318493	-1.781862
	-0.004535	-0.555129	3.070994
	-4.063154	0.001870	-0.000180
	0.006858	-2.381260	-2.018206
	1.539523	0.324449	-1.775608
	-1.541176	-1.706546	0.608015
	1.540905	-1.701399	0.615608
	4.063283	0.000552	-0.002515
	-0.002321	2.938119	-1.055796
	1.541381	1.382622	1.172833
12	-3.258237	-1.060607	1.300901
	1.429222	-2.462852	-1.321388
	-1.222357	1.307979	1.267585
	0.053147	0.238036	-1.536727
	1.730007	2.018534	0.429311
	2.868558	-0.849995	0.987503
	1.046189	0.467072	3.140395
	-0.150140	-1.695581	1.287218
	-3.039380	0.836239	-1.238423
	3.119240	0.253638	-1.876596
	-1.817014	-2.196364	-1.255328
	-0.759234	3.143902	-1.184451

Table B.13: Coordinates of atoms in the LDA optimised Hartke isomers. (N = 11-12)

N	x	y	z
13	-2.229902	-0.627590	1.724795
	0.378387	-1.858246	0.310800
	0.389593	1.192793	1.447159
	-2.197817	-1.159769	-1.438055
	0.401134	0.652118	-1.738944
	3.029320	-1.151757	-1.370577
	3.014654	1.796870	-0.305838
	-4.645755	-0.033023	-0.032710
	2.997128	-0.619903	1.693138
	-2.241293	1.829929	-0.292298
	0.394121	-2.248573	-2.716262
	0.354890	-1.248018	3.303189
	0.355540	3.475169	-0.584397
14	-4.367820	0.097308	-0.616286
	0.976590	2.825998	-0.987624
	0.223818	-2.333102	-0.039285
	0.001710	0.693478	0.941537
	2.729659	-0.990242	1.362177
	3.400983	0.878458	-1.026928
	2.905802	-2.124713	-1.572126
	-2.862183	1.727197	1.562809
	0.627884	-0.091844	-2.191696
	-2.442454	-1.359781	1.265617
	-2.105732	-1.567530	-1.955042
	2.624251	2.148009	1.685618
	-1.844980	1.615678	-1.423241
	0.132473	-1.518913	2.994470

Table B.14: Coordinates of atoms in the LDA optimised Hartke isomers. (N = 13-14)

N	x	y	z
7	0.000000	0.000000	0.000000
	3.335384	1.009138	0.000000
	-1.587507	-0.769596	-3.005111
	1.587507	0.769596	3.005111
	-2.461445	2.118931	-1.262760
	-3.335384	-1.009138	0.000000
	2.461445	-2.118931	1.262760
8	-1.171263	-0.001424	1.621619
	0.830360	-1.709302	-0.552872
	2.349415	-0.001203	2.042067
	-2.331586	2.986626	0.166953
	-2.329878	-2.987159	0.165568
	0.830274	1.712588	-0.551629
	-1.964346	-0.000508	-1.694335
	3.787024	0.000380	-1.197372
9	1.517083	1.275398	-1.712285
	0.343576	-1.954665	-1.711341
	3.265546	-1.186895	-0.002761
	-1.867240	0.677118	-1.710724
	-0.605175	3.421347	-0.000655
	1.521734	1.277322	1.710619
	0.347659	-1.953071	1.711463
	-2.660659	-2.234644	0.003337
	-1.862525	0.678090	1.712348

Table B.15: Coordinates of atoms in the MP2 optimised Hartke isomers.

N	x	y	z
7	0.000000	0.000000	0.000000
	0.000000	2.258416	3.098878
	0.000000	-2.258416	-3.098878
	-1.955845	-1.129208	3.098878
	1.955845	-1.129208	3.098878
	1.955845	1.129208	-3.098878
	-1.955845	1.129208	-3.098878

Table B.16: Coordinates of atoms in the CCSD(T) optimised Hartke isomers.

N	x	y	z
7	0.000000	0.000000	0.000000
	-0.044477	0.031448	3.383681
	2.960613	0.028911	1.658966
	0.958826	-2.798578	1.657606
	0.044477	-0.031448	-3.383681
	-2.960613	-0.028911	-1.658966
	-0.958826	2.798578	-1.657606
8	1.734432	-1.234984	0.000000
	-0.000013	1.234655	1.733987
	-0.000013	1.234655	-1.733987
	2.938801	2.051945	0.000000
	-1.734227	-1.234794	0.000000
	-0.000013	-2.051818	2.939324
	-0.000013	-2.051818	-2.939324
	-2.938954	2.052160	0.000000
9	1.904689	0.633831	1.742083
	-1.506082	1.327954	1.739931
	0.684349	3.360897	0.003197
	-0.403959	-1.970505	1.739087
	2.570527	-2.271610	0.000129
	1.908690	0.638099	-1.739582
	-1.502573	1.332057	-1.739168
	-3.254844	-1.085063	-0.003427
	-0.400797	-1.965660	-1.742251
10	0.000307	-1.986544	1.272707
	1.720244	0.993538	1.272707
	-1.720551	0.993006	1.272707
	0.000732	-2.002942	-2.171262
	1.734233	1.002105	-2.171262
	-1.734965	1.000837	-2.171262
	0.000000	3.454586	-0.460547
	-2.991759	-1.727293	-0.460547
	2.991759	-1.727293	-0.460547
	0.000000	0.000000	4.077307

Table B.17: Coordinates of atoms in the PW91 optimised Hartke isomers, $N = 7-10$.

N	x	y	z
11	-1.706452	0.814935	-1.809258
	-1.708237	-1.980701	0.201483
	-0.004352	3.442080	-0.346225
	-4.531479	0.002402	0.000133
	0.006547	-1.423794	3.152402
	1.706685	-1.976391	0.194420
	-1.707626	1.158573	1.617391
	1.706954	1.164090	1.610666
	4.531355	0.000420	0.002542
	-0.002083	-2.021334	-2.808484
	1.708688	0.819721	-1.815072
12	-3.604844	-2.134498	0.425715
	1.517396	-1.029144	-2.630737
	-1.178347	0.039507	1.188153
	0.116542	1.909344	-1.351784
	1.861072	1.454868	1.676957
	3.086166	-1.495735	0.368960
	1.008325	-1.690941	3.058678
	-0.088323	-2.911121	-0.066695
	-3.388889	1.816954	-0.622134
	3.545902	1.465329	-1.363780
	-1.839500	-0.840677	-2.182038
	-1.035500	3.416113	1.498706

Table B.18: Coordinates of the PW91 optimised Hartke isomers, $N = 11 - 12$.

N	x	y	z
13	-2.574962	2.004786	0.295058
	0.657252	1.473494	1.684448
	0.053311	0.568318	-1.487963
	-1.660405	-1.181352	1.129797
	1.273608	-2.583381	0.381057
	3.632691	-0.376646	1.452404
	3.028626	-1.078768	-2.057525
	-4.958490	-0.332546	1.048791
	3.043646	2.159577	-0.792160
	-3.170840	-0.666940	-1.892511
	0.871529	-1.360415	3.488087
	0.074123	3.915155	-0.665484
	-0.270089	-2.541282	-2.583999
14	-4.913194	0.053362	-0.687385
	1.031981	3.050556	-1.321639
	0.287053	-2.609570	0.184693
	0.031429	0.765791	0.924368
	2.978294	-0.931456	1.568462
	3.758136	0.929304	-1.202265
	3.257230	-2.482603	-1.548375
	-3.126995	2.063222	1.578173
	0.740350	-0.279520	-2.358555
	-2.652543	-1.348352	1.417577
	-2.305077	-1.901512	-2.011803
	2.832166	2.568470	1.680502
	-2.042752	1.561549	-1.670428
	0.123922	-1.439239	3.446676

Table B.19: Coordinates of the PW91 optimised Hartke isomers, $N = 13 - 14$.

B.3 Tetrahedral isomers

N	x	y	z
10	0.000000	2.466046	0.000000
	-2.466046	0.000000	0.000000
	-2.408458	2.408458	2.408458
	0.000000	0.000000	2.466046
	2.408458	-2.408458	2.408458
	-2.408458	-2.408458	-2.408458
	0.000000	0.000000	-2.466046
	2.408458	2.408458	-2.408458
	2.466046	0.000000	0.000000
	0.000000	-2.466046	0.000000

Table B.20: Coordinates for PW91 Tetrahedral Hg_{10}.

Appendix C

Frequencies

The vibrational frequencies were calculated for each isomer in both LDA, and MP2. They are listed here for the optimised isomers given above, in cm^{-1}. Negative values correspond to imaginary solutions, and so indicate the presence of a transition state (or higher order saddle point in the case of multiple negative frequencies).

N	Symmetry	PW91	Symmetry	LDA	Symmetry	MP2
2	Σ_g	27.5659	Σ_g	53.2561	Σ_g	19.9269
3	E	29.9857	E	45.6739	E	20.7531
	A_1	37.7872	A_1	64.2347	A_1	25.1812
4	E	26.1186	E	38.8282	E	20.8265
	T_2	33.8878	T_2	53.3916	T_2	26.3024
	A_1	44.6342	A_1	75.1052	A_1	30.3421
5	E	18.8879	E	26.2578	E	16.6853
	A_1	29.1085	A_1	41.9160	A_1	24.6548
	E	30.5391	E	43.5109	E	26.9664
	E	32.2452	E	48.9992	E	28.6957
	A_2	38.1449	A_2	58.2955	A_2	31.2515
	A_1	44.7927	A_1	74.8317	A_1	34.5653
6	E_g	19.3713	E_g	29.1421	E_g	17.7513
	T_{2u}	22.7022	T_{2u}	33.3925	T_u	21.0277
	T_{2g}	29.4365	T_{2g}	43.8716	T_g	27.6134
	T_{1u}	35.1218	T_{1u}	55.5426	T_u	30.2591
	A_{1g}	44.1107	A_{1g}	73.8569	A_g	33.6482

Table C.1: Frequencies for N = 1 - 6.

N	Symmetry	PW91	Symmetry	LDA	Symmetry	MP2
7	E_2	15.1229	E_2	24.8131	E_2	16.5096
	E_1	20.9965	E_1	30.9449	A	22.0371
	A	23.5497	A	33.5029	E_1	22.8269
	E_2	24.7446	E_2	39.0708	E	25.3959
	A_2	25.1303	A_2	42.1194	A_2	25.5608
	E_1	30.5427	E_1	46.5056	E_2	31.6703
	E_1	30.7105	E_1	47.4334	B	35.6975
	E_1	38.8202	E_1	64.6411	B	37.0997
	A_1	42.6535	A_1	73.8719	B	37.0999
8	B_2	4.9119	B_2	14.0652	B_1	12.3584
	B_1	17.4333	B_1	26.1057	B_2	14.0912
	E	18.9729	E	28.6583	A_1	16.0537
	A_1	19.5663	A_1	31.6371	A_2	16.4967
	E	22.4232	E	34.8781	A_1	18.9024
	A_2	23.4786	A_2	38.1674	A_1	20.5760
	A_1	24.2274	A_1	38.2897	B_2	21.9688
	B_2	29.6501	B_2	49.9884	A_1	22.4672
	B_1	31.4092	B_1	50.7246	B_1	24.8471
	E	33.0509	E	55.8799	A_1	27.0308
	A_1	35.6655	A_1	59.9693	B_2	28.0511
	E	36.5229	E	60.4291	B_1	30.8099
	A_1	38.8699	A_1	70.0646	A_1	32.2600
	B_2	41.8990	B_2	73.8895	A_2	36.9649
					A_1	37.6727
					B_1	40.1464
					B_2	42.7649
					A_1	45.5632

Table C.2: LJ Frequencies for N = 7,8.

N	Symmetry	PW91	Symmetry	LDA	Symmetry	MP2
9	A_1	13.7790	A_1	19.1957	A_1	14.2813
	A_2	14.2333	A_2	19.6778	A_2	14.5783
	B_2	14.5154	B_2	21.4838	B_2	15.6966
	B_2	21.1219	B_2	23.8732	B_2	22.9712
	B_1	21.8260	B_1	25.5617	B_1	23.6114
	A_1	22.5694	A_1	25.8374	A_1	23.9615
	A_1	22.9890	A_1	26.8202	A_1	25.7113
	B_1	23.3479	B_1	27.3270	B_1	25.7989
	A_2	23.5315	A_2	27.3577	A_2	26.3793
	A_2	24.2863	A_2	27.3639	A_2	27.9937
	A_1	25.2072	A_1	29.0642	A_1	28.5547
	B_2	26.6198	B_2	30.0411	B_2	29.0335
	A_1	28.5662	A_1	30.8439	A_1	29.6258
	B_1	30.9748	B_1	33.4892	B_1	31.9532
	B_1	32.9891	B_1	36.2679	B_1	32.9212
	B_2	33.2665	B_2	36.4028	B_2	35.5874
	A_2	35.3926	A_2	38.8362	A_2	35.7486
	A_1	37.0950	A_1	42.9440	A_1	36.9488
	B_2	41.3050	B_2	50.5611	B_2	43.3507
	A_1	43.2181	A_1	51.4983	A_1	43.4037
	B_1	46.6780	B_1	56.5853	B_1	49.2666

Table C.3: LJ Frequencies for $N = 9$.

N	Symmetry	PW91	Symmetry	LDA
10	E	13.0324	A	19.2960
	A_1	14.9447	A	19.2963
	E	20.4414	A	20.3769
	A	22.2900	A	25.1383
	A	22.3638	A	25.1403
	E	23.2521	A	25.9653
	A	24.2691	A	25.9656
	A	24.2692	A	26.1037
	A	26.0056	A	28.3354
	A	26.0057	A	28.4642
	A	26.3035	A	28.4661
	B	28.8395	A	29.2691
	A_2	30.6164	A	29.8949
	B	32.6509	A	29.8954
	B	32.6511	A	30.9805
	E	35.8699	A	34.0841
	A_1	37.1308	A	36.2735
	B	44.0762	A	36.2739
	B	47.5960	A	41.4196
	B	47.5966	A	41.4212
			A	43.5162
			B	57.0337
			B	57.0340
			B	58.5591

Table C.4: LJ Frequencies for $N = 10$.

N	Symmetry	PW91	Symmetry	LDA
11	A_1	11.4761	A_1	20.1423
	A_2	12.1137	A_2	20.5402
	B_2	15.1346	B_2	24.4312
	B_1	18.4555	B_1	25.3374
	A_1	19.4142	A_1	25.6764
	A_2	21.2415	A_2	29.7098
	B_2	21.7558	B_2	30.3110
	A_1	22.0054	A_1	30.3398
	B_1	22.6458	B_1	32.7809
	B_2	22.8597	B_2	33.1635
	A_2	23.4201	A_2	33.5661
	B_1	23.7431	B_1	34.9041
	A_1	24.9579	A_1	39.1311
	A_1	25.6713	A_1	41.5375
	A_2	27.5441	A_2	41.9461
	B_2	28.1535	B_2	44.5783
	A_1	29.6959	A_1	47.2846
	B_2	30.5124	B_2	48.3736
	B_1	31.0339	B_1	53.7437
	B_1	32.7340	B_1	56.0211
	A_1	34.2192	A_1	57.3750
	A_2	36.0960	A_2	61.9234
	B_2	36.3261	B_2	62.7232
	A_1	37.7110	A_1	65.0989
	A_1	43.9383	A_1	69.3720
	B_1	48.6130	B_1	77.9062
	B_2	51.6328	B_2	86.3254

Table C.5: LJ Frequencies for $N = 11$.

N	Symmetry	PW91	Symmetry	LDA
12	E_2	12.8952	A	20.0253
	A	17.5631	A	20.0255
	A	19.7234	A	20.1851
	A	19.8458	A	22.5962
	A	19.8461	A	22.5970
	E	21.8993	E_2	26.8927
	B	23.4657	B	31.1350
	B	23.4658	B	31.2742
	B	24.0800	B	31.2743
	B	24.0802	B	32.2654
	B	24.2039	B	32.7533
	B	24.2040	B	32.7534
	B	25.6476	B	35.9543
	C	28.4922	B	35.9544
	C	28.4923	B	43.6434
	C	28.4928	B	43.6436
	C	28.4928	B	45.6400
	D	30.8205	B	45.6402
	D	30.8206	B	47.6439
	D	31.5247	B	47.6444
	E	33.6726	A_1	50.9380
	E	34.3082	C	57.1119
	A_1	39.2718	C	57.1131
	A_1	48.4367	C	58.4552
	E_1	53.6435	C	58.4553
			A_1	64.7560
			A_1	71.1154
			E_1	87.9327

Table C.6: LJ Frequencies for $N = 12$.

N	Symmetry	PW91	Symmetry	LDA
13	A	18.6021	A	25.5918
	A	18.6023	A	25.5920
	A	18.6023	A	25.5921
	A	18.6023	A	25.5922
	A	18.6025	A	25.5925
	A	23.2171	A	30.5109
	A	23.2172	A	30.5111
	A	23.2172	A	30.5113
	A	23.2174	A	30.5115
	A	23.3667	A	30.6339
	A	23.3668	A	30.6340
	A	23.3668	A	30.6344
	A	23.3669	A	32.7823
	A	23.3670	A	32.7823
	A	23.6822	A	32.7825
	A	23.6823	A	32.7828
	A	23.6827	A	32.7828
	B	28.6069	A	42.2816
	B	28.6070	A	42.2818
	B	28.6071	A	42.2826
	B	30.7353	A	42.2827
	B	30.7354	A	43.6911
	B	30.7356	A	43.6919
	B	30.7356	A	43.6925
	B	33.8152	A	51.3720
	B	33.8153	A	51.3721
	B	33.8153	A	51.3723
	B	33.8154	A	51.3725
	B	33.8155	A	51.3726
	A_g	41.0106	A_g	67.0694
	T_{1u}	53.3863	T_{1u}	85.7667

Table C.7: LJ Frequencies for $N = 13$.

N	Symmetry	PW91	Symmetry	LDA
14	E	11.0534	A	17.2152
	A	18.0414	A	17.2152
	A	18.0694	A	22.8044
	A	18.0695	A	23.1161
	B	19.3581	A	24.5739
	B	20.0439	A	24.5740
	B	20.0439	A	25.9082
	C	22.4894	A	28.8091
	C	22.8964	A	28.8095
	C	22.8965	A	30.3791
	C	23.0918	A	30.9431
	C	23.1619	A	30.9434
	C	23.1621	A	31.9968
	C	23.7183	A	31.9971
	C	23.7184	A	32.4948
	C	23.8558	A	33.6799
	B	26.1496	A	33.6799
	B	26.1496	A	38.3467
	B	26.3053	A	38.3469
	A_1	28.7262	A	38.9063
	A	28.8968	A	42.6784
	A	28.8969	A	42.6789
	A	30.0500	A	43.9944
	E	31.4672	A	44.0526
	B	32.5616	A	47.1169
	B	33.9197	A	47.1171
	B	33.9199	A	50.2401
	E	35.7729	A	50.2406
	A_1	39.0207	A	52.6784
	A_1	42.0024	E	58.7938
	B	53.6809	A_1	64.6362
	B	53.6815	A_1	72.5809
	B	55.0071	B	84.2578
			B	87.1982
			B	87.1997

Table C.8: LJ Frequencies for $N = 14$.

N	Symmetry	PW91	Symmetry	LDA	Symmetry	MP2
7	A_u	-5.0365	A_u	-6.1740	A	-3.8972
	A_u	-2.9717	A_u	-3.7271	A	-2.8248
	A_u	3.9187	A_u	5.5978	A	-2.8248
	A_g	15.7928	A_g	29.3000	A_{1g}	13.5315
	A_g	18.0028	A_g	31.8762	E_g	18.4377
	A_g	18.7631	A_g	32.3999	E_u	25.7444
	A_u	23.1796	A_u	39.5173	A	28.7758
	A_u	23.8790	A_u	40.0551	A	28.7763
	A_g	27.5040	A_g	49.1185	B	31.4833
	A_g	28.3786	A_g	49.2635	B	31.4836
	A_u	32.0505	A_u	55.9136	B	33.2774
	A_u	33.1135	A_u	57.8319	A	34.0626
	A_u	33.2506	A_u	58.4164	A_{2u}	44.6188
	A_g	36.1533	A_g	67.0750		
	A_u	51.4556	A_u	94.5369		
8	A	8.2025	A	9.5992	A	10.4489
	A	9.0464	A	12.4650	A	11.2134
	A	14.5524	A	22.8391	A	14.1386
	A	14.5579	A	23.3110	A	16.0359
	A	15.9779	A	24.1368	A	18.9484
	A	24.8062	A	36.5154	A	24.0588
	A	24.8125	A	36.7241	A	24.6601
	A	25.3822	A	37.2897	A	26.9831
	A	26.8062	A	41.5774	A	27.1044
	A	27.0016	A	41.9785	A	27.2497
	A	27.0091	A	42.6116	A	28.2890
	A	28.3787	A	44.1772	A	31.4710
	A	33.3311	A	52.1102	A	33.1298
	A	33.3883	A	52.2344	A	34.4797
	A	38.7271	A	62.4189	A	35.9942
	A	38.8279	A	63.3564	A	39.8831
	A	38.8322	A	63.4194	A	41.2266
	A	43.4073	A	72.3393	A	42.2960

Table C.9: Hartke Frequencies for N = 7,8.

N	Symmetry	PW91	Symmetry	LDA	Symmetry	MP2
9	A	11.8366	A	19.8019	A	6.9750
	A	12.3731	A	29.8822	A	6.9839
	A	17.9160	A	34.5367	A	20.3049
	A	18.9771	A	41.0819	A	20.3089
	A	19.9589	A	60.1057	A	22.4498
	A	20.1542	A	62.7039	A	22.4520
	A	20.3029	A	67.7229	A	22.6215
	A	20.5787	A	20.2330	A	22.6223
	A	21.9112	A	32.8494	A	24.2418
	A	24.3863	A	34.6432	A	25.0515
	A	25.0598	A	42.4639	A	26.4689
	A	31.7485	A	60.2718	A	32.5931
	A	33.9925	A	63.4272	A	33.2709
	A	34.2868	A	73.8261	A	35.5875
	A	35.2843	A	28.9028	A	35.5943
	A	35.3002	A	33.4425	A	37.2668
	A	35.8998	A	35.0537	A	37.6606
	A	36.1158	A	53.8145	A	37.6654
	A	36.5609	A	62.0834	A	39.1318
	A	40.2793	A	63.6818	A	40.1957
	A	40.6359	A	74.0993	A	40.2011

Table C.10: Hartke Frequencies for $N = 9$.

N	Symmetry	PW91	Symmetry	LDA
10	E	10.1981	E	16.4117
	E	14.2536	E	23.2071
	E	19.0524	E	31.2276
	A	20.1035	A	34.226
	E	20.8348	A	35.1847
	A	23.405	A	35.1847
	A	24.2295	A_2	38.0781
	E	24.7417	A_1	39.1742
	A	29.2184	A	43.3408
	A	31.3059	A	43.3408
	A	35.9705	A_1	51.0164
	A	35.9705	A_2	51.9757
	A	35.972	E	60.9423
	A	37.2282	A_1	63.9547
	E	38.1356	B	66.5411
	E	40.995	B	66.5411
	A	43.1092	B	67.7493
			E	73.7483
			A_1	78.1254

Table C.11: Hartke Frequencies for $N = 10$.

N	Symmetry	PW91	Symmetry	LDA
11	A	9.77370	A	14.9514
	A	10.1781	A	15.5418
	A	10.8862	A	19.2195
	A	11.4298	A	19.5965
	A	15.2659	A	24.3065
	A	15.4397	A	24.3760
	A	19.6477	A	34.4598
	A	20.5720	A	34.6181
	A	20.7776	A	34.8107
	A	21.4646	A	35.1739
	A	21.5615	A	36.4684
	A	21.6565	A	37.6055
	A	23.7445	A	37.6868
	A	27.2329	A	45.7558
	A	28.0911	A	46.4577
	A	28.3593	A	48.9735
	A	30.7197	A	50.6763
	A	30.7241	A	51.9437
	A	36.1094	A	60.2996
	A	36.3746	A	60.5577
	A	36.9401	A	67.3033
	A	39.9832	A	68.7022
	A	40.1819	A	68.7649
	A	40.2906	A	72.2114
	A	41.6181	A	73.4815
	A	41.9281	A	73.8054
	A	44.9933	A	80.4964

Table C.12: Hartke Frequencies for $N = 11$.

N	Symmetry	PW91	Symmetry	LDA
12	A	-4.1701	A	11.0722
	A	8.8743	A	15.9203
	A	10.4157	A	19.7389
	A	12.1645	A	22.6560
	A	12.8892	A	25.2951
	A	15.7950	A	25.9766
	A	16.8699	A	26.8932
	A	18.2220	A	28.9138
	A	18.6475	A	30.2948
	A	19.2134	A	32.3800
	A	20.3888	A	32.8321
	A	22.4401	A	34.3803
	A	22.8605	A	36.0832
	A	24.2325	A	38.8126
	A	26.1030	A	40.9487
	A	27.4722	A	41.9514
	A	28.1930	A	42.7918
	A	29.4690	A	45.6769
	A	30.1353	A	47.7819
	A	31.9977	A	49.6492
	A	34.2673	A	52.8049
	A	34.9715	A	59.2927
	A	36.3046	A	60.5015
	A	37.3211	A	61.5700
	A	38.7156	A	66.5096
	A	39.2061	A	68.9485
	A	41.4243	A	70.7756
	A	42.5358	A	75.1827
	A	48.7107	A	78.9663
	A	51.3026	A	84.8673

Table C.13: Hartke Frequencies for $N = 12$.

N	Symmetry	PW91	Symmetry	LDA
13	A	-9.0436	A	16.6484
	A	3.0863	A	19.6711
	A	9.7292	A	20.5448
	A	10.7604	A	21.5978
	A	13.2025	A	23.9616
	A	14.1653	A	24.4541
	A	14.7919	A	24.8410
	A	17.4483	A	25.3284
	A	18.5537	A	26.3595
	A	19.5919	A	27.1878
	A	20.3165	A	30.6368
	A	20.5329	A	31.6093
	A	22.0498	A	31.9951
	A	22.4835	A	35.1206
	A	23.3860	A	38.8756
	A	24.9291	A	38.9413
	A	25.8052	A	45.2432
	A	26.9357	A	45.3353
	A	27.3781	A	45.9547
	A	28.6231	A	47.7912
	A	31.3237	A	48.5613
	A	32.1290	A	51.0796
	A	34.8344	A	58.0237
	A	35.0977	A	58.4415
	A	36.3772	A	64.0236
	A	37.7058	A	65.3065
	A	39.1721	A	66.1645
	A	41.4138	A	66.2896
	A	42.1256	A	66.8375
	A	45.1276	A	70.2562
	A	46.1718	A	83.3875
	A	50.6004	A	85.3195
	A	51.9931	A	86.2163

Table C.14: Hartke Frequencies for $N = 13$.

N	Symmetry	PW91	Symmetry	LDA
14	A	5.1928	A	11.4947
	A	7.1658	A	19.3365
	A	9.9357	A	26.0452
	A	11.2345	A	30.8852
	A	14.4747	A	33.7334
	A	15.3374	A	37.7988
	A	17.2336	A	42.3998
	A	17.6794	A	50.7803
	A	18.2377	A	55.9806
	A	19.0798	A	64.9856
	A	20.2505	A	70.8083
	A	20.7777	A	78.2234
	A	21.7533	A	14.4226
	A	21.9975	A	22.6052
	A	23.2944	A	27.3781
	A	23.5886	A	32.4686
	A	25.1853	A	34.3332
	A	25.5637	A	40.0876
	A	26.0598	A	43.2112
	A	26.5228	A	52.1266
	A	28.5169	A	59.6407
	A	29.6636	A	65.6873
	A	31.1323	A	71.2083
	A	31.7293	A	80.1980
	A	33.3227	A	15.0214
	A	35.2615	A	24.4494
	A	36.5307	A	28.8925
	A	38.1028	A	32.9009
	A	38.7980	A	36.6607
	A	39.6559	A	41.4920
	A	41.0145	A	47.7914
	A	42.3634	A	53.3588
	A	42.6295	A	63.1595
	A	46.2831	A	66.8316
	A	47.0318	A	74.0501
	A	51.2087	A	87.8044

Table C.15: Hartke Frequencies for $N = 14$.

N	Symmetry	PW91
	T_1	13.4524
	T_2	15.4430
	E	16.1090
	E	19.0328
	T_2	24.0816
	A_1	27.7898
	T_2	33.9009
	T_1	37.4597
	A_1	42.7350
	T_2	46.7938

Table C.16: Frequencies for tetrahedral $N = 10$.

Bibliography

[Akola et al., 2001] Akola, J., Rytkönen, K., and Manninen, M. (2001). Metallic evolution of small magnesium clusters. *Eur. Phys. J. D*, 16:21–24.

[Allen and Tildesley, 1986] Allen, M. P. and Tildesley, D. J. (1986). *Computer Simulation of Liquids.* Clarendon Press, Oxford.

[Allouche et al., 1995] Allouche, A. R., Aubert-Frécon, M., Nicolas, G., and Spiegelmann, F. (1995). Theoretical study of the electronic structure of the Ba_2 molecule. *Chem. Phys.*, 200:63–77.

[Andrae et al., 1990] Andrae, D., Haeussermann, U., Dolg, M., Stoll, H., and Preuss, H. (1990). *Theor. Chim. Acta*, 77:123.

[Axilrod and Teller, 1943] Axilrod, B. M. and Teller, E. (1943). Interaction of the van der Waals type between three atoms. *J. Chem. Phys.*, 11:299–300.

[Aziz, 1993] Aziz, R. A. (1993). A highly accurate interatomic potential for argon. *J. Chem. Phys.*, 99:4518–4526.

[Aziz and Chen, 1968] Aziz, R. A. and Chen, H. H. (1968). An accurate intermolecular potential for argon. *J. Chem. Phys.*, 67:5719–5726.

[Becke, 1988] Becke, A. D. (1988). *J. Chem. Phys.*, 88:2547.

[Boutou et al., 1998] Boutou, V., Allouche, A. R., Spiegelmann, F., Chevaleyre, J., and Frécon, M. A. (1998). Predictions of geometrical structures and ionisation potentials for small barium clusters Ba_n. *Eur. J. Phys D*, 2:63–73.

[Boys and Bernardi, 1970] Boys, S. F. and Bernardi, F. (1970). *Mol. Phys.*, 19:553.

[Brack, 1993] Brack, M. (1993). The physics of simple metal clusters: self-consistent jellium model and semiclassical approaches. *Rev. Mod. Phys.*, 65:677–732.

[Bradely and Cracknell, 1972] Bradely, C. J. and Cracknell, A. P. (1972). *The Mathematical theory of symmetry in solids.* Clarendon Press, Oxford.

[Bréchignac et al., 1988] Bréchignac, C., Broyer, M., Cahuzac, P., Delacretaz, G., Labastie, P., Wolf, J. P., and Wöste, L. (1988). Probing the transition from van der Waals to metallic mercury clusters. *Phys. Rev. Lett.*, 60:275–278.

[Buckingham, 1967] Buckingham, A. D. (1967). *Adv. Chem. Phys.*, 12:107.

[Buckingham and Pople, 1955] Buckingham, A. D. and Pople, J. A. (1955). The dielectric constant of an imperfect non-polar gas. *Trans. Faraday Soc.*, 51:1029.

[Bukowski and Szalewicz, 2001] Bukowski, R. and Szalewicz, K. (2001). Complete *ab initio* three-body nonadditive potential in Monte Carlo simulations of vapor-liquid equilibria and pure phases of argon. *J. Chem. Phys.*, 114:9518–9531.

[Busani et al., 1998] Busani, R., Folkers, M., and Cheshnovsky, O. (1998). Direct observation of band-gap closure in mercury clusters. *Phys. Rev. Lett.*, 81:3836–3839.

[Christiansen et al., 1998] Christiansen, O., Jorgensen, P., and Hättig, C. (1998). Response functions from fourier component variational perturbation theory applied to a time-averaged quasienergy. *Int. J. Quantum Chem.*, 68:1–52.

[Christiansen et al., 1981] Christiansen, P. A., Pitzer, K. S., Lee, Y. S., Yates, J. H., Ermler, W. C., and Winter, N. W. (1981). Improved *ab initio* effective potentials for Ar, Kr, and Xe with applications to their homonuclear dimers. *J. Chem. Phys.*, 75:5410–5415.

[Czajkowski and Koperski, 1999] Czajkowski, M. A. and Koperski, J. (1999). The cd_2 and zn_2 van der Waals dimers revisited. correction for some moleular potential parameters. *Spectrochimica Acta A*, 55:2221–2229.

[de Heer, 1993] de Heer, W. A. (1993). The physics of simple metal clusters: experimental aspects and simple models. *Rev. Mod. Phys.*, 65:611–676.

[Deng et al., 1998] Deng, S., Simon, A., and Köhler, J. (1998). Superconductivity and chemical bonding in mercury. *Angew. Chem. Int. Ed.*, 37:640–643.

[Dolg and Flad, 1996] Dolg, M. and Flad, H.-J. (1996). *J. Chem. Phys.*, 100:6147.

[Dolg and Flad, 1997] Dolg, M. and Flad, H.-J. (1997). Size dependent properties of Hg_n clusters. *Mol. Phys.*, 91:815–825.

[Doye et al., 1995] Doye, J. P. K., Wales, D. J., and Berry, R. S. (1995). The effect of the range of the potential on the structures of clusters. *J. Chem. Phys.*, 103:4234–4249.

[Fernández et al., 1999] Fernández, B., Hättig, C., Koch, H., and Rizzo, A. (1999). *Ab initio* calculation of the frequency-dependent interaction induced hyperpolarizability of Ar_2. *J. Chem. Phys.*, 110:2872–2882.

[Fiolhais et al., 2003] Fiolhais, C., Nogueira, F., and Marques, M., editors (2003). *Lecture Notes in Physics; A Primer in DFT*. Springer-Verlag, Berlin.

[Flad et al., 1999] Flad, H.-J., Schautz, F., Wang, Y., Dolg, M., and Savin, A. (1999). On the bonding of small group 12 clusters. *Eur. Phys. J. D*, 6:243–254.

[Frisch et al., 2003] Frisch, M. J., Trucks, G. W., Schlegel, H. B., Scuseria, G. E., Robb, M. A., Cheeseman, J. R., Montgomery, J. A., Jr., Vreven, T., Kudin, K. N., Burant, J. C., Millam, J. M., Iyengar, S. S., Tomasi, J., Barone, V., Mennucci, B., Cossi, M., Scalmani, G., Rega, N., Petersson, G. A., Nakatsuji, H., Hada, M., Ehara, M., Toyota, K., Fukuda, R., Hasegawa, J., Ishida, M., Nakajima, T., Honda, Y., Kitao, O., Nakai, H., Klene, M., Li, X., Knox, J. E., Hratchian, H. P., Cross, J. B., Adamo, C., Jaramillo, J., Gomperts, R., Stratmann, R. E., Yazyev, O., Austin, A. J., Cammi, R., Pomelli, C., Ochterski, J. W., Ayala, P. Y., Morokuma, K., Voth, G. A., Salvador, P., Dannenberg, J. J., Zakrzewski, V. G., Dapprich, S., Daniels, A. D., Strain, M. C., Farkas, O., Malick, D. K., Rabuck, A. D., Raghavachari, K., Foresman, J. B., Ortiz, J. V., Cui, Q., Baboul, A. G., Clifford, S., Cioslowski, J., Stefanov, B. B., Liu, G., Liashenko, A., Piskorz, P., Komaromi, I., Martin, R. L., Fox, D. J., Keith, T., Al-Laham, M. A., Peng, C. Y., Nanayakkara, A., Challacombe, M., Gill, P. M. W., Johnson, B., Wong, W. C. M. W., Gonzalez, C., and Pople, J. A. (2003). Gaussian 03, Revision B.03, Gaussian, Inc., Pittsburgh PA.

[Furche et al., 2002] Furche, F., Ahlrichs, R., Weis, P., Jacob, C., Gilb, S., Bierweiler, T., and Kappes, M. K. (2002). The structures of small gold cluster anions as determined by a combination of ion mobility measurements and density functional calculations. *J. Chem. Phys.*, 117:6982–6990.

[Goebel and Hohm, 1996] Goebel, D. and Hohm, U. (1996). *J. Phys. Chem.*, 100:7710.

[Greif-Wüstenbecker, 2000] Greif-Wüstenbecker, J. N. (2000). *The polarisability anisotropy of mercury dimer obtained from collision induced Raman spectroscopy.* PhD thesis, Philipps University, Marburg.

[Haberland et al., 1990] Haberland, H., Kornmeler, H., Langosch, H., Oschwald, M., and Tanner, G. (1990). Experimental study of the transition from van der Waals, over covalent to metallic bonding in mercury clusters. *J. Chem. Soc. Faraday Trans.*, 86:2473–2481.

[Haberland et al., 1992] Haberland, H., von Issendorff, B., Yufeng, J., and Kolar, T. (1992). Transition to plasmonlike absorption in small Hg clusters. *PRL*, 69:3212–3215.

[Häkkinen et al., 2002] Häkkinen, H., Moseler, M., and Landman, U. (2002). Bonding in coinage metal clusters: Trends and surprises. *Phys. Rev. Lett.*, 89:033401.

[Hartke et al., 2001] Hartke, B., Flad, H.-J., and Dolg, M. (2001). Structures of mercury clusters in a quantum-empirical hybrid model. *Phys. Chem. Chem. Phys.*, 3:5121–5129.

[Hättig et al., 1996] Hättig, C., Kunz, C. F., and Hess, B. A. (1996). *Mol. Phys.*, 57:336.

[Head-Gordon et al., 1994] Head-Gordon, M., Rico, R. J., Oumi, M., and Lee, T. J. (1994). A doubles correction to electronic excited states from configuration interaction in the space of single substitutions. *Chem. Phys. Lett.*, 219:21–29.

[Hensel and Warren, 1999] Hensel, F. and Warren, W. W. (1999). *Fluid Metals.* Princeton University Press, Princeton, New Jersey.

[Hobza and Zahradnik, 1980] Hobza, P. and Zahradnik, R. (1980). *Weak Intermolecular Interactions in Chemistry and Biology.* Elsevier Scientific Publishing Company, Amsterdam.

[Ito et al., 1993] Ito, H., Sakurai, T., Matsuo, T., Ichihara, T., and Katakuse, I. (1993). Detection of electronic-shell structure in divalent metal clusters Hg_n. *Phys. Rev. B*, 48:48–53.

[Jellinek and Acioli, 2002] Jellinek, J. and Acioli, P. H. (2002). Magnesium clusters: Structural and electronic properties and the size-induced nonmetal to metal transition. *J. Phys. Chem A*, 106:10919–10925.

[Johansson and Pyykkö, 2004] Johansson, M. P. and Pyykkö, P. (2004). The importance of being tetrahedral: the cadmium pyramids Cd_N,; n =4, 10, 20, 35, and 56. *Phys. Chem. Chem. Phys.*, 6:2907–2909.

[Johnston, 1998] Johnston, R. L. (1998). The development of metallic behaviour in clusters. *Phil. Trans. R. Soc. Lond. A*, 356:211–230.

[Jones, 1924] Jones, J. E. L. (1924). *Proc. Roy. Soc. A*, 106:709.

[Kaiser and Rademann, 1992] Kaiser, B. and Rademann, K. (1992). Photoelectron spectroscopy of neutral mercury clusters Hg_x, ($x \leq 109$) in a molecular beam. *Phys. Rev. Lett.*, 69:3204–3208.

[Knickelbein, 2001] Knickelbein, M. B. (2001). Electric dipole polarizabilities of ni_{12-58}. *JCP*, 115:13.

[Knickelbein, 2003] Knickelbein, M. B. (2003). Electric dipole polarizabilities of nb_{2-27}. *JCP*, 118:14.

[Knickelbein, 2004] Knickelbein, M. B. (2004). Electric dipole polarizabilities of copper clusters. *JCP*, 120:22.

[Knight et al., 1984a] Knight, W. D., Clemenger, K., de Heer, W. A., Saunders, W. A., Chou, M. Y., and Cohen, M. L. (1984a). *Phys. Rev. Lett.*, 52:2141.

[Knight et al., 1984b] Knight, W. D., Clemenger, K., de Heer, W. A., Saunders, W. A., Chou, M. Y., and Cohen, M. L. (1984b). *Phys. Rev. Lett.*, 53:510.

[Koperski et al., 1994] Koperski, J., Atkinson, J. B., and Krause, L. (1994). The $O_u^+(6^3P_1 \leftarrow XO_g^+$ spectrum of Hg_2 excited in a supersonic jet. *Chem. Phys. Lett.*, 219:161.

[Koperski et al., 1997] Koperski, J., Atkinson, J. B., and Krause, L. (1997). The $GO_u^+(6^1P_1 - XO_g^+$ excitation and fluorescence spectra of Hg_2 excited in a supersonic jet. *Chem. Phys. Lett.*, 22:2852.

[Kresse and Hafner, 1997] Kresse, G. and Hafner, J. (1997). Ab initio simulation of the metal/nonmetal transition in expanded fluid mercury. *Phys. Rev. B*, 55:7539–7548.

[Kronik et al., 2002] Kronik, L., Fromherz, R., Ko, E., Ganteför, G., and Chelikowsky, J. R. (2002). Highest electron affinity as a predictor of cluster anion structures. *Nature Materials*, 1:49–53.

[Landman and Barnett, 1993] Landman, U. and Barnett, R. (1993). Born-Oppenheimer molecular dynamics simulations of finite systems: Structure and dynamics of $(H_2O)_2$. *Phys. Rev. B*, 48:2081–2097.

[Langlet et al., 2004] Langlet, J., Bergès, J., and Reinhardt, P. (2004). An interesting property of the Perdew-Wang 91 density functional. *Chem. Phys. Lett.*, 396:10–15.

[Lide, 2002] Lide, D. R., editor (2002). *The CRC Handbook of Chemistry and Physics.* CRC Press, New York.

[Maroulis, 2005] Maroulis, G. (2005). Personal communication.

[Martin, 1996] Martin, T. P. (1996). Shells of atoms. *Physics Reports*, 273:199–241.

[Maurice and Head-Gordon, 1996] Maurice, D. and Head-Gordon, M. (1996). *JPC*, 100:6131.

[Moore and Al-Quraishi, 2000] Moore, B. G. and Al-Quraishi, A. A. (2000). The structure of liquid clusters of Lennard-Jones atoms. *Chem. Phys.*, 252:337–347.

[Moore, 1958] Moore, C. E., editor (1958). *Atomic Energy Levels.* Natl. Bur. Stand. Circ. No. 467, U.S. Government Printing Office, Washington D.C.

[Moro et al., 2003] Moro, R., Xu, X., Yin, S., and de Heer, W. A. (2003). Ferroelectricity in free niobium clusters. *Science*, 300:126.

[Moseler et al., 2003] Moseler, M., Huber, B., Häkkinen, H., Landman, U., Wrigge, G., Hoffmann, M. A., and v. Issendorff, B. (2003). Thermal effects in the photoelectron spectrum of Na_n^- clusters ($n = 4 - 19$). *Phys. Rev. B*, 68:165413.

[Moyano et al., 2002] Moyano, G. E., Wesendrup, R., Söhnel, T., and Schwerdtfeger, P. (2002). Properties of small- to medium-sized mercury clusters from a combined *ab* initio, density-functional, and simulated-annealing study. *Phys. Rev. Lett.*, 89:10.

[Nakatsuji et al., 2002] Nakatsuji, H., Hada, M., Ehara, M., Toyota, K., Fukuda, R., Hasegawa, J., Ishida, M., Nakajima, T., Honda, Y., Kitao, O., and Nakai, H. (2002). SAC/SAC-CI Program, Department of Synthetic Chemistry and Biological Chemistry, Graduate School of Engineering, Kyoto University, Japan.

[Northby, 1987] Northby, J. A. (1987). Structure and binding of Lennard-Jones clusters: $13 \leq N \leq 147$. *J. Chem. Phys.*, 87:6166–6177.

[Paulus, 2004] Paulus, B. (2004). Personal communication.

[Paulus and Rościszewski, 2004] Paulus, B. and Rościszewski, K. (2004). Metallic binding due to electronic correlations: a quantum chemical ab initio calculation of the cohesive energy of mercury. *Chem. Phys. Lett.*, 394:96–100.

[Perdew and Wang, 1991a] Perdew, J. P. and Wang, Y. (1991a). Correlation hole of the spin-polarized electron gas, with exact small-wave-vector and high density scaling. *Phys. Rev. B*, 44:13298.

[Perdew and Wang, 1991b] Perdew, J. P. and Wang, Y. (1991b). Spin scaling of the electron gas correlation energy in the high density limit. *Phys. Rev. B*, 43:8911.

[Perdew and Wang, 1992] Perdew, J. P. and Wang, Y. (1992). Accurate and simple analytic representation of the electron-gas correlation energy. *Phys. Rev. B*, 45:13244.

[Pisani et al., 1988] Pisani, C., Dovesi, R., and Roetti, C. (1988). *Hartree-Fock Ab Initio Treatment of Crystalline Systems.* Springer-Verlag, Berlin.

[Pyykkö, 1988] Pyykkö, P. (1988). Relativistic effects in structural chemistry. *Chem. Rev.*, 88:563–594.

[Rademann et al., 1992] Rademann, K., Dimopoulou-Rademann, O., Schlauf, M., Even, U., and Hensel, F. (1992). Evolution of surface plasmon resonance absorption in large gas phase clusters of mercury. *Phys. Rev. Lett.*, 69:3208–3212.

[Rigby et al., 1986] Rigby, M., Smith, E. B., Wakeham, W. A., and Maitland, G. C. (1986). *The Forces between Molecules.* Clarendon Press, Oxford.

[Saue, 2003] Saue, T. (2003). Personal communication.

[Saue et al., 2000] Saue, T., Bakken, V., Enevoldsen, T., Helgaker, T., Jensen, H. J. A., Laerdahl, J. K., Ruud, K., Thyssen, J., and Visscher, L. (2000). "DIRAC, a relativistic *ab initio* electronic structure program, release 3.2", (http://dirac.chem.sdu.dk).

[Saue and Jensen, 2003] Saue, T. and Jensen, H. J. A. (2003). Linear response at the 4-component relativistic level: Application to the frequency-dependent polarizabilities of the coinage metal dimers. *J. Chem. Phys.*, 118:522–536.

[Saunders et al., 2003] Saunders, V., Dovesi, R., Roetti, C., Orlando, R., Zicovich-Wilson, C., Harrison, N., Doll, K., Civalleri, B., Bush, I., D'Arco, P., and Llunell, M. (2003). Crystal03, (www.crystal.unito.it), Turin.

[Schwerdtfeger et al., 1994] Schwerdtfeger, P., Li, J., and Pyykkö, P. (1994). *Theor. Chim. Acta*, 87:313.

[Schwerdtfeger et al., 2001] Schwerdtfeger, P., Wesendrup, R., Moyano, G. E., Sadlej, A. J., Greif, J., and Hensel, F. (2001). The potential energy curve and dipole polarizability tensor of mercury dimer. *J. Chem. Phys.*, 115:16.

[Seth et al., 1997] Seth, M., Schwerdtfeger, P., and Dolg, M. (1997). The chemistry of the superheavy elements. I. Pseudopotentials for 111 and 112 and relativistic coupled cluster calculations for $(112)H^+$,$(112)F_2$, and $(112)F_4$. *J. Chem. Phys.*, 106:3623.

[Singh, 1994] Singh, P. P. (1994). Relativistic effects in mercury: Atom, clusters and bulk. *Phys. Rev. B*, 49:4954–4958.

[T. H. Dunning, 1989] T. H. Dunning, J. (1989). *J. Chem. Phys.*, 90:1007.

[Tikhonov et al., 2001] Tikhonov, G., Kasperovich, V., Wong, K., and Kresin, V. V. (2001). A measurement of the polarisability of sodium clusters. *PRA*, 64:063202.

[Trouillier and Martins, 1991] Trouillier, N. and Martins, J. L. (1991). *Phys. Rev. B*, 43:1993.

[van der Hoeven and Keesom, 1964] van der Hoeven, B. J. C. and Keesom, P. H. (1964). Specific heat of mercury and thallium between 0.35 and 4.2 K. *Phys. Rev.*, 135:A631.

[van der Waal, 1996] van der Waal, B. W. (1996). No evidence for size-dependent icosahedral $\rightarrow$ fcc structural transition in rare-gas clusters. *Phys. Rev. Lett.*, 76:1083–1086.

[van der Waal et al., 2000] van der Waal, B. W., Torchet, G., and de Feraudy, M.-F. (2000). Structure of large argon clusters Ar_N, $10^3 \leq N \leq 10^5$: experiments and simulations. *Chem. Phys. Lett.*, 331:57–63.

[Visscher et al., 1997] Visscher, L., Saue, T., and Oddershede, J. (1997). *Chem. Phys. Lett.*, 274:181.

[von Issendorff, 1994] von Issendorff, B. (1994). *Photofragmentation massenselektierter ionischer Edelgas- und Quecksilbercluster.* PhD thesis, Albert-Ludwigs-Universität, Freiburg im Breisgau.

[Wales et al., 2004] Wales, D. J., Doye, J. P. K., Dullweber, A., Hodges, M. P., Naumkin, F. Y., Calvo, F., Hernández-Rojas, J., and Middleton, T. F. (2004). "The Cambridge cluster database", (http://www-wales.ch.cam.ac.uk/ccd.html).

[Wang et al., 2000] Wang, Y., Flad, H.-J., and Dolg, M. (2000). Realistic hybrid model for correlation effects in mercury clusters. *Phys. Rev. B*, 61:3.

[Werner et al., 2003] Werner, H.-J., Knowles, P. J., Lindh, R., Schütz, M., Celani, P., Korona, T., Manby, F. R., Rauhut, G., Amos, R. D., Bernhardsson, A., Berning, A., Cooper, D. L., Deegan, M. J. O., Dobbyn, A. J., Eckert, F., Hampel, C., Hetzer, G., Lloyd, A. W., McNicholas, S. J., Meyer, W., Mura, M. E., Nicklass, A., Palmieri, P., Pitzer, R., Schumann, U., Stoll, H., Stone, A. J., Tarroni, R., and Thorsteinsson, T. (2003). Molpro, version 2002.6, a package of ab initio programs, http://www.molpro.net/, Birmingham, UK.

[Wilson and Peterson, 2003] Wilson, A. K. and Peterson, K. A., editors (2003). *Recent Advances in Electron Correlation Methodology.* ACS, in press.

[Wilson et al., 1999] Wilson, A. K., Woon, D. E., Peterson, K. A., and T. H. Dunning, J. (1999). *J. Chem. Phys.*, 110:7667.

[Woon and T. H. Dunning, 1993] Woon, D. E. and T. H. Dunning, J. (1993). *J. Chem. Phys.*, 98:1358.

[Yamaguchi et al., 1994] Yamaguchi, Y., Goddard, J. D., Osamura, Y., and Schaefer, H. (1994). *A New Dimension to Quantum Chemistry: Analytic Derivative Methods in Ab Initio Molecular Electronic Structure Theory.* Oxford University Press, Oxford.

[Zehnacker et al., 1987] Zehnacker, A., Duval, M., Jouvet, C., Lardeux-Dedonder, C., Solgadi, D., Soep, B., and d'Azy, O. B. (1987). *J. Chem. Phys.*, 86:6565.